EFFECT OF BUOYANCY ON JETS IN CROSSFLOW - APPLICATION TO THE KRAFT RECOVERY BOILER

By

Fariba F. Aghdasi

B. Sc. (Chemical Engineering) University of Maryland, 1982

M. Sc. (Chemical Engineering) University of Maryland, 1983

A THESIS SUBMITTED IN PARTIAL FULFILLMENT OF

THE REQUIREMENTS FOR THE DEGREE OF

DOCTOR OF PHILOSOPHY

in

THE FACULTY OF GRADUATE STUDIES

DEPARTMENT OF MECHANICAL ENGINEERING

We accept this thesis as conforming

to the required standard

THE UNIVERSITY OF BRITISH COLUMBIA

August 1994

© Fariba F. Aghdasi, 1994

In presenting this thesis in partial fulfillment of the requirements for an advanced degree at the University of British Columbia, I agree that the Library shall make it freely available for reference and study. I further agree that permission for extensive copying of this thesis for scholarly purposes may be granted by the head of my department or by his or her representatives. It is understood that copying or publication of this thesis for financial gain shall not be allowed without my written permission.

(Signature)

Department of Mechanical Engineering

The University of British Columbia
Vancouver, Canada

Date AUG. 1994

Abstract

This thesis investigates the effect of buoyancy forces on jets in a crossflow, with specific application to kraft recovery furnaces. Both experimental and numerical studies are presented. Experiments were conducted to investigate the concentration profiles of variable density slot jets issuing into a confined crossflow. A recently-developed multigrid computational fluid dynamics code is used to find the flow pattern of variable density jets in a crossflow. The governing equations of motion for non-isothermal flow, i.e. mass continuity, Navier-Stokes equations, and energy equation, are discretized using the control volume technique. The turbulence phenomena are modelled using modified $k - \epsilon$ equations. The validity of the code for variable density conditions is verified by comparison with experimental results. Numerical modelling of two-dimensional slot jets in crossflow, simulating the primary air jets in the kraft recovery furnace, is carried out. The effect of buoyancy force on the penetration and spread of these jets is investigated. It is found that, for horizontal jets being issued into an upwards crossflow, excluding the buoyancy force from the momentum equation results in under prediction of the jet penetration and spread. The effect of buoyancy force on the penetration of the jet is found to be significantly affected by the orientation of the jet and the crossflow. The effects of buoyancy force on the flow field of three-dimensional single jets and a row of jets issuing into a crossflow, which simulates the tertiary air jets in a kraft recovery furnace, are investigated. The penetration of the row of jets is found to be more significantly affected by buoyancy than is the penetration of a single jet. Numerical simulation of the flow field inside the full kraft recovery furnace is carried out. The gross features of the gas flow fields inside the furnace for cases both with and without the buoyancy force are similar.

Table of Contents

Abstract ii

Table of Contents iii

List of Tables vi

List of Figures vii

Nomenclature xiii

Acknowledgment xviii

1 Introduction 1

1.1 A Description of the Kraft Recovery Furnace 2

1.2 Air Delivery System 4

1.3 Operational Problems of the Kraft Recovery Furnace 6

1.4 Literature Review 8

1.5 Purpose and Scope of the Present Work 13

2 Mathematical Model and Computational Procedure 17

2.1 Mathematical Model for Jet Flows and Time-Averaging 17

2.2 Turbulence Modelling : $k - \epsilon$ Turbulence Model 20

2.3 General Transport Equation 24

2.4 Boundary Conditions 24

2.5 Computational Procedure 26

2.5.1 Finite Volume Formulation and Discretization 27
2.5.2 Solution Procedure 32
2.5.3 Multigrid Technique 35
2.5.4 Segmentation Capability 37
2.6 Convergence Criterion 38

3 Experimental Study **40**
3.1 Experimental Set-Up and Apparatus 40
3.2 Concentration Measurement Technique 41
3.2.1 FID Calibration 44
3.3 Experimental Results 47
3.3.1 Two-dimensionality 49
3.3.2 Effect of Density variations on Jet in Crossflow 53

4 Effects of Buoyancy on Two-Dimensional Jets in Cross-Flow **62**
4.1 Comparison of Experimental and Numerical Results 62
4.1.1 Problem Description and boundary Conditions 62
4.1.2 Comparison of Calculations and Experimental Data 64
4.2 Two-Dimensional Investigation of the Primary Air Jets 73
4.2.1 Primaries: Problem Description and Boundary Conditions 76
4.2.2 Effect of Confinement, Velocity Ratio, and Density Ratio 79
4.2.3 Effect of the Jet Orientation 93

5 Effects of Buoyancy on Three-Dimensional Jets in Cross-Flow **106**
5.1 Three-Dimensional Single Jet in a Confined Crossflow 107
5.2 Array of Three-Dimensional Jets 127

6 Effects of Buoyancy in the Kraft Recovery Boiler **138**

6.1 Problem Description and Boundary Conditions 138

6.2 Results and Discussion 143

7 Conclusions and Recommendations **169**

Appendices **177**

A Mixing of Variable Density Jets with Crossflow **177**

References **180**

List of Tables

2.1 Parameters in the $k - \epsilon$ model 24

2.2 Diffusion coefficients and source terms for the governing equations. 25

2.3 Discretized source terms. 31

3.1 Range of dimensionless numbers for the experiments 59

4.1 Summary of the flow variables 65

4.2 Summary of the flow variables for calculations of the primaries 76

4.3 Summary of the flow variables for study of the jet/crossflow orientation . 95

5.1 Summary of the flow variables for calculations of the tertiaries 107

List of Figures

1.1 Schematic presentation of a kraft recovery furnace. 3

1.2 Schematic presentation of a cold jet in a hot crossflow. 'Stable' and 'Unstable' refers to the interface of the jet and crossflow at the top and the bottom. 13

2.1 Grid arrangement in MGFD code. 27

2.2 Presentation of Multigrid cycle. 37

3.1 Schematic presentation of the experimental set-up. 41

3.2 Schematic presentation of FID. 42

3.3 Linearity of FID for air and carbon dioxide. 46

3.4 Calibration of FID for carbon dioxide and helium/air gas 48

3.5 Test of tunnel two-dimensionality, velocity measurements for $U_c = 2$ and $5\ m/s$, and no jet injected. 50

3.6 Test of tunnel two-dimensionality, velocity measurements for $U_c = 5m/s$ and $R = 0.4$. 51

3.7 Test of tunnel two-dimensionality, concentration measurements for $U_c = 2m/s$ and $R = 0.2$ and 0.6. 52

3.8 Cross-stream concentration profiles at $G = 0.4$ for air, carbon dioxide and helium/air jets. 55

3.9 Cross-stream concentration profiles at $G = 0.6$ for air, carbon dioxide, and helium/air jets. 56

3.10 Cross-stream concentration profiles at $G = 0.8$ for air, carbon dioxide, and helium/air jets. 57

3.11 Variation of 'film cooling effectiveness' η with dimensionless distance from the slot for air, carbon dioxide, and heliume/air jets and three mass ratios G. 58

4.1 Schematic representation of a two dimensional jet into crossflow. 63

4.2 Grid distribution. 65

4.3 Comparison of measured and calculated cross-stream concentration profiles for carbon dioxide jet, $G = 0.4$. 66

4.4 Comparison of measured and calculated cross-stream concentration profiles for carbon dioxide jet, $G = 0.6$. 67

4.5 Comparison of measured and calculated cross-stream concentration profiles for carbon dioxide jet, $G = 0.8$. 68

4.6 Comparison of measured and calculated cross-stream concentration profiles for helium/air jet, $G = 0.4$. 71

4.7 Comparison of measured and calculated cross-stream concentration profiles for air jet, $G = 0.4$. 72

4.8 Comparison of measured and calculated cross-stream concentration profiles for air jet, $G = 0.6$. 73

4.9 Comparison of measured and calculated cross-stream concentration profiles for air jet, $G = 0.8$. 74

4.10 Schematic representation of a two-dimensional jet into crossflow. 77

4.11 Computational mesh. 78

4.12 Normalized velocity profiles, $\rho_j/\rho_c = 3$. 80

4.13 Normalized velocity profiles. 81

4.14 Jet fluid concentration trajectories, NB refers to No Buoyancy. 83
4.15 Jet fluid concentration profiles, $\rho_j/\rho_c = 3$. 85
4.16 Jet fluid concentration profiles, $R = 4$. 86
4.17 Effect of buoyancy on degree of mixing. 89
4.18 The decaying process of jet concentration along the jet concentration trajectory. 91
4.19 Total velocity profiles along the velocity trajectory. 92
4.20 Convergence histories for different cases of R, ρ_j/ρ_c, and D/S. 94
4.21 Schematic representation of simulated two-dimensional flow domain. . . . 96
4.22 Normalized velocity vectors for $R = 4$, 'Down' refers to the jet injected from the bottom, and 'Up' refers to the jet injected from the top. 98
4.23 Jet fluid concentration profiles for $R = 4$, 'Down' refers to the jet injected from the bottom, and 'Up' refers to the jet injected from the top. 99
4.24 Jet fluid concentration profiles for $R = 2$, 'Down' refers to the jet injected form the bottom, and 'Up' refers to the jet injected from the top. 100
4.25 Effect of buoyancy on degree of mixing. 101
4.26 Jet fluid concentration trajectories. 102
4.27 Recirculation region of two-dimensional jets, J refers to jet, XF refers to the crossflow, NB refers to the case with no buoyancy force, and the arrows show the flow direction. 104
4.28 Convergence histories for different cases of R 105

5.1 Schematic representation of a three-dimensional jet into crossflow. 108
5.2 Jet fluid concentration trajectories. 110
5.3 Normalized vector velocity profiles for $D/S = 28$ and $R = 6$ and 8 along the jet center plane. 112

5.4 Jet fluid concentration profiles for $D/S = 28$ along the jet center plane. . 113
5.5 Normalized vector velocity profiles for $R = 6$ and $D/S = 14$ and 28. . . . 115
5.6 A zoom in view of normalized vector velocity profiles for $R = 6$ and 8 and $D/S = 14$. 116
5.7 The decaying process of jet concentration along the jet concentration trajectory. 117
5.8 Jet concentration profiles for $R = 6$ and $D/S = 14$ (including buoyancy terms). 119
5.9 Jet concentration profiles for $R = 6$ and $D/S = 14$ (excluding buoyancy terms). 120
5.10 Jet concentration profiles for $R = 6$ and $D/S = 28$ (including buoyancy terms). 121
5.11 Jet concentration profiles for $R = 6$ and $D/S = 28$ (excluding buoyancy terms). 122
5.12 Jet concentration profiles for $R = 8$ and $D/S = 28$ (including buoyancy terms). 123
5.13 Jet concentration profiles for $R = 8$ and $D/S = 28$ (excluding buoyancy terms). 124
5.14 Effect of buoyancy on diffusion parameter or mixing. 126
5.15 Convergence histories for different cases of R and D/S. 128
5.16 Schematic representation of array of jets into crossflow. 129
5.17 Jet fluid concentration trajectories. 130
5.18 Velocity profiles along the jet center plane. 132
5.19 Jet fluid concentration profiles along the jet center plane. 133
5.20 The decaying process of jet concentration along the jet concentration trajectory. 134

5.21 Jet concentration profiles (including buoyancy terms). 135
5.22 Jet concentration profiles (excluding buoyancy terms). 136
5.23 Effect of buoyancy on diffusion parameter or mixing. 137
5.24 Convergence histories for array of jets. 137

6.1 Schematic representation of the kraft recovery furnace. 140
6.2 Mesh distribution for furnace simulations. 142
6.3 Concentration contours, $x = 5m$, computed heat source distribution. . . . 150
6.4 Concentration contours, $x = 5m$, assumed heat source distribution. . . . 150
6.5 Concentration contours, $x = 4m$, computed heat source distribution. . . . 151
6.6 Concentration contours, $x = 4m$, assumed heat source distribution. . . . 151
6.7 Concentration contours, $x = 2m$, computed heat source distribution. . . . 152
6.8 Concentration contours, $x = 2m$, assumed heat source distribution. . . . 152
6.9 Concentration contours, $x = 3m$, computed heat source distribution. . . . 153
6.10 Concentration contours, $x = 3m$, assumed heat source distribution. . . . 153
6.11 Concentration contours, $x = 1m$, computed heat source distribution. . . . 154
6.12 Concentration contours, $x = 1m$, assumed heat source distribution. . . . 154
6.13 Concentration contours, $y = 5m$, computed heat source distribution. . . . 155
6.14 Concentration contours, $y = 5m$, assumed heat source distribution. . . . 155
6.15 Concentration contours, $y = 2.5m$, computed heat source distribution. . . 156
6.16 Concentration contours, $y = 2.5m$, assumed heat source distribution. . . 156
6.17 Concentration contours, $y = 3.75m$, computed heat source distribution. . 157
6.18 Concentration contours, $y = 3.75m$, assumed heat source distribution. . . 157
6.19 Vertical velocity contours, $x = 5m$, computed heat source distribution. . 158
6.20 Vertical velocity contours, $x = 5m$, assumed heat source distribution. . . 158
6.21 Vertical velocity contours, $x = 4m$, computed heat source distribution. . 159

6.22 Vertical velocity contours, $x = 4m$, assumed heat source distribution. . . 159
6.23 Vertical velocity contours, $x = 3m$, computed heat source distribution. . 160
6.24 Vertical velocity contours, $x = 3m$, assumed heat source distribution. . . 160
6.25 Vertical velocity contours, $x = 1m$, computed heat source distribution. . 161
6.26 Vertical velocity contours, $x = 1m$, assumed heat source distribution. . . 161
6.27 Vertical velocity contours in horizontal planes, computed heat source distribution. 162
6.28 Vertical velocity contours in horizontal planes, computed heat source distribution. 163
6.29 Concentration contours in horizontal planes, computed heat source distribution. 164
6.30 Concentration contours in horizontal planes, computed heat source distribution. 165
6.31 Temperature contours in horizontal planes, computed heat source distribution. 166
6.32 Temperature contours in horizontal planes, computed heat source distribution. 167
6.33 Extent of mixing of the jets and the crossflow in the furnace. 168

Nomenclature

a_i	coefficients of finite difference equations
A	cross-sectional area
A_d	cross-sectional area where the jet fluid concentration is 3% or more
AR	Aspect ratio of jet orifice ($= H/W$)
B	confinement depth
B'	constant of proportionality for the flame ionization detector
C	concentration
C_m	maximum jet fluid concentration
C_1, C_2, C_3, C_4	turbulence model constants
$\bar{d}$	defect or residual quantity
D	confinement width
D_e	diffusive flux through the east cell face
E	flame ionization detector output voltage
E_0	flame ionization detector output voltage when no propane present
f	instantaneous form of a general variable
f'	fluctuating part of f
$f(\dot{Q})$	function of $\dot{Q}$
F	time averaged part of f
F_e	sum of convective and diffusive fluxes through the east cell face
F_b/F_d	ratio of buoyancy force to drag force
Fr	Froude number $\left(= \frac{V_j}{\sqrt{gS(\rho_c-\rho_j)/\rho_c}}\right)$
g	gravitational acceleration
G	jet to crossflow mass ratio ($= \rho_j U_j/\rho_c U_c$)

G_k	generation of turbulent kinetic energy due to shear stress
G_B	generation of turbulent kinetic energy due to buoyancy
G_H	size of the coarse grid used in discretization of domain
G_h	size of the fine grid used in discretization of domain
H	height of jet orifice
h	spacing between jet centerlines
I	turbulence intensity $(= \sqrt{\frac{1}{3}(\overline{u_i'^2})}/U_i)$
I_H^h	prolongation operator
I_h^H	restriction operator
J	jet to crossflow momentum flux ratio $(= \rho_j U_j^2/\rho_c U_c^2)$
K	jet fluid diffusion parameter $(= A_d/A)$
k	turbulent kinetic energy
$\aleph$	non-linear differential operator
L	confinement length
L_h, L_H	discrete approximations to $\aleph$ on grids G_h and G_H, respectively
l	length scale of turbulence dissipation $(\propto k^{3/2}/\epsilon)$
M	total jet to crossflow momentum flux ratio $(= \rho_j U_j^2 A_j/\rho_c U_c^2 A_c\ )$
m	gas mass fraction
P	Pressure
P_{eff}	modified pressure $\left(= P + \frac{2}{3}\left(\rho k + \mu_t \partial U_i/\partial x_i\right)\right)$
$P(\zeta)$	probability function of ζ
$P_z(\zeta)$	$P(\zeta)$ computed at the streamwise location z
Q	solution vector
Q_1	volume flow rate of the crossflow
Q_2	volume flow rate of the jet

Q_H	discrete approximation to Q
$\dot{Q}$	volume flow rate
q	approximation to Q_H
$\bar{q}$	smoothed version of q
R	jet to crossflow velocity ratio ($= V_j/U_c$)
R_f	flux Richardson number ($= G_B/G_k$)
Ri_0	jet exit Richardson number ($= gS(\rho_c - \rho_j)/\rho_c V_j^2$) square inverse of Fr
R'	ideal gas constant
$\bar{s}$	correction to $\bar{q}$
S	characteristic length scale of jet orifice ($= \sqrt{HW}$)
S_ϕ	source term in the transport equation for Φ
S_P^ϕ, S_C^ϕ	coefficients of linearized source term
t	time
T	temperature
T_c	temperature of crossflow
T_j	temperature of jet
U_c	crossflow velocity far upstream of the jet
U_i	mean velocity components (i = 1,2,3)
u_i	instantaneous velocity components
$\overline{u_i'}$	time average fluctuating velocity components
v	velocity vector
V_j	jet velocity
V_t	total velocity ($=\sqrt{U_1^2 + U_2^2 + U_3^2}$)
W	width of jet
x, y, z	Cartesian coordinates

Greek Symbols

α, β, γ	sum of descritized coefficients
β'	volumetric gas constant
δ_x	normalized standard deviation measuring the degree of mixing
δx_i	grid spacing
ϵ	dissipation rate of turbulent kinetic energy
ζ	deviation of C from $\bar{C}$ $(= C - \bar{C})$
η	film cooling effectiveness
θ	general scalar variable (concentration, temperature, etc.)
$\theta_{\prime}$	fluctuating component of θ
Θ	time averaged component of θ
Γ_ϕ	diffusion coefficient for Φ
κ	von Karman constant
λ	molecular diffusivity
μ	dynamic viscosity
μ_t	turbulent viscosity
μ_{eff}	effective viscosity $(= \mu + \mu_t)$
ν	kinematic viscosity
ρ	density
Φ	general variable
Ψ	general function
$\sigma_k, \sigma_\epsilon, \sigma_\theta$	parameters in k, ϵ, and Θ equations
σ_z^2	variance of $P_z(\zeta)$

σ_0^2	maximum variance computed before mixing

Superscript

j	generic index representing the stage of iteration

Subscript

c	value associated with the crossflow
h	value associated with the fine grid
H	value associated with the coarse grid
j	value associated with the jet
n, s, e, w, b, t	cell faces
$P, N, S, E,$	grid points
W, B, T	
0	exit value
∞	reference value

Acknowledgment

I wish to express my gratitude to my supervisors, Dr. Martha E. Salcudean and Dr. Ian S. Gartshore for their continued support, care and guidance. I wish to acknowledge the suggestions and contributions of friends and colleagues Dr. Zia Abdullah, Dr. Paul Nowak, Mr. Mike Savage, Mr. Kegang Zhang, Dr. Peri Sabhapathy, Mr. Paul Matys, Mr. Jeffry Quick, and Dr. Daniel Tse. Thanks are also due to Mr. Alan Steeves for his helpful assistance with the computer facilities. I am grateful to the staff at the Mechanical Engineering workshop for assisting me with my experimental set-up. My sincere appreciations to my dear friend Prof. Karin Mickelson for her assistance during the write-up of this thesis. The moral support and encouragement of other friends, too many to be mentioned by name here, will be always remembered. Special thanks to my husband Farzin for his patience, love, faith, and helpful ideas, and to my son Bayan, much of whose companionship has been sacrificed for the completion of this work; to them I dedicate this work. This study was supported by the Canadian Commonwealth Scholarship.

Chapter 1

Introduction

To study the effect of density variations and buoyancy force on the interaction of a jet with a crossflow, which is relevant to the design and operation of a kraft recovery furnace, it is first necessary to describe the furnace and its functions. Understanding the complexities of the processes involved clarifies the need for numerical modelling as a means to investigate alternative operating conditions and furnace designs.

As measurement is not easily possible in a kraft recovery furnace during operation, Adams (1987) advocates the use of isothermal flow physical models for optimizing the design of the furnace. Such small scale models have been used to determine such things as the air jet penetration, mixing efficiencies, and velocity profiles. To date much of the information available on the gas flow patterns in the kraft recovery furnace is based on such isothermal flow modelling of these furnaces. The limitation of the isothermal scale models is that buoyancy force effects, and other effects due to variable density in the flow, are not present.

In subsequent sections a brief description of the kraft recovery furnace is given. Then, a review of the literature relevant to modelling of the kraft recovery furnace and the effect of variable density and buoyancy force on jet in crossflow is presented. Finally the objectives of the present investigation are identified.

1.1 A Description of the Kraft Recovery Furnace

The kraft recovery furnace is an integral part of the pulping process. The main function of this combustion unit is to burn 'black liquor', which is a by-product of the kraft pulping process. By burning black liquor one may both recover inorganic chemicals involved in the pulping process and produce steam. An efficient combustion process reduces pollutants, such as hydrogen sulfide and carbon-monoxide present, in the combustible gases. Detailed description of kraft recovery furnaces, the physical and chemical processes occuring in a furnace, and the considerations that go into their design, are given by Grace (1985), Blackwell (1990), Barsin (1989), and Adams and Frederick (1988).

The kraft recovery furnace is a large and expensive piece of equipment. A typical kraft recovery furnace is $10m$ by 10 m in cross-section and about 40 m high. Due to the high fouling rate of the black liquor, recovery furnaces require larger heat exchange areas than other industrial furnaces with the same steaming rate. For a mill producing 1000 ton per day of pulp, the approximate cost of the furnace is $80 million (Jones, 1989). Due to the high capital cost of the furnace and the furnace's potential for producing air pollution, its efficient operation is of utmost importance.

The walls of the furnace are composed of numerous vertical tubes that are insulated on the outside. The top of the furnace is partially blocked by the bullnose. The purpose of the bullnose is to direct the flow of gas over the superheater and to shield the heat transfer surfaces from the direct radiation from the combustion in the lower furnace. A schematic of a typical kraft furnace is shown in Figure 1.1.

The bullnose side of the furnace is referred to as the back of the furnace. In this investigation the furnace cavity, which extends from below the bullnose to the furnace floor, is the region of interest. The region above the bullnose is usually referred to as the convective heat transfer section. The main mechanism of heat transfer in the furnace

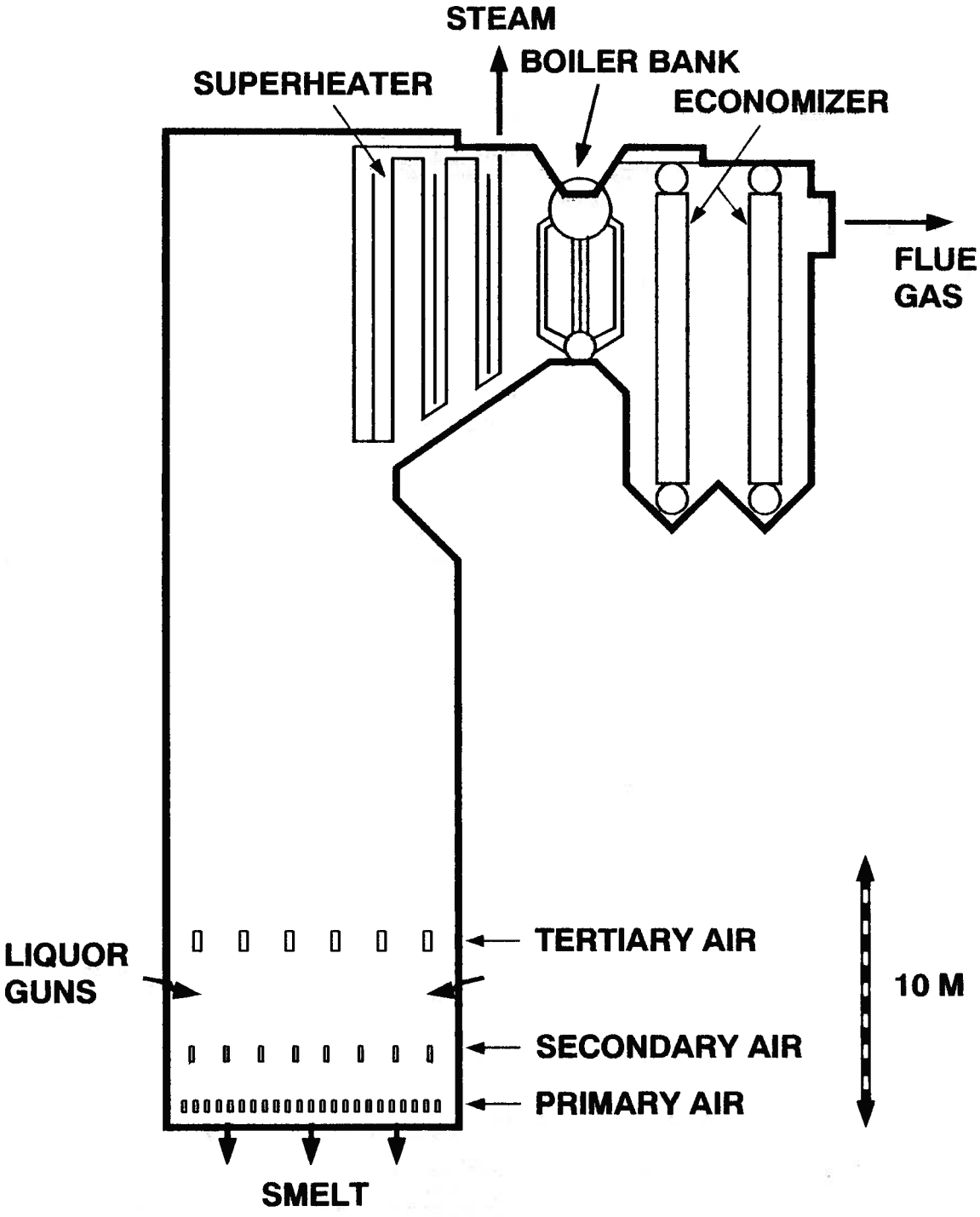

Figure 1.1: Schematic presentation of a kraft recovery furnace.

cavity is by radiation from the gases to the furnace walls. Water passing through the wall tubes absorbs the generated heat. At the exit from the furnace cavity the gases come in contact with the superheater, followed by the boiler bank and the economizer.

Black liquor, a by-product of the pulping process, is the fuel fired in the kraft recovery furnace. Dilute black liquor is recovered during washing of pulp. The solid portion of black liquor is composed of about 50% organics from lignin materials in the wood, and 50% inorganics from spent pulping chemicals; the exact composition of the black liquor depends on the wood species processed. In a pulp mill with a capacity of 1000 tons per day, about 15 kilograms per second of black liquor is fired. The liquor is sprayed into the furnace through nozzles which are located on the walls about 4 meters from the floor.

The inorganics and unburned organics form a char bed on the floor of the furnace. Maintaining a constant height of the char bed is important to the smooth operation of the furnace. Generally the ultimate capacity of the recovery furnaces is limited by two factors:

- The ability of the furnace to burn all the liquor that is sprayed into it without having the bed grow uncontrollably.
- The ability to prevent carryover. Carryovers result in plugging of the gas passages through the superheaters and boiler bank.

Therefore one of the main considerations in the design and operation of kraft recovery furnaces is the way in which combustion air enters the furnace. This is the topic of the next section.

1.2 Air Delivery System

The black liquor sprayed into the boiler requires oxygen for combustion. This oxygen is supplied in the form of air force through rectangular ports that are distributed on the

furnace walls. These ports are formed by bending several of the wall tubes, and cutting longitudinal holes in the tube walls. In order to minimize the number of tubes that require bending, these ports are in the shape of slender vertical slots. The functions of the combustion air are:

- To provide sufficient air for complete combustion,
- To provide appropriate reduction environments in the lower furnace and oxidation environment in the upper furnace,
- To control the bed shape,
- To minimize carryover.

To fulfill these requirements in a modern recovery furnace, the air is introduced into the furnace at three different levels. The primary air ports are located just above the floor of the furnace, typically on all four walls. The primary air supplies about 40% of the total air for combustion. The secondary air ports are located about two to three meters above the floor, just below the liquor spray nozzles, on two or four walls. Secondary air supplies additional air to complete the combustion of the liquor on the char bed. Tertiary air ports are located about ten meters above the floor, usually only on the front and back walls. They are placed above the level of the liquor spray nozzles. Tertiary air supplies about 20%of the required combustion air. The function of the tertiary air jets is to provide adequate oxygen and the mixing required to complete the combustion of unburned fuel. In a typical size kraft recovery furnace, about 50 kilograms of air per second is introduced into the furnace. As stated by Lefebvre and Burelle (1988) it is thought to be desirable that the gases above the tertiaries have relatively uniform velocity and temperature profiles.

Kraft recovery furnaces differ from other combustion devices in a number of ways. These differences impose certain operating constraints that make the efficient operation of the furnace a complex task. These matters are the subject of the following section.

1.3 Operational Problems of the Kraft Recovery Furnace

One of the important features of the kraft recovery furnace, which imposes severe constraints on its operation, is the separate introduction of the fuel and oxygen. Optimum mixing of the fuel and oxygen is essential for improved efficiency of the boiler. The design of the air distribution system is affected by the variety of tasks that the furnace has to fulfill. The completion of the reduction reactions in the bed for recovery of the inorganics, the control of the size of the bed, and the complete combustion of organics are among the many tasks of the system. The evaluation of the size, number, and the location of the air ports is mainly based on the oxygen requirement of the furnace. The production in the pulp mill is often limited by the amount of black liquor that the recovery furnace can burn. Increasing the liquor throughput beyond the capacity of the furnace or incorrect operation of the boiler results in an excessive amount of carryover. Carryovers are partially burned black liquor or smelt drops. Upon leaving the furnace cavity, carryovers build up on the heat exchanger surfaces and cause blockage of the gas flow passages. Incorrect operation of the furnace may also result in the emission of large amounts of reduced sulfur species (H_2S). Elimination of other pollutants such as carbon monoxide in the furnace can be achieved through better mixing, or by increasing the amount of excess air. Usually about 30% to 50% excess air is used beyond stochiometric. However, the increased air can augment the problem of carryover. Incorrect operation of the furnace can also cause high levels of corrosion in the furnace.

Operational problems can be corrected to some extent by modifying the operating

parameters such as air jet location and geometry, air flow ratio between the three levels (primary, secondary, tertiary), liquor gun location, and black liquor spray characteristics. Variations of air or fuel flow while the furnace is in operation can lead to dangerous conditions if care is not taken. For this reason, too, there is a need to predict the flow characteristics in a furnace.

Much of the available information regarding the flow patterns inside kraft recovery furnaces is based on physical scale models of these furnaces. Scale models are useful flow visualization tools (Khalil (1982), Perchanok et al. (1988 ,1989), Bianca et al. (1981), Patterson and Abrahamsen (1962), Spalding (1962)). Water or air at room temperature is the fluid usually used in these models. To preserve similarity between the scale model and the prototype, investigators such as Thring and Newby (1952) and Davison (1968) have suggested that scaling parameters be applied to the inlet velocities and/or air port dimensions, to allow the simulation of density/temperature differences between the incoming air and the upgoing gases in the furnace.

Investigators such as Chapman and Jones (1990), and Ketler et al. (1993), have reported valuable information regarding the flow patterns in the recovery furnace based on their experiments in the scale models. For example, they have reported the presence of large recirculating flow regions and unsteadiness which makes measurements in these models difficult. The flows that are created with this technique are 'cold flows', as they do not include the effect of temperature distributions and complicated chemical and thermal processes inside the furnace. Before using the information obtained from scale models in the design of the full scale furnace it is essential to understand the effect of buoyancy forces on the flow field of the furnace. Due to the complexity of the flow and the multitude of processes underway in the recovery furnace, there are few analytical techniques available for the prediction of the gas aerodynamics inside these furnaces. Therefore, the use of computational fluid dynamics is an important tool for predicting

flows in recovery furnaces.

Although some studies of the effect of density variations on the flow of a jet in a crossflow have been carried out, most of the findings are not of direct application to the kraft recovery furnace. A review of the available literature is the topic of the next section.

1.4 Literature Review

The literature that is of relevance to this study can be classified into two categories:

1. Previously developed models of the kraft recovery furnace
2. Studies of the effect of density variations on jet in crossflow

A summary of this literature is presented below.

The application of computational fluid dynamics to the kraft recovery furnace has intensified over the last decade. A fairly recent comprehensive summary of mathematical models of recovery furnaces is given in the Ph.D. thesis by Jones (1989). The focus of the earlier models is on the chemical processes inside the furnace. The flow field is assumed to be one-dimensional or it is imposed. As these models do not deal with the three dimensional nature of the gas flow patterns, temperature, and species concentration, the relevance of their predictions to the highly three-dimensional flow field in the recovery furnace is questionable.

The simulations by Jones (1989), and Grace et al. (1990) are among the first in this field. Those simulations used a commercially available CFD code, FLUENT. Simplifying assumptions were made in the representation of the actual furnace. The focus of their work was the development of a three-dimensional model of the furnace, including the chemical and thermal processes. No attempt was made to isolate the effect of the buoyancy force on the flow characteristics.

Though valuable insight has been gained through these simulations, their numerical solutions were not efficient in computer time nor completely satisfactory. The computer time required to achieve this convergence is too long for a feasible parametric study.

A comprehensive summary of the semi-empirical methods developed to solve the problem of the buoyant jet in crossflow is given by Wright (1977). The main drawback of these models is that they require empirical relationships for such variables as the rate of entrainment of ambient fluid by the jet, or the rise of the jet. For flow conditions similar to the stack plume, Wright (1977) has proposed an empirical equation to estimate the distance a jet has to travel into the crossflow before buoyancy effects and momentum effects become equally important. For the same parameter and similar flow conditions, Chu and Goldberg (1974) have proposed a different expression.

Abramovich (1963) and Niessen (1978) have reviewed the literature on the effect of buoyancy on a jet injected into a crossflow of different density. Their reviews indicate the high degree of empiricism in these correlations. In some cases (e.g. Gray and Robertson (1956)) the experimental conditions are not clearly stated.

Niessen (1978) has developed an empirical correlation to compare the magnitude of the buoyancy and drag force exerted on a jet. The relationship relies heavily on the empirical value of the effective drag coefficient. Niessen has specified a range of 1 to 5 for this value. No basis for this assumption is presented.

The existing empirical correlations do not compare well with each other and their simple boundary conditions are not comparable to the situation in recovery furnaces.

Haniu (1979) has summarized the experimental data available on the measurement of buoyant jets in crossflow. The bulk of data on buoyant jets, however, is from studies on cooling tower plumes. Up to 1979, data on the velocity distribution across buoyant jets in crossflow were scarce. The measurement of velocity and temperature distributions for a two dimensional buoyant water jet injected into a crossflow, by Haniu (1979) is among

the first in this field. Haniu (1979) and Ramaprian and Haniu (1983) have reported the presence of a recirculation bubble and reported that the flow two dimensionality breaks down for exit Richardson number (defined as $Ri_o = ((\rho_\infty - \rho_j)/\rho_\infty)gD/V_j^2$) larger than 0.14. The maximum temperature difference between the jet and the crossflow was 40^oC.

As the subject of variable density jets injection into a crossflow has practical application in the design of gas turbine blades with film cooling, some investigations of 'film cooling effectiveness' are of interest. These studies are performed at low mass ratio of jet to crossflow (defined as $G = \rho_j V_j/\rho_c U_c$) and therefore are not directly applicable to the kraft recovery furnace. However, they can provide some general understanding of the effect of density differences.

Ramsey and Goldstein (1971) introduced a circular heated jet at angles of 90 and 35 degrees to the crossflow (streamwise direction) for a range of jet to crossflow mass ratios (0.1< G <2.0). They report that the maximum temperature occurs at or near the wall for $G = 0.1$ while for $G = 2.0$ the maximum is at a height greater than two jet diameters above the wall even quite close to the jet exit. Based on their experimental results they concluded that increasing the mass ratio G influences the wall temperature in two counteracting ways. The increased jet flow and resulting increased enthalpy addition to the stream tend to increase the temperature while the increased penetration moves the path of the jet's maximum temperature farther from the wall and tends to lower the wall temperature. The first effect predominates at the lower mass ratios ($G \leq 0.5$). At larger mass ratios the effect of increased penetration causes the wall temperature to decline with increasing mass ratio G. At $G = 2.0$ the jet penetration is such that the jet has very little effect on the wall temperature.

Kamotani and Greber (1972,1974) conducted experiments on a single, and a row of, circular heated jets injected upward into a crossflow. The experiments indicate that in the well-mixed downstream region, the temperature decay of a single row of jets, for

moderate spacing, is similar to that of a two-dimensional jet .

Goldstein (1971) has summarized the studies conducted in film cooling effectiveness. Among the most recent studies on variable density film cooling, the work of Hass et al. (1991), Kikkawa et al. (1989), Ammari et al. (1989), and Pietrzyk et al. (1989) can be mentioned. These studies concern the measurement of the jet fluid concentration at the wall (equivalent to film cooling effectiveness), except for the work of Pietrzyk et al., which investigates the effect of density ratio on the hydrodynamics of film cooling. The jet is often injected through a row of circular openings and the mass ratio of the jet to crossflow is small (less than 1.5).

For example, Hass et al. (1991) have reported that the film cooling effectiveness increases as the ratio ρ_j/ρ_∞ increases, at the same mass flow ratio of jet to crossflow. Similarly, based on their experimental work injection through a row of rectangular holes, Kikkawa et al. (1989) reported that film cooling effectiveness on a turbine blade for normal and inclined injections increases by increasing the density ratio. However, Ammari et al. (1989) report that for jets injected normally into the crossflow the effectiveness over the flat plate at a fixed mass ratio, is insensitive to the variation of density ratio, whereas for inclined injection there is a strong dependence.

Pietrzyk et al. (1989) have measured the effect of density differences on the velocity field for a row of inclined jets issuing into a crossflow, at mass ratio of jet to crossflow $G = 0.5$, and jet to crossflow density ratio of 2.0. Comparing the data with two unit density cases with momentum flux ratios that bracketed the high density case, they report that downstream of the hole, the dense jet has lower velocities in the near wall region than either unit density jets. Farther downstream the velocity field of the dense jet compared well with the unit density case with the same mass flux ratio.

The literature indicates that numerous parameters such as angle of injection, jet geometry, mass ratio, momentum ratio and density ratio play a role in the jet-in-crossflow

flow.

Andreopoulos (1983) presented results for mean temperature in a heated jet issuing perpendicularly into a cold air stream, for velocity ratios of 0.25, 0.5, 1, and 2. The mean temperature profiles at the jet exit were found to be quite non-uniform at low velocity ratios, indicating the mixing between the cold and hot fluids.

Sherif and Pletcher (1989) measured the velocity and temperature fields of a heated circular water jet injected vertically into a crossflowing stream in a water channel. The range of velocity ratios tested was from 1 to 7 with the jet discharge temperatures 28 to $40°C$ higher than the crossflow temperature and the exit densimetric Froude number, defined as $Fr = V_j/gS(1-\rho_j/\rho_\infty)^{1/2}$, ranging from 9 to 63. Based on their measurements of temperature they reported that the initial mixing region between the jet and the crossflow gets shorter for larger velocity ratios with better mixing at higher velocity ratios. Therefore, as shown by the experiments of Sherif and Pletcher, even at high values of jet exit Froude number ($Fr > 10$), where originally the momentum forces dominate over the buoyancy forces, further downstream the effect of buoyancy force can alter the flow field.

Most of the published work on jets in crossflow has concentrated on unconfined problems. The problem of jet in confined crossflow recently became of interest to combustor flow field researchers (Ferrell et al. (1984, 1985), McMurry et al. (1987), and Ong et al. (1986)). However these investigations considered the problem of isothermal jets in confined crossflow.

Chao and Ho (1992) have investigated numerically the behavior of circular heated jets injected vertically into a tubular confined swirling and nonswirling crossflow for application to combustors. In the case of the heated jet, the maximum temperature difference between the crossflow and the jet was $150°C$. They reported that the jet penetration increases with the velocity ratio of jet to crossflow. The decay of maximum

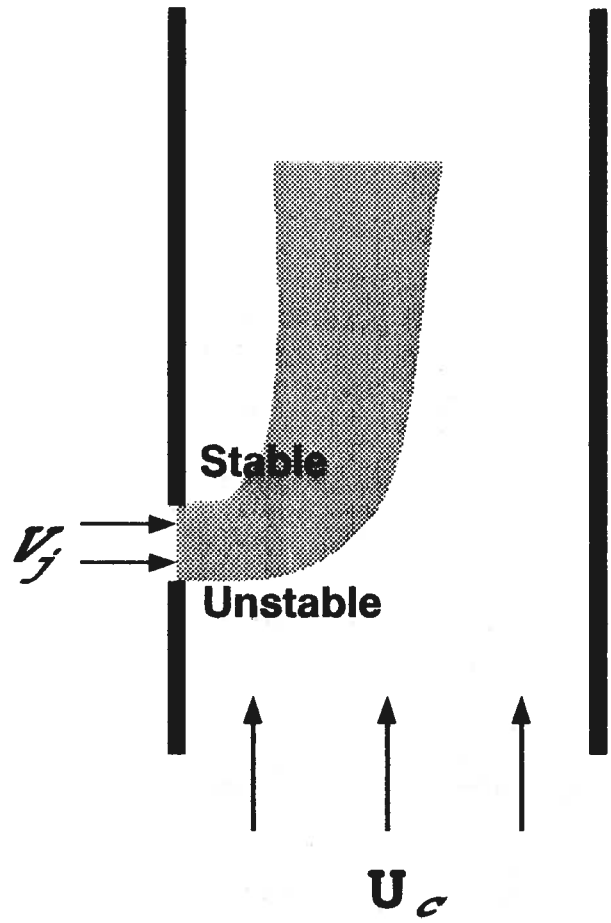

Figure 1.2: Schematic presentation of a cold jet in a hot crossflow. 'Stable' and 'Unstable' refers to the interface of the jet and crossflow at the top and the bottom.

jet concentration at a constant jet to crossflow velocity ratio is nearly independent of the temperature difference between the jet and the crossflow.

1.5 Purpose and Scope of the Present Work

The literature review has shown that there is a lack of information on the effect of buoyancy force on the flow field of a variable density jet injected into a crossflow, for flow conditions similar to those in recovery furnaces.

To analyze the effect of buoyancy force on a jet in crossflow, consider the schematic of a cold jet entering a hot crossflow presented in Figure 1.2.

Upon entering the hot crossflow, the jet mixes with hot fluid and expands because of temperature increases at nearly constant pressure. However before mixing between the jet and crossflow is complete, the buoyancy force acting on the jet can pull the jet downward. Additionally the presence of stratifications in the flow field, can alter the generation or destruction of the turbulent kinetic energy (k) and the rate of its dissipation (ϵ). In general, the presence of unstable stratification, (when the heavy fluid is above the light fluid), enhances the generation of turbulent kinetic energy, and the presence of stable stratification dampens it (Reynolds 1974).

In large geometries such as recovery furnaces, where large regions of low velocities are present (Adams, 1987), the effect of buoyancy force should not be judged only by its value at the jet exit plane. The presence of combustion and radiation processes can cause further non-uniformity of the temperature distributions. In recirculation regions where velocities are generally low, these non-uniformaties can enhance the effect of buoyancy forces.

The available theoretical and experimental literature on the variable density jet in a crossflow deals mainly with circular jets and low mass flow ratios. Furthermore, when the density ratio of jet to crossflow is varied in these studies, the mass and momentum flux ratios are simultaneously changed. Therefore it is not possible to isolate the effect of the buoyancy force.

These conditions are remote from those prevailing in the recovery furnace. The specific needs of kraft recovery furnaces, such as the use of large rectangular jets of high density injected into a non-uniform low density crossflow in a large flow domain, have not been addressed.

A review of numerical modelling of recovery furnaces highlights the inefficiency of the standard numerical techniques in simulations of large flow domains where a large number of grids is required. This problem is exacerbated in simulations of recovery furnaces

due to large differences in the dimensions of the air ports and the furnace. To resolve each of the ports within such a large domain, a very fine grid relative to the domain is needed. This requirement increases the computational time and memory allocation required. Moreover, it is known that the convergence of most numerical schemes deteriorate and error reduction often stalls as the number of grid points increases. Therefore, our research group at UBC has been developing a CFD code which has the capability to model recovery furnaces. Some details of this code will be presented in Chapter 2. Preliminary results based on isothermal flow simulations have been reported by Salcudean et al. (1992) and show fast convergence.

The above considerations indicate the need for a systematic approach to investigate the buoyancy effects in flow conditions that are of relevance to the kraft recovery furnace. The effect of buoyancy on the flow field of rectangular jets injected into a crossflow is investigated numerically. The effect of density variations is included in the calculations through density appearing as a coefficient in the conservation equations. In addition, the buoyancy as a body force is included in the vertical momentum equation, and the generation or destruction of turbulence due to buoyancy is modelled in the $k-\epsilon$ equations. The concentration field of variable density two-dimensional slot jet injected vertically into a crossflow for three values of jet to crossflow density ratio of 1, 1.5, and 4 is measured using a Flame Ionization Detector. The objectives of this study are summarized below.

1. The experimental objectives were:

    - To gain further insight into the behavior of a two-dimensional variable density jet injected into a crossflow.
    - To provide dependable data for comparison and evaluation of numerical predictions.

2. The numerical study objectives were:

- To gain some understanding of the effect of buoyancy force on the flow of two-dimensional jets, three-dimensional single jets, and an array of jets all injected into a crossflow.
- To gain a better understanding of the effect of buoyancy force on the flow field inside the kraft recovery furnace.
- To determine the sensitivity of the flow field of the recovery furnace to the distribution of heat sources inside the furnace.

Chapter 2

Mathematical Model and Computational Procedure

An accurate description of the flow of non-isothermal turbulent jets into crossflow requires the use of equations expressing the principles of conservation of mass, momentum (the Navier-Stokes equations), and energy. In this chapter the mathematical formulation of our problem is first presented. The averaging procedure of the Navier-Stokes equations is briefly described and the $k-\epsilon$ turbulence model used in this study is reviewed. The general form of the various transport equations governing the flow is given. Next, the numerical method and the solution procedure employed are presented.

2.1 Mathematical Model for Jet Flows and Time-Averaging

The governing equations of incompressible fluid mechanics are the conservation equations of mass, momentum, and energy. In Cartesian tensor notation these partial differential equations are given by Bird, et al. (1960) and Schlichting (1978) in the following form:

<u>Mass Conservation</u>

$$\frac{\partial \rho}{\partial t} + \frac{\partial}{\partial x_i}(\rho u_i) = 0 \tag{2.1}$$

<u>Momentum Conservation</u>

$$\frac{\partial}{\partial t}(\rho u_i) + \frac{\partial}{\partial x_j}(\rho u_i u_j) = -\frac{\partial p}{\partial x_i} + g_i \rho + \frac{\partial}{\partial x_j}\left[\mu\left(\frac{\partial u_i}{\partial x_j} + \frac{\partial u_j}{\partial x_i}\right)\right] \tag{2.2}$$

Energy and/or scalar Conservation

$$\frac{\partial}{\partial t}(\rho\theta) + \frac{\partial}{\partial x_j}(\rho\theta u_j) = \frac{\partial}{\partial x_j}\left[\lambda\left(\frac{\partial\theta}{\partial x_j}\right)\right] \tag{2.3}$$

Here u_i (i = 1,2,3), p and θ represent instantaneous velocities, the pressure, and a scalar respectively. For example, the scalar quantity can represent the temperature, jet concentration, turbulent kinetic energy, or its dissipation. μ is the molecular dynamic viscosity, and λ is the molecular diffusivity for the scalar θ.

The numerical solution of the above set of equations for turbulent flows in their three-dimensional, time-dependent form, for flows of practical importance, is not feasible at present. The speed and storage capacity of present day computers are insufficient for refined grids required to resolve the smallest scales of turbulent motion. Consequently, the ensemble or time-averaging procedure (Reynolds, 1974) has to be employed to obtain equations for average quantities.

In the time-averaging procedure, the instantaneous general variable f is decomposed into a mean, F, and a fluctuating component, f', as

$$f = F + f' \tag{2.4}$$

where the time averaged value, F, is defined as

$$F = \frac{1}{\Delta t}\int_t^{t+\Delta t} f\,dt \tag{2.5}$$

with the averaging time, Δt much greater than the longest time scales of the turbulent motion, but shorter than any time scale describing trends in the turbulent statistics.

Introducing the above definitions to decompose u_i, p, and θ into mean and fluctuating components, and time averaging, we obtain for a statistically steady flow,

$$\frac{\partial}{\partial x_i}(\rho U_i) = 0 \tag{2.6}$$

$$\frac{\partial}{\partial x_j}(\rho U_i U_j) = -\frac{\partial P}{\partial x_i} + g_i(\rho_\infty - \rho) + \frac{\partial}{\partial x_j}\left[\mu\left(\frac{\partial U_i}{\partial x_j} + \frac{\partial U_j}{\partial x_i}\right) - \overline{\rho u_i' u_j'}\right] \tag{2.7}$$

$$\frac{\partial}{\partial x_j}(\rho \Theta U_j) = \frac{\partial}{\partial x_j}\left[\lambda\left(\frac{\partial \Theta}{\partial x_j}\right) - \overline{\rho \theta' u_j'}\right] \tag{2.8}$$

In these derivations the turbulent fluctuations in density ρ' are regarded as negligible compared to mean value of ρ, thus all the correlations containing ρ' in equations (2.1-2.3) are neglected. For nearly incompressible flows this is a reasonable assumption (Watkins, 1977). The term $\rho_\infty g_i$ in Equation (2.7) is due to the hydrostatic pressure and ρ_∞ refers to a reference density. Equations 2.7-2.8 contain new unknown terms, $\overline{\rho u_i' u_j'}$ and $-\overline{\rho \theta' u_j'}$ known as Reynolds stresses and turbulent scalar fluxes. These terms, which are the products of fluctuating components, arise from the averaging of the non-linear convective terms in Equations (2.2-2.3). Physically, these terms represent diffusion of momentum or scalar quantities by turbulent motion. The above set of equations are not closed, as there are more unknowns than equations. In order to obtain a closed set of equations, some assumptions are necessary to relate the mean products of fluctuating quantities to existing mean variables. Additionally to complete the set of equations for the non-isothermal flow the equation of state for the gas should be known. In this study it is assumed that the gas follows the ideal gas law. Therefore, the relationship between the gas density and its temperature is (Wylen and Sonntag, 1985):

$$\rho = \frac{P}{R'T} \tag{2.9}$$

In equation (2.9) R' is the ideal gas constant for the gas involved.

If the density variations are due to the changing compositions of two mixing gases, then the density of the mixture will be defined as:

$$\rho = \frac{\rho_1 \rho_2}{(1 - m_1)\rho_1 + m_1 \rho_2} \tag{2.10}$$

where ρ_1 and ρ_2 refer to the density of each gas at its inlet and m_1 and m_2 refer to the gas mass fraction defined as:

$$m_1 = \frac{\text{mass of gas 1}}{\text{mass of mixture}} \tag{2.11}$$

and

$$m_2 = 1 - m_1 \tag{2.12}$$

2.2 Turbulence Modelling : $k - \epsilon$ Turbulence Model

The objective of turbulence modelling is to express the unknown correlations of fluctuating components in terms of mean flow variables and characteristic turbulence properties in order to 'close' the above set of equations. Turbulence modelling has been an active field of research for many years. The models are approximate and rely on empirical information.

The $k - \epsilon$ model of Launder and Spalding (1974) used in this study, has been most widely used. In terms of generality and computational economy the model offers the best compromise at present. It requires the solution of two additional transport equations: one for the time mean turbulent kinetic energy, k, and another for its dissipation rate, ϵ. The basis of the $k - \epsilon$ model is the eddy viscosity concept. The model assumes the following relations for the Reynolds stresses and turbulent scalar fluxes:

$$-\overline{\rho u_i' u_j'} = \mu_t \left(\frac{\partial U_i}{\partial x_j} + \frac{\partial U_j}{\partial x_i} \right) - \frac{2}{3} \left(\mu_t \frac{\partial U_i}{\partial x_i} + \rho k \right) \delta_{ij} \tag{2.13}$$

$$-\overline{\rho \theta' u_j'} = \frac{\mu_t}{\delta_\theta} \frac{\partial \Theta}{\partial x_j} \tag{2.14}$$

Here k is defined as:

$$k = \frac{1}{2} \left(\overline{u_1'^2} + \overline{u_2'^2} + \overline{u_3'^2} \right) \tag{2.15}$$

The term involving the Kronecker delta on the right hand side of equation (2.13) ensures that the sum of the normal stresses is equal to $2k$. The term expressing the velocity divergence, $\partial U_i / \partial x_i$, remains in the formulation as this study is considering the non-isothermal flow of jets in crossflow. The turbulent or eddy viscosity μ_t has been related by Prandtl to definable quantities using a mixing length concept and dimensional analysis. The expression for μ_t is:

$$\mu_t = C_\mu \rho k^2 / \epsilon \tag{2.16}$$

where C_μ is an empirically determined constant of proportionality and a length scale of turbulence can be defined as:

$$l \propto k^{\frac{3}{2}} / \epsilon \tag{2.17}$$

so that:

$$\mu_t \propto k^{\frac{1}{2}} l \tag{2.18}$$

Therefore if the values of k and ϵ are known, the turbulent stresses and turbulent scalar fluxes can be determined. Exact transport equations for k and ϵ can be obtained by manipulating equation (2.2). However the resulting equations are of little use because they contain higher order correlation terms which are unknown. To obtain a closed set, these terms must be modelled. The standard modelled transport equations for k and ϵ suggested by Launder and Spalding (1974) ignore the terms due to buoyancy force. These equations written for incompressible flows do not include the terms due to the divergence of velocity. In this study we employ the $k-\epsilon$ equations modified by Watkins (1977). Although including the velocity divergence terms Watkins ignored the terms due to the production or destruction of turbulence by buoyancy. To include these terms in our calculations we follow the model suggested by Rodi (1984). The final $k-\epsilon$ equations used in this study are written as:

$$\frac{\partial}{\partial x_j}(\rho U_j k) = \frac{\partial}{\partial x_j}\left(\frac{\mu_{eff}}{\sigma_k}\frac{\partial k}{\partial x_j}\right) + \mu_t\left(\frac{\partial U_i}{\partial x_j} + \frac{\partial U_j}{\partial x_i}\right)\frac{\partial U_i}{\partial x_j} - \frac{2}{3}\frac{\partial U_i}{\partial x_i}\left(\mu_t\frac{\partial U_i}{\partial x_i} + \rho k\right) - \rho\epsilon + G_B \tag{2.19}$$

$$\frac{\partial}{\partial x_j}(\rho U_j \epsilon) = \frac{\partial}{\partial x_j}\left(\frac{\mu_{eff}}{\sigma_\epsilon}\frac{\partial \epsilon}{\partial x_j}\right) + C_1\epsilon/k\,(G_k + G_B) - C_2\frac{\rho\epsilon^2}{k} + \rho\epsilon\frac{\partial U_i}{\partial x_i}C_4 + C_1C_3\frac{\epsilon}{k}(G_k + G_B)\,R_f \tag{2.20}$$

where G_k is the turbulence production due to shear and G_B refers to the production or destruction of turbulence due to buoyancy. R_f is the flux Richardson number which is usually defined as the ratio of the production or destruction of turbulence due to buoyancy to that due to shear. Rodi (1984) has suggested an alternative definition of the

flux Richardson number which enables a single value of C_3 to be used. In mathematical form G_k, G_B, and R_f are defined as follow:

$$G_k = \mu_t \left(\frac{\partial U_i}{\partial x_j} + \frac{\partial U_j}{\partial x_i} \right) \frac{\partial U_i}{\partial x_j} - \frac{2}{3} \frac{\partial U_i}{\partial x_i} \left(\mu_t \frac{\partial U_i}{\partial x_i} + \rho k \right) \tag{2.21}$$

$$G_B = g_i \beta' \frac{\mu_t}{\delta_\theta} \frac{\partial \Theta}{\partial x_i} \tag{2.22}$$

where β' is the volumetric expansion coefficient which for $\Theta = T$ becomes:

$$\beta' = \frac{1}{\rho} \frac{\partial \rho}{\partial T} \tag{2.23}$$

or for a general function $\Theta = \Psi$ becomes:

$$\beta' = \frac{1}{\rho} \frac{\partial \rho}{\partial \Psi} \tag{2.24}$$

where following Rodi (1984) R_f is put equal to:

$$R_f = -\frac{G_B}{G_k + G_B} \tag{2.25}$$

The effective viscosity μ_{eff} is the sum of the laminar and eddy viscosities:

$$\mu_{eff} = \mu + \mu_t \tag{2.26}$$

The values of the empirical constants appearing in the model are listed in table 2.1.

Table 2.1: Parameters in the $k-\epsilon$ model

C_μ	C_1	C_2	κ	σ_k	σ_ϵ	σ_ϕ	C_3	C_4
0.09	1.44	1.92	0.4187	1.0	$\frac{\kappa^2}{(C_2-C_1)}C_\mu^{1/2}$	1.0	0.8	1.0

In stable stratification G_B becomes a sink term so that the turbulent mixing is reduced. In unstable stratification the buoyancy will enhance turbulence since G_B is positive. The buoyancy extended version of the $k-\epsilon$ model suggested by Rodi (1984) has been used extensively by researchers in the field. Among these are the work of Leschziner and Rodi (1982), Markatos and Malin (1981), and Franke et al. (1987). Good agreement with the experimental results has been obtained.

2.3 General Transport Equation

The governing equations presented in the previous section can be conveniently represented for numerical purposes by the following general equation:

$$\frac{\partial}{\partial x_j}(\rho U_j \Phi) = \frac{\partial}{\partial x_j}\left(\Gamma_\phi \frac{\partial \Phi}{\partial x_j}\right) + S_\phi \tag{2.27}$$

where Φ is a general dependent variable, Γ_ϕ a general diffusivity coefficient, and S_ϕ a general source term. For each of the transport equations the particular values taken by Γ_ϕ and S_ϕ are given in Table 2.2. The value of P_{eff} in table 2.2 is defined as:

$$P_{eff} = P + \frac{2}{3}\left(\rho k + \mu_t \frac{\partial U_i}{\partial x_i}\right) \tag{2.28}$$

2.4 Boundary Conditions

The complete description of the problem requires the specification of the boundary conditions. For the problem of turbulent jets in crossflow considered here, there are four

Table 2.2: Diffusion coefficients and source terms for the governing equations.

Φ	Γ_ϕ	S_ϕ
1	0	0
U_i	μ_{eff}	$-\partial P_{eff}/\partial x_i + \partial/\partial x_j\left[\mu_{eff}\left(\partial U_i/\partial x_j\right)\right] + (\rho_\infty - \rho)g_i$
Θ	μ_{eff}/σ_θ	Heat sources in case of energy equation
k	μ_{eff}/σ_k	$G_k + G_B - \rho\epsilon$
ϵ	$\mu_{eff}/\sigma_\epsilon$	$C_1\epsilon/k(G_k + G_B) - C_2\rho\epsilon^2/k + C_4\rho\epsilon\partial U_i/\partial x_i + C_1C_3\epsilon/k(G_k + G_B)R_f$

types of boundaries. These boundary conditions are explained below.

Inlet plane

The values of all the flow variables, except pressure, are specified at the inlet plane. In the present study uniform profiles for streamwise velocity, jet concentration, temperature, k and ϵ are imposed. The cross-stream and lateral velocity profiles are set to zero at the inlet plane. The inlet values of k and ϵ are specified via the turbulence intensity I and turbulent length scale l of the flow entering the domain. As suggested by Lai (1987) the value of k and ϵ are evaluated from

$$k = \frac{3}{2}U^2I^2 \tag{2.29}$$

$$\epsilon = C_\mu^{3/4}k^{3/2}/l \tag{2.30}$$

Typically I is assigned a value of the order 0.01 - 0.05, while l is made a small fraction of the dimension of the inlet.

Outlet plane

Zero streamwise gradient condition is applied to all flow variables at the outlet plane. This condition implies a fully developed flow at the outlet. For this assumption to be valid

the outlet plane must be located sufficiently far downstream from the recirculating flow region as to ensure that the flow in the upstream region is not affected by downstream conditions.

Symmetry plane

The boundary conditions on the symmetry plane are given by zero normal gradient condition for all the flow variables except the normal velocity, which is itself zero.

Solid walls

The no-slip boundary condition is imposed at all solid boundaries. Additional complications arise at the solid wall boundaries using $k - \epsilon$ turbulence model as the model ignores viscous effects based on the high Reynolds number assumption. In the vicinity of solid boundaries due to the no-slip condition, the Reynolds number is sufficiently small for viscous effects to become important. To correct for this deficiency in the model, the wall function treatment proposed by Launder and Spalding (1974) is invoked. The wall function method connects the wall shear stress to the velocity just outside the viscous sublayer by assuming Couette flow and local equilibrium. The use of this method eliminates the need to cluster a large number of grid points close to the wall, which would otherwise be required to account for the sharp gradients present in the viscous sublayer. The details of this model are not provided here, as they are standard and well described by other researchers (see Lai 1987, and Djilali 1987).

2.5 Computational Procedure

In this section the solution procedure employed to solve the governing equations presented in the previous section is discussed. A summarized account is given of the finite volume method and the staggered grid system used to discretize the equations. An overview of the iterative algorithm employed and the use of the multigrid technique to accelerate the

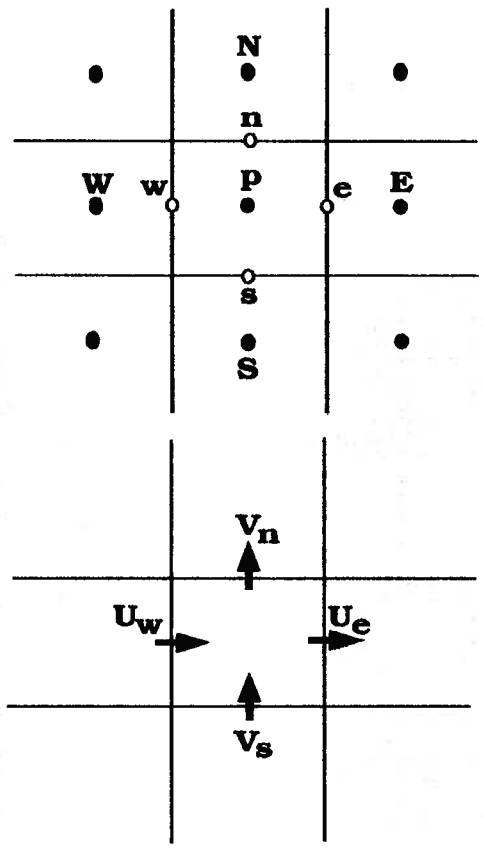

Figure 2.1: Grid arrangement in MGFD code.

convergence, is provided. The criterion for convergence is presented.

2.5.1 Finite Volume Formulation and Discretization

To discretize the set of governing partial differential Equations (2.1-2.3) describing the conservation of mass, momentum, energy, chemical species, turbulent kinetic energy, and dissipation rate of turbulent kinetic energy, the computational domain is divided into a number of adjacent control volumes or cells. The resultant finite difference equation set has to be accurate and stable. To satisfy the requirement of stability, the staggered grid arrangement for the scalar and velocity variables, suggested by Patankar (1980), is used. For clarity a two-dimensional lay-out of this grid arrangement is shown in Figure 2.1.

Extension to three dimensions is straightforward. The location of the grids at which the variables are to be calculated differs depending on the variable in question. All scalar variables are calculated at the grid point. In Figure 2.1 these points are labeled as E, W, N, S, P. The velocity components U and V which lie between the pressures driving them, are displaced in the x and y directions respectively to the mid-point of the boundaries of the control volume surrounding the scalar quantities location. In Figure 2.1 these points are labeled as e, w, n, s denoting the east, west, north, and south of the scalar quantity P. This positioning has the advantage that the velocities are directly available for calculation of convection through the scalar cell walls. Additionally, the velocity-pressure staggering eliminates physically unrealistic 'wiggles' in the solution domain (Patankar, 1980). The scalar control volumes are the ones centered on grid nodes such as P. The momentum control volumes are defined around the velocity location and are split between the two scalar volumes, such that the boundaries normal to the velocity direction pass through the scalar nodes.

In accordance with the finite volume approach of Gosman (1969), Patankar (1980), and Anderson (1984), the integration of this general transport equation (2.27) over a typical control volume can be expressed as:

$$\int\int\int \left[\frac{\partial}{\partial x}(\rho U \Phi) + \frac{\partial}{\partial y}(\rho V \Phi) + \frac{\partial}{\partial z}(\rho W \Phi)\right] dV \quad =$$

$$\int\int\int \left[\frac{\partial}{\partial x}\left(\Gamma_\phi \frac{\partial \Phi}{\partial x}\right) + \frac{\partial}{\partial y}\left(\Gamma_\phi \frac{\partial \Phi}{\partial y}\right) + \frac{\partial}{\partial z}\left(\Gamma_\phi \frac{\partial \Phi}{\partial z}\right)\right] dV + \int\int\int S_\phi dV \qquad (2.31)$$

Using the divergence theorem, the volume integrals can be transformed into surface integrals:

$$F_e - F_w + F_n - F_s + F_t - F_b \quad = \quad \int\int\int S_\phi dV \qquad (2.32)$$

where $(F_e, ..., F_b)$ represent the sums of convective and diffusive fluxes across the faces of a three-dimensional control volume cell with t and b referring to the top and bottom cell faces. For example the expression for F_e is:

$$F_e = \int\int \left(\rho U \Phi - \Gamma_\phi \frac{\partial \Phi}{\partial x}\right)|_{x_e} \, dydz \tag{2.33}$$

$$F_e = C_e + D_e \tag{2.34}$$

where x_e is the location of the cell's east face. C_e and D_e, the convective and diffusive fluxs, are:

$$C_e = \int\int (\rho U \Phi))|_{x_e} \, dydz \tag{2.35}$$

$$D_e = \int\int \left(-\Gamma_\phi \frac{\partial \Phi}{\partial x}\right)|_{x_e} \, dydz \tag{2.36}$$

Fluxes through other faces can be written in a similar fashion.

The exact integrals in equation (2.31) can be reduced to algebraic forms using finite difference approximations. This is accomplished by expressing the convective and diffusive fluxes across the control volume boundaries in terms of the nodal values of the dependent variable Φ. This requires that the value of the dependent variable be determined at the control volume faces. Applying central differencing to approximate the convective and diffusive flux C_e and D_e:

$$C_e \approx \rho_e U_e \left(\frac{\Phi_E + \Phi_P}{2}\right) \Delta y_j \Delta z_k \tag{2.37}$$

$$D_e \approx \Gamma_\phi |_{x_e} \left(\frac{\Phi_P - \Phi_E}{\delta x_i}\right) \Delta y_j \Delta z_k \tag{2.38}$$

where Φ_P and Φ_E are the values of Φ at grid points P and E, respectively. δx_i refers to the distance between nodal points P and E, and Δy_j and Δz_k are the dimensions of the east cell face. The expression for D_e is formally second order accurate in δx. Usually where diffusion is the dominant mode of transport the central differencing scheme is appropriate. Approximating C_e is critical to the stability of the numerical scheme. It is well established that for convection dominated flows, where the cell Peclet number $Pe = C_e/D_e$ is greater than 2, the use of central differencing leads to numerical instabilities. Several methods are available to counteract this instability (Patankar, 1980). Upwind differencing has been widely used. In this approach the value of the dependent variable at the upstream node is assumed to prevail at the control volume face. This leads to an approximation which is unconditionally stable, but first order accurate in δx. The hybrid scheme combines both central and upwind differencing. In the present work, the power law differencing scheme of Patankar (1980) is used. In this approach the central and upwind differencing are blended smoothly. Central differencing is applied when the cell Peclet number is low and upwind differencing when the cell Peclet number is high.

To discretize the source term it is first linearized into the following form :

$$\int\int\int S_\phi dV \approx S_P^\phi \Phi_P + S_C^\phi \tag{2.39}$$

The variable S_C^ϕ represents the constant part of the linearized source term for each control volume. The dissipation or generation of a quantity represented by the dependent variable Φ can be expressed through the source terms. Following the suggestions of Patankar (1980), the term S_P^ϕ must be non-positive in order to have stability. S_P^ϕ and S_C^ϕ are derived using central differencing approximations. The various expressions are given in Table 2.3.

Table 2.3: Discretized source terms.

Φ	S_P^ϕ	S_C^ϕ
U	0	$P_{eff}\,\vert_e^w\,\Delta y\Delta z + \left(\mu_{eff}\frac{\Delta U}{\Delta x}\right)\vert_w^e\,\Delta y\Delta z$ $+\left(\mu_{eff}\frac{\Delta V}{\Delta x}\right)\vert_s^n\,\Delta x\Delta z + \left(\mu_{eff}\frac{\Delta W}{\Delta x}\right)\vert_b^t\,\Delta x\Delta y$
V	0	$P_{eff}\,\vert_n^s\,\Delta x\Delta z + \left(\mu_{eff}\frac{\Delta U}{\Delta y}\right)\vert_w^e\,\Delta y\Delta z$ $+\left(\mu_{eff}\frac{\Delta V}{\Delta y}\right)\vert_s^n\,\Delta x\Delta z + \left(\mu_{eff}\frac{\Delta W}{\Delta y}\right)\vert_b^t\,\Delta x\Delta y$
W	0	$P_{eff}\vert_b^t\Delta x\Delta y + \left(\mu_{eff}\frac{\Delta U}{\Delta z}\right)\vert_w^e\Delta y\Delta z$ $+\left(\mu_{eff}\frac{\Delta V}{\Delta z}\right)\vert_s^n\,\Delta x\Delta z + \left(\mu_{eff}\frac{\Delta W}{\Delta z}\right)\vert_b^t\,\Delta x\Delta y + (\rho-\rho_\infty)g$
k	$-\frac{C_\mu\rho^2 k}{\mu_t}\vert_P\Delta x\Delta y\Delta z$	$(G_k+G_B)\vert_P\Delta x\Delta y\Delta z$
ϵ	$-\frac{C_2\rho\epsilon}{k}\vert_P\Delta x\Delta y\Delta z$	$\{C_1(G_k+G_B)\epsilon/k + C_4\rho\epsilon\partial U_i/\partial x_i$ $+C_1C_3\epsilon/k(G_k+G_B)R_f\}\,\vert_P\Delta x\Delta y\Delta z$

Substituting the source and flux terms obtained by incorporating the power law scheme into equation (2.32), we obtain the following general finite volume equation:

$$\left(a_P - S_P^\phi\right)\Phi_P = a_N\Phi_N + a_S\Phi_S + a_E\Phi_E + a_W\Phi_W + a_B\Phi_B + a_T\Phi_T + S_C^\phi \quad (2.40)$$

$$a_P = \sum_i a_i \qquad (i = N, S, E, W, B, T) \quad (2.41)$$

for each node P, which relates a general variable Φ at the node P to its north (n), south (s), east (e), west (w), bottom (b), and top (t) neighbors. The coefficients a_n, a_s, ..., etc. express the magnitudes of the convection and diffusion which occur across the control volume boundaries.

Treatment of Boundary Conditions

The boundary conditions are incorporated into the numerical calculations by appropriately modifying the flux transport terms at the cell faces adjacent to the boundary

in question. To implement this, the usual flux expressions for such cells will first be suppressed by setting the relevant coefficients a_i to zero. The desired flux will then be inserted into the finite volume equations as the fictitious source terms through modifications to the linearized source coefficients. The details of the implementation are given by Ideriah (1977) and are not repeated here.

2.5.2 Solution Procedure

To solve the large set of algebraic equations presented above, our research group has developed a code called MGFD. The relaxation procedure used in MGFD is based on that suggested by Vanka (1986). A detailed description of the code is given by Nowak (1992). A brief description of the solver for a two-dimensional case, along with some specific features of MGFD is presented in the following.

Rewriting equation (2.40) for variable U_e shown in Figure 2.1 yields:

$$a_e U_e = \sum a_{nb}^e U_{nb}^e + S_C^e + (P_P - P_E) A \tag{2.42}$$

where U_{nb}^e are the neighbor values for U_e, a_{nb}^e are their coefficients, $A = \Delta y / \Delta x$, Δy and Δx being the appropriate mesh sizes. Rearranging equation (2.42) in terms of U_e:

$$U_e = B_e + (P_P - P_E) C_e \tag{2.43}$$

where

$$B_e = \frac{\sum a_{nb}^e U_{nb}^e + S_C^e}{a_e} \tag{2.44}$$

$$C_e = \frac{A}{a_e} \tag{2.45}$$

Similar expressions can be derived for variable U_w:

$$U_w = B_w + (P_W - P_P)\, C_w \tag{2.46}$$

where the expressions for C_w and B_w are similar to those for C_e and B_e. Similar equations can be written for V_n and V_s:

$$V_n = B_n + (P_P - P_N)\, C_n \tag{2.47}$$

$$C_n = \frac{1}{Aa_n} \tag{2.48}$$

$$V_s = B_s + (P_S - P_P)\, C_s \tag{2.49}$$

The continuity equation for the control volume surrounding P can be written as:

$$D_e U_e + D_w U_w + D_n V_n + D_s V_s = 0 \tag{2.50}$$

where for each control volume face:

$$D = \rho A' \tag{2.51}$$

ρ is the density and A' the area of the control volume face. Substituting the expressions for the velocities into the continuity equation gives:

$$D_e\,[B_e + (P_P - P_E)C_e] + D_w\,[B_w + (P_W - P_P)C_w] + D_n\,[B_n + (P_P - P_N)\, C_n]$$

$$+D_s\left[B_s + (P_S - P_P)\,C_s\right] \;=\; 0 \tag{2.52}$$

Equation (2.52) can be written in the form:

$$\alpha P_W + \beta P_P + \gamma P_E \;=\; \delta \tag{2.53}$$

where

$$\alpha \;=\; D_w C_w \tag{2.54}$$

$$\beta \;=\; D_e C_e - D_w C_w + D_n C_n + D_s C_s \tag{2.55}$$

$$\gamma \;=\; -D_e C_e \tag{2.56}$$

$$\delta \;=\; -D_e B_e - D_w B_w - D_n B_n^{'} - D_s B_s^{'} \tag{2.57}$$

with

$$B_n^{'} \;=\; B_n - C_n P_N \tag{2.58}$$

$$B_s^{'} \;=\; B_s + C_s P_S \tag{2.59}$$

To obtain the general form of equation (2.53) it can be written for the ith cell in a row as:

$$\alpha_i P_{i-1} + \beta_i P_i + \gamma_i P_{i+1} \;=\; \delta_i \tag{2.60}$$

With the appropriate set of boundary conditions, equation (2.60) represents a complete tri-diagonal system which can be solved by a Gauss-Seidel type relaxation method. In our MGFD code the above set of equations are solved for the nodal values of pressure using a technique known as the line-Vanka procedure (Vanka, 1986). This line-relaxation method is repeated for all the lines parallel to the three coordinate directions in a 'black and white' fashion: odd-numbered rows of cells are swept first, followed by the even-numbered rows. The velocities are updated using the explicit Equations (2.43), (2.46), (2.47), and (2.49). The additional equations, such as $k - \epsilon$ equations, energy equation, and equation for the chemical species, are solved after the pressure and velocity fields are computed. If the velocity and pressure are updated simultaneously, good efficiency in reducing the errors present in the equation set is obtained.

2.5.3 Multigrid Technique

In numerical simulation of the transport phenomena, it has been observed that generally the convergence rate of the solution algorithm slows down or stalls as the number of grids increases. However, at the initial stages of the solution process good error reduction is obtained. The reason for this is explained by Briggs (1987), using a discrete Fourier analysis on the error or residual functions. Decomposing the residual function into its frequency components or modes shows that the conventional iterative procedures are most efficient in smoothing out the errors of wavelengths comparable to the mesh size, but are inefficient in eliminating low frequency components. These low frequency error components can be smoothed out on a grid coarser than the grid in question. The multigrid technique is specifically designed to remedy this situation (Brandt, 1977). The multigrid technique cycles between coarser and finer grids until all the frequency components are appropriately smoothed. The details of the multigrid procedure used in the present work are given by Nowak (1992). A brief summary of this for a two-grid cycle

called coarse and fine, is presented in the following:

Consider a nonlinear differential equation system such as equation (2.27) written as:

$$\aleph Q = 0 \tag{2.61}$$

where $\aleph$ is some nonlinear differential operator and Q is the solution vector. The discretized form of the equation set (2.61) on a grid G_H can be written as:

$$L_H Q_H = 0 \tag{2.62}$$

where H denotes the coarse grid size, L_H is a linear difference operator approximation to $\aleph$, and Q_H is a discrete approximation to Q. An approximation to the solution Q_H, denoted as q_H^j is obtained by n times relaxation on the coarse grid. Here j refers to the iteration index. This solution is 'prolongated' to the fine grid to provide an initial guess for the fine grid computations. Let q_h^j denote the prolongated result, and h the size of the fine grid. The fine grid is obtained by dividing the cells of the coarse grid along each direction by two. Thus, for a three-dimensional domain, the fine grid has eight times the number of cells of the coarse grid. The prolongation to the fine grid is done by interpolating the solution to the new grid points which lie between the coarse grid points. To remove the high frequency components of the error from the solution, q_h^j is relaxed a few times on the fine grid. The result of this relaxation is denoted by $\overline{q}_h^j$.

The residuals are calculated on the fine grid level. These residuals or defect quantities denoted as d_h^j, contain the low frequency component of the error in the solution. If the solution was fully converged, the residuals would be close to zero. The residuals are 'restricted' to the coarse grid by interpolation. A set of equations can now be formed on the coarse grid called the 'auxiliary problem'. In this set of equations, the right hand side

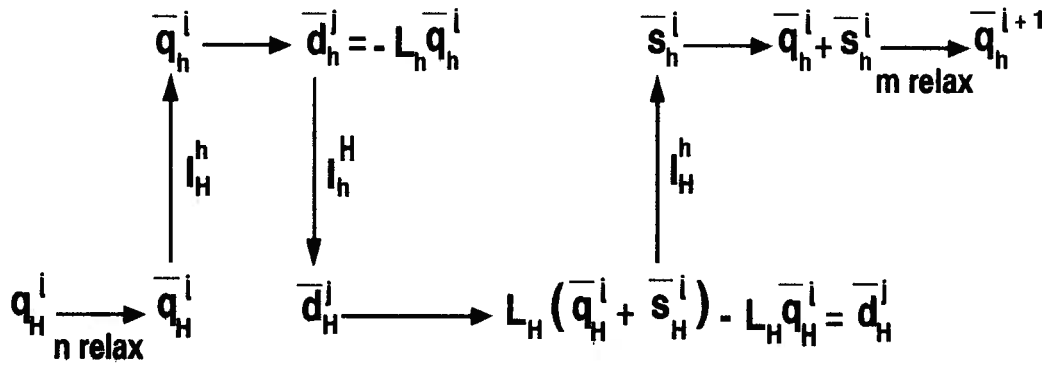

Figure 2.2: Presentation of Multigrid cycle.

is the residual obtained from fine grid, $\bar{d}_H^j$. The auxiliary problem is solved by relaxation on the coarse grid. Subtracting the solution to the auxiliary problem from the actual solution at the coarse grid yields the 'multigrid correction', s_H^j. The multigrid correction is prolongated to the fine grid, and then used to correct the fine grid solution. The solution is then relaxed a few times on the fine grid. This final solution can now be used to start the next multigrid cycle by calculating the residuals for the iteration $(j+1)$. Figure 2.2 illustrates the above multigrid cycle.

2.5.4 Segmentation Capability

Considering the simulation of the kraft recovery boiler, there is a large variation in dimension within the domain. The overall dimension of the boiler is much larger than its air ports. For this class of problems the algorithm may not be efficient even with the multigrid technique. The segmental capability of MGFD code is to address these kinds of problems in particular. The MGFD code allows the domain to be subdivided into a number of segments for efficient grid distribution. These segments are rectangular blocks of cells and the grid in each segment is completely independent of the grid at the other

segments. Thus, the grid distribution in each segment can be done based on the local flow resolution required in that segment. Since the segments are independent of each other, the control volume faces at the segment interfaces do not necessarily match. Therefore, to have a conservative system the conservation of flow quantities (i.e. mass, momentum, etc.) across the segmental boundaries are monitored. The details of the implementation are presented in the report by Nowak (1992).

The iterative relaxation process is performed on each segment sequentially. Additionally, each segment is divided into a number of smoothing blocks. Each block consists of a cube of cells. The smoothing within each segment takes place by smoothing within each block in a 'zebra' fashion to ensure efficient coverage of all the cells with a minimum number of sweeps. The main advantage with the usage of blocks is reduction in the calculation time as the smoothing in different blocks can be done simultaneously. The details of the implementation are reported by Nowak (1992) and Salcudean, et al. (1992).

2.6 Convergence Criterion

A convergence criterion has to be established to ensure the degree to which a computed solution at each iteration satisfies the finite difference equations. In the present computations this convergence criterion is based on the value of the normalized absolute residual errors of the continuity equation. That is, the convergence of the solution process is monitored by observing the reduction in the normalized mass error. The total mass error is calculated by summing the absolute values of the mass residue of all cells. To normalize the total mass residue is divided by the total inlet mass flow. Assuming r_i to be the mass residue of the ith cell, the total normalized mass error is obtained by the following expression:

$$\text{Total normalized mass error} = \frac{\sum_{\text{all cells}} |r_i|}{\text{Total inlet mass flow}} \tag{2.63}$$

Obviously when the solution is obtained, the total normalized mass error becomes zero. The solution is assumed to have converged when the steadily decreasing sum of the normalized absolute residuals has fallen below a specified level, typically 10^{-3}.

For the simulations presented in the following chapters the results of these normalized mass error reduction histories are displayed in their relevant sections. In all cases the total normalized mass residue is less than 10^{-4}.

Chapter 3

Experimental Study

In this chapter, the wind tunnel used, the arrangement for the injection of the jet fluid, the measurement technique, and related calibration procedures are discussed. The experimental results are presented and discussed.

3.1 Experimental Set-Up and Apparatus

Experiments were conducted in the test section of a suction type wind tunnel 320 *mm* high, 160 *mm* wide and 1500 *mm* long. Air entering the tunnel passes through a filter, a flow straightener, a series of three screens, and a contraction section before entering the test section. A plexiglass plenum chamber, 300 *mm* high, 160 *mm* wide, and 750 *mm* long was installed beneath the floor of the wind tunnel, its top flush with the floor of the tunnel (see Figure 3.1).

A slot 2 *mm* wide and normal to the floor, connected the plenum to the test section. To reduce gas consumption, the length of the slot was reduced to 60 *mm*. Two interior tunnel walls were installed to act as end plates for the slot. These interior walls extend upstream to the inlet of the test section and downstream a distance of 1000 *mm* and were the full height of the tunnel. The jet fluid enters through the bottom of the plenum chamber and is injected into the air cross-flow through the slot opening.

The boundary layer at the entrance to the test section is tripped by a wire to ensure that it is both turbulent and uniform across the width of the test section.

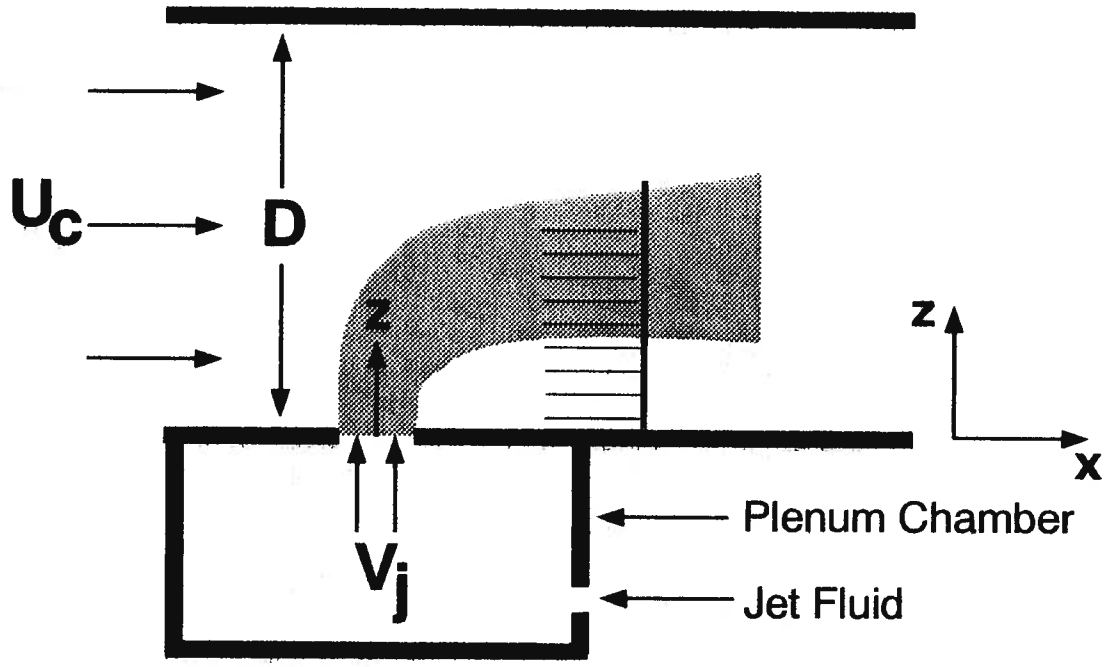

Figure 3.1: Schematic presentation of the experimental set-up.

3.2 Concentration Measurement Technique

On line measurements of jet concentrations were done using a Flame Ionization Detector (FID). In this thesis the terms 'jet concentration' and'jet mass fraction' are used interchangebly. A brief description of this apparatus is presented here. A complete description of FID and its theoretical foundation can be found in monographs by McWilliam (1970), Bolton et al. (1971), David (1974), Robins (1975), Fackrell (1978, 1980).

In essence, a FID consists of a hydrogen/air flame burning in an insulated flame chamber across which a voltage is applied. The introduction of an organic compound into the flame leads to the production of ions. The three main parts of the FID are: a base body, a flame jet, and a detector cell. A schematic presentation of the FID is shown in Figure 3.2. The flame jet is at the center of the stainless steel base body.

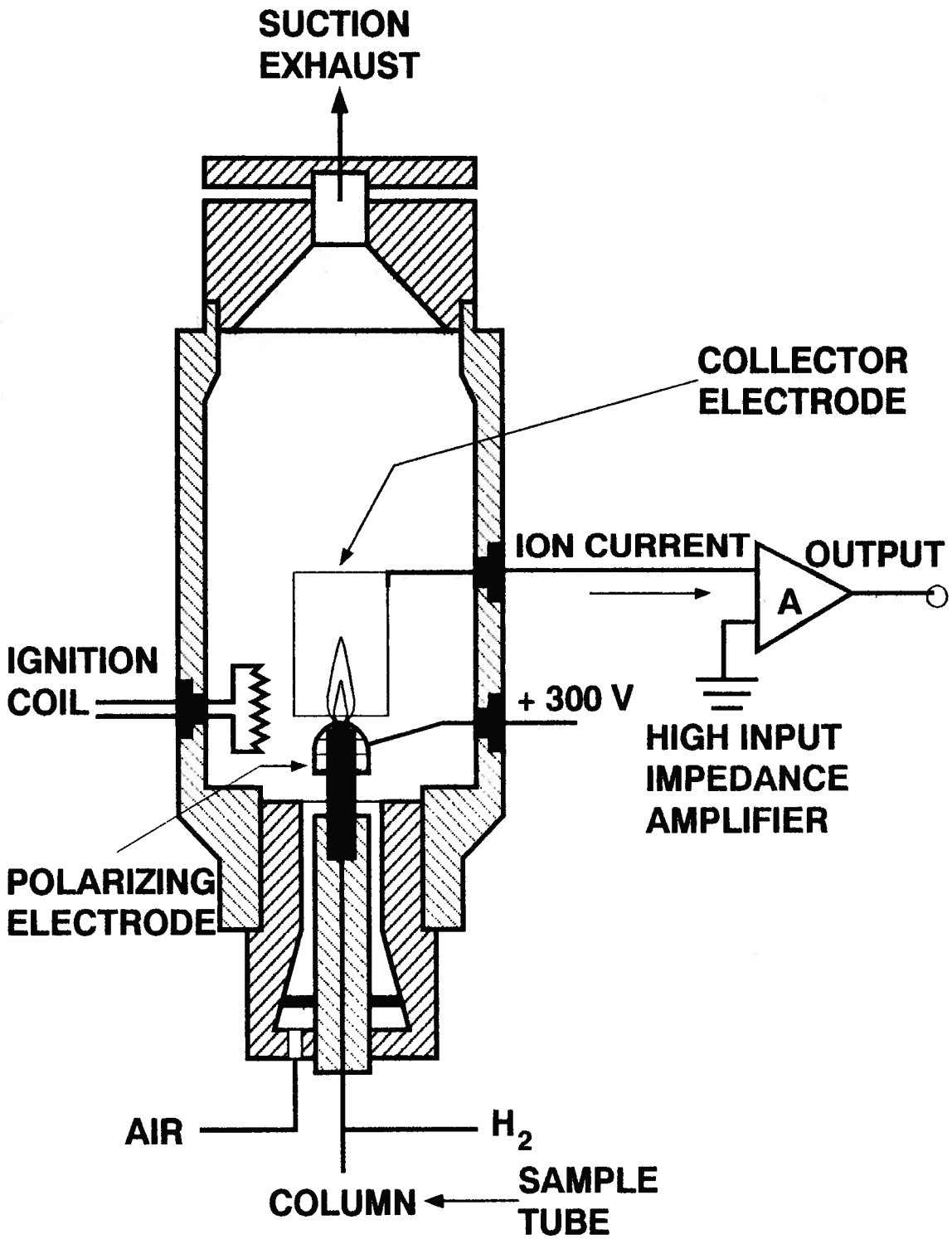

Figure 3.2: Schematic presentation of FID.

The collector electrode consisting of a 10 *mm* diameter cylinder lies at the center of the combustion chamber. At the center of this collector lies a metallic jet that delivers fuel to the flame. This jet also acts as one of the two polarization electrodes. The flame igniter is also positioned inside the detector cell. The electrodes and the igniter are electrically connected to the power supply unit. Due to the presence of the two polarization electrodes, the ions produce a small current. An amplifier is used to convert the current to a suitable output voltage. For a given instrument, the magnitude of the current depends on the mass flow and carbon content of the hydrocarbon gas. The output voltage is then a function of the concentration of the organic compound present in the sampled gas.

The measurements of concentration are made through a specifically designed rake of very fine tubes (0.5 *mm* outside diameter). The rake can stand vertically on the floor of the tunnel. The location of the tubes is adjustable. However, a minimum of 2 *mm* distance (from the tube centers) is necessary to eliminate interference of the adjacent tubes. Due to the thickness of the tubes the closest measuring point to the floor of the tunnel is 0.25 *mm*. A schematic presentation of this arrangement is shown in Figure 3.1.

The flame chamber is sealed and suction is applied to the exhaust to draw the sample gas (also called the carrier gas) contaminated by the organic compound into the chamber along the rake and the sampling tube. Hydrogen, air and carrier gas are carried via separate tubes into the jet assembly. A narrow bore (0.25 *mm* ID, 30 *mm* long) metal tube carries the sample to 1 *mm* from the jet tip. Hydrogen and air are carried to the combustion chamber via nickel tubing. A rotary multiport sampling valve with 12 streams was used to time share the FID. This arrangement enables measurement of concentration at 12 points consecutively without repositioning the sampling probe assembly. The procedure is controlled using an on-line computer. The computer is programmed such that at each point the sampling is done over a sufficiently long time to obtain an

average jet fluid mass fraction. In addition when switching from one measurement point to another, sufficient time is allowed to elapse to ensure the system is flushed from the gas flow corresponding to the previous point.

3.2.1 FID Calibration

The FID responds to the mass per unit time of hydrocarbons entering the flame chamber. Hence the FID output voltage for a constant volume concentration $\mathcal{V}$ entering the flame should be

$$E = B'\rho\mathcal{V}\dot{Q} \tag{3.64}$$

where E is the FID output voltage, ρ is the density of the tracer gas or the contaminant (hydrocarbon gas), $\mathcal{V}$ is the volume fraction of the tracer gas per unit volume of mixture, $\dot{Q}$ is the volume flow rate sucked through the tubing into the FID and B' is the constant of proportionality for the specific FID. Since in practice the efficiency of the ionization process varies at different flow rates the output is a more complicated function of the flow rate, i.e.

$$E = B'\rho\mathcal{V} \cdot f(\dot{Q}) \tag{3.65}$$

When the volume flow rate is constant, this function may be treated as a constant of proportionality.

We note that according to Equation (3.65) the FID output is a linear function of the hydrocarbon's concentration. To calibrate the system two points of this line have to be determined. To maintain uniform conditions for the two set points the measuring probe is put inside the plenum through the slot and the jet fluid is sent into the plenum at

the required flow rate. The hydrocarbon gas is mixed with the jet fluid in a mixing box before entering the plenum. In our experiments propane gas is used as the contaminant in low (less than 3%) concentrations. The FID output is recorded for the following two conditions. With no propane added to the jet fluid the FID output voltage is denoted E_0 and referred to as the 0% propane calibration point. A known amount of propane is then added to the gas flowing through the plenum. This is sampled and the FID output voltage is again recorded. This is denoted E_{max} and is referred to as the 100% plenum calibration point. Using these two set points a linear relationship is established between the FID output voltage and the percentage of plenum propane concentration for the given flow rate of the carrier gas.

Before beginning each experiment, each tube is calibrated individually and the calibration is recorded in a microcomputer. During the experiment the jet fluid (mixed with propane) is injected into the wind tunnel through the slot. Due to the entrainment of the jet fluid into the crossflow, propane concentrations are diluted. The measuring probe is located inside the wind tunnel at locations of interest. Using the calibration curve, the voltage output from the FID can yield the local gas concentration. All measurements of propane concentration in the wind tunnel should result in FID output voltage readings between the two extreme values of E_0 and E_{max}.

As a check of our FID, the linearity of Equation (3.65) tested. Two gases are selected for this purpose, namely, air and carbon dioxide. Carbon dioxide is selected as representing a gas with higher density than air; carbon dioxide is 1.5 times heavier than air. The volume flow rate of each gas through the plenum chamber is kept constant, while the volume flow rate of the propane gas changes. The FID output voltage for each volume flow rate of propane is then recorded (E). To scale the results, the FID output voltage for the case with no propane (i.e. E_0) is measured first. The normalized FID output voltage calculated as $(E_0 - E)/E_0$ is plotted against the volume concentration of propane

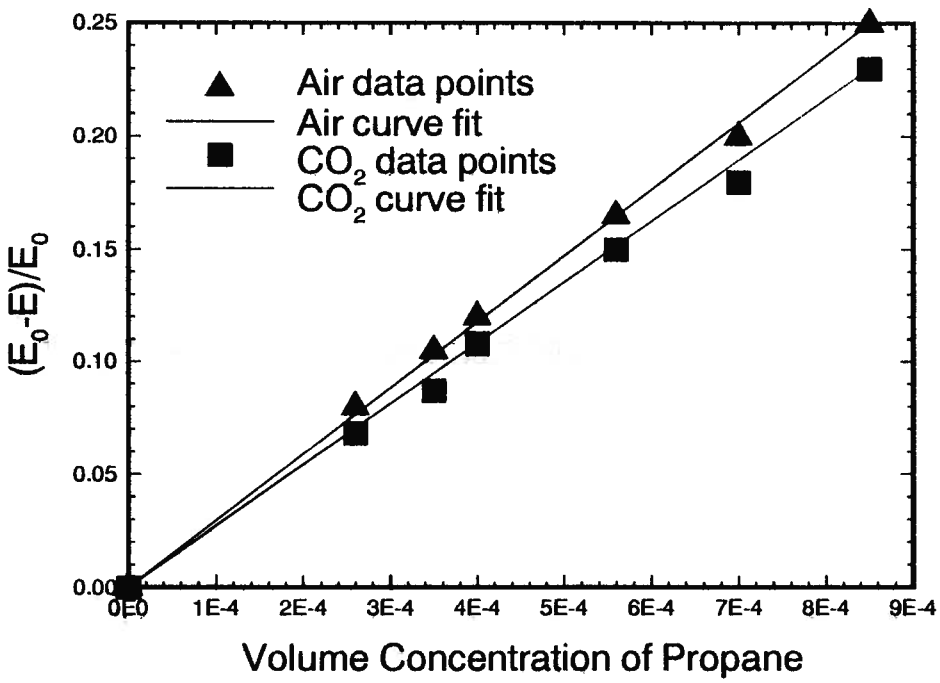

Figure 3.3: Linearity of FID for air and carbon dioxide.

for each gas. These results are shown in Figure 3.3.

The estimated error in measurements of flow rates of gases is $\pm 2\%$. These results show a linear relationship between the FID output voltage and concentration of propane, confirming the validity of Equation (3.65) within the experimental accuracy.

The above calibration procedure, however, is not sufficient when the composition of the carrier gas is not fixed. In our experiments the jet fluid is different from crossflow. Therefore the composition of the carrier gas is a function of its location inside the wind tunnel. Because the jet mixes with the crossflow, the composition of the carrier gas sucked into the FID will be different for many measuring points inside the wind tunnel. Therefore, the concentration of the contaminant passing through the FID changes due to two factors: dilution of the jet fluid with the crossflow, and the variation of $f(\dot{Q})$ due to changing flow rate as the carrier gas composition changes. The above calibration procedure incorporates the changes in the contaminant concentration due to the first

factor only. Therefore the resultant concentration values have to be corrected. To obtain the correction curve for each jet fluid used, a series of calibration experiments has to be performed. A fixed volume flow rate of the jet fluid plus the contaminant (Q_1') is sent into the plenum chamber after passing through a mixing box. To this mixture is added known volume flow rates of air (Q_2'). The FID measuring probe is set inside the plenum chamber and the FID output voltage (E) is recorded for each jet fluid/air mixture. Denoting the FID output voltage for the jet fluid plus the contaminant without any air added as E_{max}, the values of E can be expressed in dimensionless form as $\left(\frac{E}{E_{max}}\right)$. As during the calibration experiments the addition of the jet fluid and air is done under controlled conditions, the response of the FID to different values of jet fluid mass fraction can be measured. Such calibration curves were obtained for carbon dioxide and a mixture of 50% helium+50% air (by mass) gases and are shown in Figure 3.4.

In Figure 3.4 the ordinate represents the normalized output voltage of the FID and the abscissa represents the corresponding jet fluid mass fraction. The concentration values measured inside the wind tunnel during each experiment correspond to the values of the normalized voltage shown on the y axis in Figure 3.4. Therefore the corrected value of jet mass fraction can be read from the x axis.

3.3 Experimental Results

The concentration profiles of a two-dimensional slot jet injected vertically upward into a horizontal crossflow is discussed in this section. First, the results of velocity and concentration measurement experiments, carried out to examine the two-dimensionality of the flow at different locations and for different flow variables, are presented. In the second section concentration measurements for different jet to crossflow density ratios, and three different values of jet to crossflow mass ratios are presented, and some conclusions on the

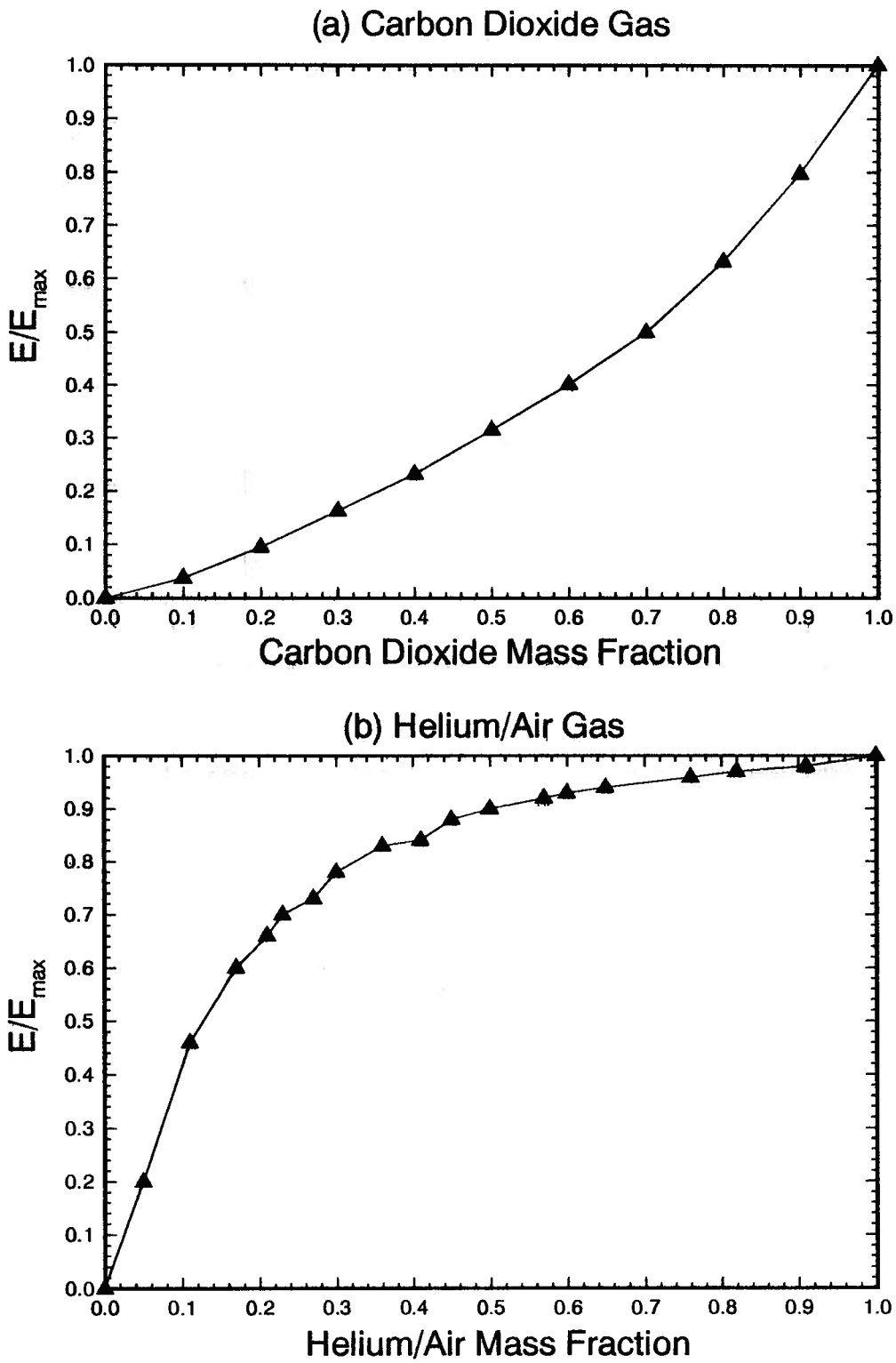

Figure 3.4: Calibration of FID for carbon dioxide and helium/air gas

effect of density variations on jet concentration profiles are drawn.

3.3.1 Two-dimensionality

To investigate the assumption of two-dimensionality of the flow, experiments were conducted to measure fluid velocity and jet concentration in crossflow at various locations and for different flow conditions. Fluid velocity was measured using a hot wire anemometer and jet concentration was measured using a flame ionization detector (FID). During the two-dimensionality tests air contaminated with a weak concentration of propane was used as the jet fluid.

The two-dimensionality of the tunnel can be measured by the extent of the dependence of the velocity and concentration on lateral dimension y measured from the center of the tunnel. As our experiments are done at the center of the tunnel in the central plane xz (where $y/S = 0$) we are interested in the degree of two-dimensionality of the flow close to the center, and assume that the region of interest is $-5 \leq y/S \leq +5$. If the flow is 100% two-dimensional, the curves of the lateral measurements of the flow variables (i.e. velocity and concentration) will be straight, horizontal lines.

Figure 3.5 shows the values of the normalized velocity for the case where there is no jet fluid injected. Therefore these measurements only indicate the tunnel two-dimensionality. Measurements are done for two tunnel velocities $U_c = 2$ and $5\ m/s$ at $5.5S$ upstream and $10S$ and $20S$ downstream of the slot. The maximum deviation from two-dimensionality is present at $U_c = 2\ m/s$, $y/S = 5$, $x/S =$ -5.5 and $z/S = 0.5$. This maximum value is less than $\pm 2\%$ in U/U_c. It should be noted that the maximum error is present closest to the floor of the wind tunnel where a small error in positioning the probe at the z/S location would contribute significantly to errors in measurements, since the velocity gradients near the wall are largest and the velocities are smallest. Thus, the assumption that the tunnel flow is two-dimensional is reasonable.

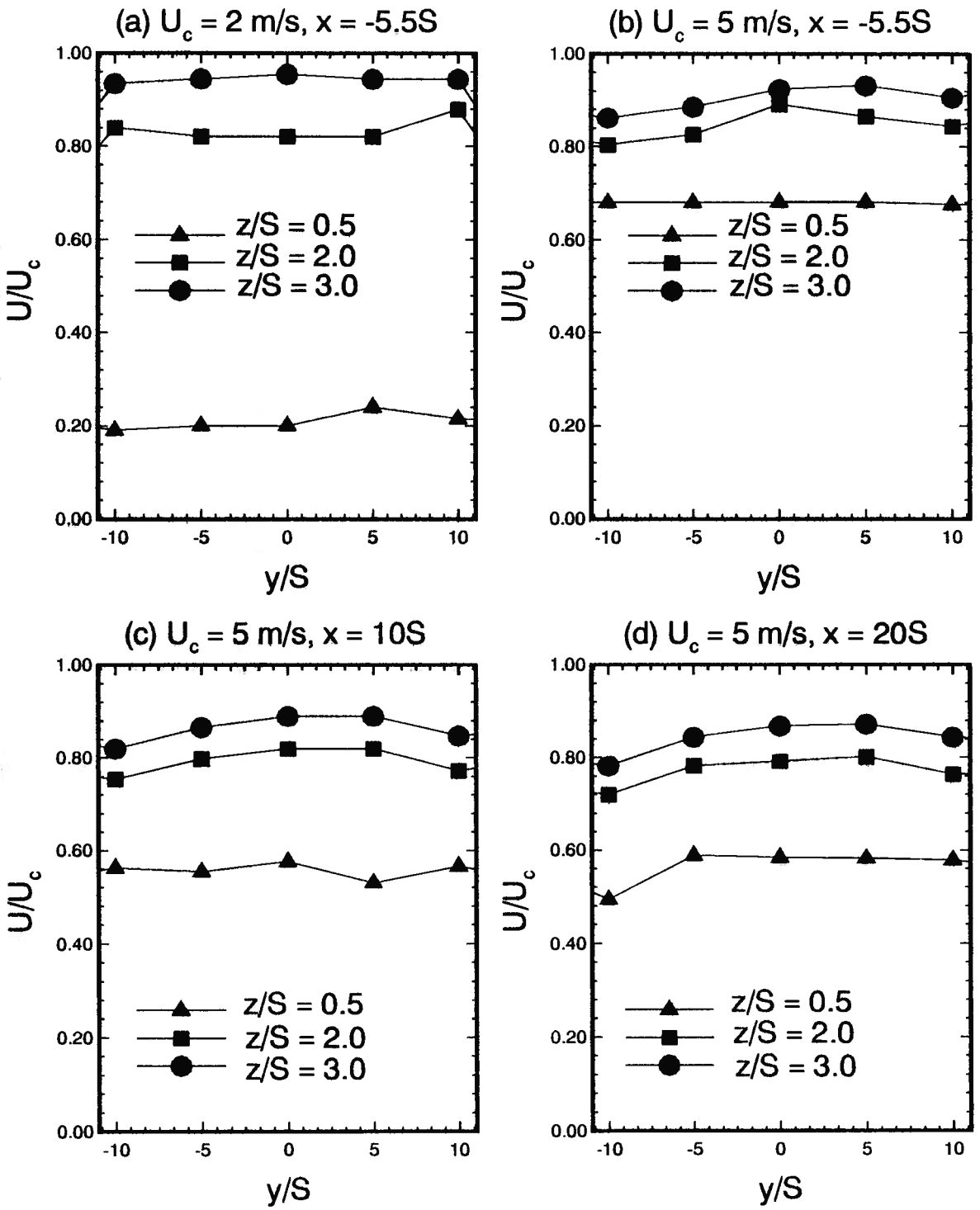

Figure 3.5: Test of tunnel two-dimensionality, velocity measurements for $U_c = 2$ and 5 m/s , and no jet injected.

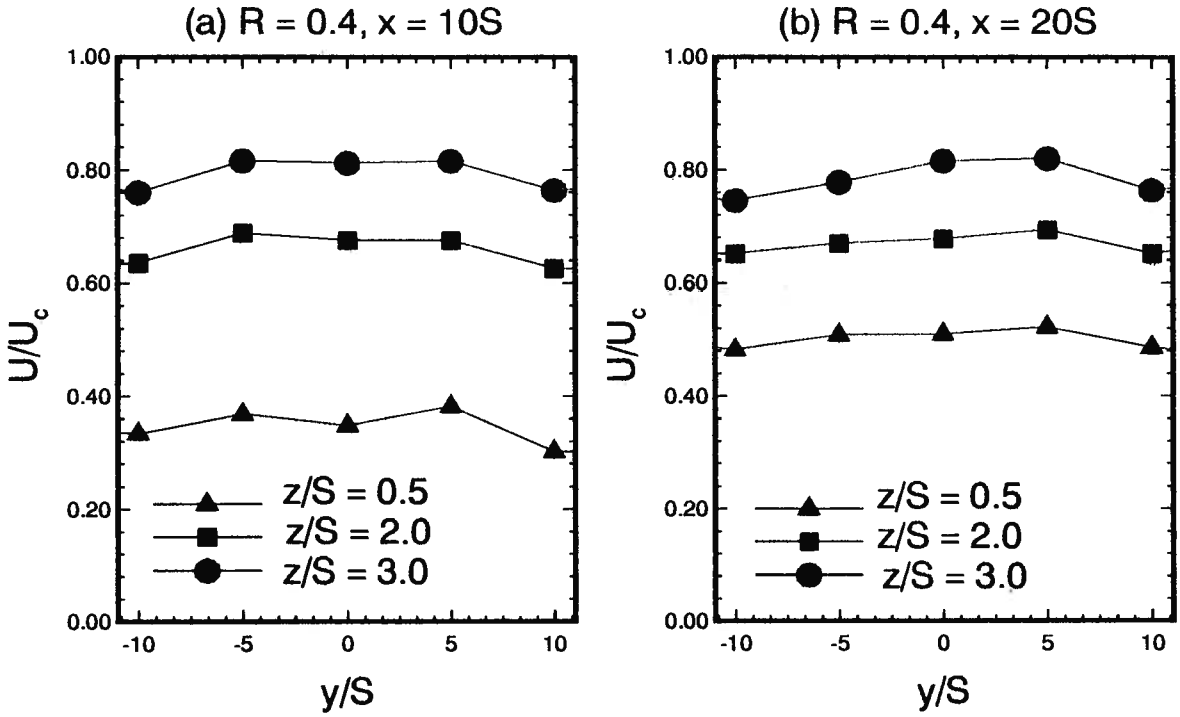

Figure 3.6: Test of tunnel two-dimensionality, velocity measurements for $U_c = 5m/s$ and $R = 0.4$.

Figure 3.6 shows the velocity measurements at velocity ratio $R = 0.4$ at two locations $x/S = 10$ and 20 downstream of the jet slot and the $z/S = 0.5$, 2 and 3 above the wall. Here again the maximum error between $-5 \leq y/S \leq +5$ is small (less than $\pm$ 3%) and occurs at $z/S = 0.5$, $y/S = 5$, and $x/S = 10$.

Figure 3.7 shows the measurement of jet concentrations for two values of $R = 0.2$ and 0.6 ($U_c = 2\ m/s$) at downstream locations $x/S = 10$ and 20 and $z/S = 0.25$, 0.75, and 1.75. The estimated experimental errors in measurements of velocity and concentration here are $\pm$5%. For all cases shown in Figure 3.7 the maximum deviation from two-dimensionality occurs at $R = 0.6$, y/S = -5, $z/S = 1.75$, and $x/S = 20$, and is about $\pm$5% of concentration at $y/S = 0$. As the weak jet is deflected by the crossflow it remains close to the floor, and the values of the jet concentrations at higher z/S locations are small. Close to the edge of the jet where the jet fluid concentration is low, the flow can

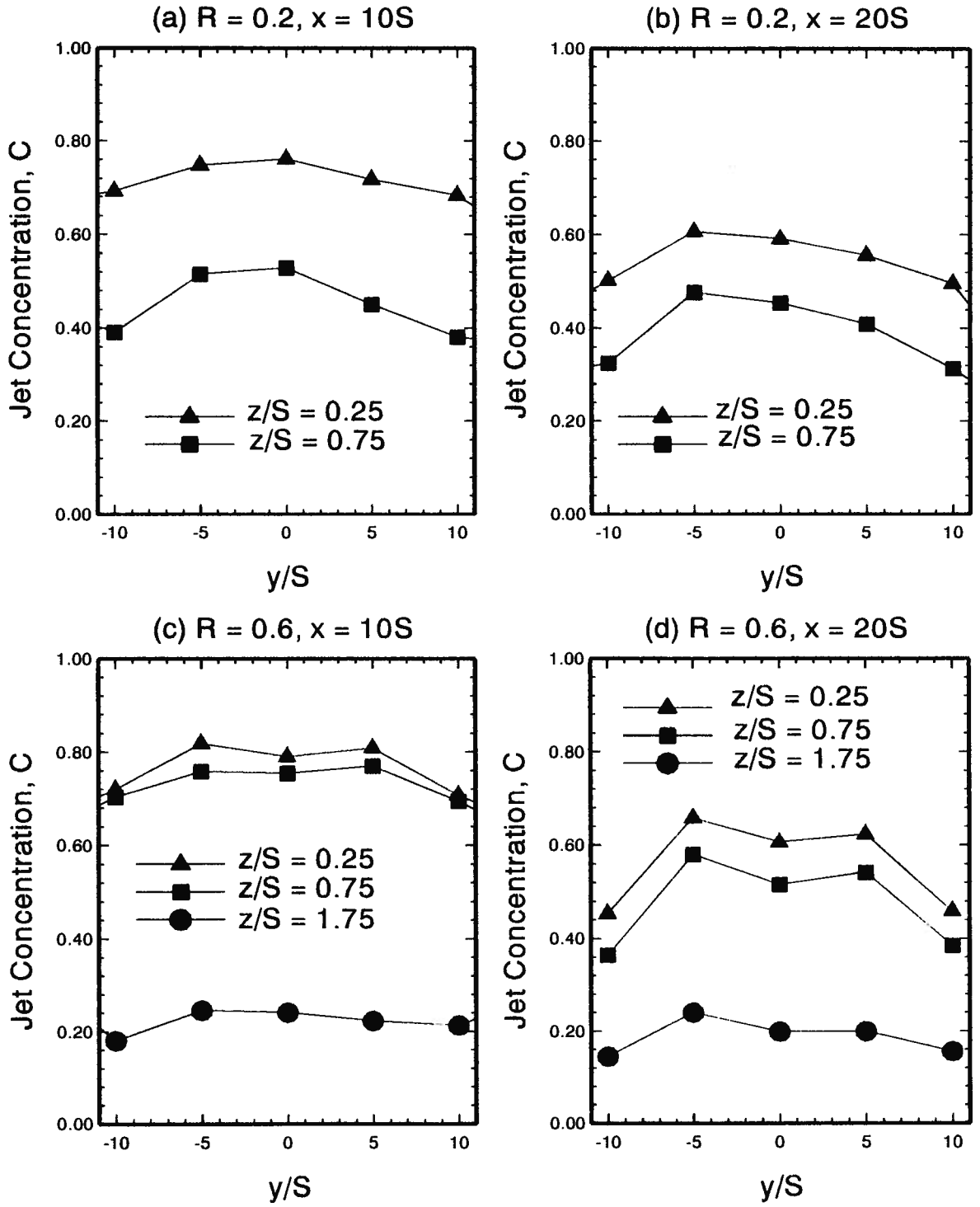

Figure 3.7: Test of tunnel two-dimensionality, concentration measurements for $U_c = 2m/s$ and $R = 0.2$ and 0.6.

be intermittent with bursts of propane where the turbulent jet passes. Therefore a higher deviation from two-dimensionality is present. However, in the region of interest, that is for $-5 \leq y/S \leq +5$, the flow two-dimensionality is reasonable.

3.3.2 Effect of Density variations on Jet in Crossflow

To examine the effect of density variations on the jet concentration profiles, measurements were done using air, carbon dioxide, and a mixture of 50% helium+50% air as the jet fluid injected into the air crossflow. Carbon dioxide gas is 1.5 times heavier than air and the mixture of 50% helium+50% air gas is 4 times lighter than air. Concentration measurements downstream of the jet slot were done for three mass flow ratios, $G = 0.4$, 0.6, and 0.8. The estimated experimental errors for measurements of concentrations and velocities are $\pm 5\%$.

Before proceeding to analyze the experimental results clarification of certain definitions or assumptions is necessary. The jet deflects under the effect of the cross flow. The locus of the maximum jet concentration defines the jet trajectory. Commonly a separation or recirculation region is formed on the lee side of the jet. The point on the wall having zero velocity in the streamwise direction is called the reattachment point. The distance between the jet exit and this latter point is called the reattachment length. On any given cross-section if the streamwise velocity is positive everywhere then it is assumed that no recirculation region exists at that cross-section. In the following discussion if the point of maximum jet concentration is at the wall (i.e. at the first z/S location), it is assumed that at that cross-section no separation is present and that the measurements are outside the recirculation region. If the point of maximum concentration is at some distance from the wall, and there are points with lower concentration values closer to the wall, this is taken as evidence of the presence of a separation region.

Figure 3.8 shows the concentration profiles at $G = 0.4$ at 4 downstream locations

x/S = 1.5, 3, 5, and 10. Considering the results in the near field region (close to injection point) the lighter gas penetrates deeper into the crossflow and forms a larger separation region. In the near field region the concentration profile of carbon dioxide gas is similar to air. Farther downstream, at $x/S = 10$, the carbon dioxide jet shows higher concentrations closer to the wall. The concentration profile of the lighter gas (helium/air) at $x/S = 10$ is becoming more like that of the air and carbon dioxide jets.

Figure 3.9 shows similar results at $G = 0.6$. Comparing the results in the near field we notice that at $x/S = 1.5$, and 5, the air jet and the carbon dioxide measurements are similar. The observed differences at the first measurement point ($z/S = 0.25$) can be attributed to the experimental errors. Farther downstream, at $x/S = 10$, the differences between the air and carbon dioxide concentration profiles increase with higher values of carbon dioxide concentration closer to the wall. The helium/air jet has formed a larger separation region which seems to persist up to $x/S = 10$. Therefore the values of concentrations close to the wall for this gas are much smaller than those for air or carbon dioxide.

Figure 3.10 shows the concentration profiles at $G = 0.8$. The trends are similar to those seen in Figures 3.8-3.9. It is clear that the size of the separation regions for air and helium/air jets have increased. Thus, in the near field region the concentration values close to the wall have further decreased. These differences in case of carbon dioxide jet are not significant.

As the experiments of low jet to crossflow mass ratios are of direct application to the gas turbine industry, it is useful to compare the values of 'film cooling effectiveness' (η) which is equivalent to the value of the jet concentration at the wall in these experiments. Figure 3.11 shows the values of the film cooling effectiveness η for each gas for three values of mass ratios $G = 0.4$, 0.6, and 0.8.

For all three values of G the heavier gas has higher values of η in comparison to the

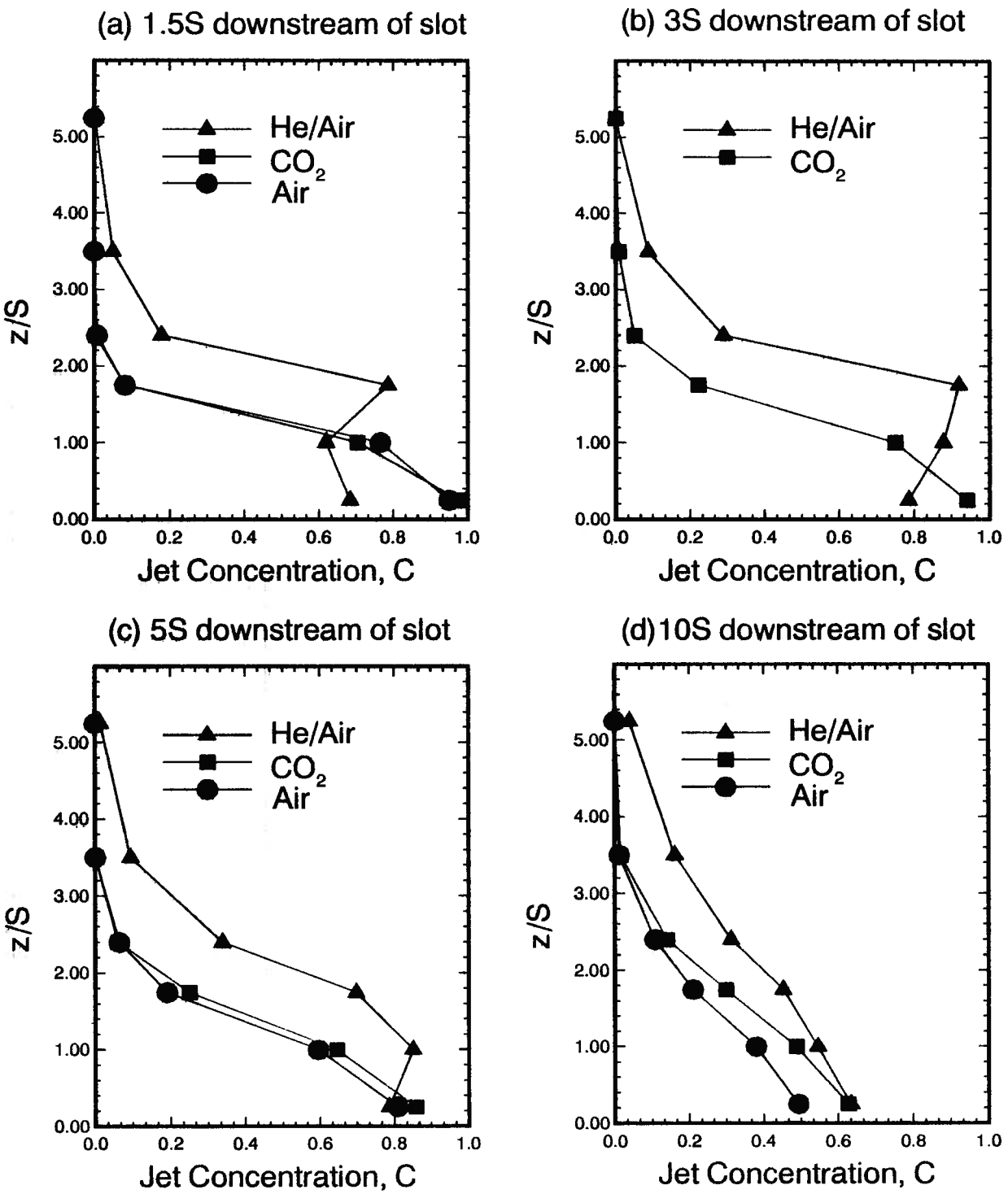

Figure 3.8: Cross-stream concentration profiles at $G = 0.4$ for air, carbon dioxide and helium/air jets.

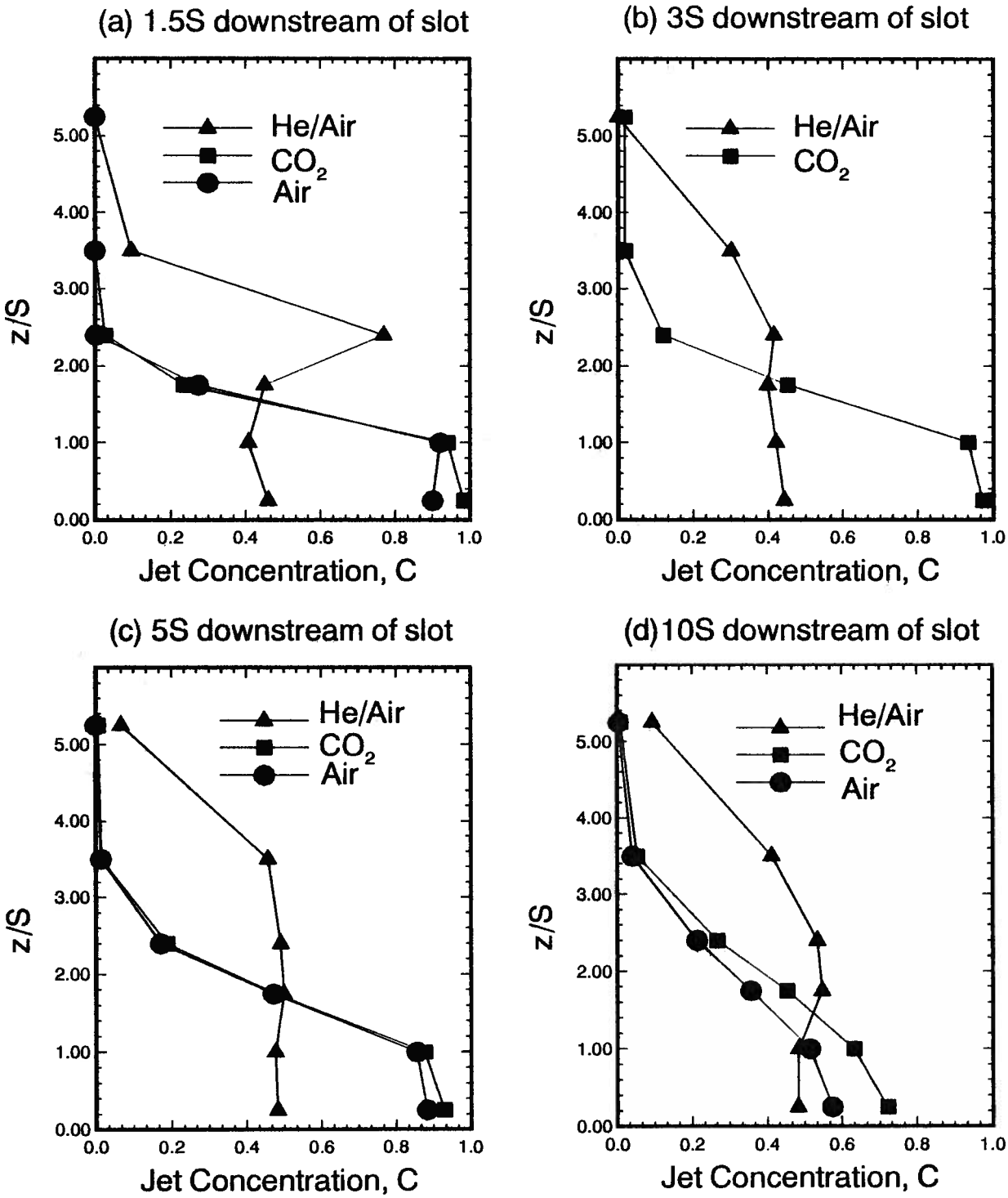

Figure 3.9: Cross-stream concentration profiles at $G = 0.6$ for air, carbon dioxide, and helium/air jets.

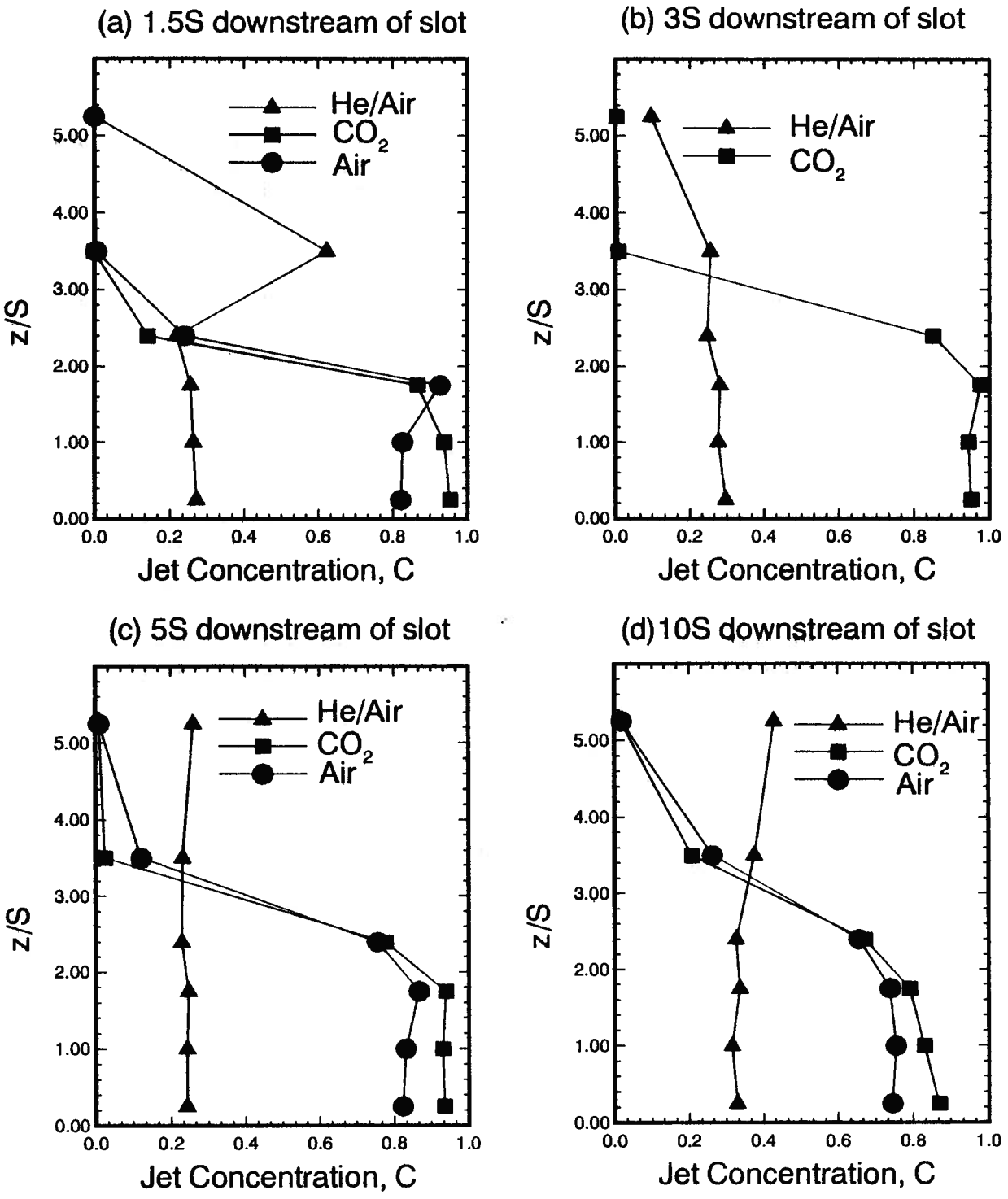

Figure 3.10: Cross-stream concentration profiles at $G = 0.8$ for air, carbon dioxide, and helium/air jets.

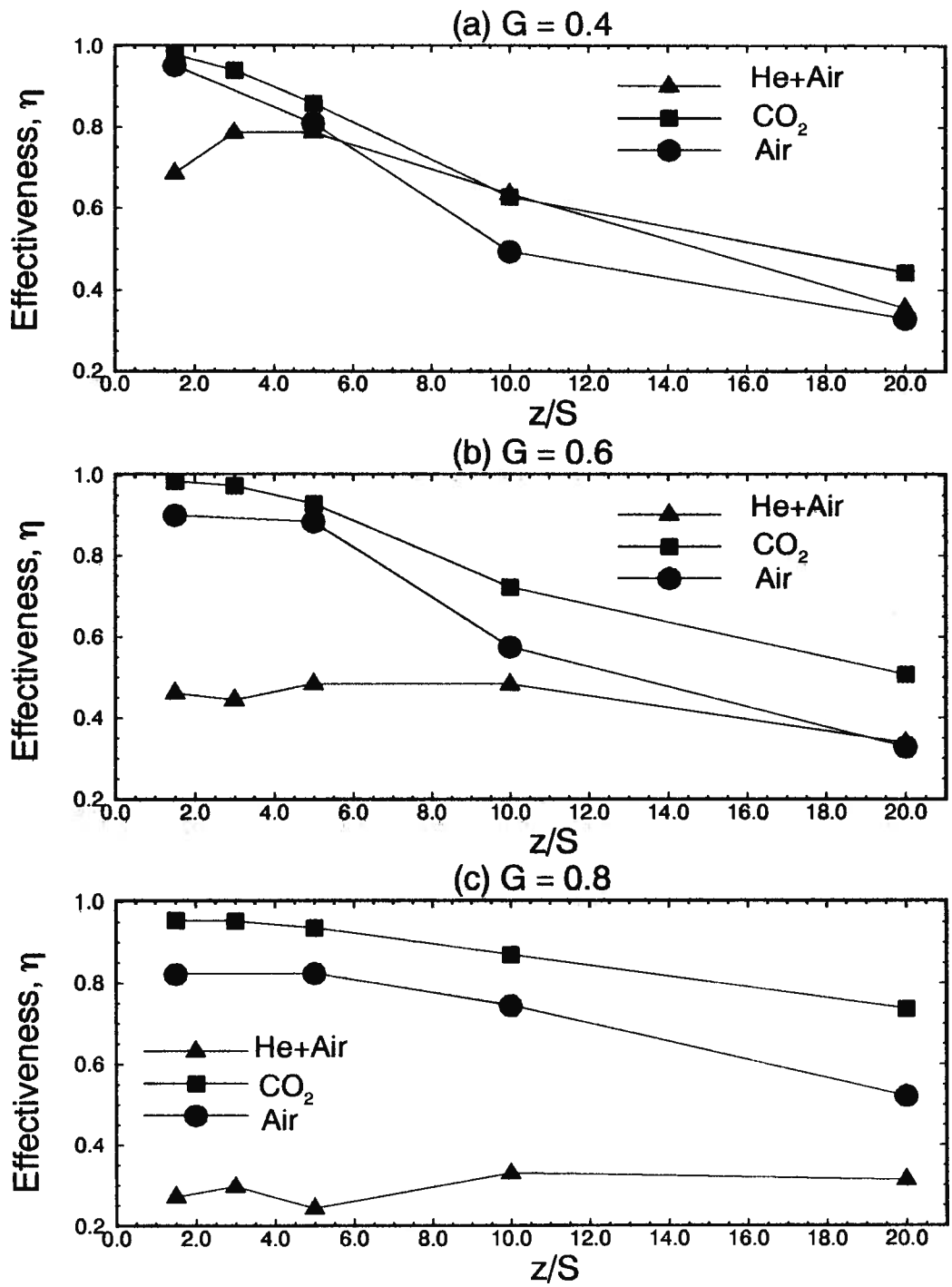

Figure 3.11: Variation of 'film cooling effectiveness' η with dimensionless distance from the slot for air, carbon dioxide, and heliume/air jets and three mass ratios G.

Table 3.1: Range of dimensionless numbers for the experiments

G	CO_2			Air			He+Air		
	J	Ri	F_b/F_d	J	Ri	F_b/F_d	J	Ri	F_b/F_d
0.4	0.11	0.0055	0.0004	0.16	0.0	0.0	0.66	0.0009	0.0006
0.6	0.24	0.0055	0.0009	0.36	0.0	0.0	1.49	0.0009	0.0013
0.8	0.43	0.0055	0.0015	0.64	0.0	0.0	2.65	0.0009	0.0023

other two gases, with the highest values of η for the near field at $G = 0.4$. As G increases, η for carbon dioxide and air increases in the far field and decreases in the near field. At $G = 0.8$, however, the helium/air jet has smaller values of η.

The behavior described can be explained by comparing the momentum flux ratio $J = \frac{\rho_j V_j^2}{\rho_c U_c^2}$ of the three gases for the same values of mass flux ratio G. Table 3.1 gives the values of J for each gas at different values of G.

As the ratio of the jet fluid density to the crossflow decreases, the velocity ratio of the jet to crossflow R has to increase in order to maintain the same value of mass flux ratio G. This will result in much higher values of J for the lighter gas. As J increases the jet penetration and the size of the separation region increases. At $G = 0.4$ the helium/air jet has a much larger momentum ratio (J) than both the carbon dioxide and air jets. The momentum ratio of the air jet is about 1.5 times larger than that of the carbon dioxide. The same trend is clear for values of $G = 0.6$ and 0.8. The gas with larger J penetrates deeper into the crossflow and forms a larger separation region. The larger the separation region the more significant an effect it has on the flow. Since the mass ratios are equal, the larger penetration of the jet results in lower values of jet concentration closer to the wall. The carbon dioxide jet has the lowest momentum flux ratio at a given mass ratio. Therefore it forms a smaller separation region and has higher concentration values closer to the wall.

The values of jet exit Richardson number defined as

$$Ri_0 = \frac{\rho_c - \rho_j}{\rho_c} \frac{gS}{V_j^2} \tag{3.66}$$

are also listed in Table 3.1. The jet exit Richardson number, which is a measure of the ratio of the buoyancy force to the momentum of the jet at the exit, is generally used in the literature as a criterion to quantify the significance of the buoyancy force in a flow. Referring to Table 3.1 the values of Ri_0 are larger in the case of the carbon dioxide jet than for the helium/air jet. Moreover, the values of Ri_0 remain constant as G increases. In our experiments the jet velocity is kept constant and the different values of G are obtained through changing the crossflow velocity. It is clear from Equation 3.66 that the effects of the crossflow velocity are not included in this definition. Therefore using the jet exit Richardson number or the square root of its inverse, defined as the densimetric Froude number, as a criterion to compare the effect of the buoyancy force in flows with different crossflow velocities is misleading or incomplete.

To include the effects of the crossflow we recommend the use of an expression suggested by Niessen (1978), which compares the buoyancy force to the drag force exerted by the crossflow on the jet. That is:

$$\frac{F_b}{F_d} = \frac{gS}{U_c^2} \frac{\rho_c - \rho_j}{\rho_c} \tag{3.67}$$

where F_b refers to the buoyancy force and F_d refers to the drag force exerted on the jet at its exit plane. A similar expression is suggested by Wright (1978). The values of F_b/F_d are also presented in Table 3.1. However the above expression for $\frac{F_b}{F_d}$ does not include the effect of jet velocity V_j. Considering that the drag force exerted on the jet depends on the exposed jet area, and that this area is affected by the jet penetration a parameter such as momentum flux ratio of jet to crossflow, J can provide a link between V_j and

U_c. The buoyancy force at each point depends on the local density differences, however, the expression for J does not include the density difference term. Therefore it becomes evident that more than one parameter is required for a more complete analysis of the problem of variable density jet in crossflow.

In Table 3.1 the values of F_b/F_d for helium/air jets are higher than carbon dioxide jets at the same value of G. Also as the value of G increases, indicating less significant effect of buoyancy force on the flow field as the momentum forces increase, the value of F_b/F_d increases. Therefore care must be taken when using ratios, such as the jet exit Richardson number, F_b/F_d, etc. to analyze the effects of the variations of the flow variables on different flows.

Chapter 4

Effects of Buoyancy on Two-Dimensional Jets in Cross-Flow

This chapter has two objectives. The first is to validate the multigrid code for the problem of a jet in a crossflow for situations where the jet and crossflow densities are different. The second objective is the numerical simulation of the effect of buoyancy force on the primary level jets in the kraft recovery boiler. The validation of the code is discussed in the next section.

4.1 Comparison of Experimental and Numerical Results

Comparisons between the results obtained using the multigrid code and the experimental measurements for constant density flows have been reported before by Abdullah et al. (1992) and Tse (1994). To validate the accuracy of the multigrid code for variable density flows, the experimental concentration measurements presented in the previous chapter are compared here with the numerical results.

4.1.1 Problem Description and boundary Conditions

A sketch of the calculated flow domain is shown in Figure 4.1. The jet slot (S) is 2 mm wide as was the case in the experiments.

The boundary conditions imposed are: plug flow conditions for the jet and the crossflow inlet velocities, the no slip condition at the bottom wall (containing the jet) and the top wall, the symmetry condition at the two lateral planes, and the zero gradient condition at the exit plane. The choice for the location of the inlet plane for the crossflow

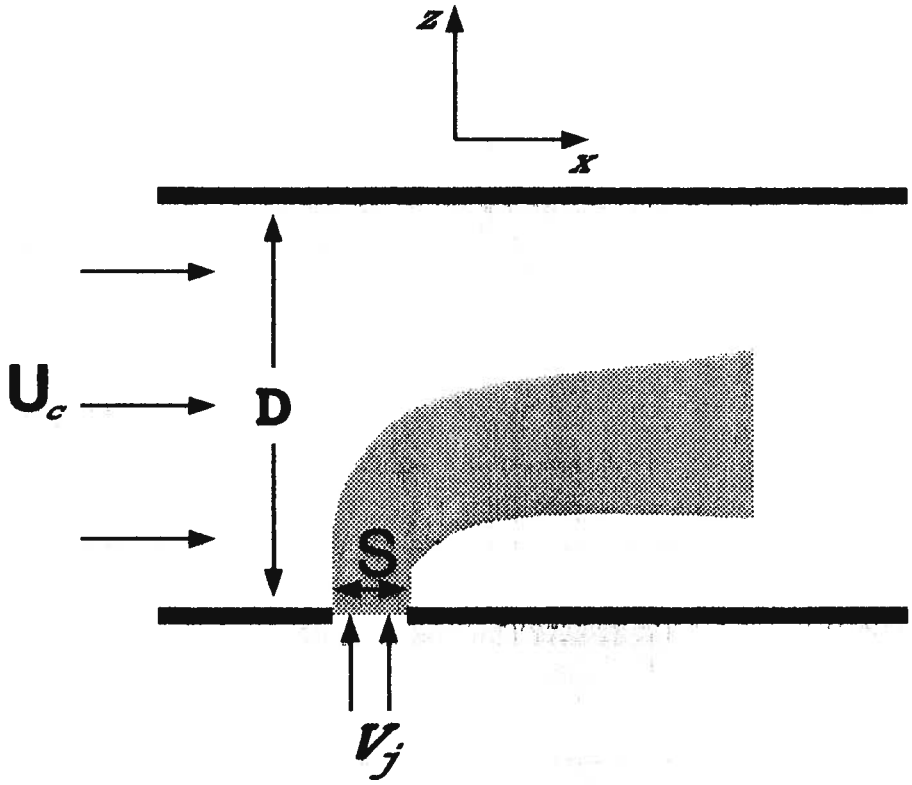

Figure 4.1: Schematic representation of a two dimensional jet into crossflow.

is such that at 10 *mm* upstream of the jet slot, the calculated boundary layer thickness is the same as was experimentally measured. The 11 *mm* thickness of the plate used during the experiment which forms the jet inlet channel is included in the calculations. This is done in order to include the possible deformation of the jet exit profile due to interaction with the crossflow. As shown by Andreopoulos (1981, 1983) and Demuren (1983), at low mass ratios of jet to crossflow, the crossflow distorts the velocity profile at the jet exit plane. The wall function formulation is used to correct for the shear stress near the no slip walls. The multigrid code is three-dimensional. In order to use it for a two-dimensional flow the third dimension should be assumed to be large and boundary conditions have to be imposed. Therefore lateral symmetry planes are used to limit the size of the domain. The flow exit plane is located at $100S$ downstream of the jet slot. This distance is sufficient for the assumption of a zero streamwise gradient at the exit to

be reasonable.

In calculations of jets in crossflow the turbulence characteristics are not very sensitive to the prescribed inlet conditions of the k and ϵ and are mainly governed by the shear produced in the flow field. However, as is the usual practice for the jet in crossflow, (White, 1980 and Crab et al., 1981), the inlet turbulent kinetic energy for the crossflow is specified as $k_c = 1.5U_c^2 I^2$ and the rate of its dissipation as $\epsilon_c = c_\mu^{3/4} k_c^{3/2}/l_c$. Here I the turbulence intensity has a range of 0.01 - 0.05, $C_\mu = 0.09$, and the turbulence length scale l_c is a fraction of the flow domain. In our calculations $I = 0.01$ and $l_c = 0.1D$. Similar conditions are used at the jet entrance. The inlet turbulence kinetic energy for the jet, is defined as $k_j = 1.5U_j^2 I^2$ and its dissipation $\epsilon = c_\mu^{3/4} k_j^{3/2}/l_j$. Here, $I = 0.01$, and $l_j = 0.1S$.

The domain is divided into three segments for efficient distribution of grid nodes. Calculations are done using a three level multigrid procedure. Therefore a fine grid resolution is obtained. The flow domain is discretized by 23296 grid points in segment one, 768 grid points in segment two, and 98304 grid points in segment three, making a total of 122368 grid points on the fine grid over the calculation domain. A finer grid is used in the vicinity of the jet to resolve the sharp gradients of the flow variables due to the interaction of the jet and the crossflow. The grid distribution is shown in Figure 4.2.

4.1.2 Comparison of Calculations and Experimental Data

Figures 4.3-4.5 show the comparison between measured and calculated concentration profiles for a pure carbon dioxide jet at mass ratios $G = 0.4$, 0.6, and 0.8 at 4 locations $x/S = 1.5$, 3, 5, and 10 downstream of the jet.

A summary of the flow variables is given in Table 4.1. Generally the agreement between calculated and measured concentration profiles is good. The shape and the maximum locations of the calculated concentration profiles are in very good agreement

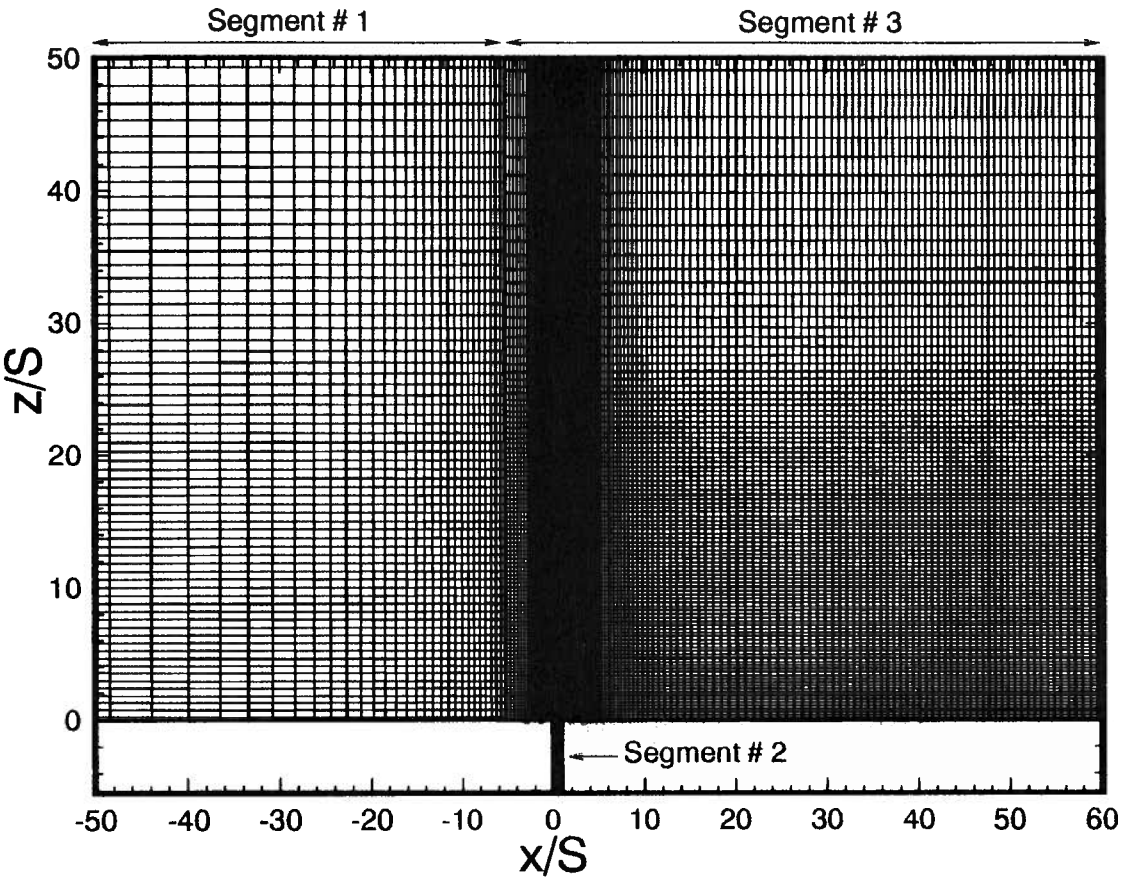

Figure 4.2: Grid distribution.

Table 4.1: Summary of the flow variables

G	CO_2			He+Air			Air		
	ρ_j/ρ_c	V_j/U_c	J	ρ_j/ρ_c	V_j/U_c	J	ρ_j/ρ_c	V_j/U_c	J
0.4	1.5	0.27	0.11	0.24	1.70	0.69	1.0	0.4	0.16
0.6	1.5	0.40	0.24	0.24	2.50	1.50	1.0	0.6	0.36
0.8	1.5	0.53	0.43	0.24	3.30	2.61	1.0	0.8	0.64

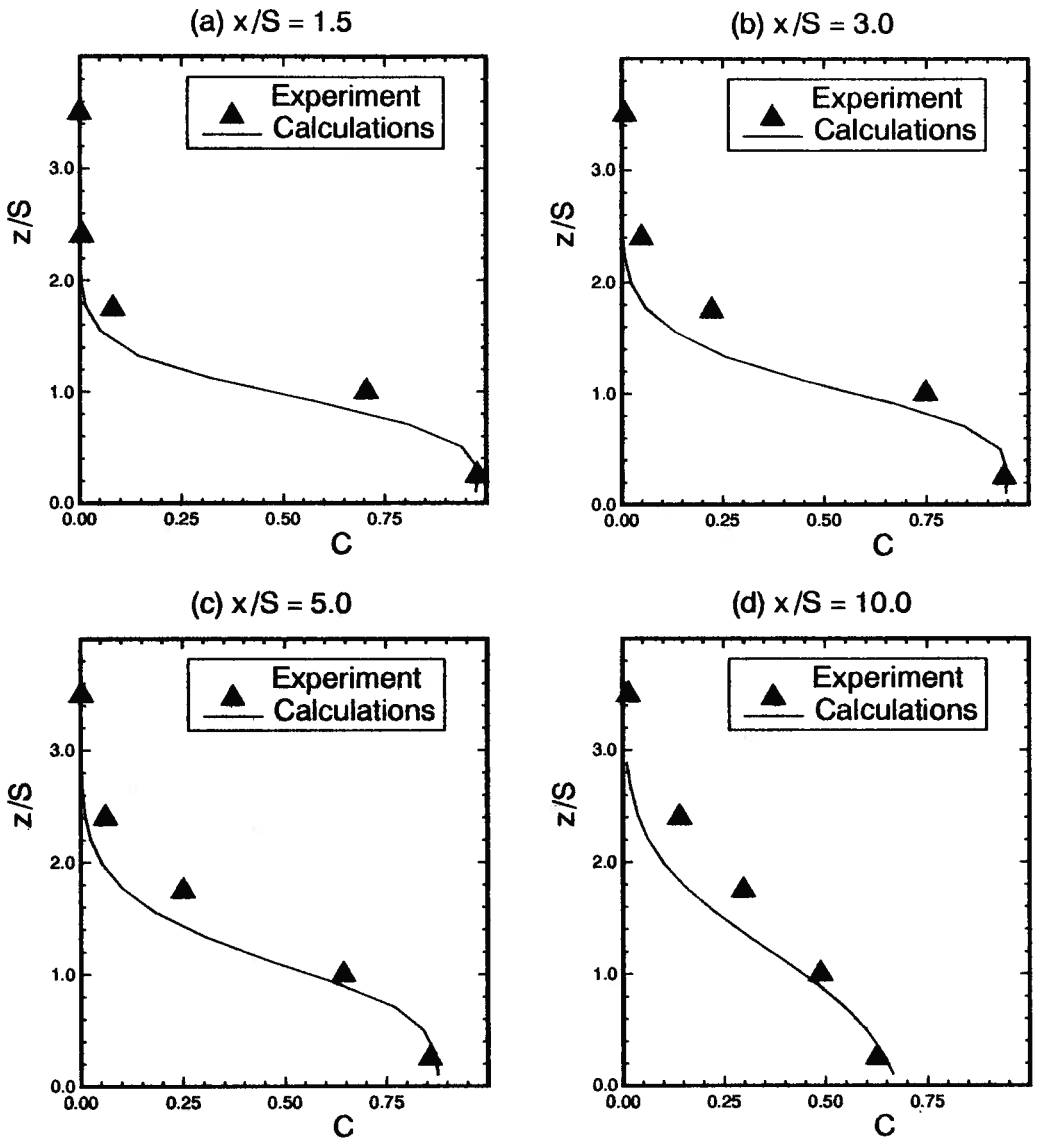

Figure 4.3: Comparison of measured and calculated cross-stream concentration profiles for carbon dioxide jet, $G = 0.4$.

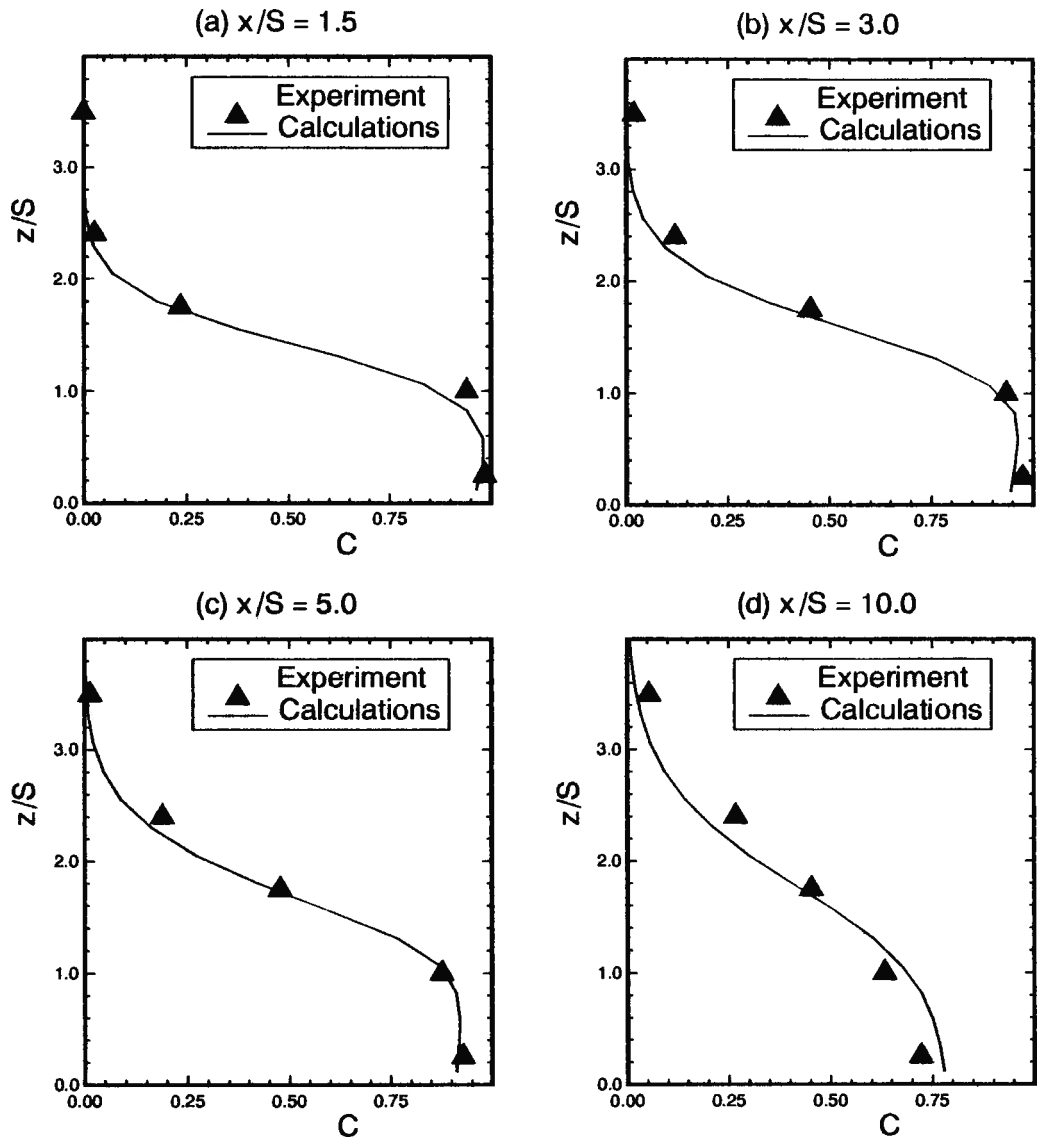

Figure 4.4: Comparison of measured and calculated cross-stream concentration profiles for carbon dioxide jet, $G = 0.6$.

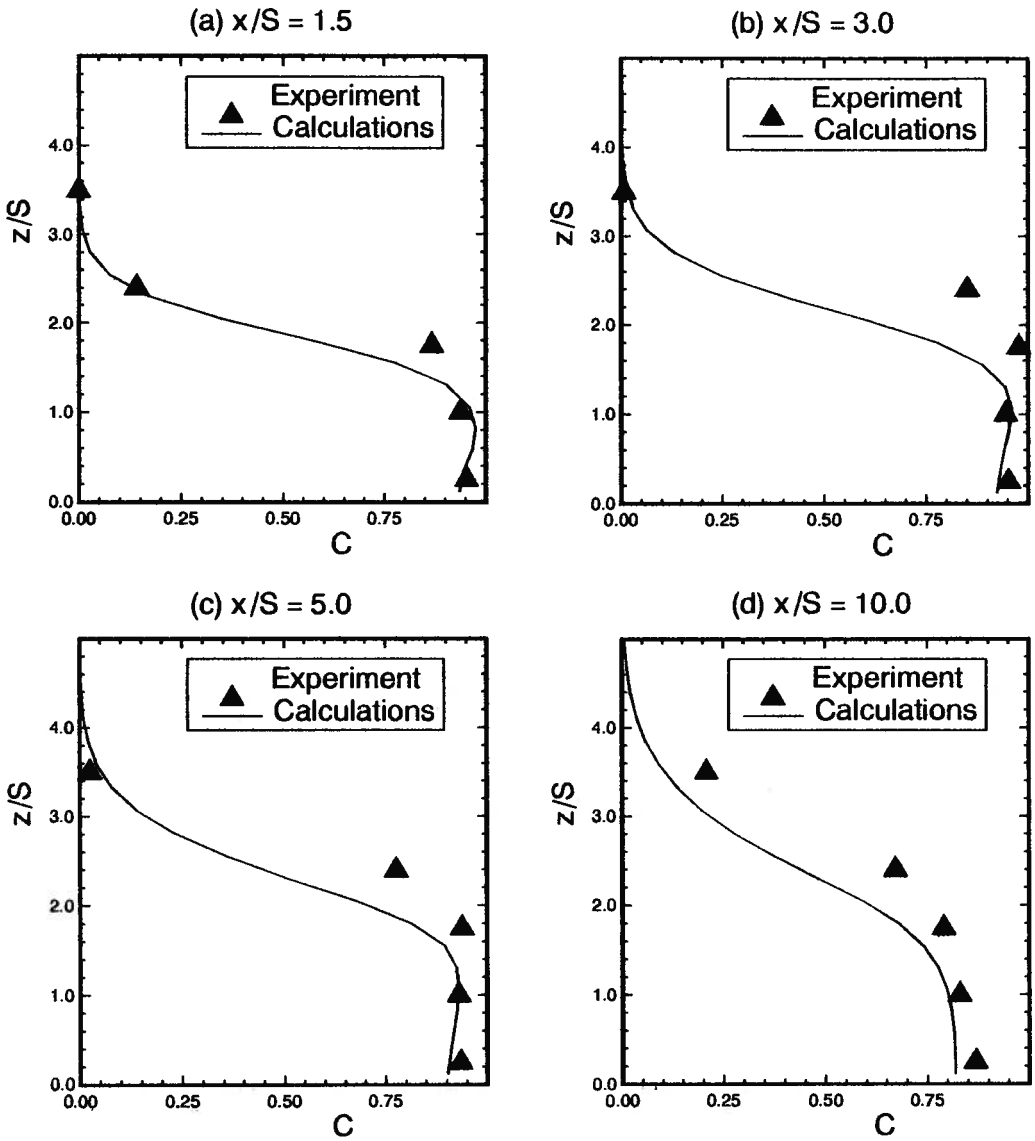

Figure 4.5: Comparison of measured and calculated cross-stream concentration profiles for carbon dioxide jet, $G = 0.8$.

with the measured data.

For $G = 0.4$ at all 4 locations $x/S = 1.5$, 3, 5, and 10 where measurements were done the calculated concentration profiles are slightly flatter than the measured data. For values of $z/S \leq 1$ (shown on the y axis) there is a good agreement between measured and calculated concentration values. At larger values of z/S the measured values of concentration are slightly higher than the calculated values. This is probably due to the increased levels of measurement uncertainties at larger z/S values. Due to the small values of the mass of the jet fluid, small deviations in the vertical location of the measuring probes can have a significant effect on the value of concentration measured. This problem is not present for measurements done at larger values of G. No separation region is shown by experimental data, however, calculations at $x/S = 1.5$ show the presence of a small separation region.

The comparison in Figure 4.4 for $G = 0.6$ shows excellent agreement between the measured and calculated concentration profiles at $x/S = 1.5$, 3, 5 and 10. The maximum difference between the measured and calculated values of concentration occurs at $x/S = 10$. However the differences are smaller than $\pm 5\%$ of measured values of concentration. Calculated results predict a separation region which extends to downstream location $x/S = 3.0$. Due to fewer number of the experimental points the presence of the separation region is not captured by the experimental measurements.

Figure 4.5 compares the calculated and the measured concentration profiles for $G = 0.8$ at 4 locations of $x/S = 1.5$, 3.0, 5.0, and 10.0. The values of jet concentration close to the wall are predicted well in all cases. The comparison of measured and calculated concentration profiles indicates that the calculated jet has deflected more. Therefore, the calculated results have under-predicted the jet penetration. This is probably due to inaccuracies involved in the complex flow field inside the recirculation region due to the turbulence modelling. Further downstream at $x/S = 10.0$ the shape of the

concentration profile is predicted well. The presence of the separation region is captured by the calculations. The separation region in case of $G = 0.8$ is larger than the case of $G = 0.6$ and 0.4 and extends to $x = 5S$ downstream of the jet.

Figure 4.6 shows the comparison between measured and calculated concentration profiles for a mixture of helium/air jet for $G = 0.4$ at 4 downstream locations $x/S = 1.5$, 3, 5, and 10. At $x/S = 1.5$ and 10 the shape of the concentration profile is not well predicted. The agreement between the measured and calculated concentration profiles improves further downstream at $x/S = 3$ and 5. Comparing the results with those for the carbon dioxide jet at $G = 0.4$, superior agreement in the case of the carbon dioxide jet is apparent.

The above observations can be explained by considering the significant differences between the velocity ratios for different gases at the same values of mass ratio G. Table 4.1 shows the summary of the flow specifications. As the jet enters the crossflow, a pressure difference is created across the jet due to its interaction with the crossflow, and the jet is deflected in the direction of the crossflow. In the region immediately downstream of the jet exit plane a region of low pressure is created and a recirculation bubble is formed. In the case of the helium/air jet which is 4 times lighter than air to keep $G = 0.4$ the velocity ratio R has to increase. Therefore the velocity and consequently the momentum ratios in the case of helium/air jet are much higher than their counterparts for the case of carbon dioxide or air jets at the same G value. The higher values of R and J result in deeper penetration of the jet into the crossflow and the formation of a larger recirculation region. The larger recirculation region has a more significant effect on the flow field. Its exact size and location are critical to the accurate evaluation of the flow field. The isotropic eddy viscosity assumption in the $k - \epsilon$ turbulence model fails to predict accurately the complex flow pattern in the recirculatory region. It is for this reason that at $x/S = 1.5$ the agreement between the predicted and measured

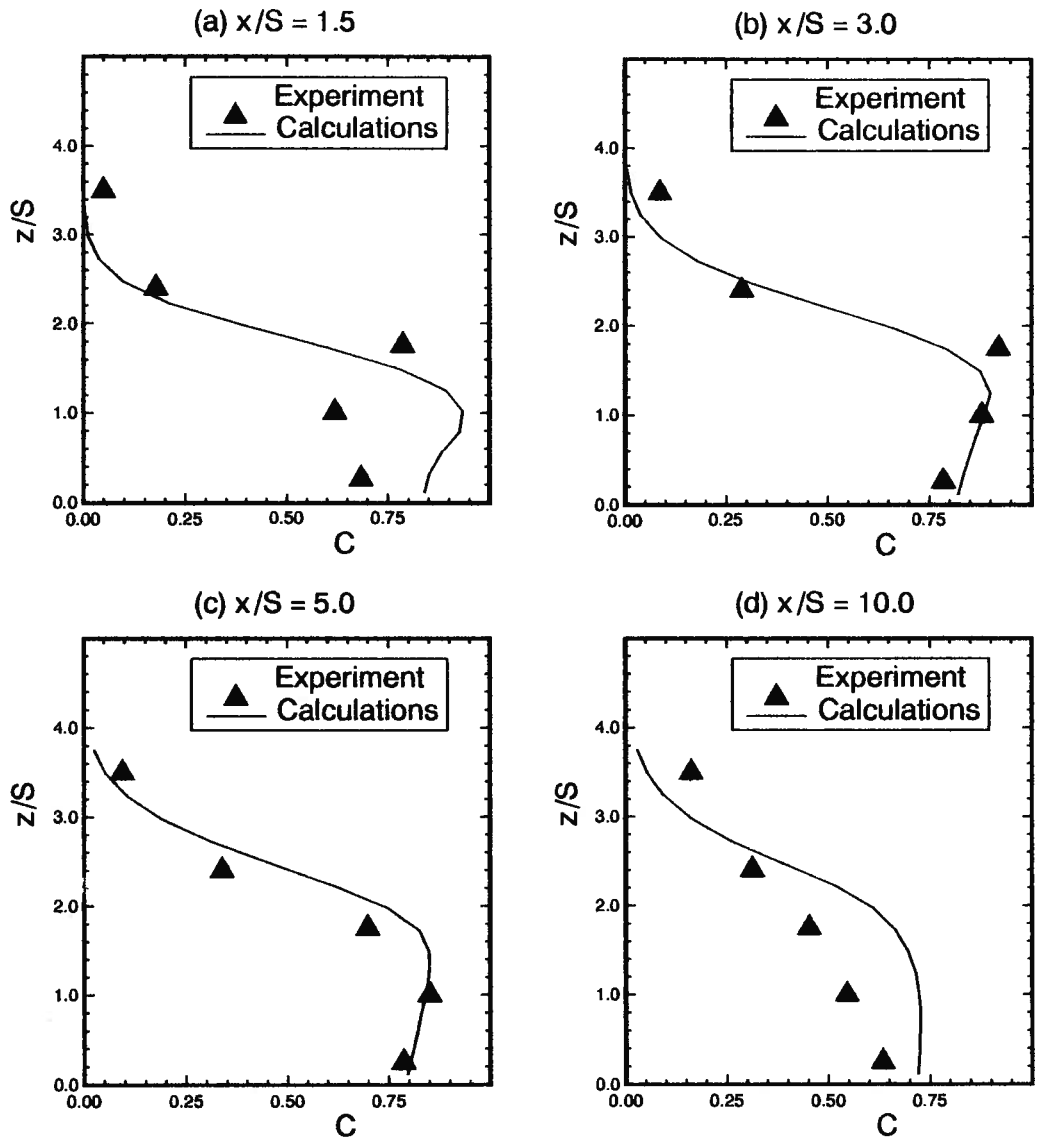

Figure 4.6: Comparison of measured and calculated cross-stream concentration profiles for helium/air jet, $G = 0.4$.

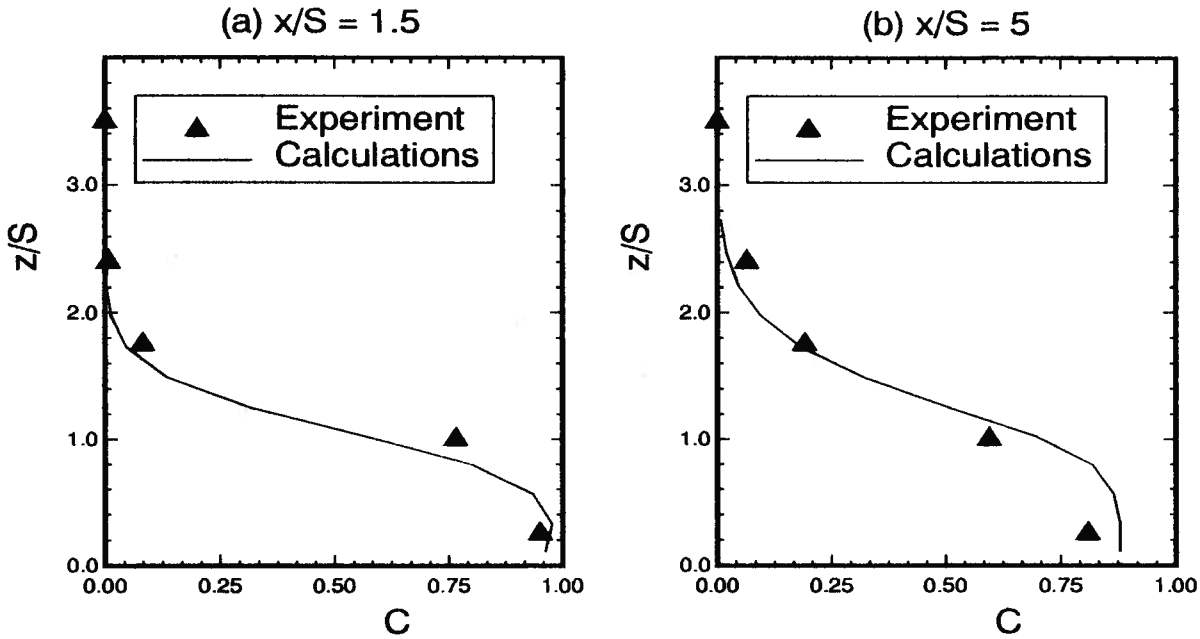

Figure 4.7: Comparison of measured and calculated cross-stream concentration profiles for air jet, $G = 0.4$.

concentration profiles in the case of the helium/air jet has deteriorated. At $x/S = 10$, which is outside the recirculation region, the measured concentration profile shows a slower recovery of the flow from the reverse flow.

A similar comparison is done for air jets in air crossflow. The results are presented in Figures 4.7-4.9. The good agreement between the experimental and predicted results is similar to that obtained in the case of the carbon dioxide jet. Therefore it can be concluded that the introduction of variable density into the calculations is reasonably accurate but that the size and location of recirculation regions is not well predicted at high mass or more importantly high momentum ratios. As the size of the recirculation region increases the numerical results seem to underpredict the jet penetration and hence the size of the recirculation region.

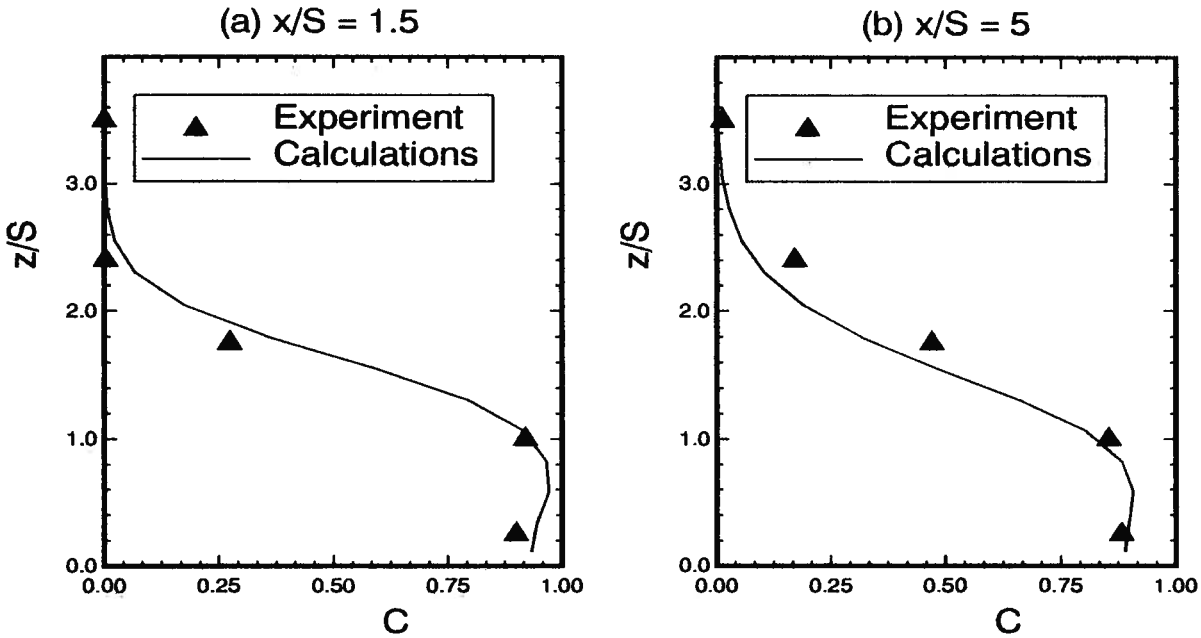

Figure 4.8: Comparison of measured and calculated cross-stream concentration profiles for air jet, $G = 0.6$.

4.2 Two-Dimensional Investigation of the Primary Air Jets

The primary air jets in the kraft recovery boiler are small, closely spaced, and numerous. In a typical design there are hundreds of these air ports distributed around the lower perimeter of the boiler. To model these air ports individually a very fine grid distribution is required. The resultant system of finite difference equations is so large that, both in terms of computer memory and cost, this detailed approach is impractical. Simplifying assumptions have to be made for numerical modeling of these air ports to become practical.

As the row of primary ports are injected into the boiler they spread out and merge together. Thus a simple and practical approach used by Salcudean et al. (1992) is to substitute for these ports a continuous slot spanning across the space that is originally occupied by a row of ports. The jet velocity in the slot model is kept the same as the

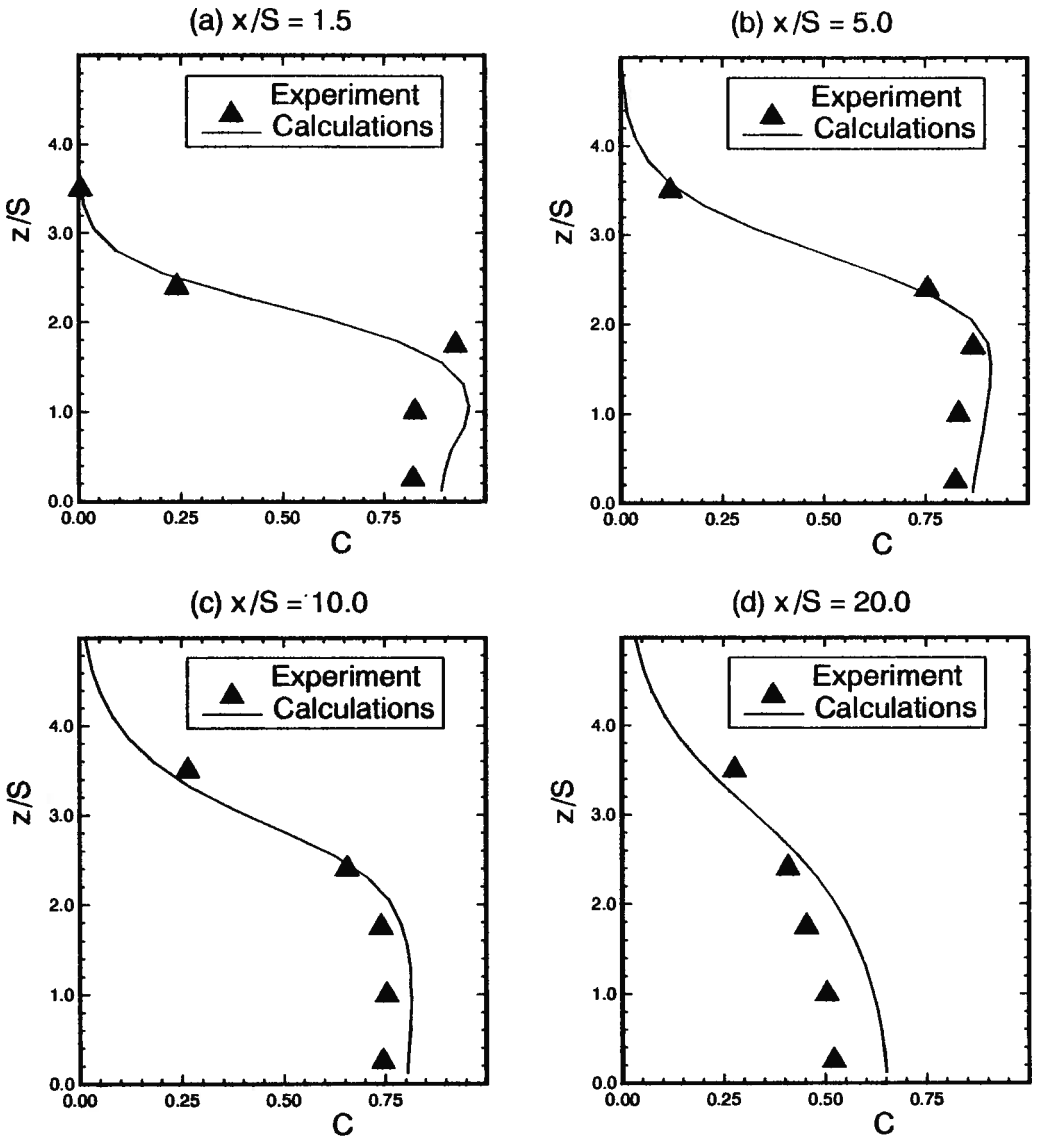

Figure 4.9: Comparison of measured and calculated cross-stream concentration profiles for air jet, $G = 0.8$.

actual air port. To maintain the same mass flow rate the height of the slot will be less than the height of an individual air port. The total area will remain the same. The implications of this assumption are investigated and reported in detail by Tse (1994).

Thus, a numerical model of the kraft recovery boiler has one continuous slot jet on each wall around the lower perimeter of the boiler. It is the purpose of this investigation to calculate the effect of the buoyancy force on the primary air jets in a kraft recovery boiler.

Buoyancy may alter the flow field in two ways, as discussed in detail in Chapter 2. Buoyancy is present in the vertical momentum equation as a body force. It can also effect the generation of the turbulent kinetic energy (k) and the rate of its dissipation (ϵ). To isolate the effect of buoyancy as a force in the momentum equation and its effect on turbulence, for each flow condition, calculations are done for three cases:

- Buoyancy is included in the momentum and turbulence equations . This is referred to as the case with 'Buoyancy'.
- Buoyancy is excluded from the momentum and turbulence equations . This is referred to as the case with 'No Buoyancy'.
- Buoyancy is included in the momentum equation but not in the turbulence equations . This is referred to as 'No Buoyancy in $k - \epsilon$'.

The results obtained in each case are then compared and the differences are noted.

The simulated slot jets in the kraft recovery boiler are long (about 9 m); thus, they can be considered as two-dimensional jets. First we consider two opposed two-dimensional slot jets injected horizontally into a crossflow. The interaction of the corner jets is not included at this stage. This will be included in Chapter 6 together with combustion and radiation processes where a full boiler geometry is simulated.

Table 4.2: Summary of the flow variables for calculations of the primaries

$U_c = 3m/s$						
$S = 0.08m$						
Case	D/S	R	ρ_j/ρ_c	G	J	M
1	62	4	3	12	48	0.77
2	62	6	3	18	108	1.74
3	62	4	2	8	32	0.52
4	30	4	3	12	48	1.6

4.2.1 Primaries: Problem Description and Boundary Conditions

A schematic drawing of the numerical model is shown in Figure 4.10.

In the simulation, the dimension of the slot jet, the jet velocity and density are adjusted to reflect the conditions in a boiler. The slot jet opening $S = 0.08\ m$. However the flow parameters, such as the ratio of the jet velocity to the crossflow at the inlet (R), the ratio of the confinement width to the jet exit width (D/S), and the ratio of the jet temperature to the crossflow at the inlet (T_j/T_c), were varied to investigate the variations of the effect of buoyancy force with these variables. The flow specifications for each case are given in Table 4.2.

The boundary conditions imposed are as follows: plug flow conditions for the jet and crossflow velocities, the no-slip condition at the wall, the symmetry condition at the middle plane and the two lateral planes enclosing the domain, and zero gradient condition at the exit plane. The wall function formulation is used to account for the shear stress near the no-slip wall. The top exit plane is located at $335S$ downstream of the jet. This distance is sufficiently far above the jet so that the assumption of zero gradient flow at the exit plane is reasonable. At the jet entrance the magnitude of jet velocity and temperature are set at $V_j = 12\ m/s$ and $T_j = 400\ K$ respectively. This condition is similar to that in the kraft recovery boiler. The inlet turbulent kinetic energy for the

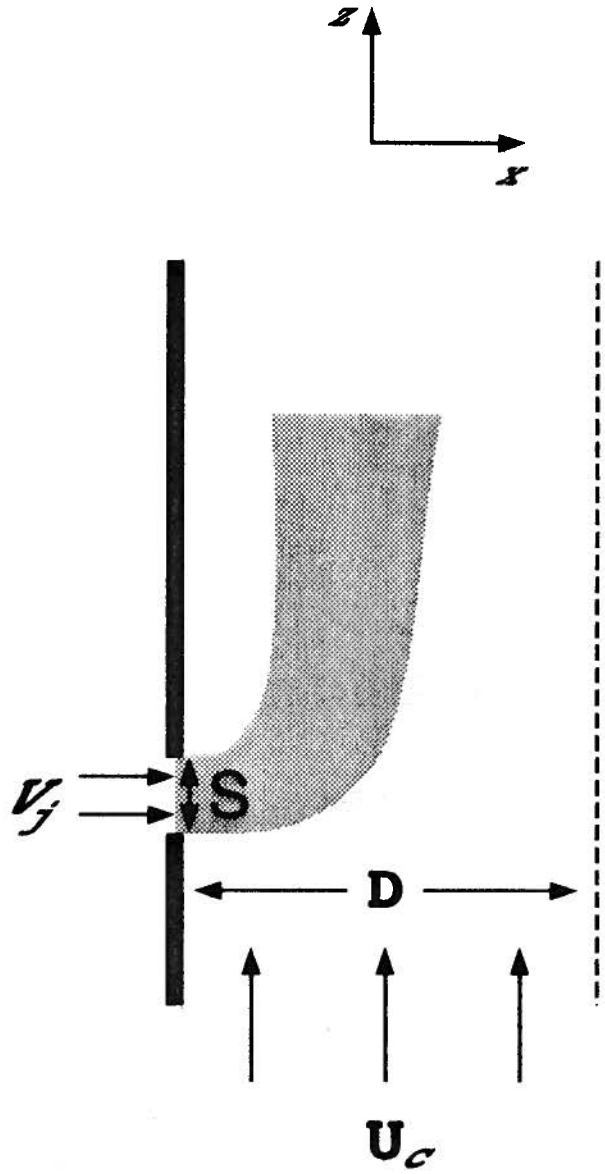

Figure 4.10: Schematic representation of a two-dimensional jet into crossflow.

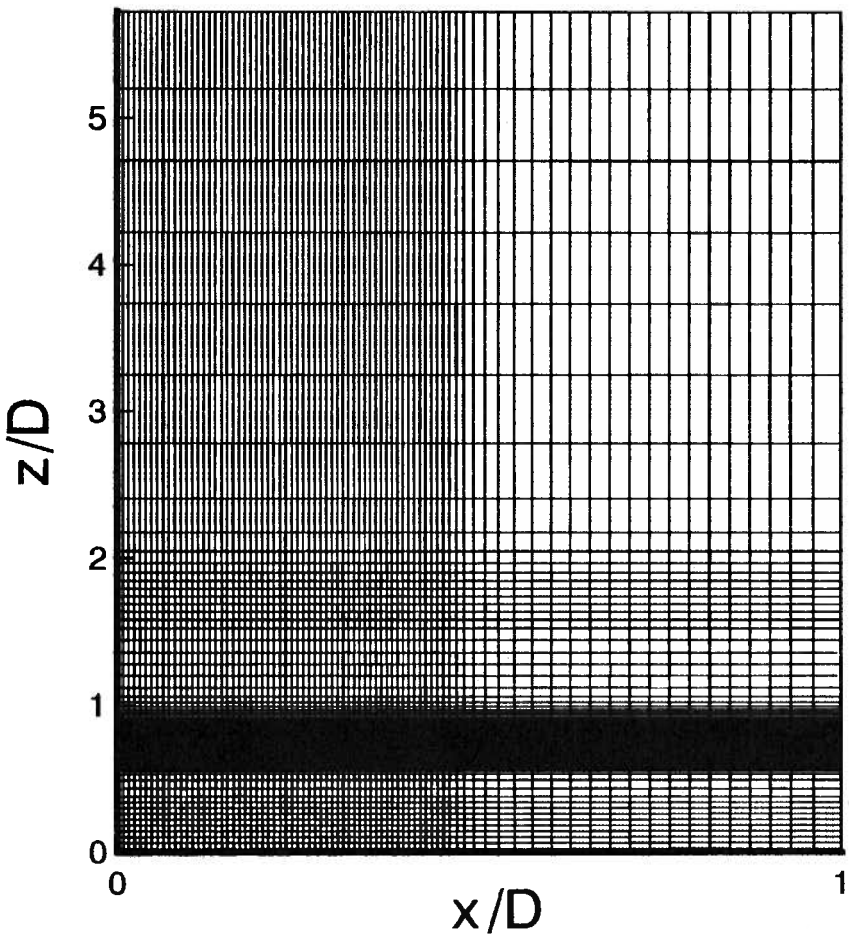

Figure 4.11: Computational mesh.

crossflow is set at $k_c = 1.5U_c^2 I^2$ and rate of its dissipation at $\epsilon_c = C_\mu^{3/4} k_c^{3/2}/l_c$, where l_c the dissipation length scale is set at $l_c = 0.1D$, and the turbulence intensity $I = 0.01$. Similarly the inlet turbulent kinetic energy for the jet is set at $k_j = 1.5V_j^2 I^2$ and rate of its dissipation $\epsilon_j = C_\mu^{3/4} k_j^{3/2}/l_j$, where l_j the dissipation length scale is set at $l_j = 0.1S$ and $I = 0.01$. These choices have been made following the usual practice used in jet in crossflow calculations.

A two-level steady state multigrid procedure is applied to calculate the flow field.

The experimental work of Ketler (1993) has shown that the flow field due to primary jets alone is quite steady. Thus, the application of a steady state solver to the problem of opposed primary jets is likely to be valid. The computational mesh used is shown in Figure 4.11.

4.2.2 Effect of Confinement, Velocity Ratio, and Density Ratio

The variation of jet structure in confined crossflow can be described by looking at the velocity profiles. The normalized velocity vector plots for four flow conditions are presented in Figures 4.12-4.13. The presence of a recirculation bubble downstream of the jet in all these flows is apparent. This bubble is due to the blockage effect caused by the jet on the crossflow. For a stronger jet this effect becomes more significant and the size of the recirculation bubble increases. For all cases presented, the jet with buoyancy force has a larger penetration into the crossflow and has formed a larger recirculation bubble. For the horizontal high density jet the buoyancy force acts against the crossflow and reduces the effect of the drag force exerted on the jet by the crossflow. When buoyancy force is not included in the calculations the net vertical force acting on the jet is larger. The jet deflects upward more easily, has smaller penetration into the crossflow and consequently forms a smaller recirculation region. In Figure 4.12 when the velocity ratio R has increased from 4 to 6 the size of the recirculation region formed downstream of the jet, both for cases with and without the buoyancy force, has increased. This is expected as the jet penetration is significantly affected by its momentum. As the jet momentum J increases from 48 to 108 (Table 4.2) its penetration and consequently the size of the recirculation region increases. The effect of the extent of the confinement is clearly shown in Figure 4.13. When the ratio D/S has decreased to half of that in Figure 4.12(a-b), the size of the recirculation region has significantly reduced. Comparing cases 1 and 4 in Table 4.2 the value of the total momentum flux ratio of jet to crossflow M, has increased

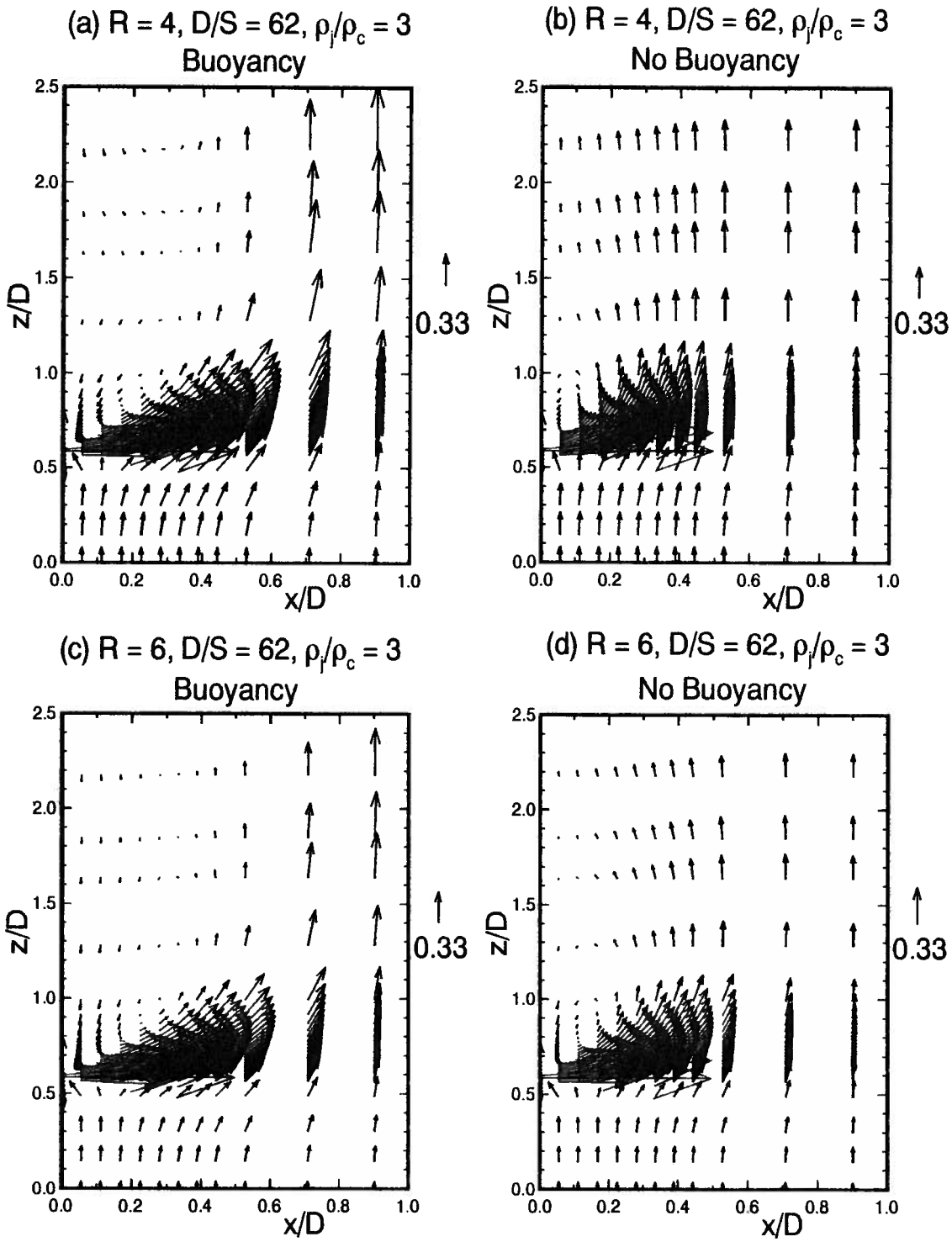

Figure 4.12: Normalized velocity profiles, $\rho_j/\rho_c = 3$.

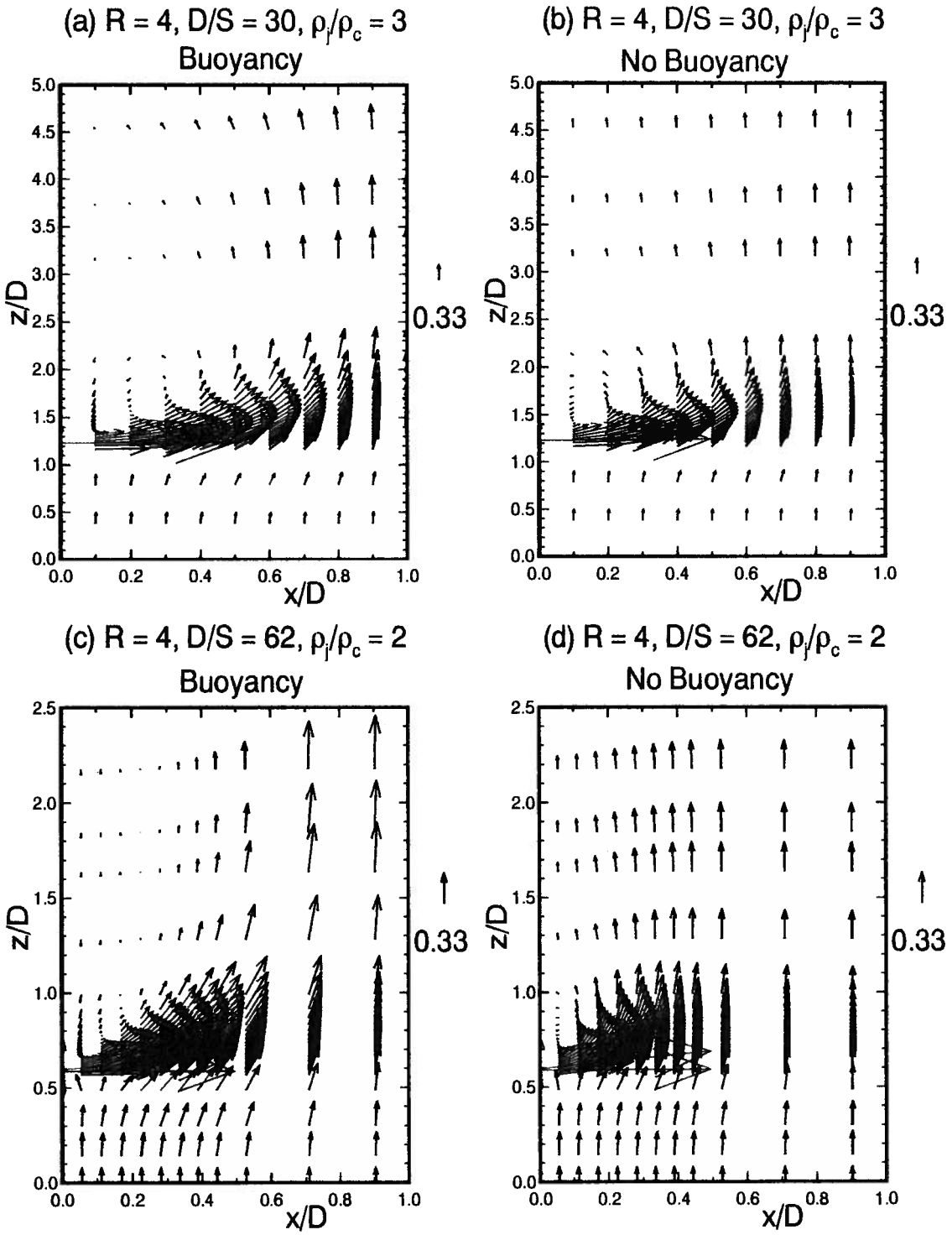

Figure 4.13: Normalized velocity profiles.

from 0.77 to 1.6 due to the reduction of D/S. The differences between the flow pattern for the cases with and without buoyancy are less, indicating smaller buoyancy effects. Due to the smaller confinement size the penetration of the jet with buoyancy force is significantly limited. The effect of this limitation on the jet without buoyancy which behaves as a weaker jet is not as significant. When the ratio of jet density to crossflow is reduced from 3 to 2, comparing Figures 4.12 (a-b) and 4.13(c-d), it is apparent that the size of the recirculation region has again decreased. As the mass and momentum ratios of the jet to the crossflow have reduced (cases 1 and 3 in Table 4.2), the jet has become weaker and its penetration has significantly decreased.

As the amount of the air jet present at any point is crucial to the boiler's operation, the jet penetration, its trajectory, and the degree of mixing of the jet fluid with the crossflow are of particular interest in the study of the flow field in the kraft recovery boiler. Generally in the study of jet in crossflow, jet penetration and trajectory are important factors. In Figure 4.14 the jet trajectory, which is defined as the locus of the maximum jet concentrations, is presented for four flow conditions. The results show an initial core jet region (jet slightly deflected) followed by a region characterized by considerable deflection of the jet. The trajectory of the jet without buoyancy force, in all cases presented, remains closer to the wall than the trajectory of the jet with buoyancy force, indicating the deeper penetration of the jet with buoyancy force as already noted. The higher penetration of the jet with buoyancy force can be explained as follows. For a jet which is heavier than the crossflow, the buoyancy force acts downward against the upward crossflow. By opposing the crossflow, the buoyancy force reduces the effect of the drag force exerted on the jet by the crossflow. This will result in higher local jet to crossflow velocity ratios and therefore better jet penetration. As the velocity ratio of jet to crossflow R, increases from 4 to 6, as shown in Figures 4.14(a-b), the jet penetration increases. This is due to the higher momentum of the jet. At velocity ratio $R = 6$ the

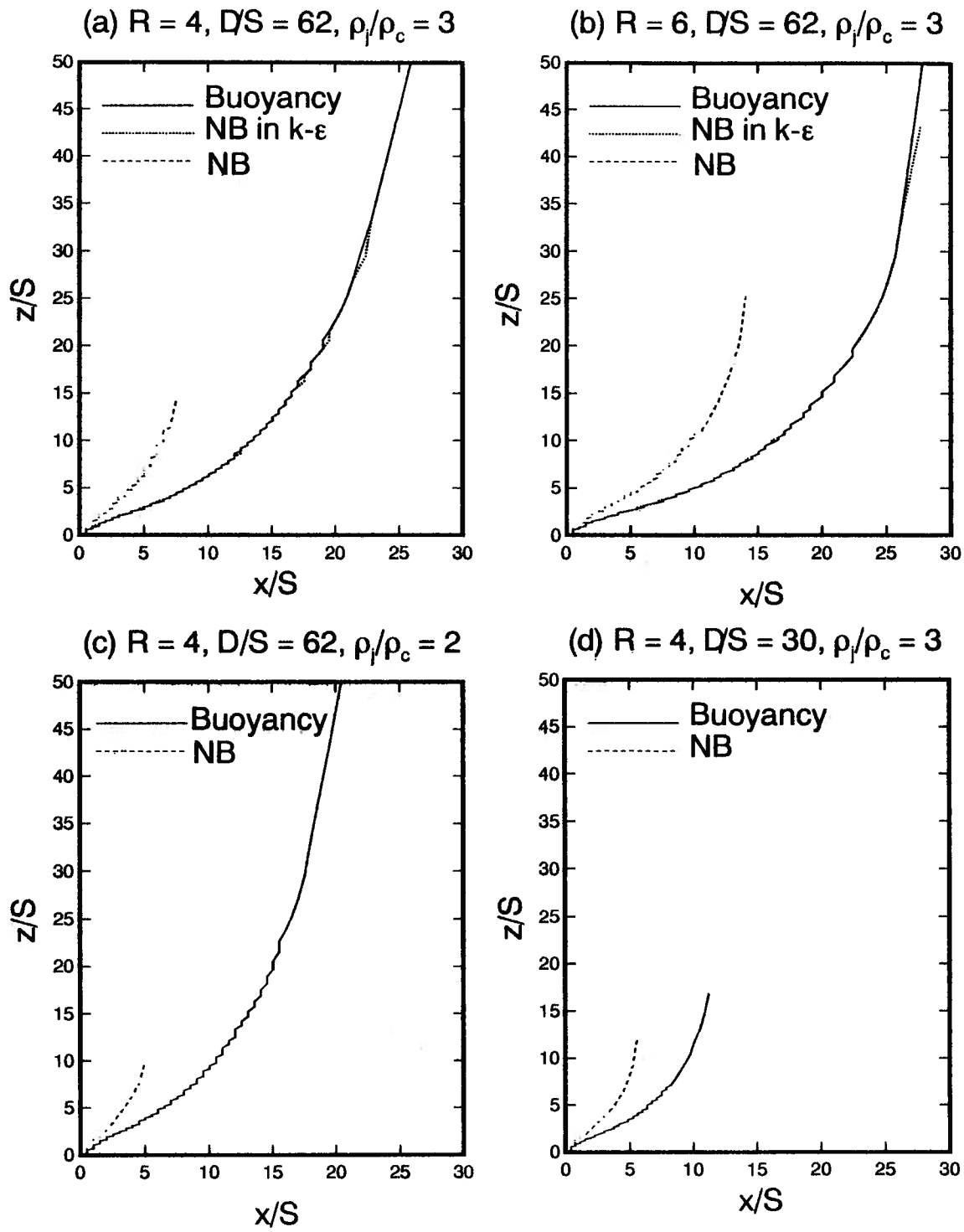

Figure 4.14: Jet fluid concentration trajectories, NB refers to No Buoyancy.

difference between the jet trajectories for the cases with and without buoyancy force is smaller than the case of $R = 4$. There are two possible reasons for this. Generally, as the momentum force becomes stronger the buoyancy effects become less pronounced. Additionally, for the confined jets, as the jet becomes stronger the presence of the opposite wall on the jet becomes more pronounced. The crossflow must pass the jet and therefore it can restrict the penetration of the stronger jets more significantly than the weaker jets. As was explained above, for the flow configuration here, the buoyancy force reduces the effect of the drag force exerted on the jet by the crossflow and results in deeper penetration and smaller deflection of the jet. Therefore comparing the jet behavior for the cases with and without the buoyancy force the jet with buoyancy appears as a stronger jet, even though the mass and momentum flux ratios (G and J) are the same in both cases. As the jets without buoyancy force are weaker, for both cases $R = 6$ and 4 the reduction of their penetration due to the crossflow is less significant. When the width of the confinement is reduced from $D/S = 62$, Figure 4.14(a), to $D/S = 30$, Figure 4.14(d), the jet penetration is significantly reduced. The jet penetration is restricted by the presence of the opposite jet and the space required for the crossflow. Therefore in the case of $D/S = 30$ the effect of the buoyancy force on the jet trajectory is less significant.

To understand the mixing pattern of the jet with the crossflow the jet concentration contour plots are shown in Figures 4.15-4.16. For all cases presented here the jet with buoyancy spreads further and its blockage effect on the crossflow is more prominent. Better penetration of the jet with buoyancy is also apparent from these plots. As the velocity ratio R increases from 4 to 6 the jet spread increases. When the confinement width D/S is reduced from 62 in Figure 4.15(a-b) to 30 in Figure 4.16(a-b) the jet spread again increases. This is expected as the same amount of jet fluid is now distributed over a smaller mainstream cross-section. As the density ratio of jet to crossflow is reduced from 3 in Figure 4.15(a-b) to 2 in Figure 4.16(c-d), the jet spread has reduced. This is

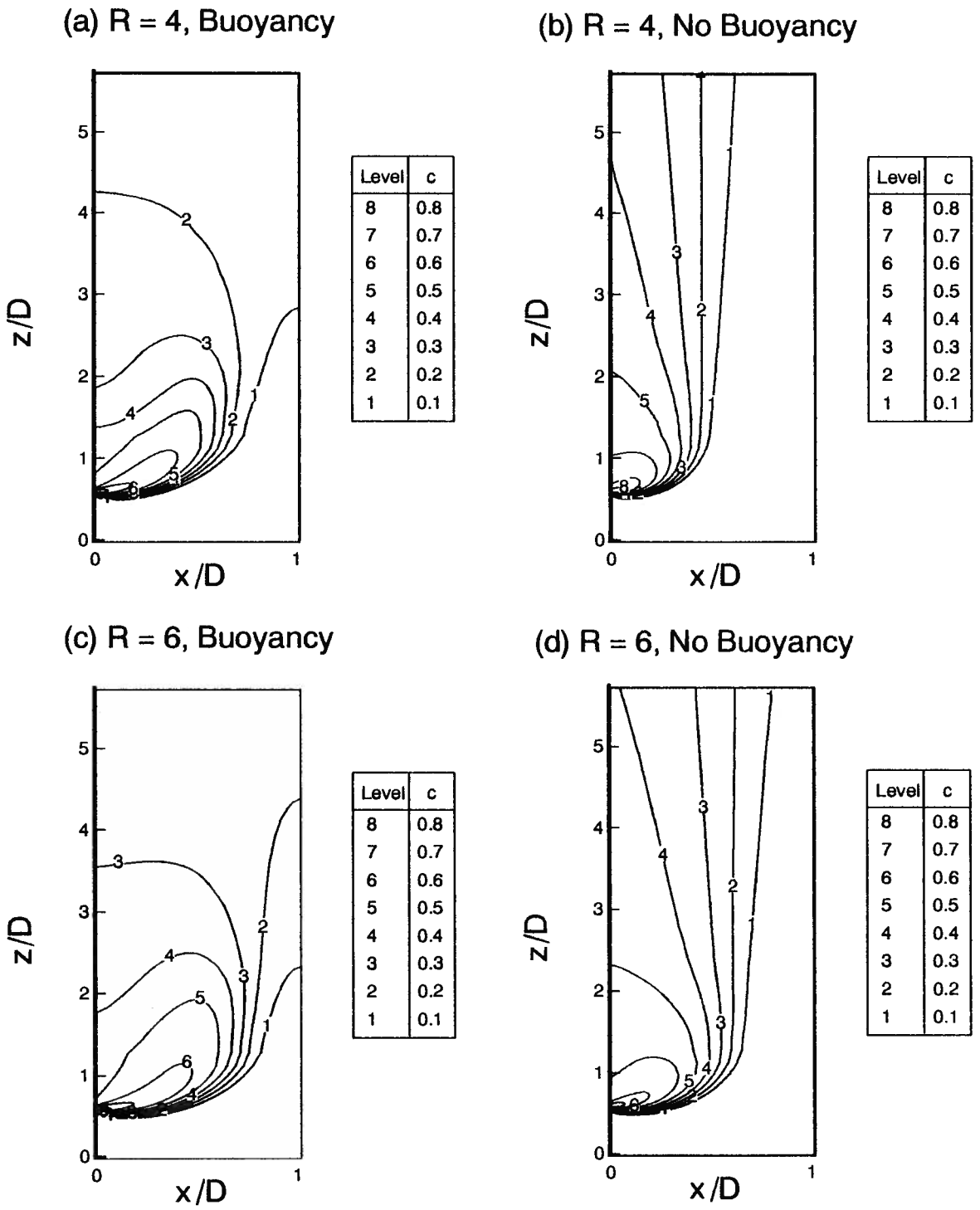

Figure 4.15: Jet fluid concentration profiles, $\rho_j/\rho_c = 3$.

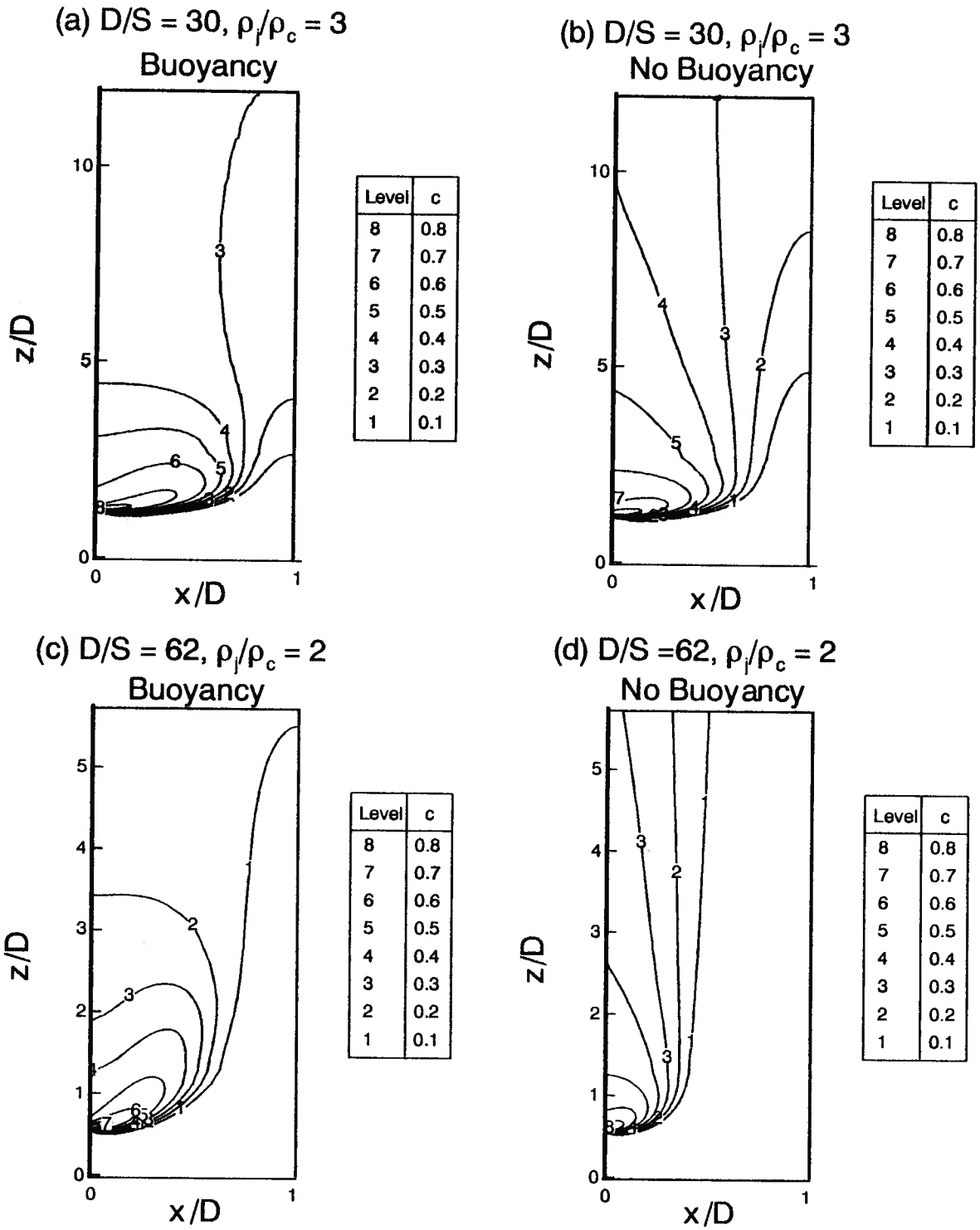

Figure 4.16: Jet fluid concentration profiles, $R = 4$.

due partly to the smaller amount of jet fluid and lower mass ratio of jet to crossflow. It is misleading to compare the buoyancy effects in this case with the case with higher density ratio 3. As the density ratio decreases from 3 to 2 one expects to see smaller effects of buoyancy force on the flow. At the same time, however, this reduction results in smaller values of mass or momentum ratios of the jet to crossflow. Considering the buoyancy effects, the influence of these two factors on the flow field is opposite to each other. This once again highlights the importance of isolating the buoyancy force in order to study the effects of density variations.

In the kraft recovery boiler it is important to know the concentration of combustibles within certain critical ranges where burning could occur. Thus, it is useful to quantify the effect of the buoyancy force on mixing of the air jet with the crossflow. To meet this objective a methodology is used to calculate the mass flow rate of the fluid passing through a cross-sectional plane having jet fluid concentration in a certain range. A similar procedure is used by Tse (1994), for constant density flows. The details of this methodology are given in Appendix A. A brief description is presented here to introduce the terminology used.

Consider the probability density function $P_z(\zeta)$ derived in Appendix A. At a cross-sectional plane with elemental area dA located at a streamwise coordinate z, this density function is;

$$P_z(\zeta) \equiv \frac{1}{\Delta\zeta}\left[\frac{(v\rho dA)|_z \text{having concentration in range} \zeta \pm \frac{\Delta\zeta}{2}}{\rho_1 Q_1 + \rho_2 Q_2}\right] \tag{4.68}$$

where $\zeta = C - \bar{C}$, with $\bar{C}$ being the average or fully mixed concentration value, and $\Delta\zeta$ being some small increment of ζ. $\rho_1 Q_1$ and $\rho_2 Q_2$ are the mass flow rates of the cross-stream and the jet, respectively. It is shown in Appendix A that the mean of $P_z(\zeta)$ is zero and that for perfectly mixed fluid the variance of $P_z(\zeta)$ is also zero. At any one

cross-sectional plane, the variance σ_z^2 of $P_z(\zeta)$ can be computed as;

$$\sigma_z^2 = \int_0^1 \zeta^2 P_z(\zeta).d\zeta \tag{4.69}$$

Defining σ_0^2 as the maximum variance before any mixing has occurred, the standard deviation of 'mixedness' δ_z is shown in Appendix B to be:

$$\delta_z = 1 - \sqrt{\sigma_z^2/\sigma_0^2} \tag{4.70}$$

δ_z will have values that range from 0, indicating no mixing, to 1, indicating fully mixed flows. In our calculations δ_z is referred to as the 'degree of mixing'.

The degree of mixing of the jet fluid with the crossflow for four different flow conditions is presented in Figure 4.17. In all four cases the predicted degree of mixing in the near field region for the jet is approximately the same with and without buoyancy force. Moving farther downstream the degree of mixing experiences a sharper increase for the jet with buoyancy force. In Figures 4.14 we have seen that the jet without the buoyancy force has smaller penetration into the crossflow and flows down the channel closer to the injection wall, resulting in smaller entrainment of the crossflow into the wake of the jet. This in turn results in less mixing between the jet and the crossflow, particularly in the far field where the momentum forces are weakened. When the velocity ratio R increases from 4 to 6 in Figure 4.17(a-b) the effect of buoyancy force on the predicted degree of mixing is further reduced. At higher velocity ratio $R = 6$ the mixing between the jet and the crossflow has increased. When the density ratio of the jet to crossflow has decreased from 3 to 2 in Figure 4.17(a-c) the effect of buoyancy force on the degree of mixing has been reduced. As the confinement width has decreased from $D/S = 62$ to 30, Figure 4.17(a-d), the mixing between the jet and the crossflow has improved. Eliminating the

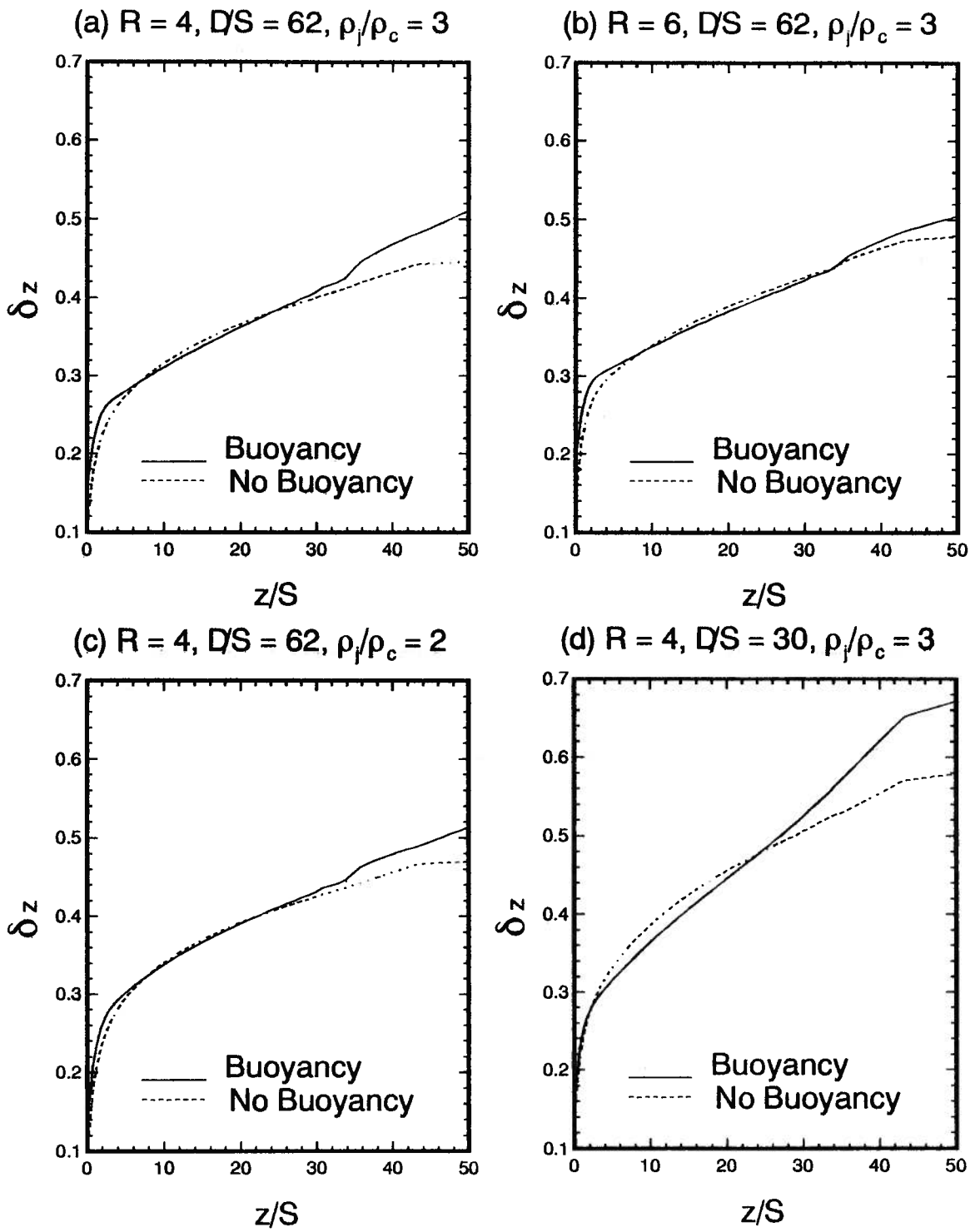

Figure 4.17: Effect of buoyancy on degree of mixing.

buoyancy force therefore results in underprediction of the degree of mixing in the far field region.

The decaying process of maximum jet concentration along the concentration trajectory is for different values of R, confinement width and density ratios shown in Figure 4.18. In all cases the decay of the jet concentration both with and without buoyancy force almost collapses into one curve. This implies that the buoyancy force plays only a minor role in the mixing process as suggested by Figure 4.17.

The decaying process of the total velocity component V_t along the jet velocity trajectory is shown in Figure 4.19. The velocity trajectory is defined as the locus of the maximum total velocities in the streamwise direction, where $V_t = \sqrt{U_x^2 + U_z^2}$ for a two-dimensional flow field in the $x - z$ plane. Due to entrainment, V_t decreases with an increase of the axial distance with the maximum limit of $V_j/V_t = R$. For the jet with the buoyancy force, V_t begins to increase beyond the point of maximum decay. The increase of V_t is due to the impingement of the opposed jets at the center of the channel. Farther downstream V_t decays at a slow rate due to the presence of the confinement. When the buoyancy force is neglected, the rate of decay of V_t in the near field is slightly affected. However the increase of V_t beyond the point of maximum decay is significantly under-predicted. This can be explained by considering the small penetration of the jets when buoyancy force is ignored. As the increase of V_t is due to the impingement of the jets, the weaker this impingement the slower the rate of decay will be.

To summarize it can be concluded that for the flow conditions tested, ignoring the buoyancy force results in under prediction of the jet penetration. The degree of mixing between the jet and the crossflow is slightly under-predicted when the buoyancy force is ignored. The jet without the buoyancy force behaves as a weaker jet and its trajectory remains closer to the wall containing the jet. When ignoring the buoyancy force the general flow characteristics remain the same, however significant quantitative differences

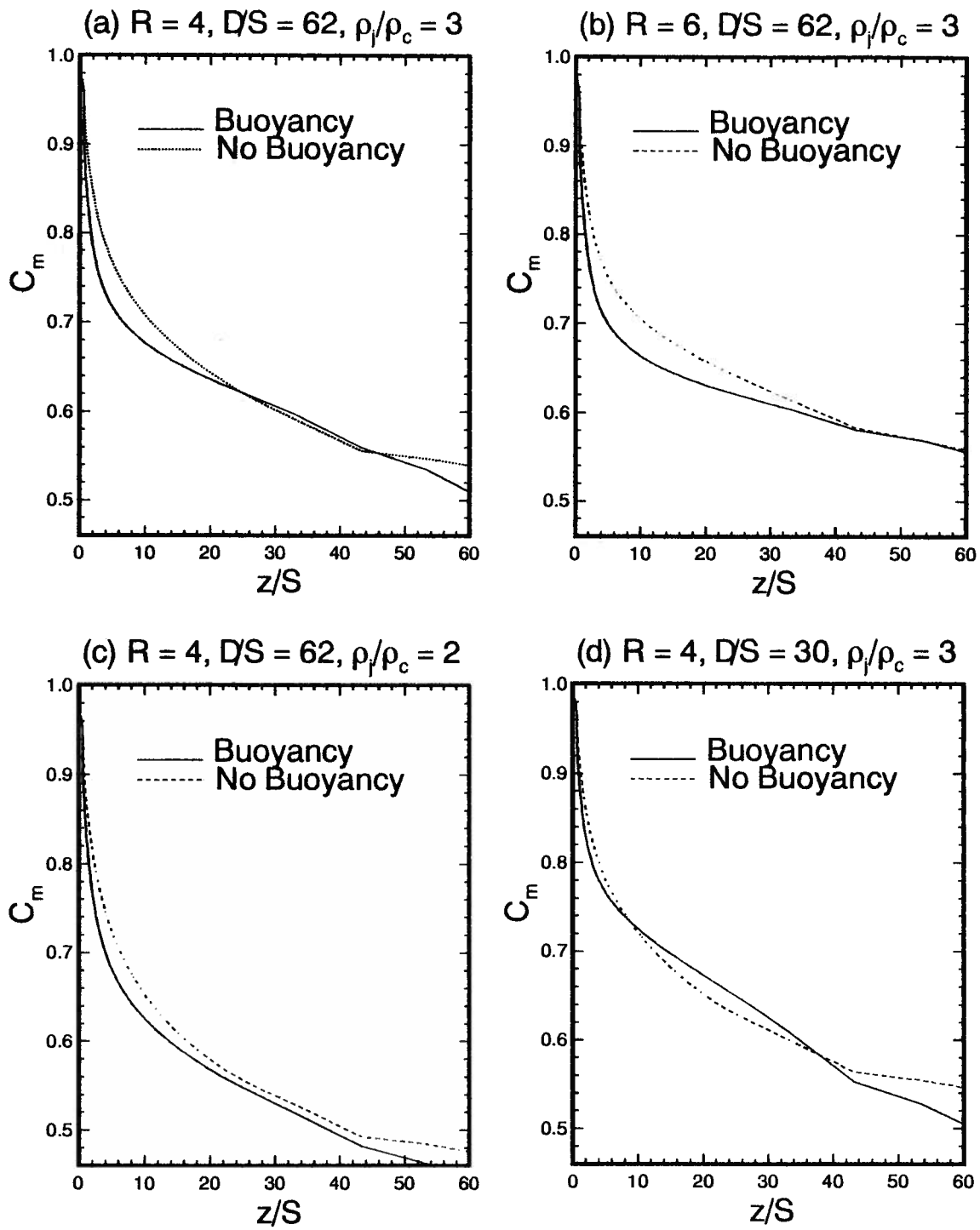

Figure 4.18: The decaying process of jet concentration along the jet concentration trajectory.

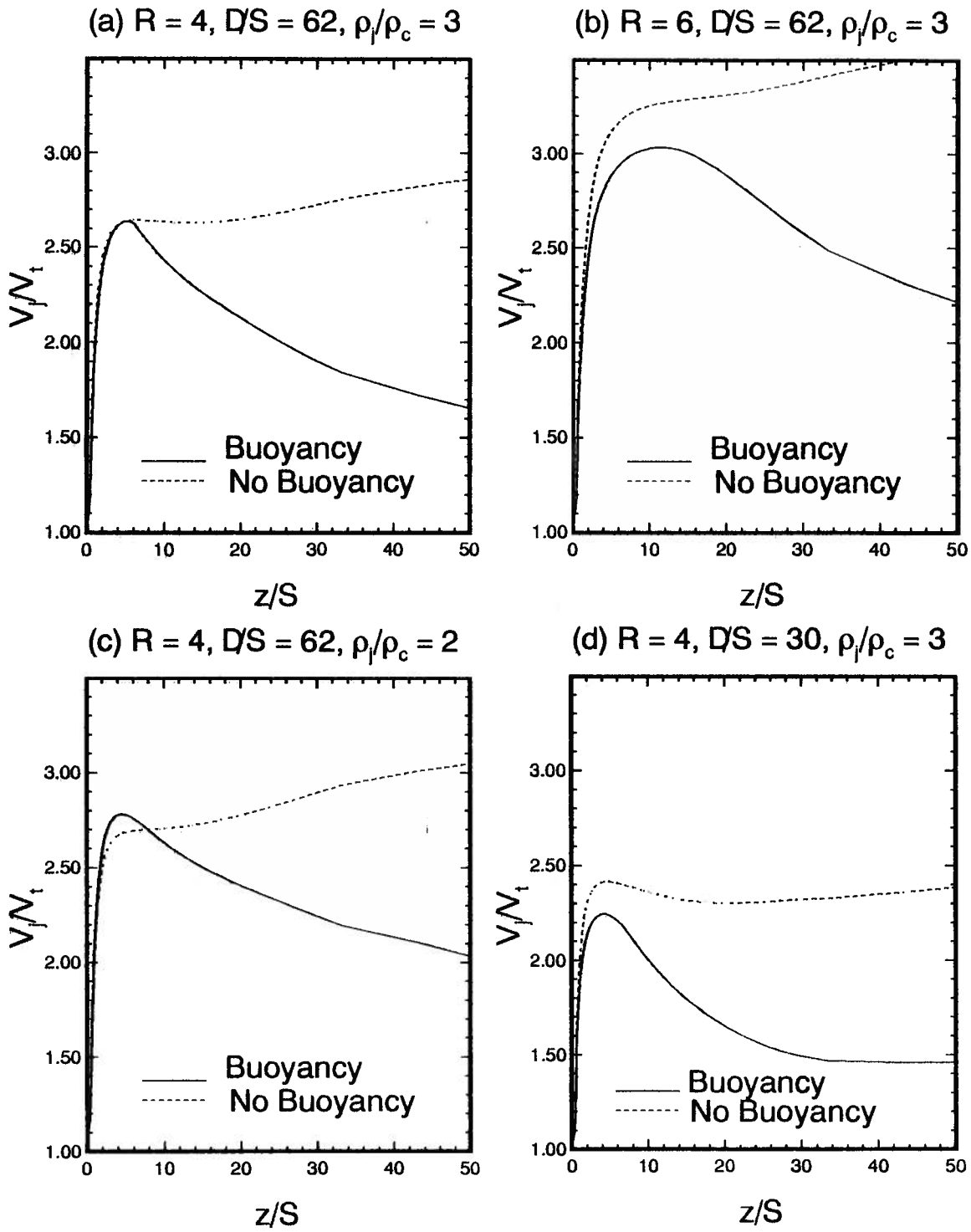

Figure 4.19: Total velocity profiles along the velocity trajectory.

are present comparing factors such as jet penetration and trajectories. These differences increase as the value of total jet to crossflow momentum flux ratio M decreases, indicating more important buoyancy effects at smaller values of M. Therefore, when a quantitative flow analysis is required, buoyancy force should not be ignored.

To illustrate the effect of the buoyancy force on convergence performance of the multigrid method, the convergence histories for the flows studied in this section are presented in Figure 4.20. The mass residues have been normalized by the total incoming mass flow from the crossflow and the jet. As Figure 4.20 shows, the multigrid method has a very fast convergence for the type of flow field considered in this section. In all cases in less than four multigrid cycles the normalized mass error is less than 10^{-4}, which is reasonably small. The slight deterioration of the performance of the multigrid solver due to the inclusion of the buoyancy terms is apparent from the above results, and depends on the the case considered. This deterioration is due to the coupling between the energy and the momentum equations.

4.2.3 Effect of the Jet Orientation

In the kraft recovery boiler the air jets are sometimes injected at an angle. The objective in this section is to investigate if the buoyancy effects will be altered due to the injection angle. Here we compare four jet/crossflow orientations:

1. The jet is injected horizontally into an upwards crossflow
2. The jet is injected horizontally into a downwards crossflow
3. The jet is injected vertically from the top wall into a horizontal crossflow
4. The jet is injected vertically from the bottom wall into a horizontal crossflow.

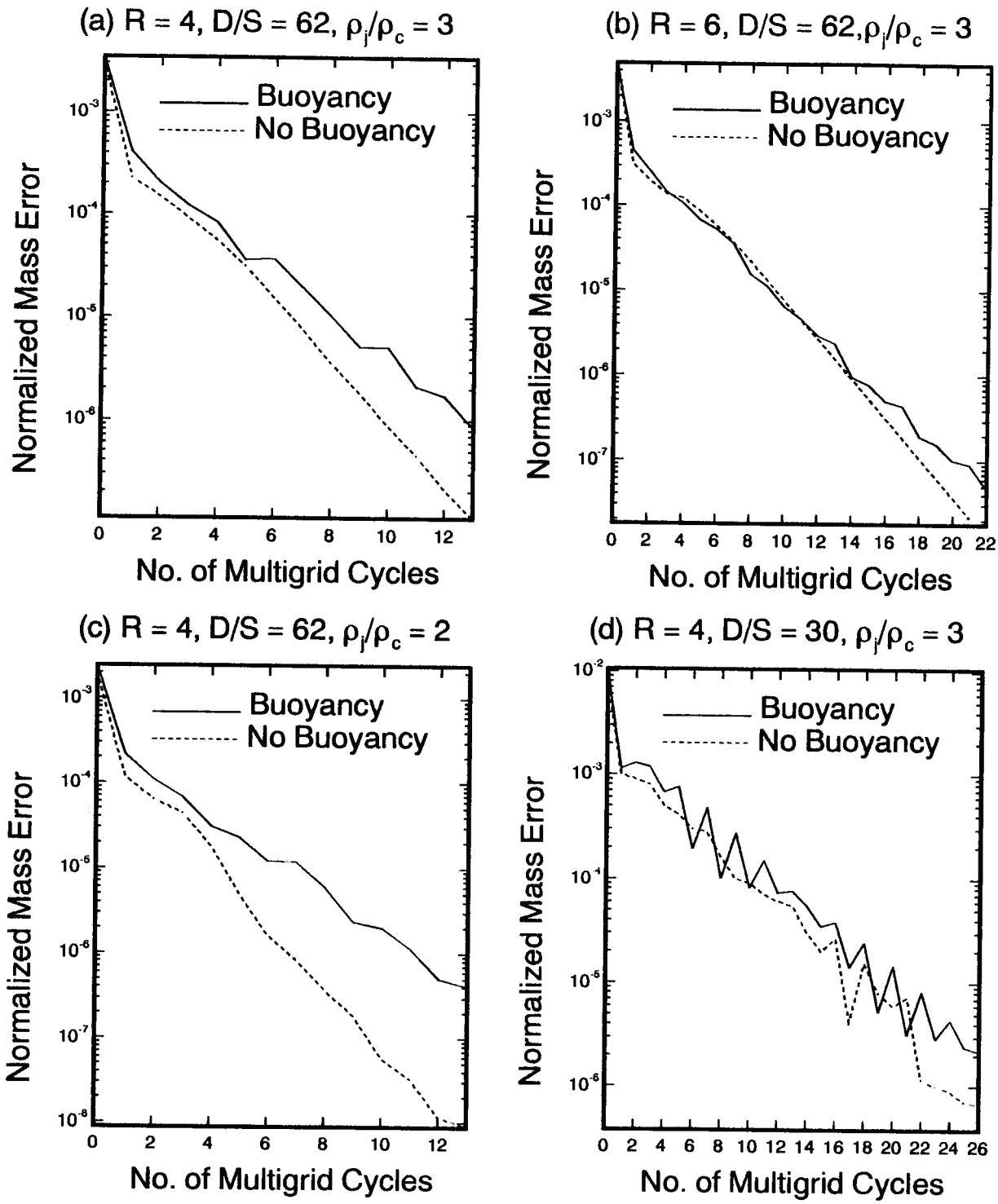

Figure 4.20: Convergence histories for different cases of R, ρ_j/ρ_c, and D/S.

Table 4.3: Summary of the flow variables for study of the jet/crossflow orientation

$U_c = 3m/s$						
$S = 0.04m$						
Case	D/S	R	ρ_j/ρ_c	G	J	M
1	60	4	3	12	48	0.8
2	60	2	3	6	12	0.2
3	60	0.5	3	1.5	0.75	0.012

In Figures 4.22-4.26, 'horizontal' refers to the first orientation, 'up' and 'down' to the third and fourth respectively. When all four conditions are compared, the flow orientation for each case is shown graphically in the figures.

The geometry of the flow field is shown in Figure 4.21. In this section all the flow variables, except the jet velocity are kept constant. Therefore in the analysis of the results the velocity ratio R is used as the defining variable. Three values of the jet to crossflow velocity ratios, $R = 4$, 2, and 0.5 are tested. A summary of the flow variables for each case is given in Table 4.3.

In the numerical model, the domain of the flow field is represented as a rectangular plane. The boundary conditions are like those in the previous section with one exception. Here we are considering a single jet, and thus no symmetry plane is present. Therefore the plane opposite to the plane of the jet is a wall.

To look into the variation of jet structure the velocity vector field normalized by the inlet jet velocity for the case of $R = 4$ is shown in Figure 4.22. It is apparent that the jet injected horizontally into an upwards crossflow penetrates deeper into the crossflow. Considering the recirculation bubble on the lee side of the jet the horizontal jet has formed a larger recirculation region than the vertical jets. A possible explanation for this is that in the case of the horizontal jet the buoyancy force is competing with the drag force exerted by the crossflow on the jet. As the jet fluid is heavier than the

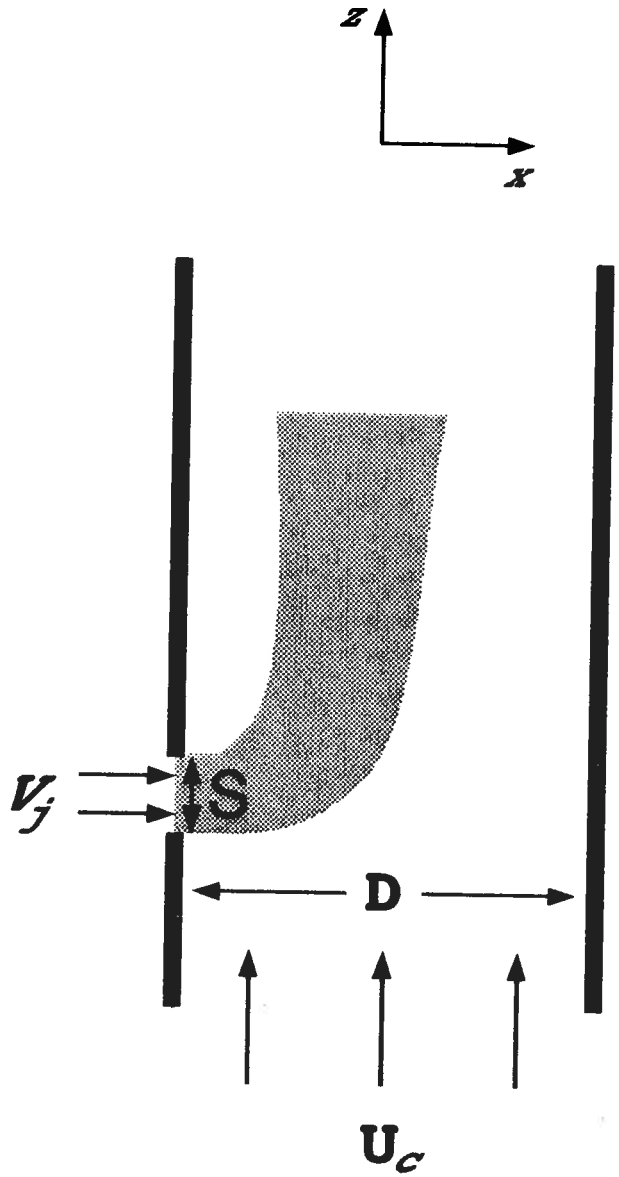

Figure 4.21: Schematic representation of simulated two-dimensional flow domain.

crossflow, the buoyancy reduces the jet deceleration in the direction perpendicular to the crossflow direction. This assists the jet penetration into the crossflow. In the case of the vertical jets the buoyancy force is perpendicular to the cross flow and acts along the jet momentum. Here buoyancy is competing against a larger force and thus is less effective. The velocity field of the vertical jets is similar to the case where buoyancy force is neglected. The recirculation bubble formed on the lee side of these jets is smaller than the recirculation bubble formed by the horizontal jet.

The mixing and the spread of the jet can be visualized by looking at the jet concentration contours presented in Figures 4.23-4.24 for $R = 4$ and 2. For both values of R the spread of the horizontal jet is more than that of either the vertical jets or the jet with no buoyancy force. The spread of the vertical jets is similar to that of the jet with no buoyancy force. However the jet injected upward spreads slightly more than the jet injected downward.

To quantify the mixing between the jet and the crossflow the method explained in the previous section is implemented here. The results are shown in Figure 4.25 for cases of $R = 2$ and 4. For $R = 2$ the horizontal jet has higher mixing than the vertical jets. The mixing of the jet injected from the bottom is slightly more than that of the jet injected from the top or the jet with no buoyancy force. The mixing of the jet injected from the top is similar to the case with no buoyancy. As the value of R increases the degree of mixing of the jets becomes more similar. In the case of $R = 4$ there is virtually no difference between the degree of mixing predicted for the four jets.

The trajectory of the jets, defined as the loci of the maximum jet concentrations for two values of $R = 2$ and 4, is shown in Figure 4.26. As expected, the jets with larger value of velocity ratio R have deflected less than the jets with smaller R. The deflection of the horizontal jet is less than the vertical jets or the jet with no buoyancy. The trajectory of the jet injected from the top is close to that of the jet with no buoyancy force.

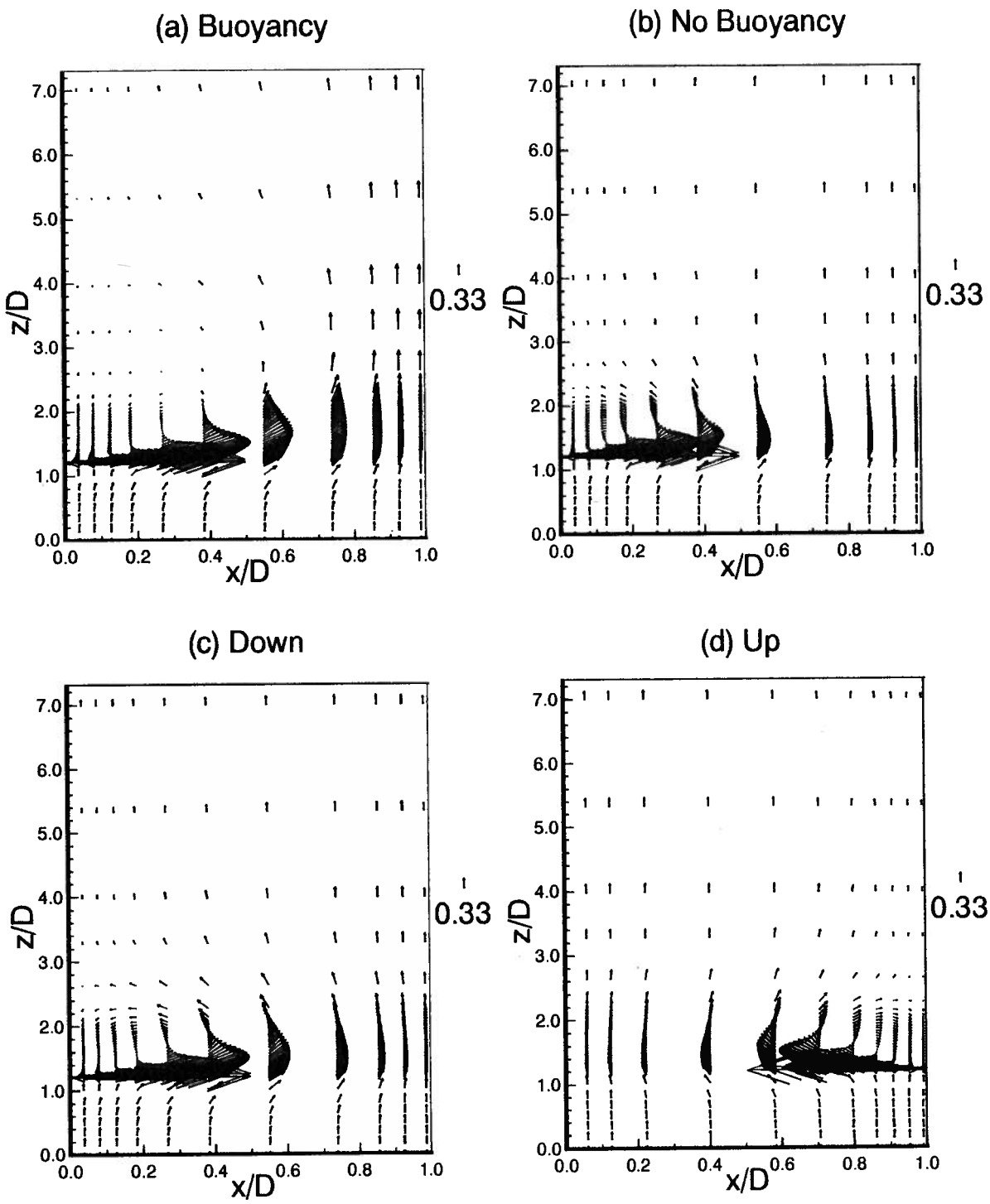

Figure 4.22: Normalized velocity vectors for $R = 4$, 'Down' refers to the jet injected from the bottom, and 'Up' refers to the jet injected from the top.

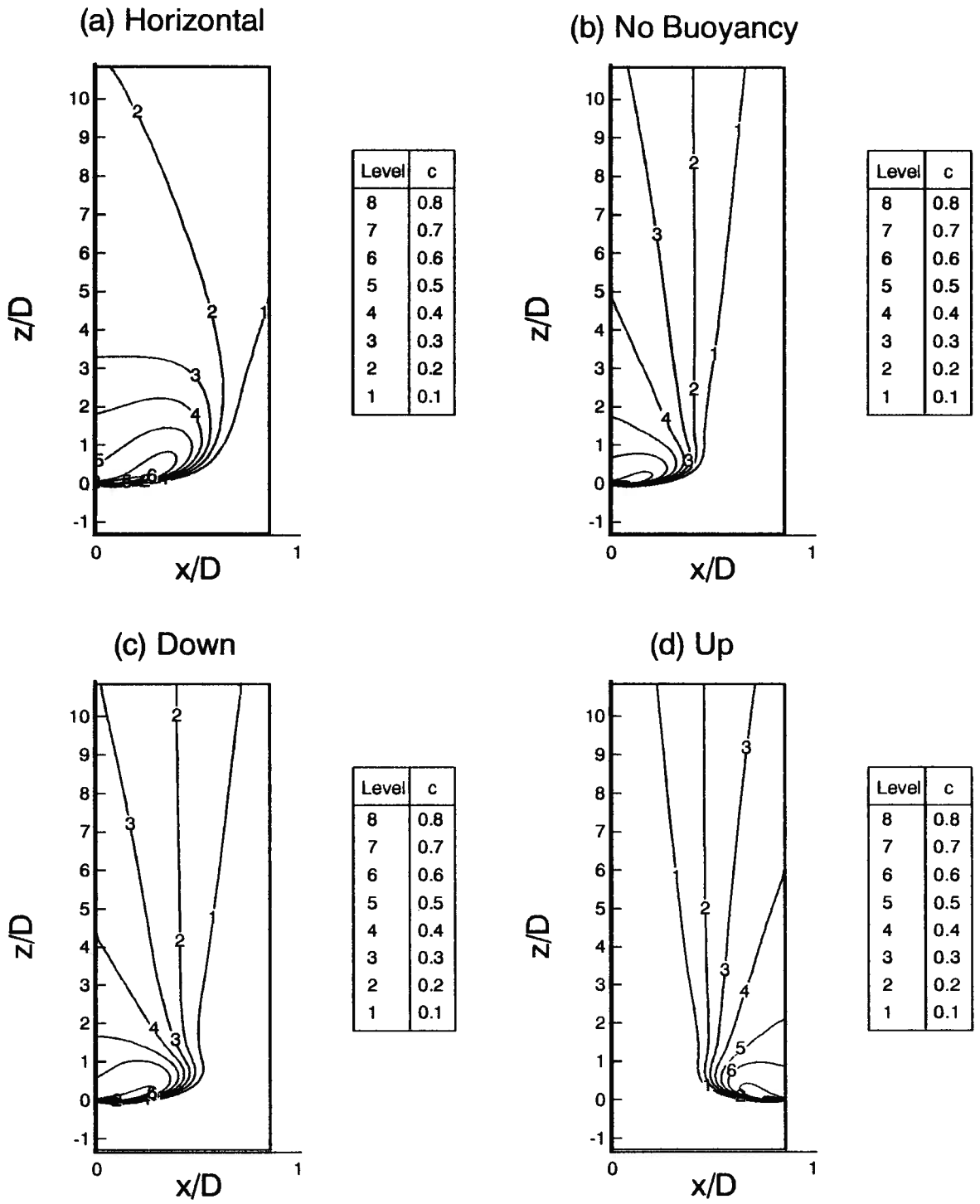

Figure 4.23: Jet fluid concentration profiles for $R = 4$, 'Down' refers to the jet injected from the bottom, and 'Up' refers to the jet injected from the top.

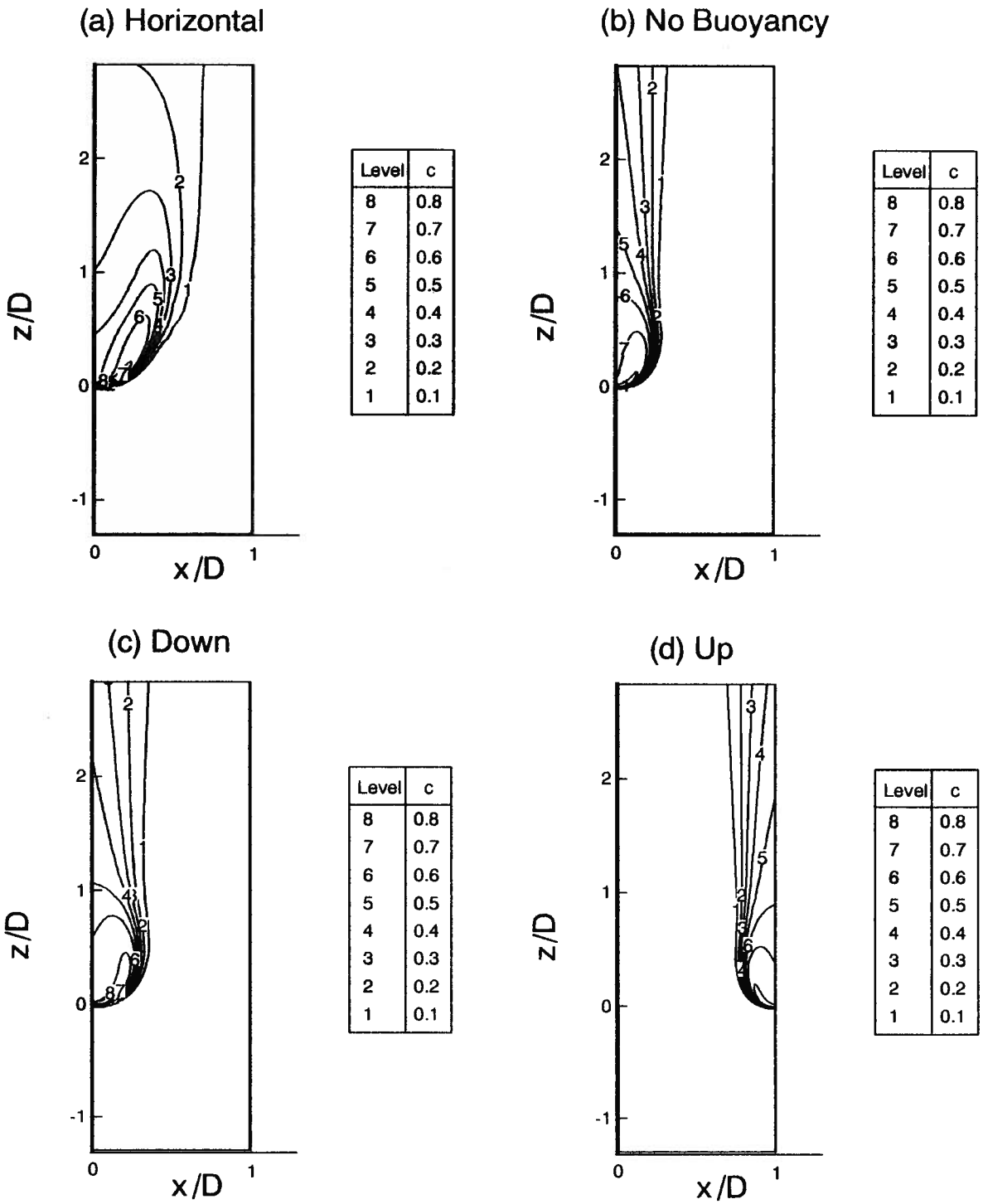

Figure 4.24: Jet fluid concentration profiles for $R = 2$, 'Down' refers to the jet injected form the bottom, and 'Up' refers to the jet injected from the top.

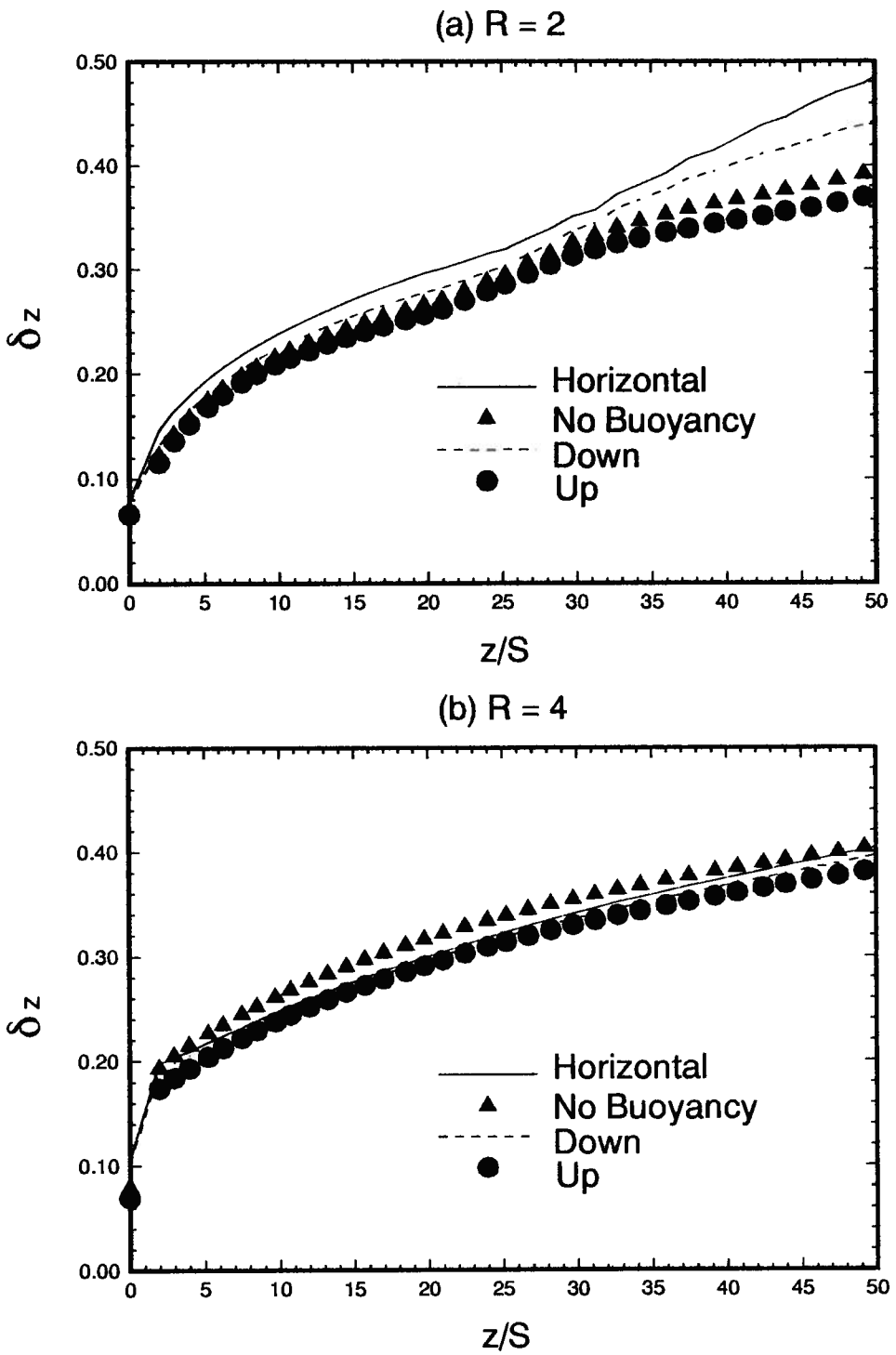

Figure 4.25: Effect of buoyancy on degree of mixing.

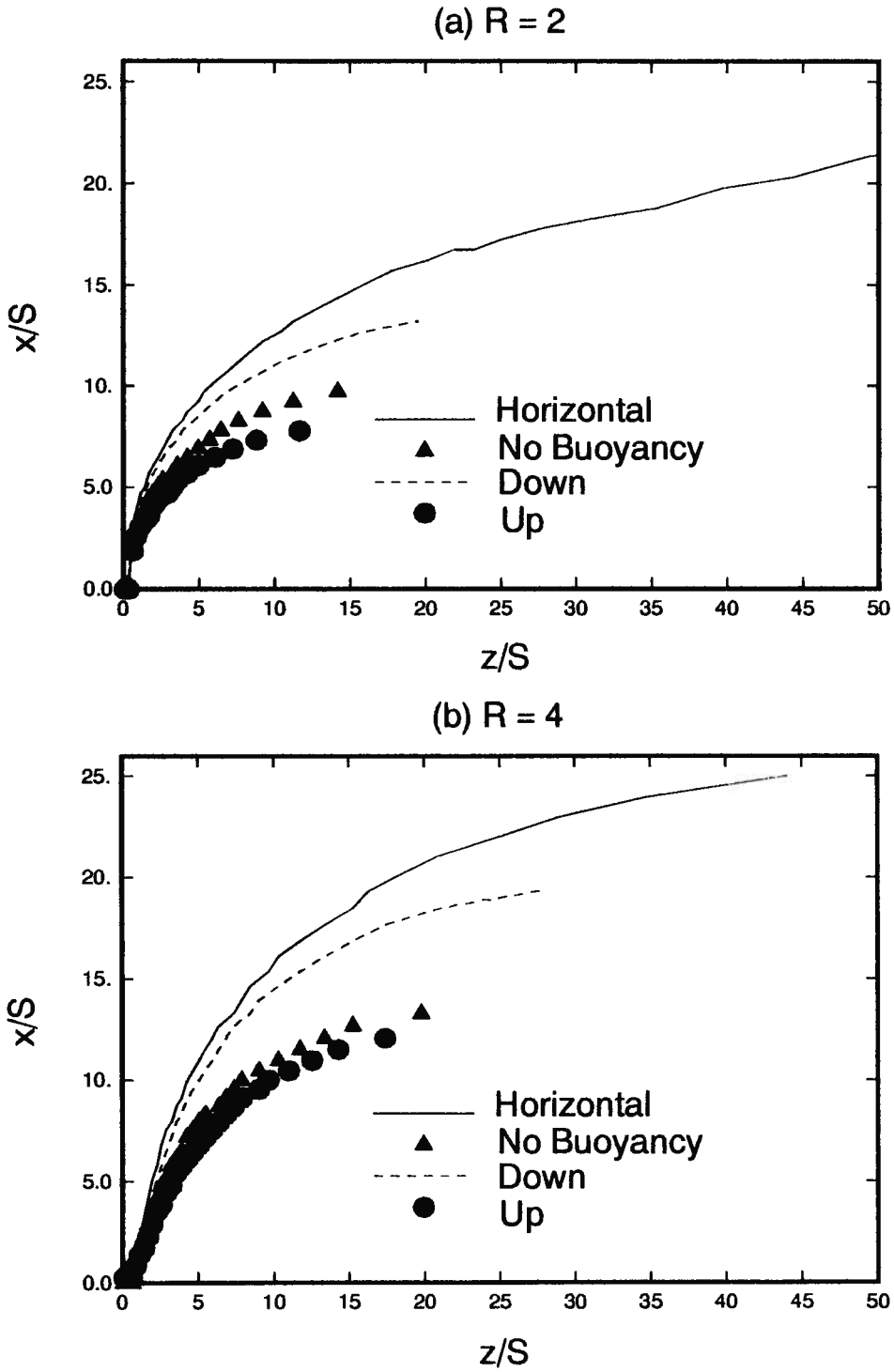

Figure 4.26: Jet fluid concentration trajectories.

For two cases of $R = 2$ and 0.5 the size of the recirculation region formed downstream of the jet for the four flow orientations described previously are compared with the case with no buoyancy force. These results are shown in Figure 4.27. As the size of the recirculation region for the case of the horizontal jet issued into an upwards crossflow is much larger than the other cases it is not shown in the same figure for reason of better scaling. The results show that the horizontal jet issued into a downwards crossflow forms the smallest recirculation region, because both the buoyancy force and the drag force exerted by the crossflow on the jet are pulling the jet downwards. The same pattern is apparent for both values of R. This further indicates the importance of the jet and crossflow orientation on the effect of buoyancy force on these flows.

To illustrate the effect of the buoyancy force on convergence performance of the multigrid method, the convergence histories for the flows studied in this section are presented in Figure 4.28. The mass residues have been normalized by the total incoming mass flow from the crossflow and the jet. As Figure 4.28 shows, for the case of $R = 2$, the multigrid method has a very fast convergence. As the value of R increases, a larger number of multigrid cycles is required to obtain a converged solution. This may be due to the increased blockage of the crossflow by the jet and a stronger impingement of the jet on the opposed wall. The strong interaction of the jets can result in unsteadiness in the flow field. Quick et al. (1991) have shown this in the case of the opposed jets. The deterioration of the performance of the multigrid solver due to the inclusion of the buoyancy terms is apparent from the above results. The main reason for this is the coupling between the set of the governing equations of motion when buoyancy is included. Due to inclusion of the buoyancy force the vertical equation of motion is coupled with the energy equation. This results in a slower rate of convergence.

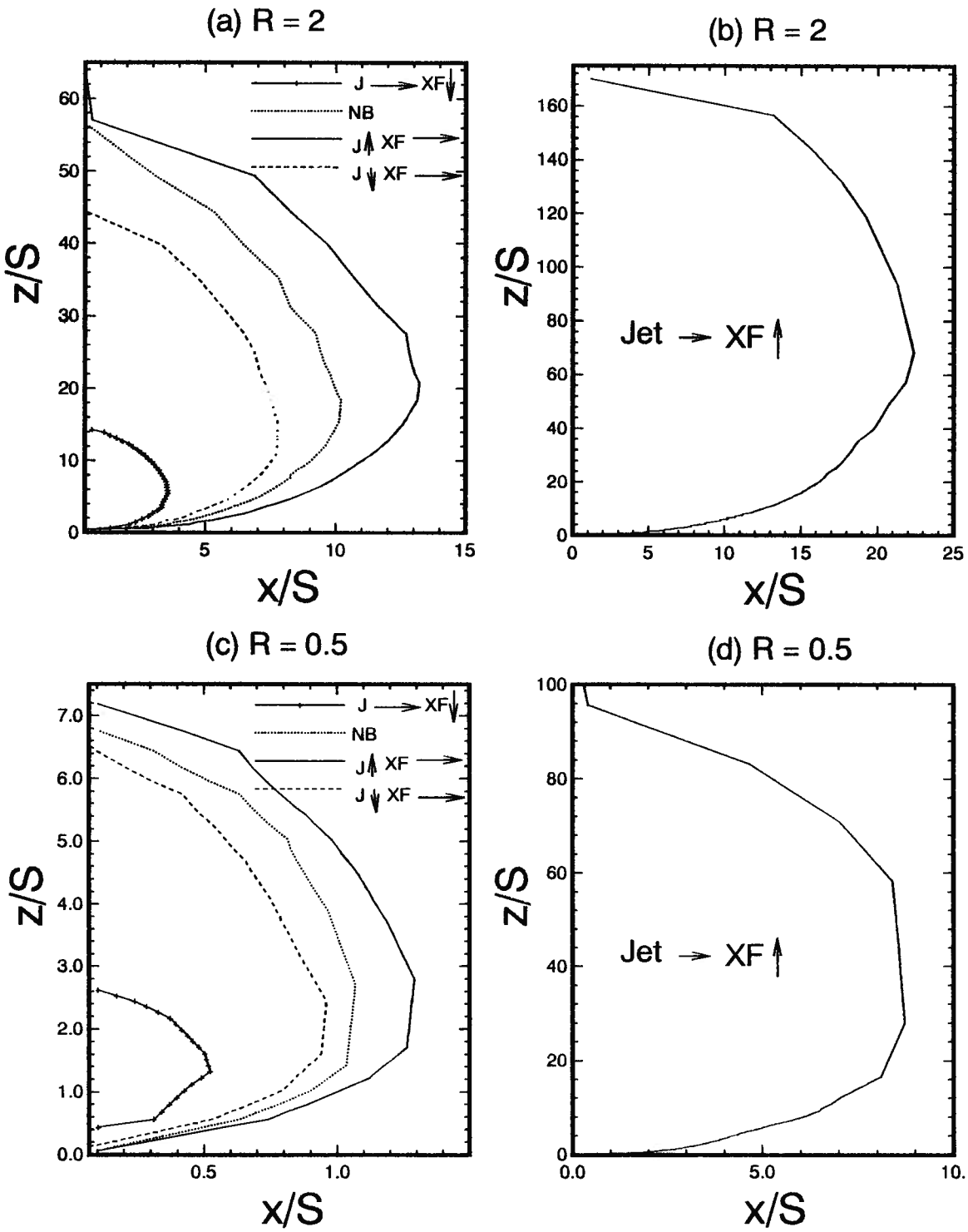

Figure 4.27: Recirculation region of two-dimensional jets, J refers to jet, XF refers to the crossflow, NB refers to the case with no buoyancy force, and the arrows show the flow direction.

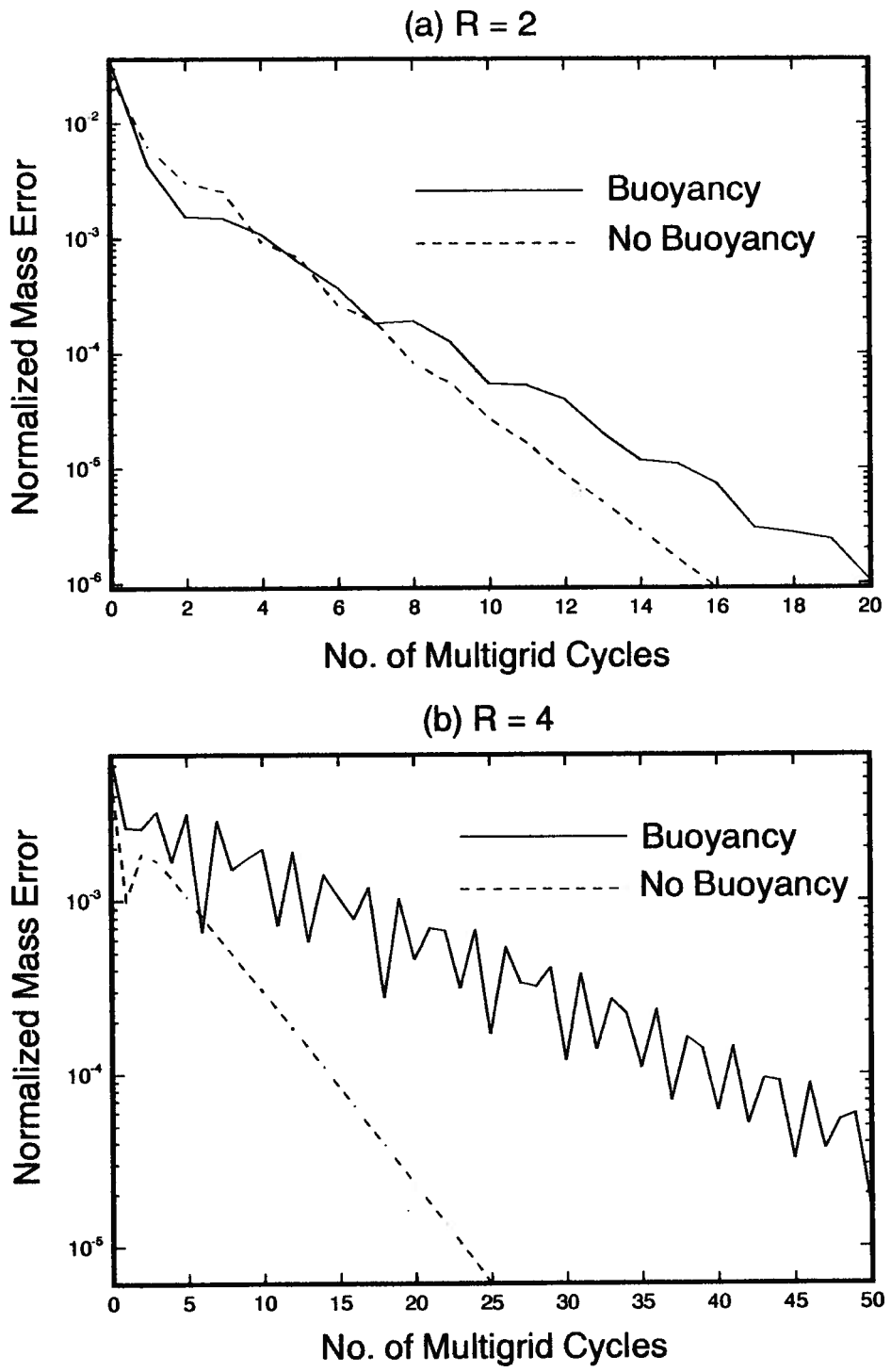

Figure 4.28: Convergence histories for different cases of R

Chapter 5

Effects of Buoyancy on Three-Dimensional Jets in Cross-Flow

In this chapter, the effect of buoyancy force on the flow field of a single jet and a row of jets injected into a confined crossflow is studied. To understand the buoyancy effects in the complex flow field of the kraft recovery boiler, a step-by-step approach to the problem is adopted here. The tertiary and secondary air jets in the kraft recovery boiler consist of an array of jets distributed either on all four or two walls of the boiler, depending on the particular design. Generally the secondary air jets are injected at higher velocities than the tertiary air jets. Secondary air jets are smaller and more numerous, than the tertiary air jets. In this chapter, therefore, the flow conditions simulated correspond to that of a typical tertiary air jet in the kraft recovery boiler where, due to lower velocities and larger jet sizes, the buoyancy effects could be more significant. Here we restrict our attention to a single jet and a row of jets injected into a confined uniform crossflow.

Among the parameters which can influence the fluid flow, the jet to crossflow velocity ratio R, density ratio ρ_j/ρ_c, and extent of the confinement D/S are tested here. Variations of the first two of these parameters result in the variation of the jet to crossflow momentum and mass flux ratios. The purpose here is to investigate the effect of buoyancy on jet penetration and the interaction of the jet with the crossflow. The effect of buoyancy on features of the flow field due to the interaction with the crossflow of a single jet and a row of jets is investigated.

The problem of a single jet in crossflow is described first, followed by an analysis of a row of jets.

Table 5.1: Summary of the flow variables for calculations of the tertiaries

$U_c = 3m/s$						
$H = 0.8m$						
$W = 0.16m$						
Case	D/S	R	ρ_j/ρ_c	G	J	M
1	28	6	3	18	108	3.85
2	28	8	3	24	192	6.85
3	14	6	3	18	108	7.71
4	14	8	3	24	192	13.71

5.1 Three-Dimensional Single Jet in a Confined Crossflow

The geometry of the three-dimensional single jet injected into the confined crossflow is shown in Figure 5.1. The jet characteristic length S is defined as $\sqrt{HW}$.

The flow conditions selected are given in Table 5.1. These conditions have been chosen to simulate conditions of typical tertiary air jets in the kraft recovery boiler. At this stage, however, combustion and radiation are not included in our calculations. These processes will be considered in Chapter 6.

The calculation domain is represented as a rectangular box. Due to flow symmetry only half of the domain needs to be calculated. The symmetry condition is imposed on the lateral plane $(z - y)$ passing through the jet central plane $(y = 0.0)$.

As in the previous computation for a two-dimensional jet in crossflow, the wall function is used to represent the shear stress near solid boundaries. Plug flow conditions are used at the jet and crossflow inlets. In calculations of strong jets in crossflow the turbulence characteristics are not sensitive to the prescribed inlet conditions of the k and ϵ and are mainly governed by the shear produced in the flow field. However, as is the usual practice for the jet in crossflow, the inlet turbulent kinetic energy for the crossflow k_c is specified as $k_c = 1.5U_c^2 I^2$ and its dissipation as $\epsilon_c = c_\mu^{3/4} k_c^{3/2}/l_c$, where the

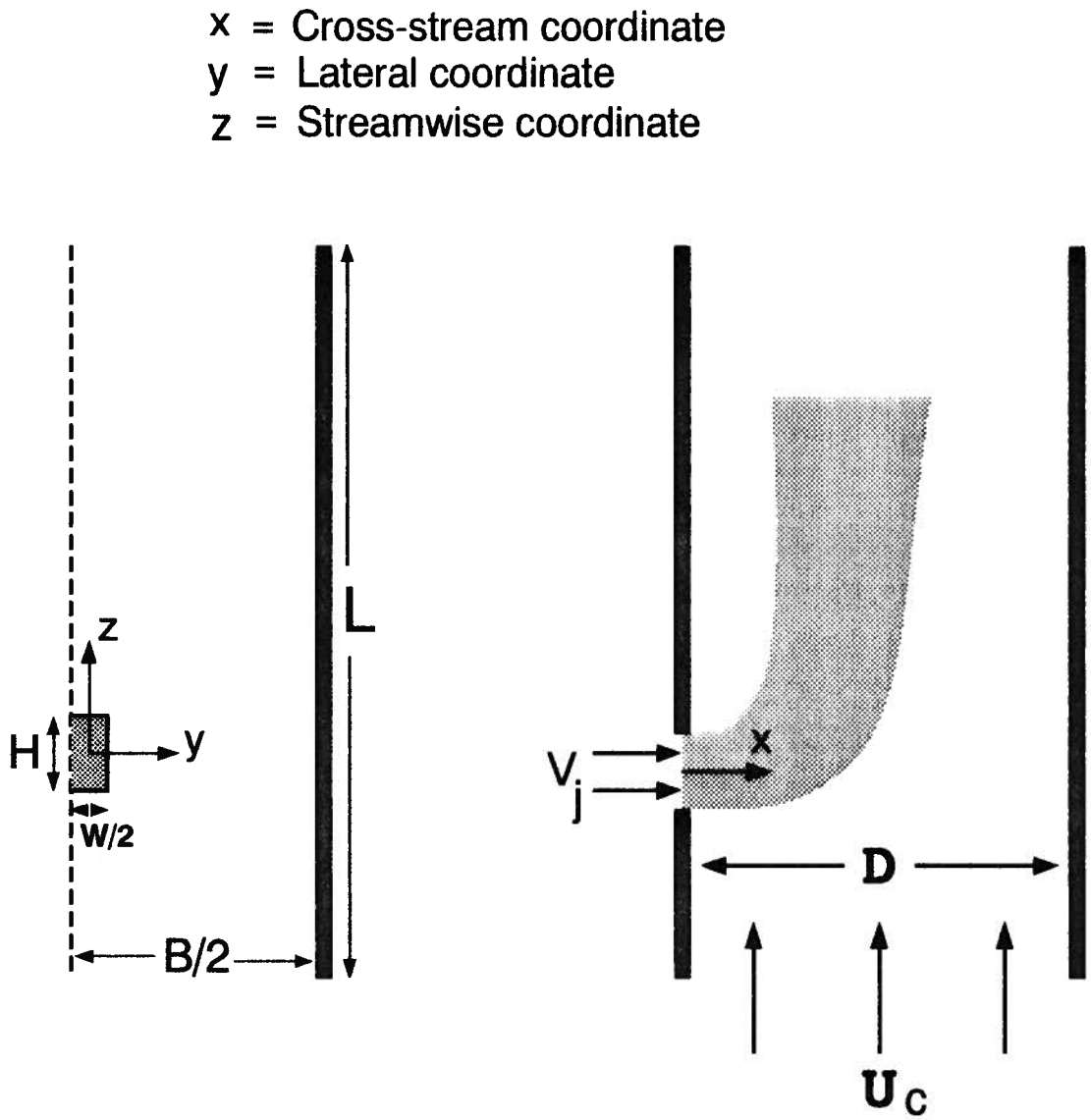

Figure 5.1: Schematic representation of a three-dimensional jet into crossflow.

dissipation length scale $l_c = 0.1D$, $I = 0.01$, and $C_\mu = 0.09$. Similar conditions are used at the jet entrance. The inlet turbulence kinetic energy for the jet is $k_j = 1.5U_j^2 I^2$ and the rate of its dissipation $\epsilon = c_\mu^{3/4} k_j^{3/2}/l_j$. Here $l_j = 0.1S$ and $I = 0.01$. The location of the inlet plane for the crossflow is about $10S$ upstream from the jet. This is sufficiently far from the jet inlet plane to avoid any disturbances at the crossflow inlet plane due to the jet. The zero gradient condition for all the dependent flow variables is imposed at the outlet. The exit plane is placed $74S$ downstream of the jet to allow the condition of fully developed flow to be made. Calculations are done using a two level multigrid.

Jet trajectory is one of the most important characteristics in studies of jets in crossflow. The effect of buoyancy on jet trajectories is presented in Figure 5.2. Here, the jet trajectory is defined as the loci of the local maximum concentration points on the plane of symmetry. The trajectories are shown for velocity ratios R of 6 and 8.

The jet with higher velocity ratio R is deflected less than the jet with lower R and therefore its trajectory is further away from the injection wall. When the jet velocity increases, the momentum ratio of jet to crossflow J, the dominant factor in jet trajectory and penetration, increases. The jet with higher R value has penetrated deeper into the crossflow. For both values of R the predicted jet trajectories for the jet without buoyancy force is closer to the injection wall than the jet with buoyancy force. The jet with buoyancy has penetrated deeper into the crossflow. As in the case of the two-dimensional jets the buoyancy force acting against the crossflow reduces the effect of the drag force on the jet. This results in the formation of a stronger jet and increases jet penetration. As a result the jet with buoyancy is deflected less than the jet without buoyancy and its trajectory is farther away from the injection wall.

The center plane velocity profiles for cases 1 and 2 of Table 5.1 are presented in Figure 5.3. The entire flow pattern in the case of the three-dimensional jets is different than that of two-dimensional jets. As is apparent from the normalized vector velocity fields (V_j is

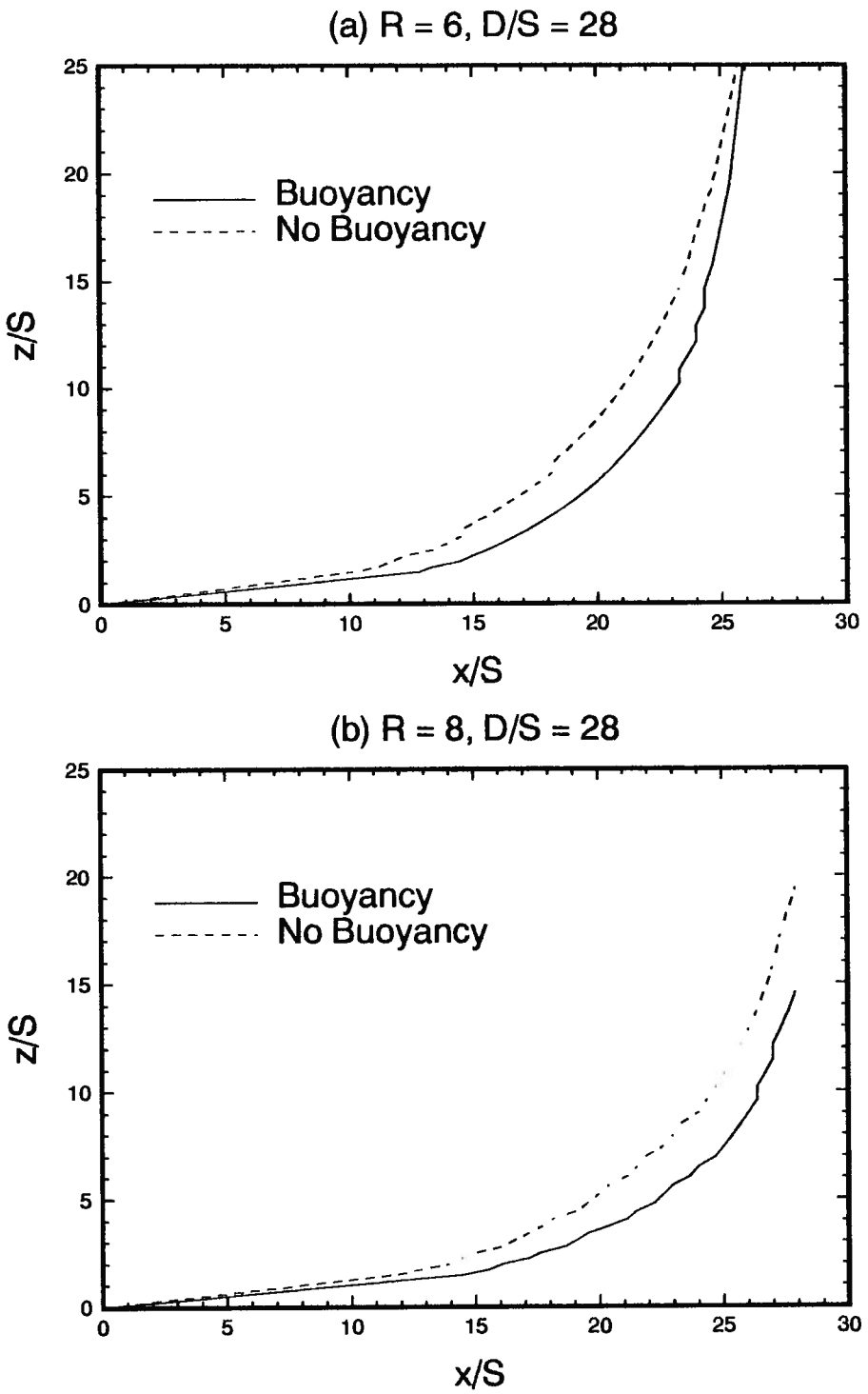

Figure 5.2: Jet fluid concentration trajectories.

used as the normalization factor) in Figure 5.3 there is no blockage effect caused by the jet on the crossflow, as the crossflow can pass by the sides of the jet. This is revealed by the absence of a recirculation bubble downstream of the jet in all cases. For both values of $R = 6$ and 8, the absence of buoyancy force leads to the prediction of a more uniform velocity vector field in the far field. This effect is more significant for the case of $R = 6$. For both cases shown here the jets do not impinge on the opposite wall, as there is no region of downward flow present on this wall.

The jet concentration profiles along the same longitudinal plane and for the same cases are shown in Figure 5.4. From Figure 5.4 it can be seen that there is an initial jet core region followed by a region of considerable jet deflection. After this region the flow becomes parallel to the opposite wall. The jet with $R = 6$ has a smaller mass and momentum flux ratio (Table 5.1) and is weaker than the jet with $R = 8$. Comparing Figures 5.4(a and c) it is apparent that the jet concentration on the opposite wall for $R = 8$ is larger than $R = 6$. When the buoyancy force is ignored the jet penetration decreases and its concentration on the opposite wall reduces.

To study the effect of the confinement width on the flow field the normalized vector velocity fields in the central $z - x$ plane for cases 1 and 3 of Table 5.1 are presented in Figure 5.5. For value of $D/S = 14$ the jet impinges on the opposite wall. This is apparent by the presence of the downward velocity vectors on the opposite wall in Figures 5.5(a-b). The presence of the downward and upward velocity vectors on the opposite wall indicate that at certain location in between there exists a region with zero vertical velocity. A zoom in view of normalized vector velocity field for cases $R = 6$ and 8 and $D/S = 14$, in the vicinity of the opposite wall is shown in Figure 5.6. For the case of $R = 6$, the center of the impingement for the jet with buoyancy, as shown in Figure 5.6(a), is at $z = 0.8D$. When the buoyancy force is ignored the location of the point of impingement moves to $z = 0.86D$ as is shown in Figure 5.6(b). Similar results are seen for the case of $R = 8$ in

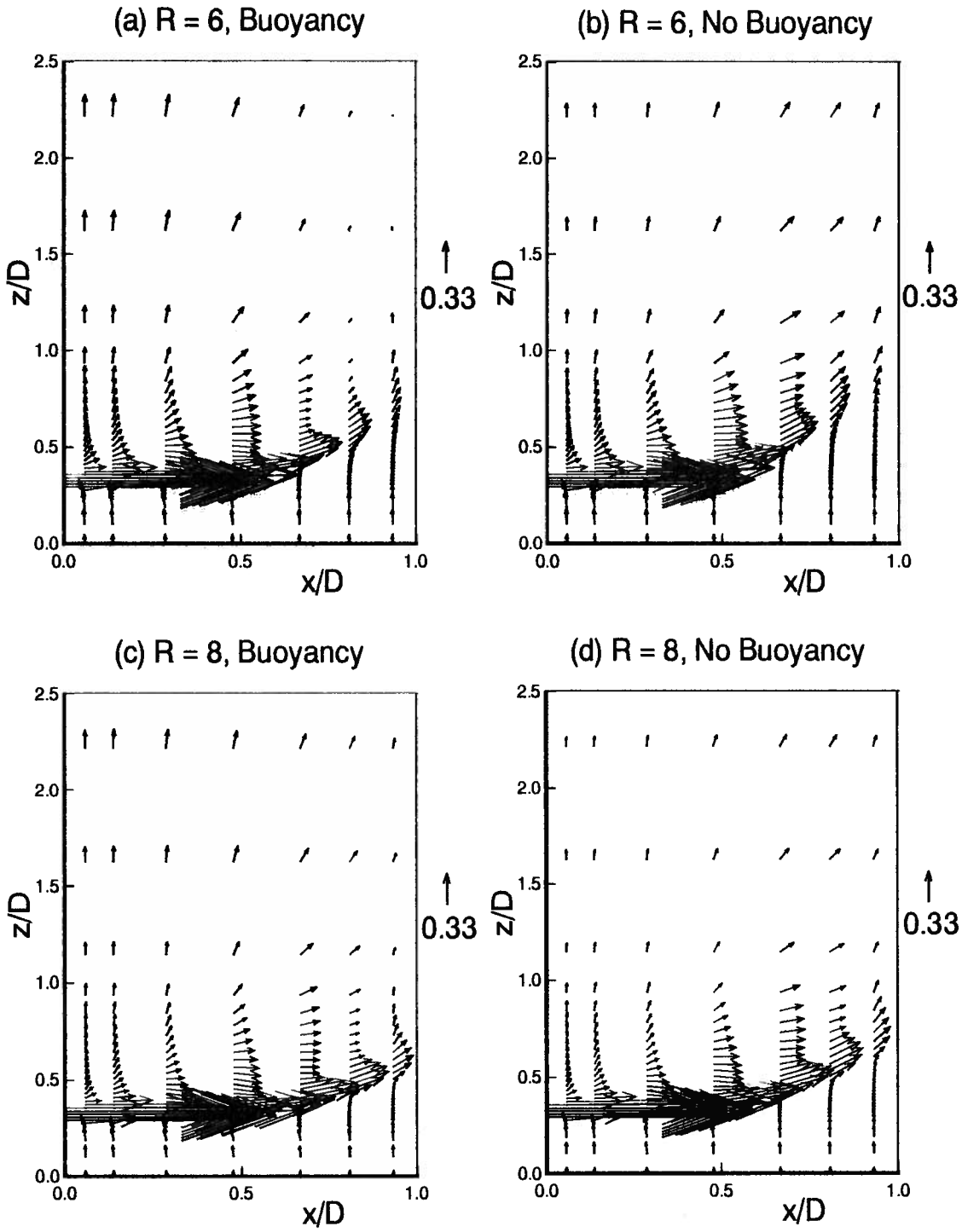

Figure 5.3: Normalized vector velocity profiles for $D/S = 28$ and $R = 6$ and 8 along the jet center plane.

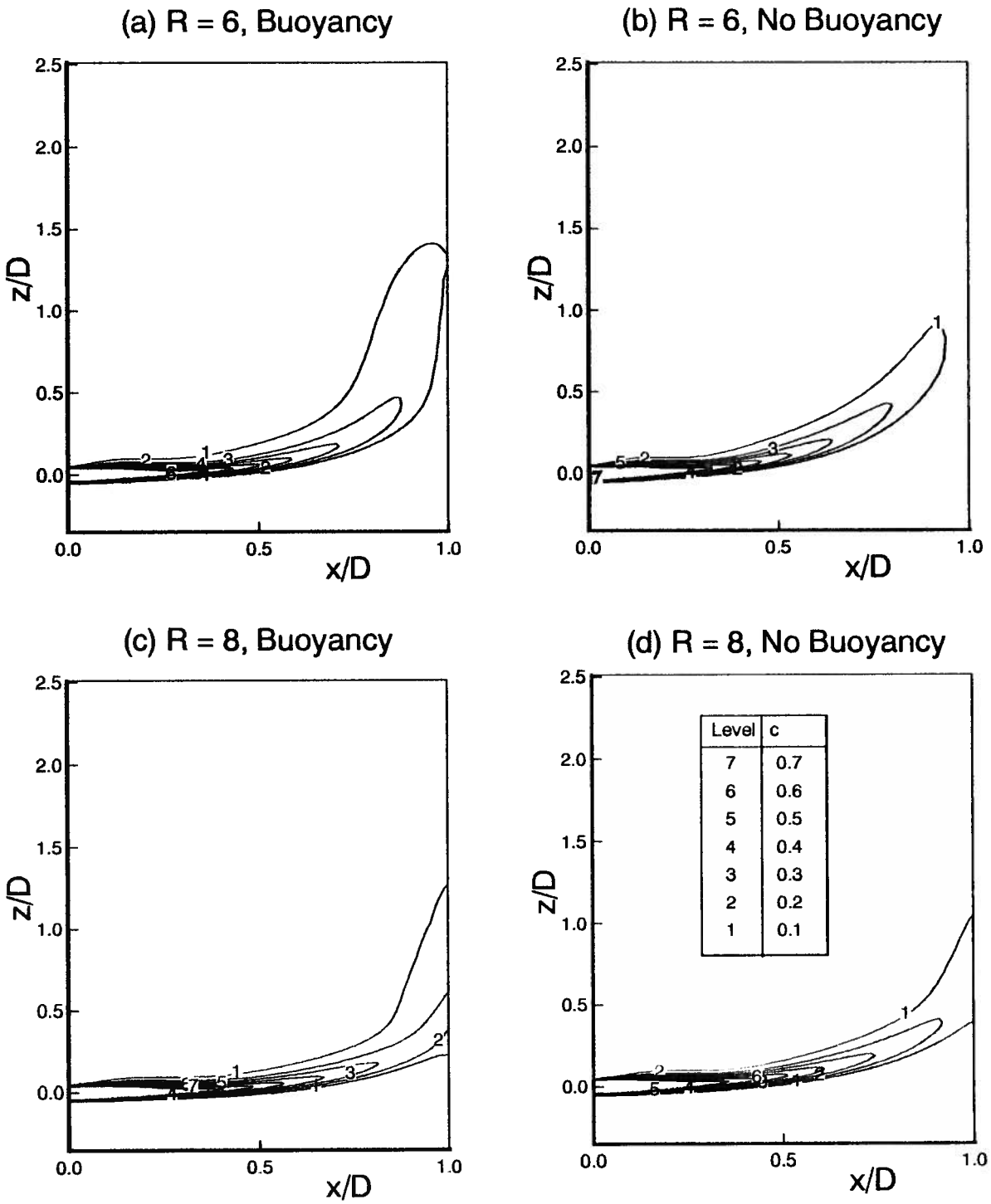

Figure 5.4: Jet fluid concentration profiles for $D/S = 28$ along the jet center plane.

Figures 5.6(c-d). As in the case of the two-dimensional jets the buoyancy force opposes the drag exerted by the crossflow on the jet and results in deeper penetration and smaller deflection of the jet. The jet without the buoyancy force therefore deflects more and hence its point of impingement on the opposite wall moves farther downstream. Comparing cases 1 and 3 of Table 5.1 at larger value of $D/S = 28$, the jet is weaker (smaller M), and therefore it does not impinge on the opposite wall. This is apparent by the absence of downward velocity vectors in Figures 5.5(c-d). A more significant effect of buoyancy force on the velocity field in the case of $D/S = 28$ is apparent.

The decay of the maximum jet concentration along the jet concentration trajectory in the center plane for two different confinement widths, $D/S = 14$ and 28, and two values of $R = 6$ and 8 are presented in Figure 5.7. The value of jet concentration decreases continuously moving downstream from the jet. Although the concentration trajectories change in accordance with the velocity ratio R and the buoyancy force, the decay of the jet concentration along the concentration trajectory for the values of R tested, follows almost the same curve for cases with and without buoyancy. As shown in Figure 5.7 the decay of the jet concentration almost collapses into one curve, for both values of R with and without buoyancy. This implies that the velocity ratio and the buoyancy force play only a minor role in the jet concentration decay process.

The effect of buoyancy on the detailed interaction of the jet with crossflow can be seen by looking into the passive scalar field in Figures 5.8-5.13. The mixing characteristics and the variations of jet structure can be better understood by looking at the jet concentration contours in Figures 5.8-5.13. These results for $R = 6.0$ and $D/S = 14.0$ for cases with and without buoyancy force are presented in Figures 5.8 and 5.9 at four locations downstream of the jet. After the impingement at $z/S = 1.0$, the jet cross-section is distorted into a kidney shape. At $z/S = 3.0$ a core of higher jet fluid concentration close to the opposite wall is formed. Farther downstream the jet is stretched laterally and has become

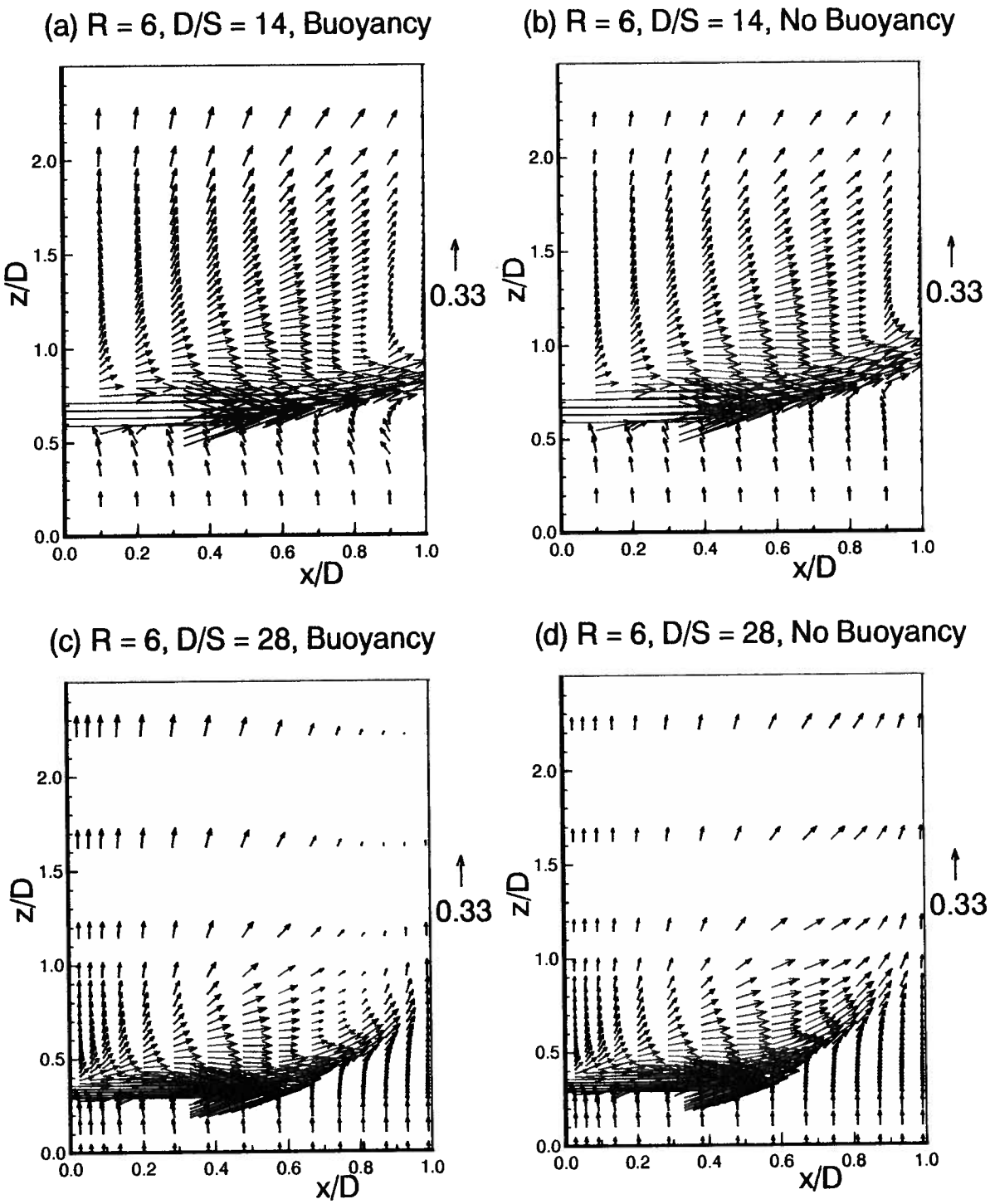

Figure 5.5: Normalized vector velocity profiles for $R = 6$ and $D/S = 14$ and 28.

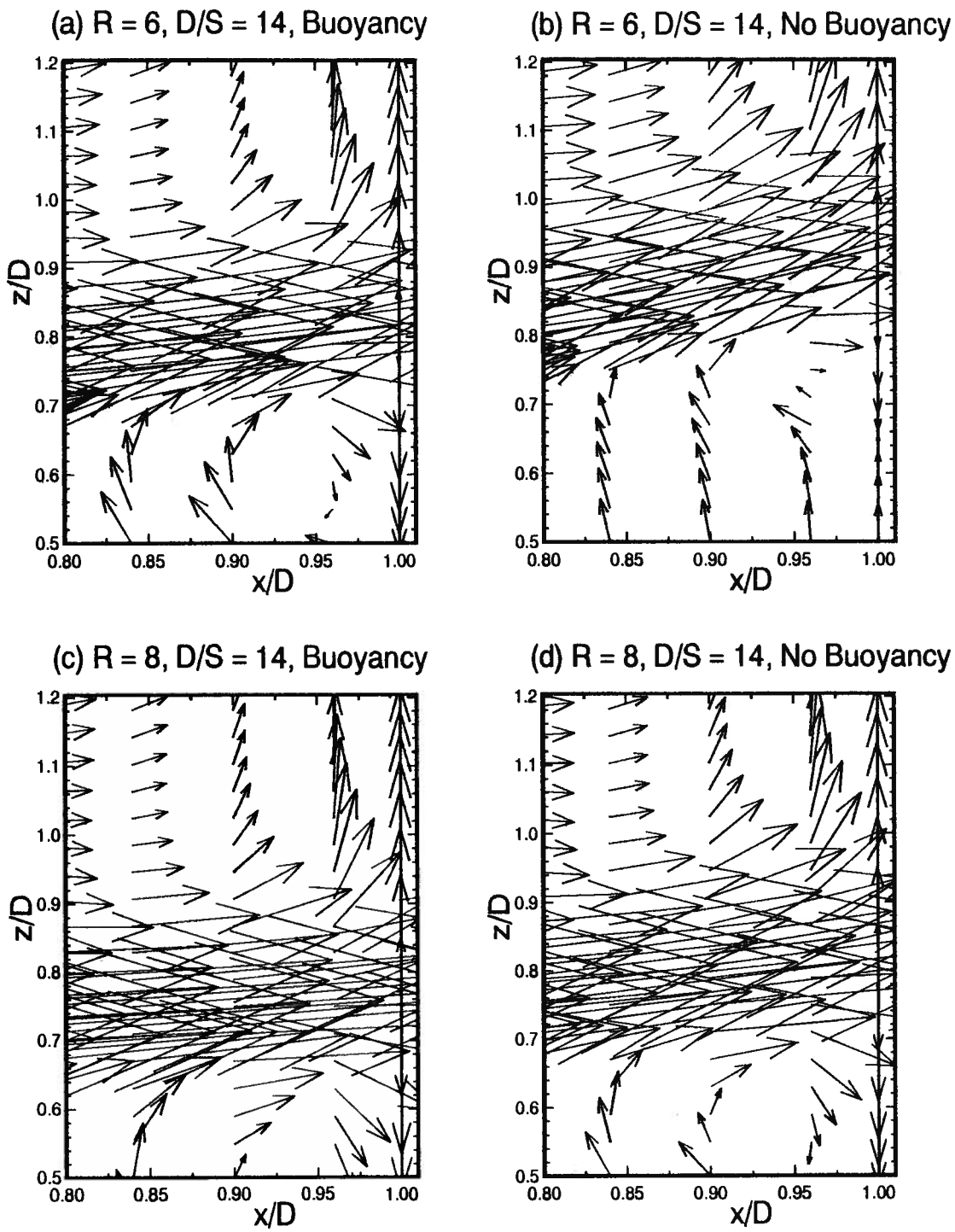

Figure 5.6: A zoom in view of normalized vector velocity profiles for $R = 6$ and 8 and $D/S = 14$.

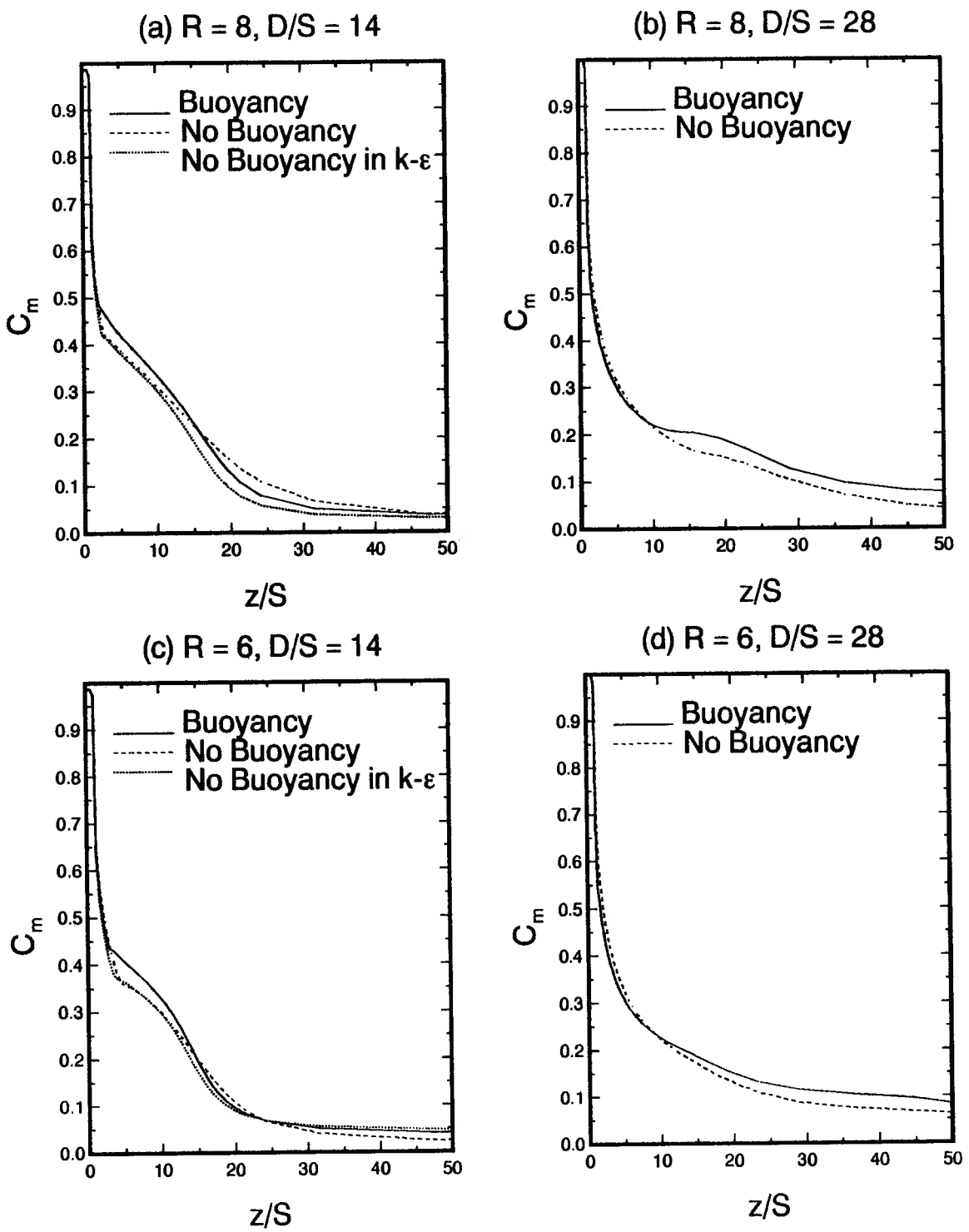

Figure 5.7: The decaying process of jet concentration along the jet concentration trajectory.

more slender. At $z/S = 5.0$ the jet begins to lose its identity. Farther downstream at $z/S = 10.0$ due to the entrainment of the crossflow into the jet low concentrations of jet fluid are present. Comparing the jet concentration contours for the case without buoyancy force (Figure 5.9) with those with buoyancy, it is evident that the buoyancy force results in a better spread of the jet. This effect is particularly significant on the lateral spread of the jet, as laterally the jet is not constrained significantly. As the impingement of the jet without buoyancy on the opposite wall is weaker, a smaller core of higher concentration is formed. The entrainment of the crossflow by the jet is weaker and the jet preserves its identity farther downstream.

The concentration profiles for $R = 6.0$ and $D/S = 28.0$ are presented in Figures 5.10 and 5.11. At $z/S = 1.0$ the jet has a horse shoe cross section. Farther downstream at $z/S = 3.0$, due to the interaction of the jet and the crossflow, the jet cross-section is distorted into a kidney shape. Moving downstream at $z/S = 5.0$ and 10.0, the jet moves to the central core of the flow and its cross-section becomes stretched and more slender. Comparing the results with those in the case of $D/S = 14.0$, it is apparent that the jet impingement on the wall results in significant distortion of the jet cross-section. For the case where buoyancy force is excluded the jet spread is less and the predicted jet cross-section is smaller. The buoyancy force results in better spreading and mixing of the jet and cross flow.

Figures 5.12 and 5.13 present the concentration profiles for the $R = 8.0$ and $D/S = 28.0$. At this higher velocity jet penetration has increased and the effect of the crossflow on the distortion of the jet is stronger. The spread of the jet is more restricted by the opposite wall than the case of $R = 6.0$. In Figure 5.13 for the case without buoyancy force the effect of the opposite wall on the spread of the jet is smaller. Comparing Figure 5.12(d) and 5.13(d) this effect is apparent. At this higher velocity ratio R, the effect of buoyancy on the jet concentration profile in the near field is smaller. Farther

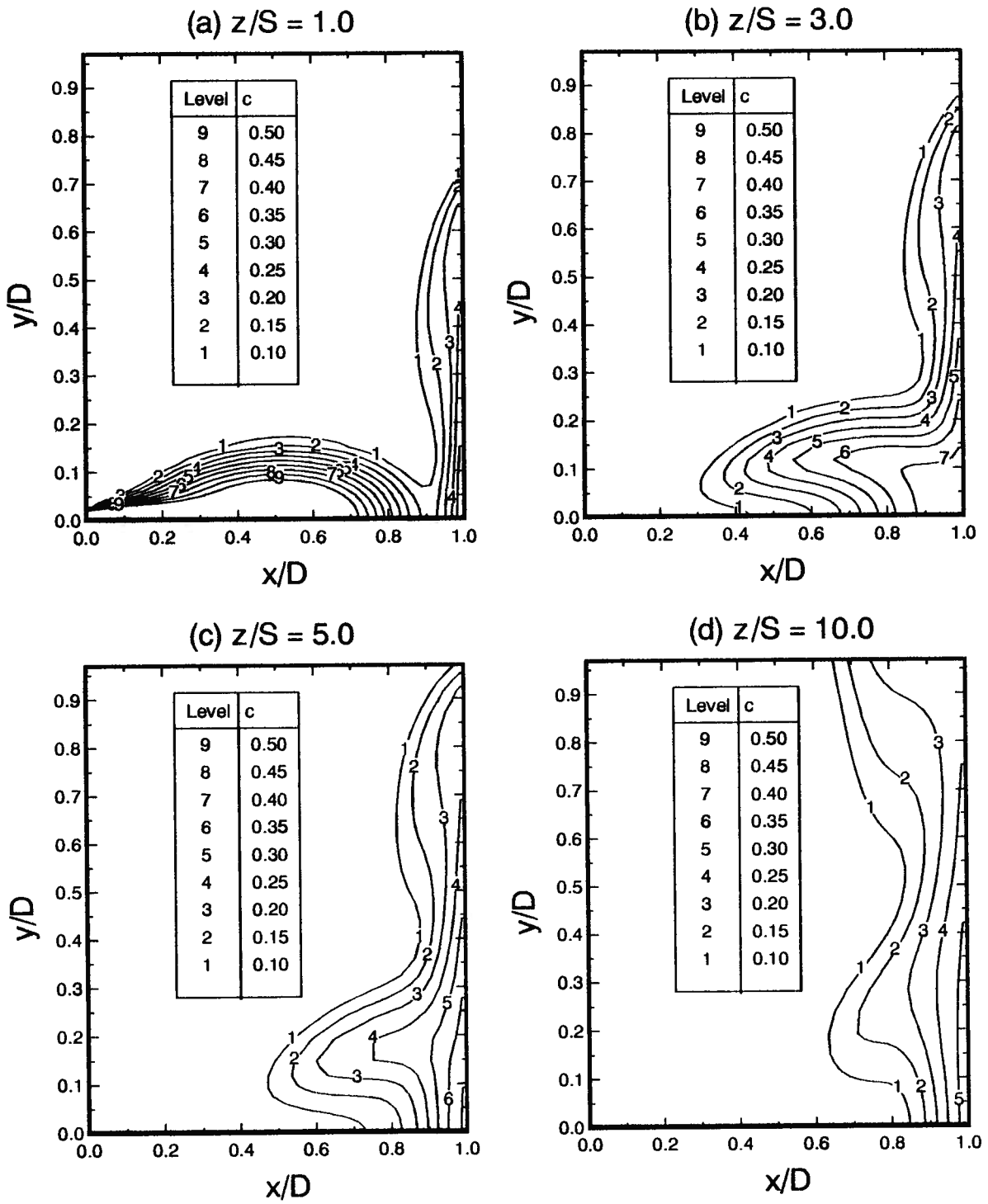

Figure 5.8: Jet concentration profiles for $R = 6$ and $D/S = 14$ (including buoyancy terms).

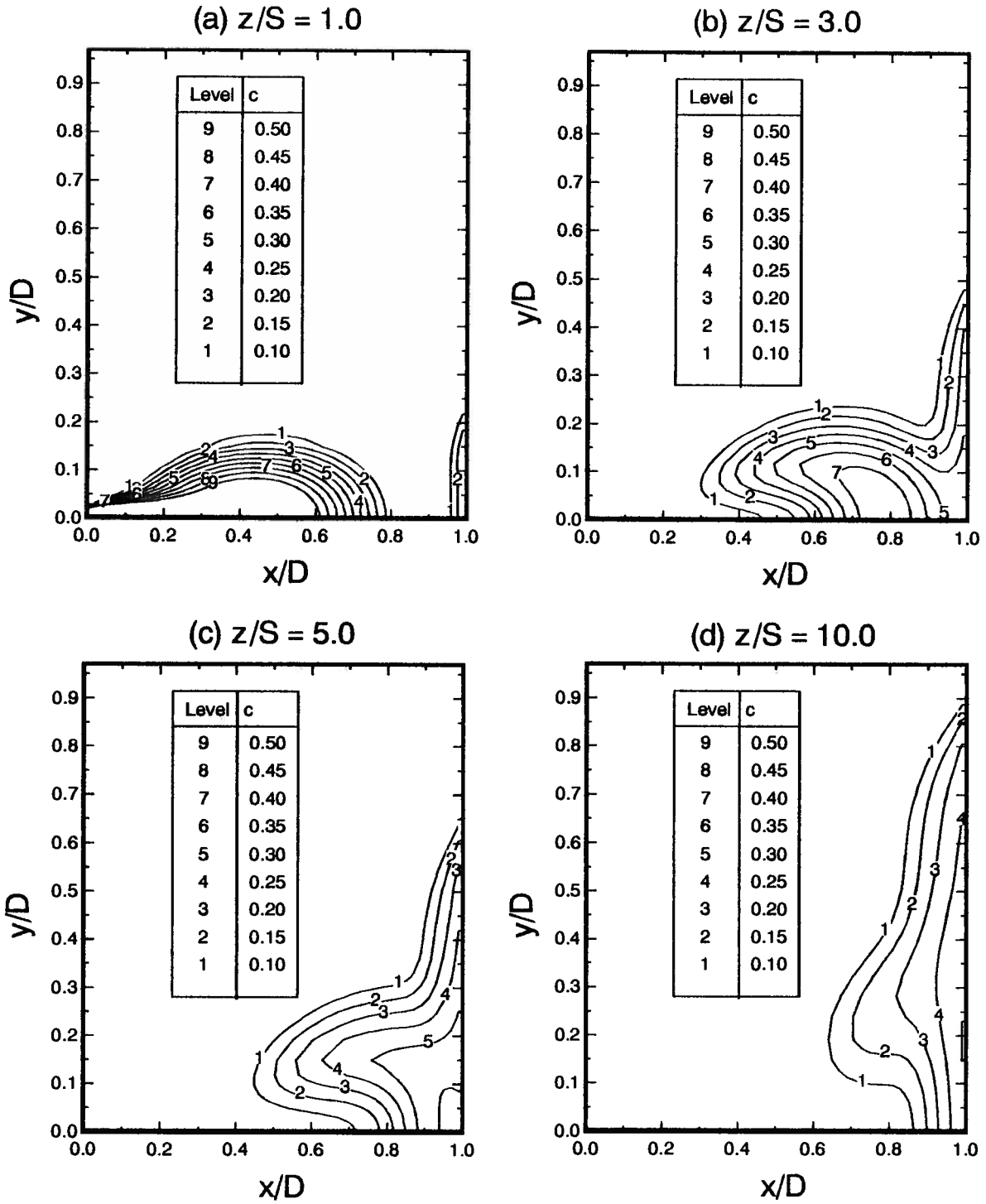

Figure 5.9: Jet concentration profiles for $R = 6$ and $D/S = 14$ (excluding buoyancy terms).

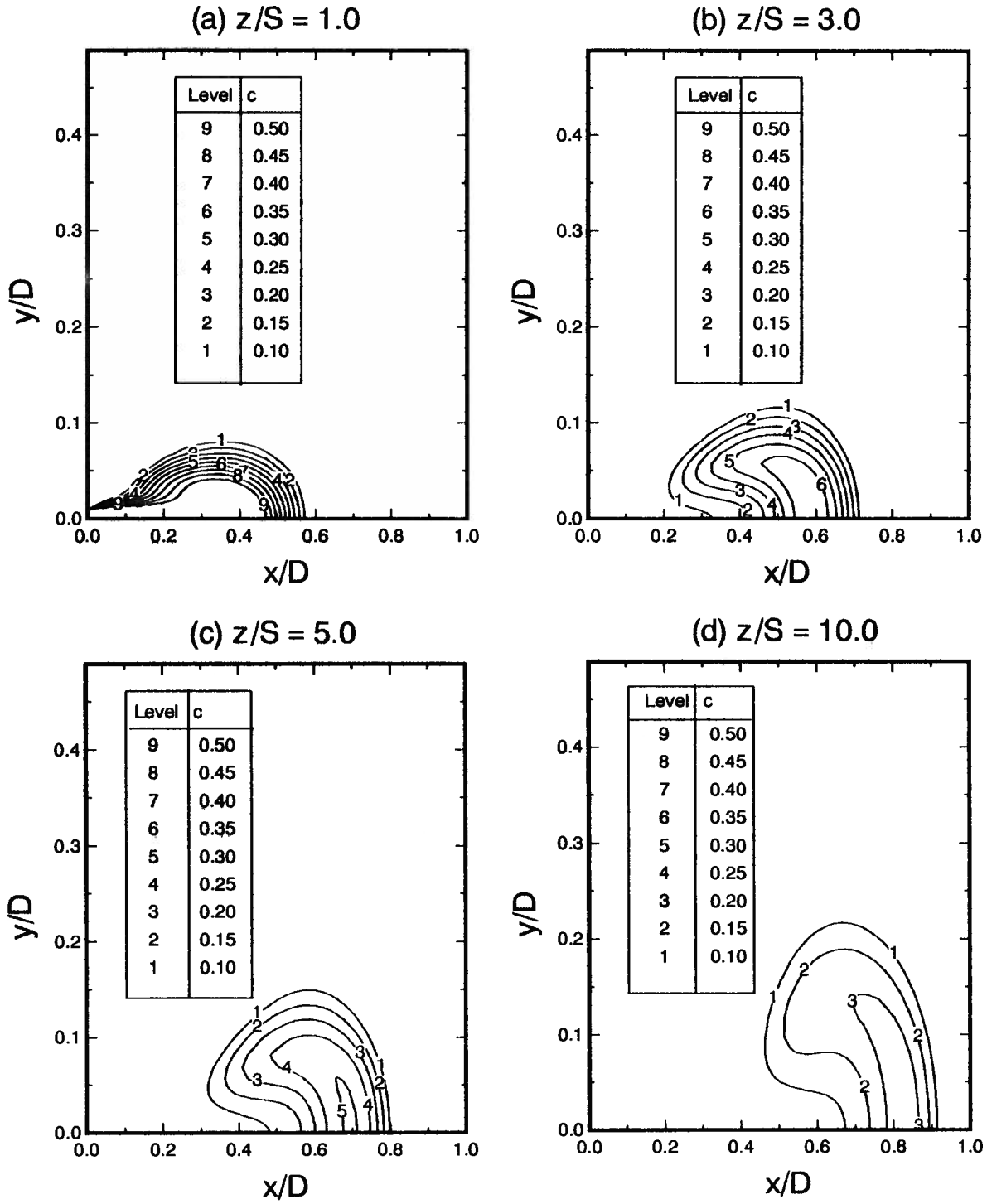

Figure 5.10: Jet concentration profiles for $R = 6$ and $D/S = 28$ (including buoyancy terms).

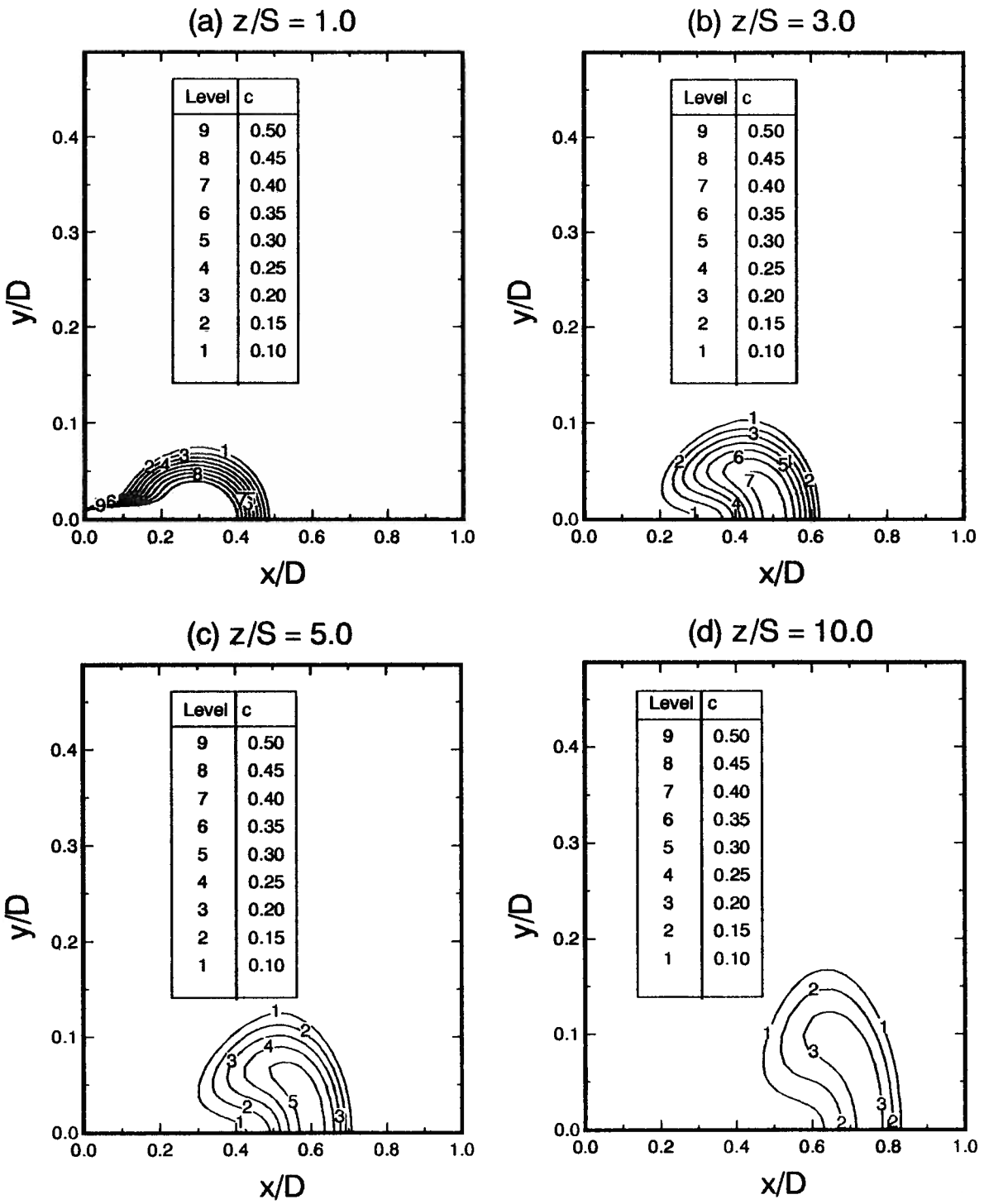

Figure 5.11: Jet concentration profiles for $R = 6$ and $D/S = 28$ (excluding buoyancy terms).

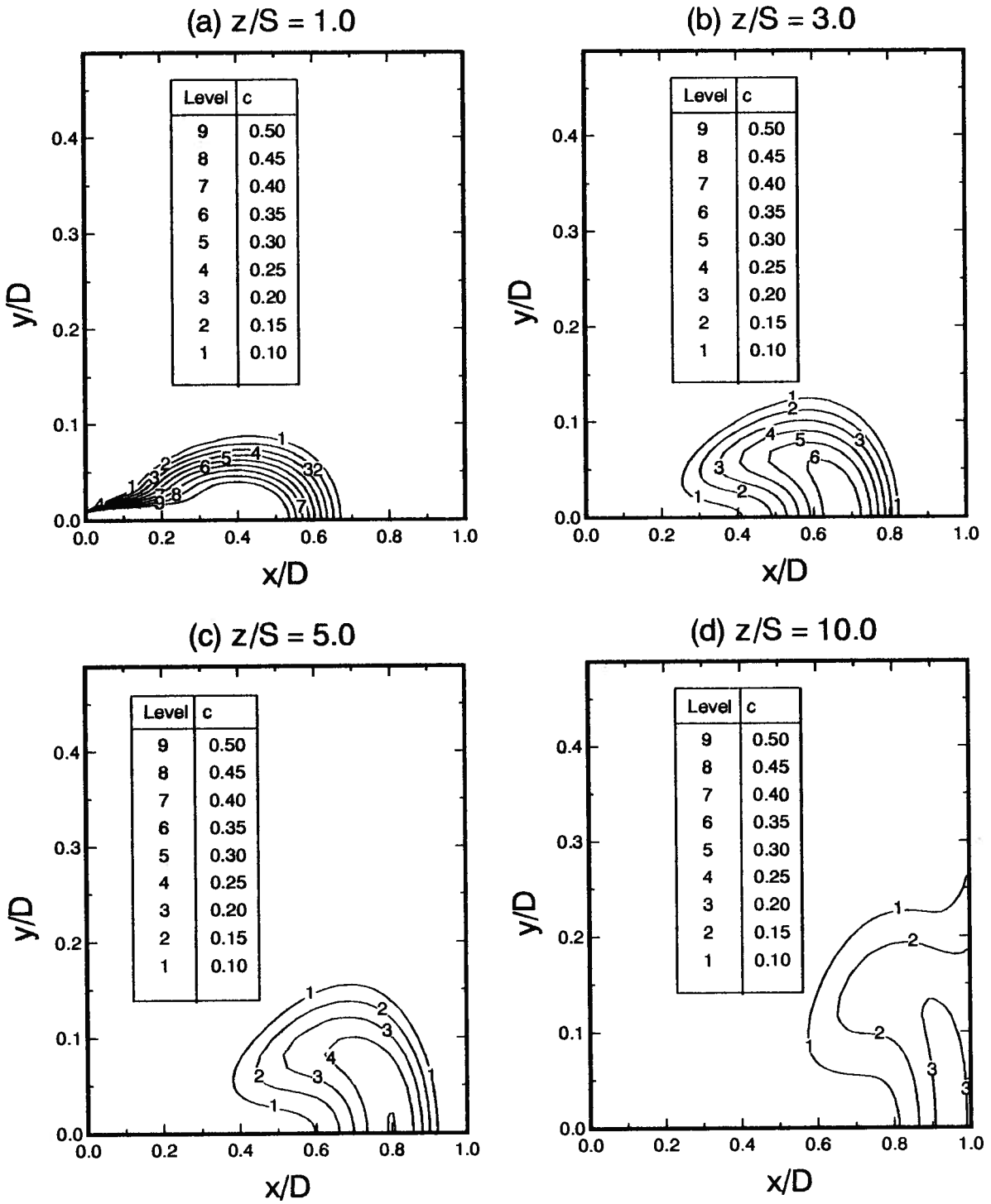

Figure 5.12: Jet concentration profiles for $R = 8$ and $D/S = 28$ (including buoyancy terms).

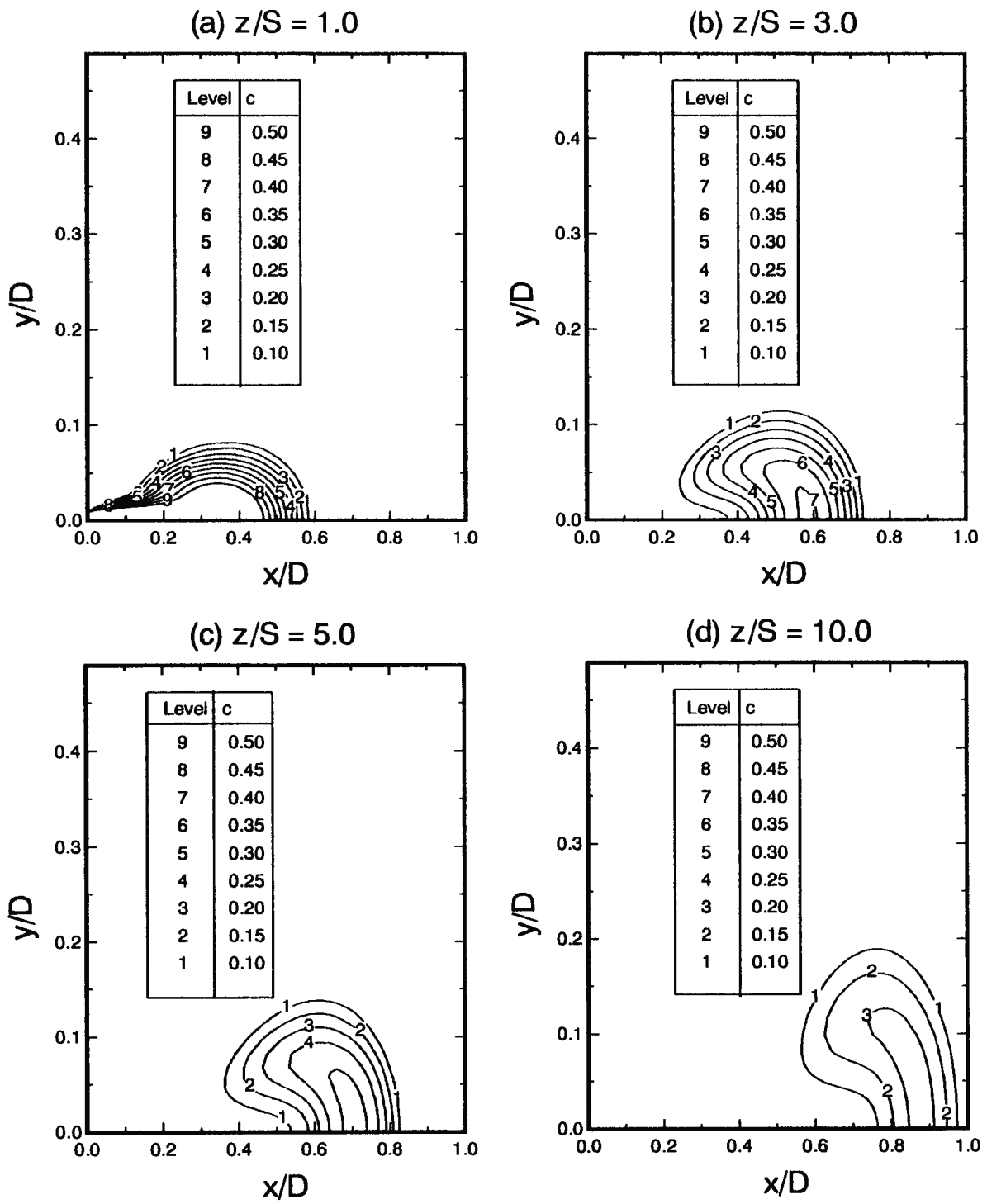

Figure 5.13: Jet concentration profiles for $R = 8$ and $D/S = 28$ (excluding buoyancy terms).

downstream at $z/S = 5.0$ and 10.0 as the jet loses its momentum the effect of buoyancy force increases. Generally the exclusion of the buoyancy force results in underprediction of the spread of the jet.

Due to the large cross-sectional area of the crossflow in comparison to the that of the jet, the total mass of the jet is about 20 times smaller than the mass of the crossflow. Since the probability density function method (described in Chapter 4) for quantifying the degree of mixing between the jet and the crossflow calculates the average mass over the flow cross-section, it smears the differences and does not provide much information in this case. Therefore, to describe the mixing and the spread of the jet in crossflow, a diffusion parameter K, suggested by Chao and Ho (1992), and defined as:

$$K = \frac{A_d}{A} \tag{5.71}$$

is used. Here A denotes the cross-sectional area of the flow field and A_d is the area affected by the jet fluid. To calculate A_d, jet concentration contours are employed here. Assume A_d represents the area enclosed by normalized concentration contour C at a certain value of C_d. In this investigation C_d is chosen to be 0.03. Figure 5.14 represent the streamwise development process of K for two ratios of $R = 6$ and 8 and for two values of $D/S = 14$ and 28. The jet with the highest R value and the smallest D/S yields the highest K development. For both values of D/S, as the value of R decreases the mixing and spread of the jet decreases. Excluding the buoyancy force results in underprediction of the mixing and spread of the jet. The results are also shown for the case when buoyancy is present as a force in the momentum equation but its effect in the turbulence equations is ignored. No significant changes in the value of K are detected.

To illustrate the effect of buoyancy force on convergence performance of the multigrid method, the convergence histories for the flows studied in this section are presented in Figure 5.15. The mass residues have been normalized by the total incoming mass flow

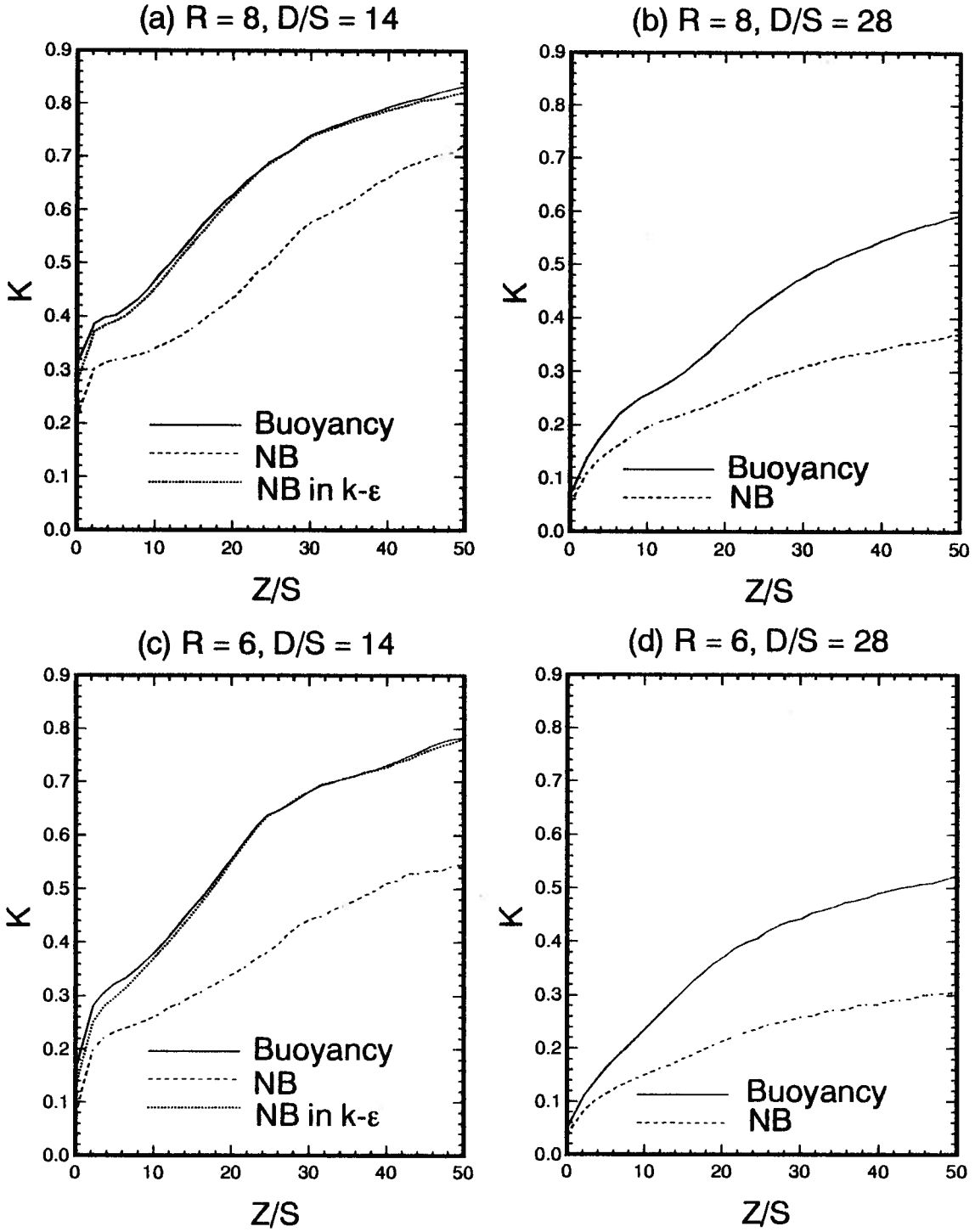

Figure 5.14: Effect of buoyancy on diffusion parameter or mixing.

from the crossflow and the jet. As Figure 5.15 shows, for the type of flow field considered in this section, the multigrid method has a very fast convergence. In all cases in less than four multigrid cycles the normalized mass error is less than 10^{-4} which is reasonably small. The deterioration of the performance of the multigrid solver due to the inclusion of the buoyancy terms is apparent from the above results. This is due to the coupling between the energy and the momentum equations.

5.2 Array of Three-Dimensional Jets

The geometry of the array of jets injected into the crossflow is shown in Figure 5.16. The geometric conditions used are similar to those used for the case of single jet. The spacing between the jets is $h = 5S$, which is similar to that of the tertiary air jets in the kraft recovery boiler. The flow conditions selected are the same as those for the case of the single jet. Here, however, calculations are done only for $R = 6$ and $D/S = 28$ (case 1 of Table 5.1).

Due to flow symmetry only a section of the domain which is confined between the plane passing through the jet center line and the plane passing through the middle of the space between the two adjacent jets needs to be calculated. The symmetry condition is imposed on these two lateral planes. The other boundary conditions used are the same as in the previous computation for the three-dimensional single jet. Calculations are done using a two level multigrid.

The effect of buoyancy force on the trajectory of the array of jets is presented in Figure 5.17. The jet trajectory is defined as the loci of the local maximum concentration points on the plane of symmetry through the jet center. The jet with buoyancy force has penetrated deeper into the crossflow and its trajectory is farther away from the injection wall than that of the jet without buoyancy force. The buoyancy force acting downward

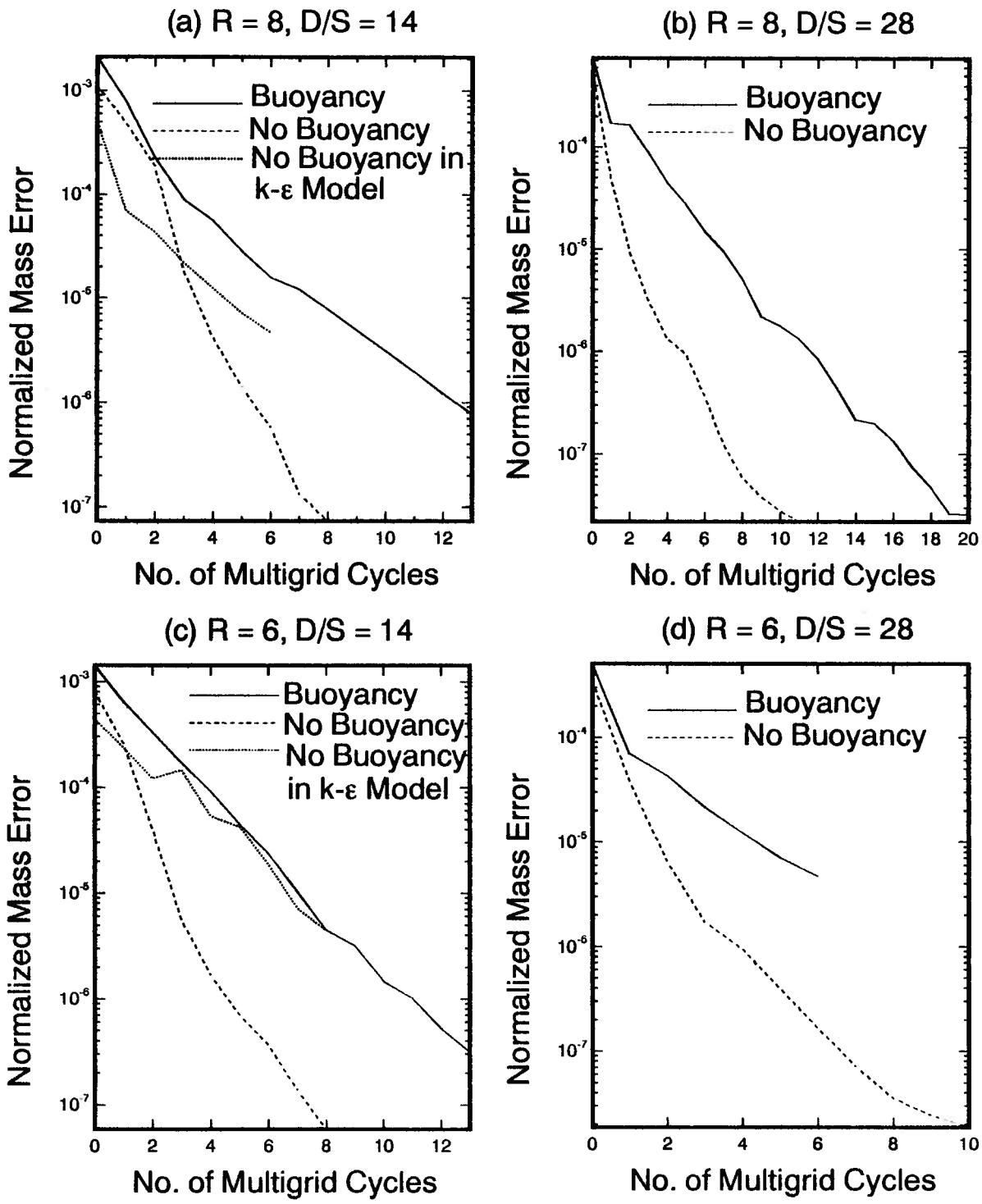

Figure 5.15: Convergence histories for different cases of R and D/S.

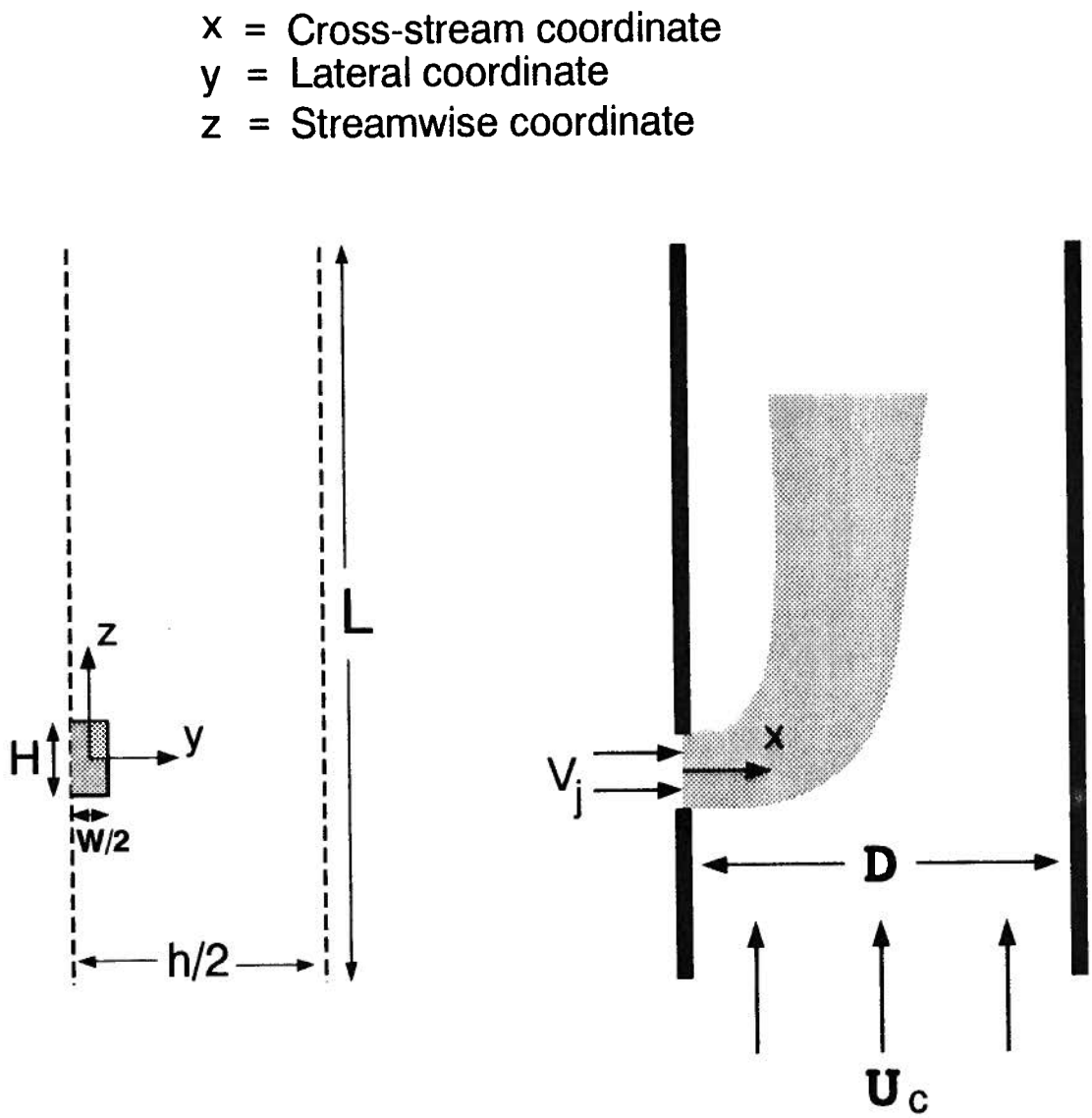

Figure 5.16: Schematic representation of array of jets into crossflow.

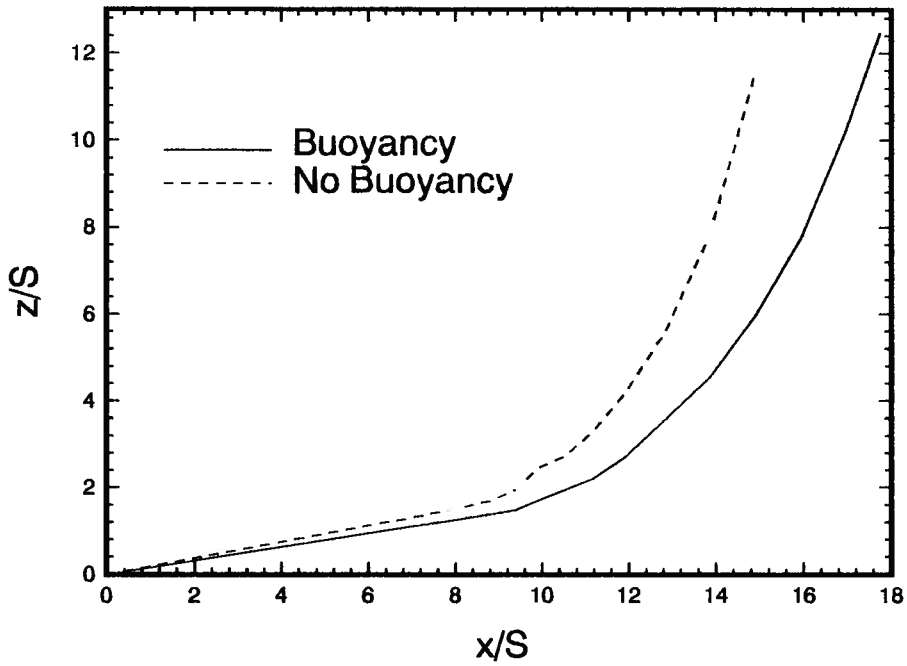

Figure 5.17: Jet fluid concentration trajectories.

against the upward crossflow, reduces the effect of the drag force exerted by the crossflow on the jet. Therefore the penetration depth of the jet with buoyancy increases and its deflection decreases.

Comparing the trajectory of the array of jets with that of a single jet in Figure 5.2(a), it is seen that the array of jets has a smaller penetration and its trajectory remains closer to the injection wall than that of the single jet. Considering the case of the single jet as an array of jets with very large jet spacing, it can be concluded that for an array of jets as the jet spacing decreases (from a very large spacing to $5S$) the jet penetration decreases. These results are in agreement with the experimental results of Kamotani and Greber (1974). This behavior can be accounted for by considering the vortex structure of well separated jets. Representing the jet in crossflow as a pair of counter-rotating vortices, two neighboring pairs of vortices will drive each other down towards the injection wall. This results in less penetration of each jet. In the experiments of Kamotani and Greber for a

range of jet spacings it is seen that for sufficiently close jet spacing (about $2S$ or smaller), however, the penetration of the array of jets increases as the jet spacing decreases and in the limit it reachs that of the two-dimensional jet. They explain that at close jet spacings the jets would start to interfere with the entrainment of crossflow fluid of their neighboring jets. This effect results in slower decay of the initial momentum flux of the jet. Consequently, for close enough spacing the jets maintain their momentum longer, and experience limited deflection.

It is also apparent from Figures 5.17 and 5.2(a) that the effect of buoyancy force on the trajectory of the single jet is less significant than is the case with the array of jets with $5S$ spacing. As was explained above, the interaction of the neighboring counter-rotating vortices reduces the momentum flux of the array of jets. As the momentum decreases the effects of buoyancy force become more significant.

The center-plane normalized velocity profiles are presented in Figure 5.18. The velocity profiles for both cases with and without buoyancy force are similar. However, in the far field ($z/D > 1.5$) the velocities are more uniform when the buoyancy force is ignored. Higher penetration and less deflection of the array of jets with buoyancy is apparent. Thus, once again, it is confirmed that the array of jets without the buoyancy force is effectively weaker. Therefore its deflection by the crossflow is more significant. For the flow conditions here no blockage effect of the crossflow by the array of jets is present.

The jet concentration profiles along the same longitudinal plane are shown in Figure 5.19. It is apparent that when the buoyancy terms are included in the calculations the array of jets has penetrated deeper into the crossflow and has spread out more.

The decay of maximum jet concentration along the jet concentration trajectory in the center plane is presented in Figure 5.20. The value of the jet concentration decreases continuously moving downstream from the jet. The decay rate of the jet concentration for cases with and without buoyancy terms are very similar. This implies that the buoyancy

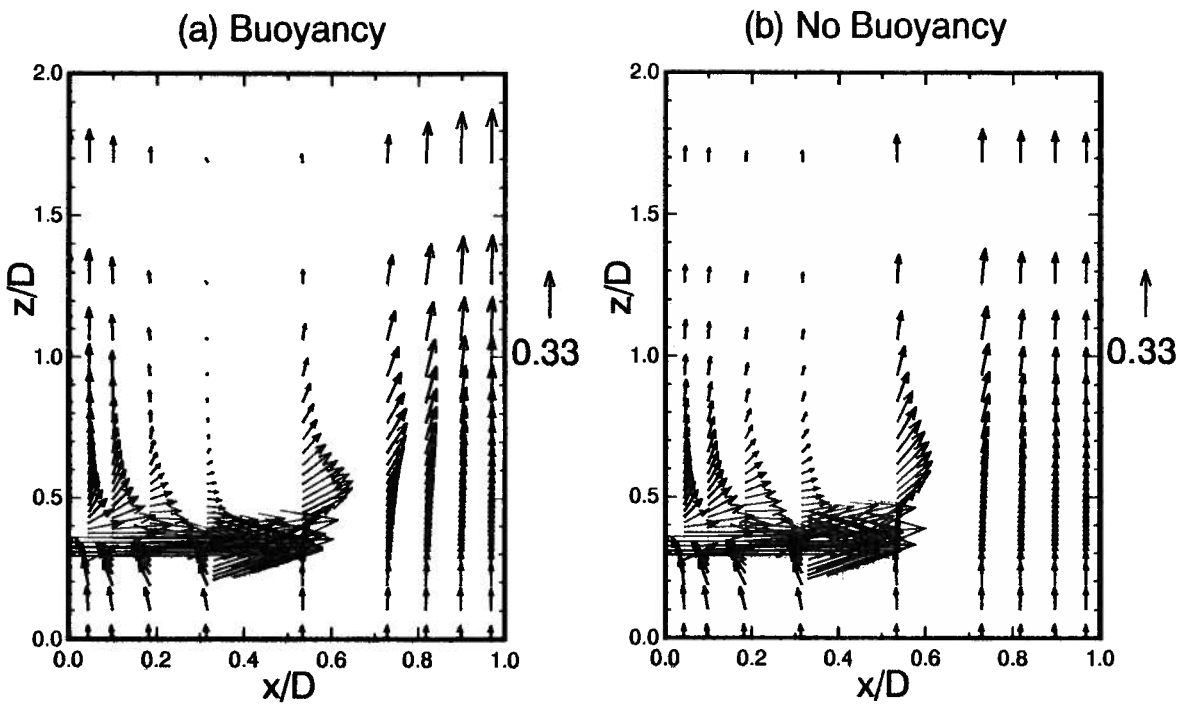

Figure 5.18: Velocity profiles along the jet center plane.

force plays a minor role in the mixing process for an array of jets.

The effect of buoyancy force on the mixing characteristics and the variations of jet structure can be better understood by looking at the jet concentration contours in Figures 5.21-5.22. The concentration contours are shown at four locations downstream of the jet. The concentration contours in cases both with and without buoyancy terms show similar behavior. At $z/S = 1$ the jet cross-section has a kidney shape due to the presence of the vortices. Moving downstream the jet moves to the central core of the flow and its cross-section becomes stretched and more slender. Farther downstream the vortices gradually expand over the whole cross-section and the jet losses its identity. The jet without the buoyancy terms remains closer to the injection wall. It forms a narrower cross-section which is more stretched in the lateral direction.

To quantify the mixing and the spread of the jet in crossflow, as in the case of the

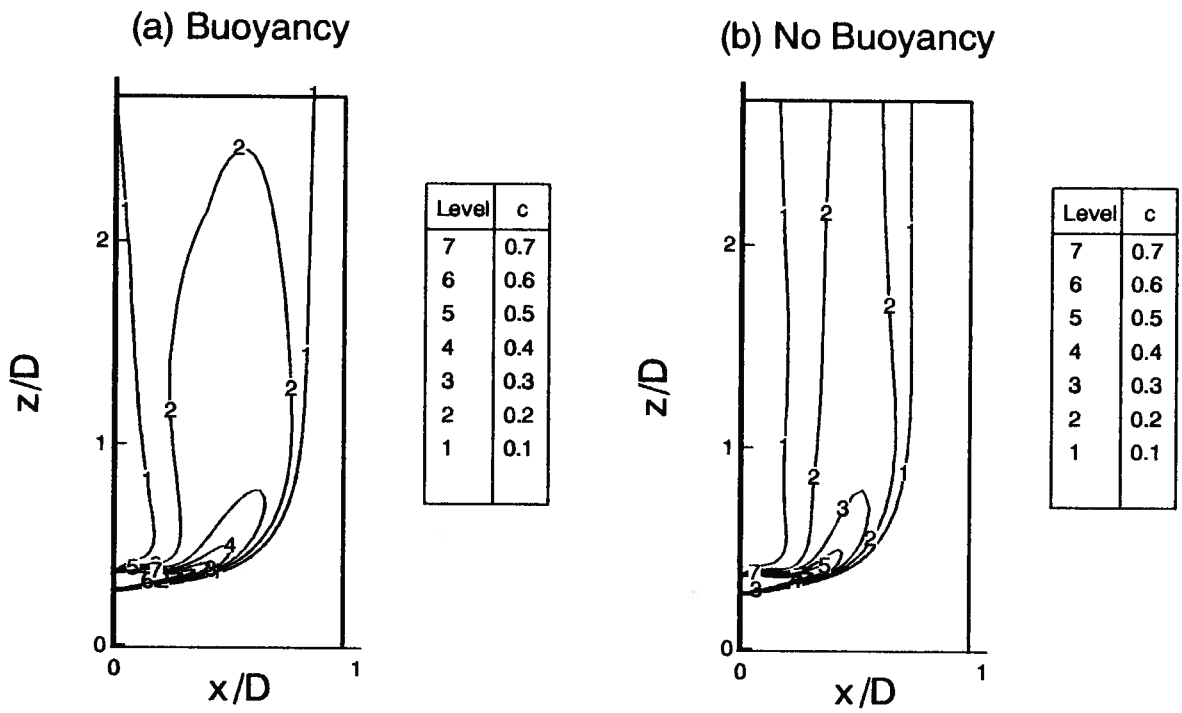

Figure 5.19: Jet fluid concentration profiles along the jet center plane.

single jet, we use the diffusion parameter, K. Figure 5.23 shows the variations of K at different downstream locations from the jet. As is seen in Figure 5.23, the buoyancy force enhances the mixing. When the buoyancy terms are ignored, the mixing and spread of the jet can be underpredicted. The differences are small in the near field where the momentum effects are still strong. Farther downstream, as the jet loses its momentum, the buoyancy effects are more pronounced.

To illustrate the effect of the buoyancy force on convergence performance of the numerical method, the convergence history of the flow studied in this section is presented in Figure 5.24. The mass residues have been normalized by the total incoming flow from the crossflow and the jet. For the type of flow considered here the multigrid method has a fast convergence. After four multigrid cycles the mass errors are less than 10^{-4}. When the buoyancy terms are not included in the calculations the mass errors decay

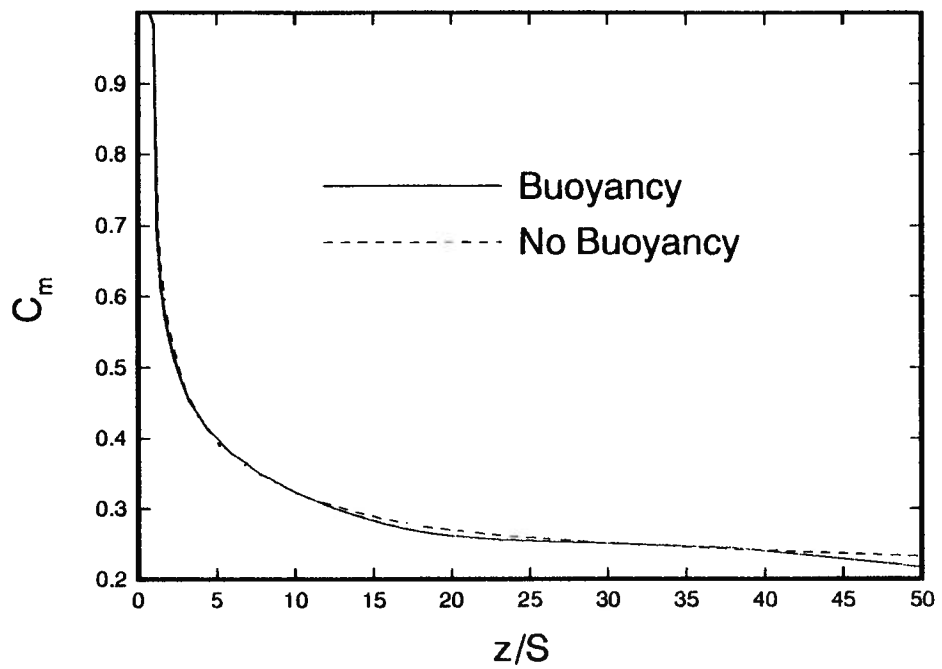

Figure 5.20: The decaying process of jet concentration along the jet concentration trajectory.

monotonically. The rate of this decay is faster than is the case when the buoyancy terms are included.

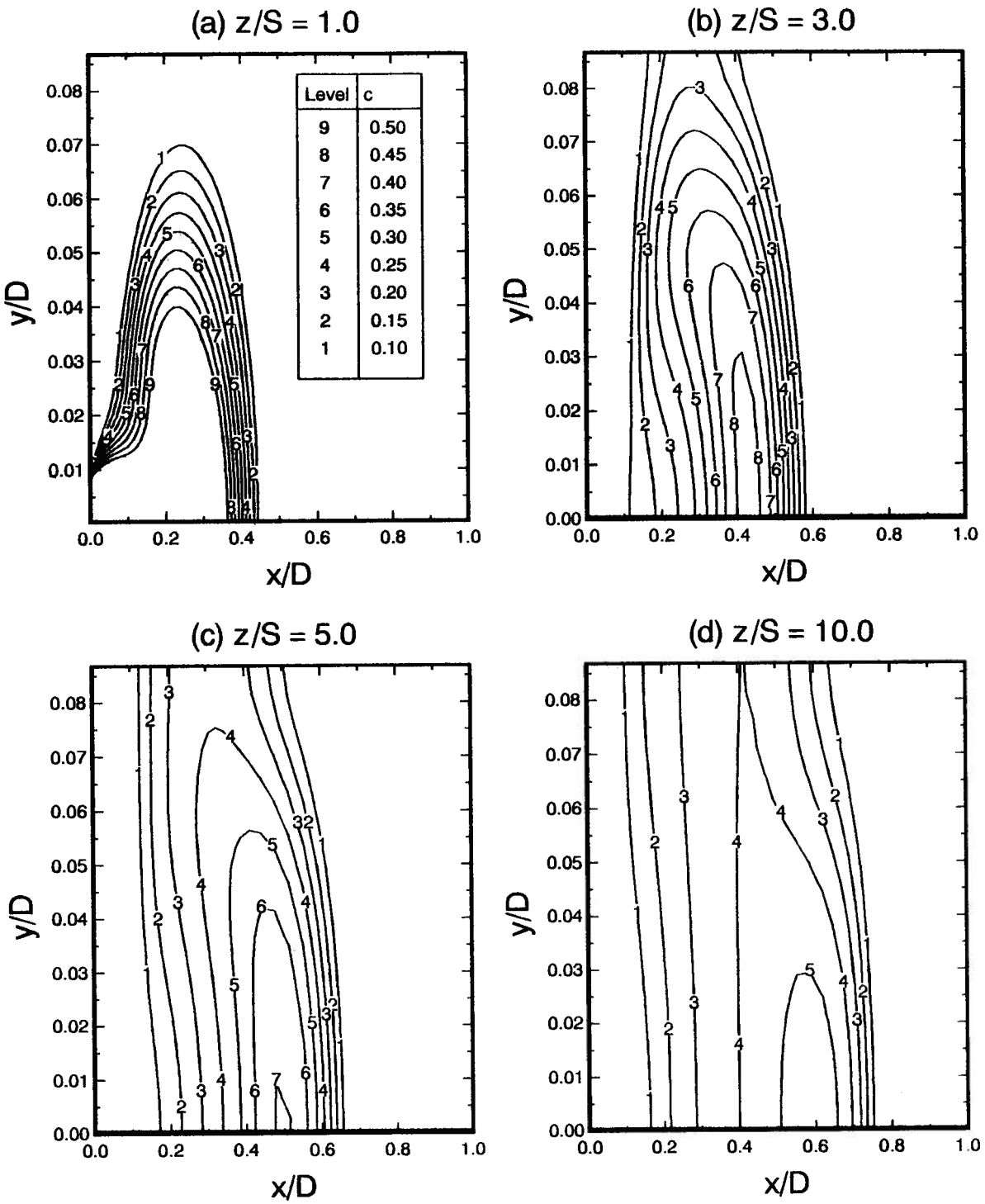

Figure 5.21: Jet concentration profiles (including buoyancy terms).

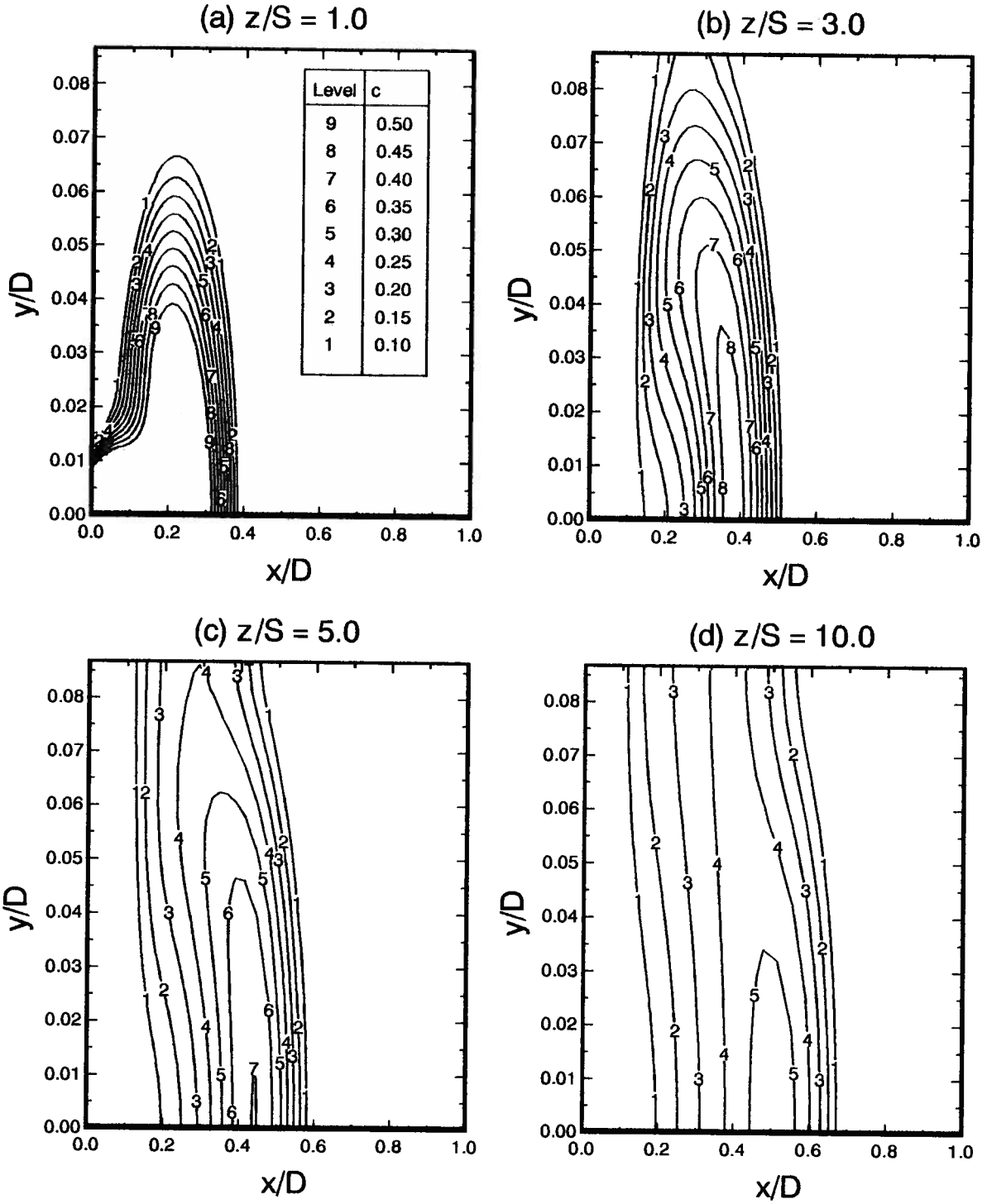

Figure 5.22: Jet concentration profiles (excluding buoyancy terms).

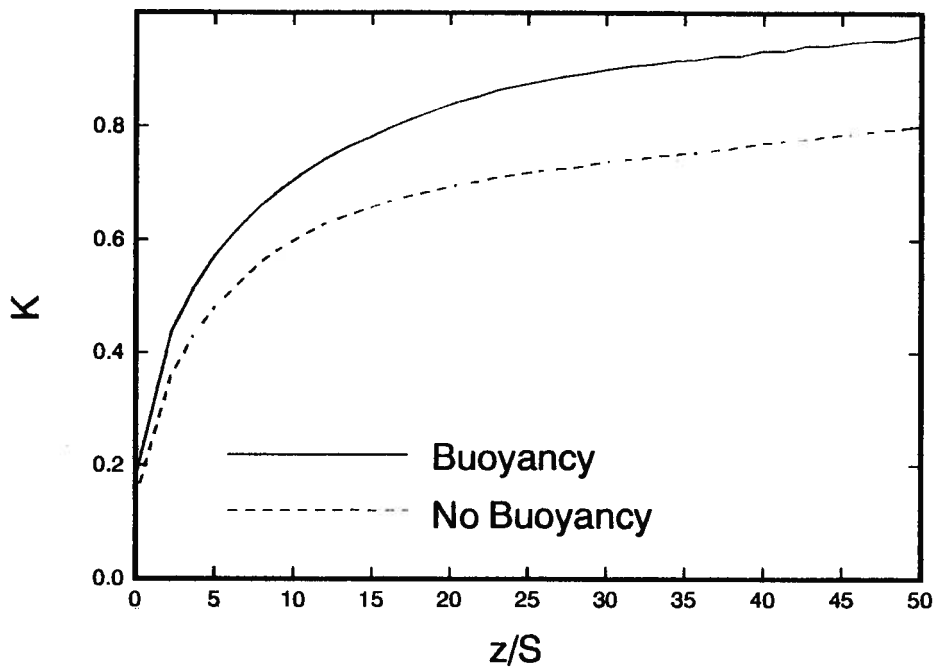

Figure 5.23: Effect of buoyancy on diffusion parameter or mixing.

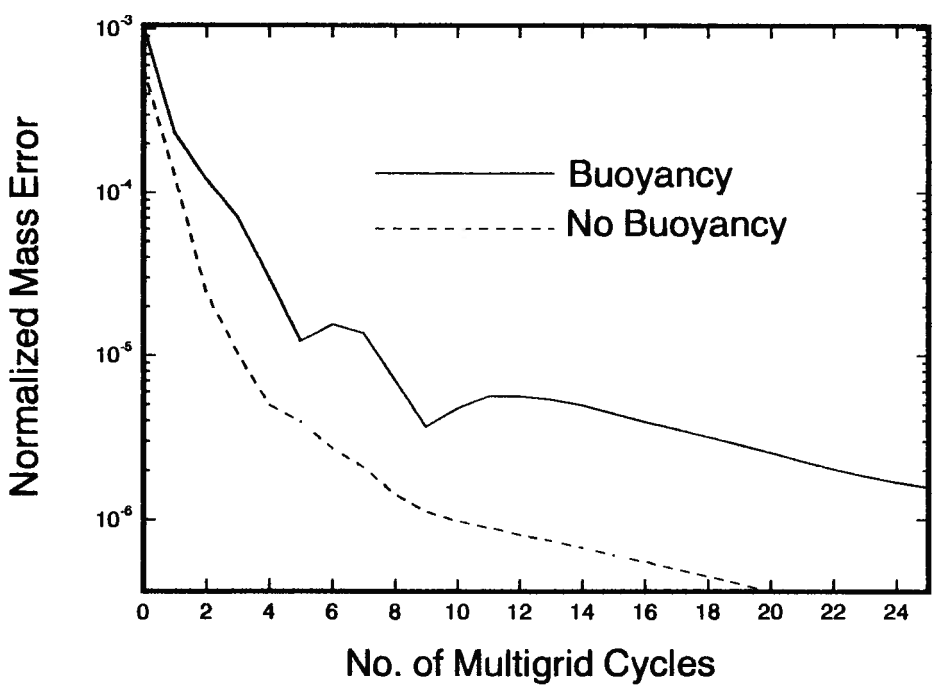

Figure 5.24: Convergence histories for array of jets.

Chapter 6

Effects of Buoyancy in the Kraft Recovery Boiler

The complex flow field inside the kraft recovery boiler is the result of many related processes. These include the injection of the air jets at three levels, namely, primary, secondary, and tertiary, the spray of the black liquor fuel, the presence of large temperature and density gradients due to the the combustion of organic materials, chemical reactions, radiation, and other heat transfer processes. Such flow fields are particularly difficult to visualize or to measure. The degree of mixing between the air jets and the combustible gases, and hence the rate of combustion inside the boiler, is determined by the flow field. This in turn affects the efficiency of the furnace and the emissions from the furnace. Therefore the fundamental need before the performance of the boilers can be improved, i.e. to increase efficiency and to reduce emissions, is to understand the flow field inside the boiler's cavity.

In the following section, we first present the boiler geometry used and the problem specifications. The results of our investigations into the effect of buoyancy force on the flow field inside the kraft recovery boiler are presented next.

6.1 Problem Description and Boundary Conditions

The boiler geometry simulated is shown in Figure 6.1. The flow domain is limited to the boiler cavity only. Therefore the bed and the bullnose are not modelled. Additionally, in order to obtain a good grid resolution, only a quarter of the boiler is simulated. However, full boiler geometry computations are necessary to allow for the investigation of the effect

of the interaction of the opposing jets. As is reported by Quick et al. (1991) at high jet to crossflow velocity ratios the interaction between the opposing jets is strong and can lead to flow unsteadiness.

The air from the jets is entering at a temperature of 400 K. The gas rising from the bed is modelled by imposing a crossflow at temperature of 1300 K. The velocity of the crossflow is calculated from the amount of the black liquor fired into the furnace. The primary jets are located on all four walls of the furnace and are modelled as slot jets. At the secondary level, there are three ports each on the west and east walls, and four ports each on the south and north walls. At the tertiary level, there are five ports each on the south and north walls, and there are no ports on the west and east walls. At each level, the size of the port, and the mass flow rate through it, are the same for all the air ports. At all levels the ports on the east walls are opposite to those on the west walls and the ports on the north walls are opposite to those on the south walls, preserving symmetry.

The height of the secondary ports is 0.4 m with an aspect ratio of 5.0. The tertiary ports are 0.8 m long with an aspect ratio of 5.0. The spacing between the tertiaries is about 2.0 m (5.5S). The primary jets enter at the velocity of 9.0 m/s. The secondary and the tertiary jets have the velocities of 68.0 and 19.0 m/s respectively. Therefore a total of 56 kg/s of air is introduced into the furnace, of which about 20% is introduced through the primaries, 45% through the secondaries and the balance through the tertiaries. A crossflow of uniform velocity of 0.77 m/s is assumed at the bottom. The locations, the sizes, and the air flow rates are such that symmetry exists along $x - z$ and $y - z$ planes. Therefore only one quadrant of the boiler is considered for numerical calculations. The furnace height is chosen to be 40 m. The primary, secondary, and tertiary ports are located 2 m, 3 m, and 8 m above the floor respectively.

The inlet turbulence kinetic energy k, and the rate of its dissipation ϵ, for the jet and the crossflow were assigned following the same guidelines given in Chapter 5.

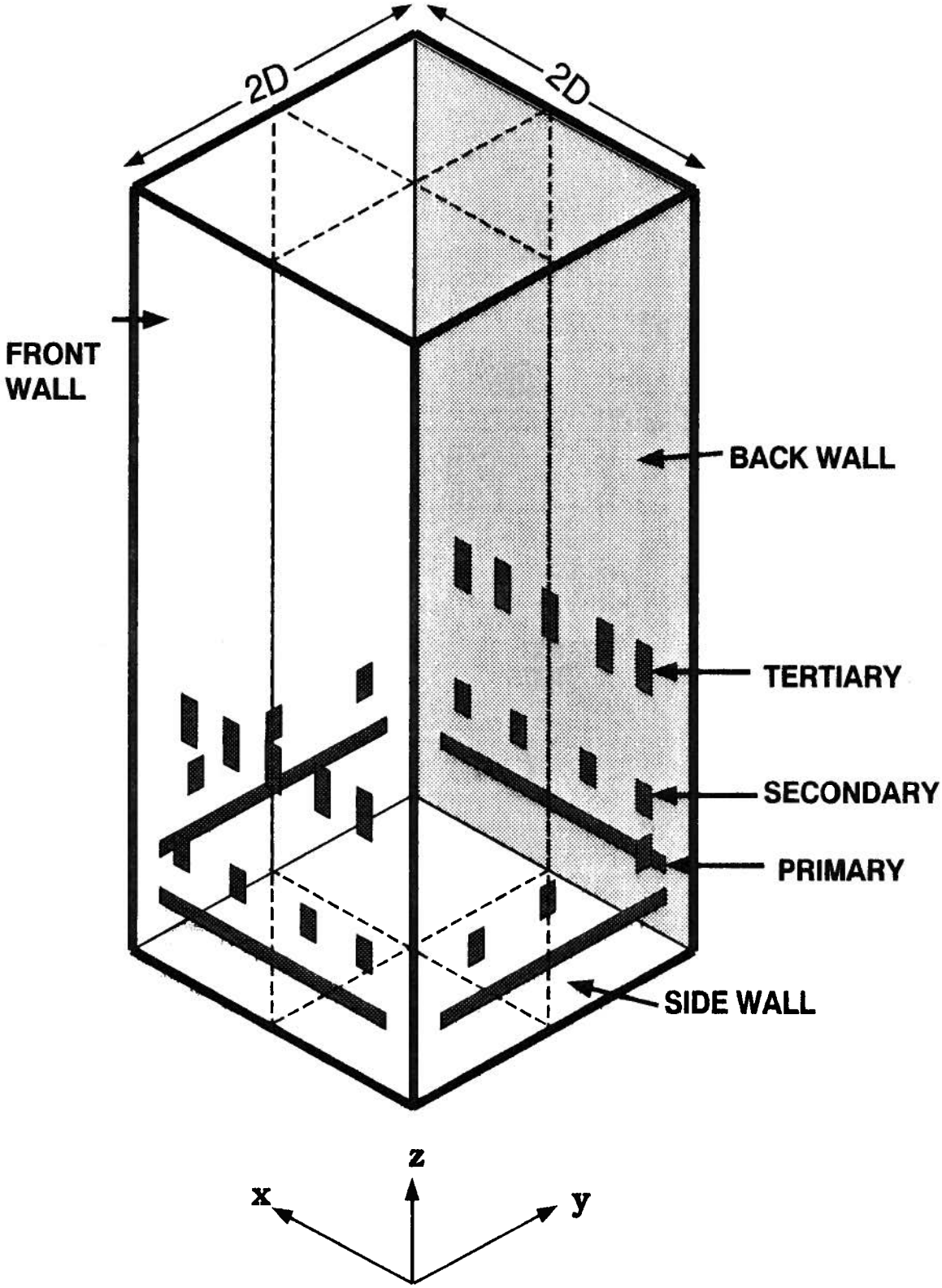

Figure 6.1: Schematic representation of the kraft recovery furnace.

Due to differences between the size of the air nozzles and the flow domain, the flow domain is divided into four segments. The grid distribution in each segment is dictated by the required grid resolution in that segment. The mesh generated is shown in Figure 6.2.

The processes of gas radiation and black liquor fuel combustion are also included in the calculation. The gas radiation is modelled using the discrete ordinates method. The walls are assumed to be gray with an emissivity of 0.8 and at the temperature of 1100 K. For radiation calculations, the bottom is assumed to be a gray wall with an emissivity of 0.8 and at the temperature of the crossflow. The details of the method and its implementation are given by Sabhapathy (1994).

Two combustion methods are considered. The first method includes the spray of the black liquor, the processes of drying, devolatilization, char burning, and volatile combustion. The heat sources/sinks calculated are then incorporated into the source term of the energy equation. The details of the model and its implementation are given by Matys (1994).

The second combustion model considered is an assumed distribution of heat sources. In both models the same amount of total heat is generated. However the heat source distributions are not similar. In the second model the heat source distribution is assumed constant over each cross section and varies only with the height. For $0 < z < 8m$, the heat source distribution is assumed constant, decreases linearly for $8m < z < 16m$, and is zero for $z > 16m$.

Comparing the flow fields obtained using different combustion models, the sensitivity of the flow field to the distribution of the heat sources can be evaluated. This is the topic of the next section.

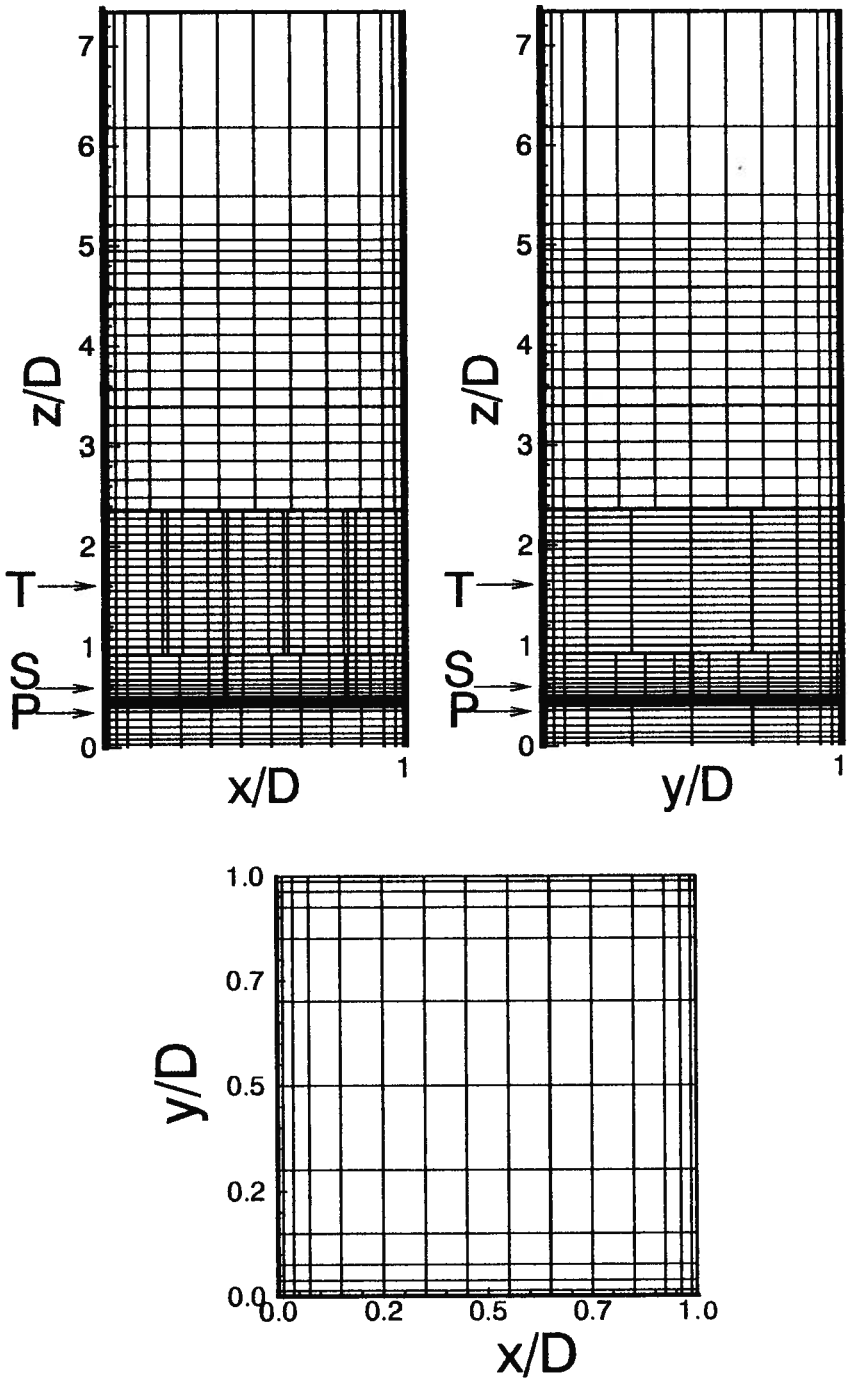

Figure 6.2: Mesh distribution for furnace simulations.

6.2 Results and Discussion

The results of predictions using the two different combustion models are presented in this section. In the case of each combustion model three flow situations were simulated. The calculations using the combustion model by Matys (1994) are referred to as the 'computed' heat source distribution. The calculations using the assumed heat source distribution model are referred to as the 'assumed' distribution of heat sources. As was explained in Chapter 4, in the figures the title 'Buoyancy' indicates that the buoyancy force in the momentum equation and the buoyancy terms in the $k-\epsilon$ turbulence equations are included in the calculations. The title 'No Buoyancy' indicates that the buoyancy force in the momentum equation and the buoyancy terms in the $k-\epsilon$ equations are not present in the calculations. The title 'No Buoyancy in $k-\epsilon$' indicates that the effect of the buoyancy force in the momentum equation is present, but the terms due to buoyancy force in the $k-\epsilon$ turbulence model are excluded from the calculations.

Due to the complexity and three-dimensionality of the flow field it is difficult to decide how to compare the flow fields. The contour plots of tracer concentration and vertical velocity in numerous vertical and horizontal planes covering the whole flow domain have been compared. Some of these results are presented here. In the figures the letters T, S, and P refer to the tertiary, secondary and the primary air jets respectively. The arrows indicate the height at which the jet enters the furnace.

The predicted tracer concentration contours in five vertical $y-z$ planes are presented in Figures 6.3 - 6.12. Figure 6.3, where $y-z$ plane is the symmetry plane ($x = 5m$), passes through the center of the mid tertiary air port. Comparing Figures 6.3(a) and (b), very little differences exist between the tracer distributions. This indicates that the effect of the buoyancy force on the turbulence modelling is not significant.

Comparing Figure 6.3(c) with Figures 6.3(a) and (b) it is shown that the penetration

of the mid tertiary air jet for the case with 'No Buoyancy' is smaller. This indicates that ignoring the effect of the buoyancy force in the momentum equation results in under prediction of the jet penetration. Similar results were seen in the case of the single jet and the row of jets (Chapter 5).

Similar trends are apparent in Figure 6.4 for the case of the assumed combustion model. This indicates that the effect of the buoyancy force on the flow field is not altered by modifying the combustion model. A slightly more uniform tracer concentration distribution is predicted in the region above the tertiary air nozzles with the assumed combustion model.

The vertical planes $y - z$, where $x = 4$ and $2\ m$, pass through the center of the secondary air nozzles. The contour plots of the tracer concentrations in Figures 6.5-6.8 indicate that the penetration of the secondary jets is not altered significantly by the buoyancy force. This is expected as these jets enter at very high velocity ($V_j = 68m/s$). Therefore the jet momentum controls the jet behavior entirely.

Figures 6.9-6.12 show the contour plots of the tracer concentrations in vertical planes $y - z$ where $x = 3$ and $1\ m$ respectively for both combustion models. Both these planes pass through the center of the tertiary air nozzles. Considering the penetration of the tertiary air jets, it can be seen that in the case without buoyancy the jet penetration is larger. This effect is particularly significant in the vertical $y - z$ plane where $x = 1$ m. This effect is the opposite of the effect seen in the case where $x = 5\ m$ (symmetry plane) and the results obtained in the case of the single jet and a row of jets study (Chapter 5). The difference is due to the presence of the side wall. The tertiary jet in the vertical plane $y - z$ where $x = 5\ m$ is far from the wall, therefore its behavior is not significantly influenced by it. Also, in the case of the single jet studies the wall effect was absent. Our calculations in Chapter 5 showed that the buoyancy force increases the spread of the jet. Therefore, where the jet is close to a wall, as it spreads it can

interact with the side wall. As a result of this interaction the jet losses its momentum and therefore has smaller penetration. When the buoyancy force is excluded the jet spread is underpredicted, and therefore its interaction with the wall is less significant. The impact of the side wall on the jet with no buoyancy force is less pronounced. This results in larger penetration of the jet.

Figures 6.13-6.16 show the contour plots of the tracer concentration in vertical planes $x - z$ where $y = 5$ and 2.5 m, for both combustion models respectively. These planes pass through the center of the secondary air nozzles. Again it is apparent that the buoyancy force does not affect the penetration of the secondary and the primary air jets significantly. This is true for both combustion models used.

Figures 6.17-6.18 show the contour plots of the tracer concentration in vertical plane $x - z$ where $y = 3.75$ m, for both combustion models. This plane is located half-way between the two adjacent secondary air nozzles. Slightly higher concentrations of the tracer are predicted in the region above the secondaries when the buoyancy force is ignored.

The contour plots of the normalized vertical velocity in vertical $y - z$ planes for values of $x = 5$, 4, 3, 2, and 1 m are presented in Figures 6.19-6.26. Figures 6.19-6.20, where $x = 5$ m, (the symmetry plane), show the presence of a core of high velocity gases flowing upward in the center of the furnace formed above the secondary air nozzles. The size of this region and the magnitude of the velocities in this core are under predicted when the buoyancy force is excluded from the momentum equation. Ignoring the buoyancy terms from the turbulence model does not alter the velocity field significantly. Similar trends are present for both combustion models. In the same plots the presence of a region of downward flow below the primary air nozzles is apparent. The size of this region is not affected by the buoyancy force. Similar trends are shown in Figures 6.21-6.24 for cases of $x = 4$ and 3 m.

In Figures 6.25 and 6.26, where the vertical plane $y - z$ passes through the center of the first tertiary air nozzle adjacent to the wall ($x = 1\ m$), the region of downward flow in the center of the furnace is no longer present. However a region of downward flow has formed downstream of the tertiary air jet in the case where the buoyancy force is excluded. In this plane, as was shown before, the jet penetration when the buoyancy force is excluded is larger than the case with buoyancy. Due to larger jet penetration a larger recirculation region downstream of the jet has formed. The size of the upgoing region is smaller for the case without the buoyancy force. These trends are the same for both combustion models.

As was shown the effect of the buoyancy force on the turbulence did not alter the flow field significantly. Therefore in the following section the flow fields obtained by the calculations where the buoyancy terms in the turbulence equations are omitted, are not presented. Additionally the flow field predictions using the assumed heat source distribution are not shown. As we have seen the effect of the buoyancy force on the flow field was not altered significantly by using different combustion models.

The predicted normalized vertical velocity fields, with and without the buoyancy force, at various heights of the furnace for the computed heat source distribution are shown in Figures 6.27 and 6.28. The gas flow field below the secondaries has a complex pattern because of the interactions of the crossflow, the flow due to primary jets and the downward flow due to the secondary jets (Figure 6.27, $z = 1.0$ to $2.5\ m$). Below the primaries, the flow is upward at locations slightly away from the walls and downwards near the center. Near the primaries, the size of the region of downward flow has increased. Through the secondaries ($z = 3.0\ m$) the flow is mostly upward. Because of higher momentum, the secondaries penetrate much further than the primaries. Part of the air from the secondaries flows downward in the center of the furnace (Figure 6.27, $z = 1.0$ to $2.5\ m$). This downward flow loses its momentum as it nears the bottom of the furnace because it

combines with the upward flow from the bottom, and flows upwards slightly away from the walls. Above the secondaries, because of the interactions of the flow due to both the secondaries and the tertiaries, the flow is mainly upwards in the center and downwards near the walls (Figures 6.27 and 6.28). Above the secondaries a high velocity region has formed in the center of the furnace. Above the tertiaries the flow is mostly upwards in the center, forming a central 'core'.

The gross features of the flow fields are nearly the same for both cases with and without buoyancy force. However, the size of the core of the upwards flow in the center is slightly under predicted when the buoyancy force is omitted from the calculations. The velocities in the central core of the upwards flow are lower for the case without buoyancy force than the case with buoyancy. As was seen in the case of the single jet for the horizontal jet which is heavier than the crossflow, the buoyancy force opposes the drag force exerted on the jet by the crossflow. Therefore the jet with buoyancy behaves as a stronger jet and with higher momentum flux. Consequently for the case with buoyancy, the local velocities are higher and a larger central core of the upwards flow is formed.

The predicted tracer concentration contour plots in horizontal planes $x - y$ at various heights of the furnace, for calculations with and without buoyancy force, are presented in Figures 6.29 and 6.30. Below the secondaries the buoyancy force has no significant effect on the tracer concentration. At $z = 2.0\ m$ (Figure 6.29) the limited penetration of the primary air jets is apparent. At $z = 3.0\ m$ the small influence of the buoyancy force on the penetration of the secondary air jets is shown. Above the secondaries, higher concentration of the tracer is present in calculations without the buoyancy force. This is due to the deeper penetration of the tertiary jets in this case. Stronger penetration of the tertiaries is apparent at $z = 8.0\ m$ in Figure 6.30.

The shape of the isotherms in the gas is influenced by the local flow field. These are

presented in Figures 6.31 and 6.32. The flow due to the primaries affects the temperature field only near the walls where the primaries are located. Below the secondaries, because of the downward flow from the secondaries, the temperature at the center of the furnace is slightly lower than that away from the center (Figure 6.31, $z = 1.0$ to $2.5\ m$). At the secondary level, sharp horizontal temperature gradients exist due to the strong penetration of secondary jets (Figure 6.31, $z = 3.0\ m$). Above the secondaries ($z = 5.0$ and $6.0\ m$) the gas temperature field is more uniform in a horizontal plane except near the walls, where strong temperature gradients exist. The gas temperature in the center increases with the height between the secondaries and tertiaries. A similar increase in the gas temperature at the center has been observed experimentally (Adams et al., 1988). At the level of the tertiaries, the shape of the isotherms is influenced by the tertiary jets ($z = 8.0\ m$). Beyond the tertiaries the gas temperature at the center decreases with height. Strong horizontal temperature gradients exist at all heights and are more pronounced at the air injection levels.

The shape of the isotherms for cases both with and without buoyancy force is similar. Above the tertiaries the predicted gas temperature for the case without the buoyancy force is slightly lower at each point and its distribution is more uniform. This is due to the deeper penetration of the tertiary jets in this case.

The mixing between the jet fluid and the crossflow inside the furnace cavity is calculated using the methodology described in Chapter 4. The results for both combustion models and cases with and without buoyancy terms in momentum and turbulence equations are shown in Figure 6.33. Here δ_z represents the degree of mixing (Equation 4.70) and the z/D is the dimensionless height of the furnace. A value of δ_z of one indicates 100% mixing. As the results show, the buoyancy terms in the turbulence model do not alter the degree of mixing significantly. Excluding the buoyancy force from the momentum equation slightly under predicts the degree of mixing in the region between the tertiaries

and the secondaries. The variations of the degree of mixing at different heights in the furnace is similar for both combustion models.

In summary, it is apparent that the effect of the buoyancy force on the gas flow field inside the kraft recovery furnace is small and localized. In addition the trends observed are similar using the two different combustion models, involving a fixed total amount of heat generated, but differing distribution of heat sources.

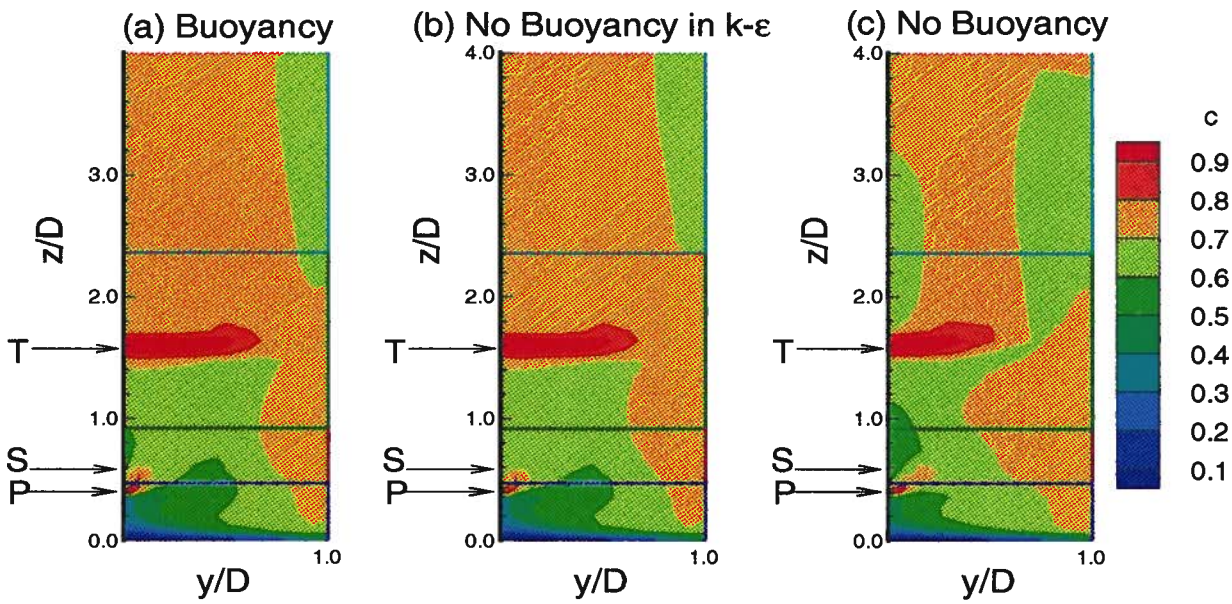

Figure 6.3: Concentration contours, $x = 5m$, computed heat source distribution.

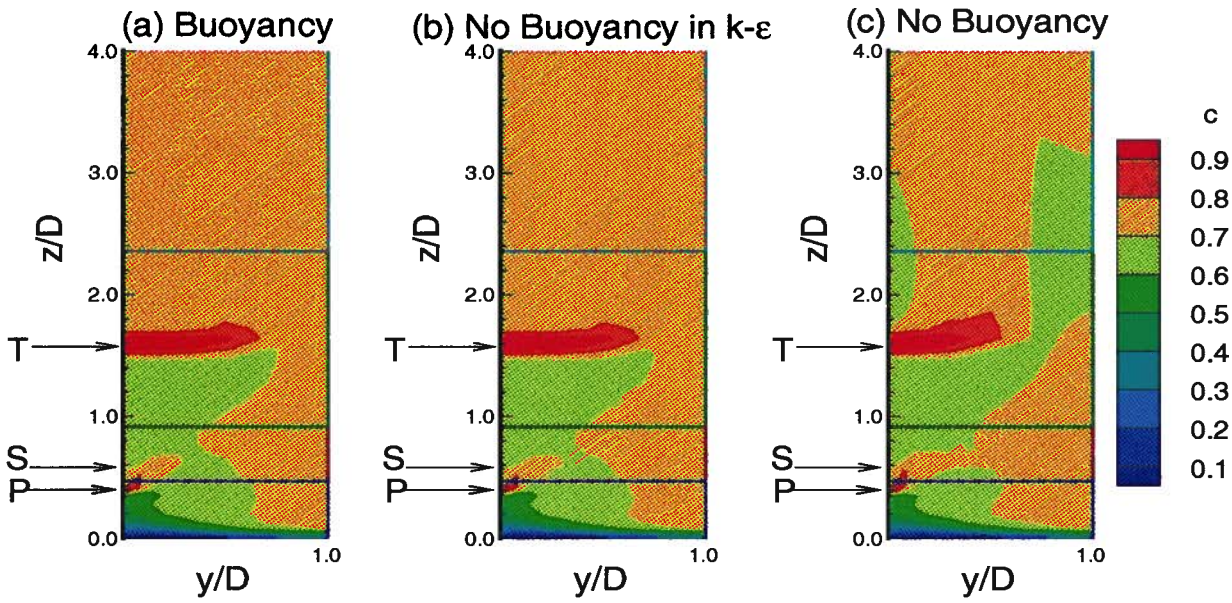

Figure 6.4: Concentration contours, $x = 5m$, assumed heat source distribution.

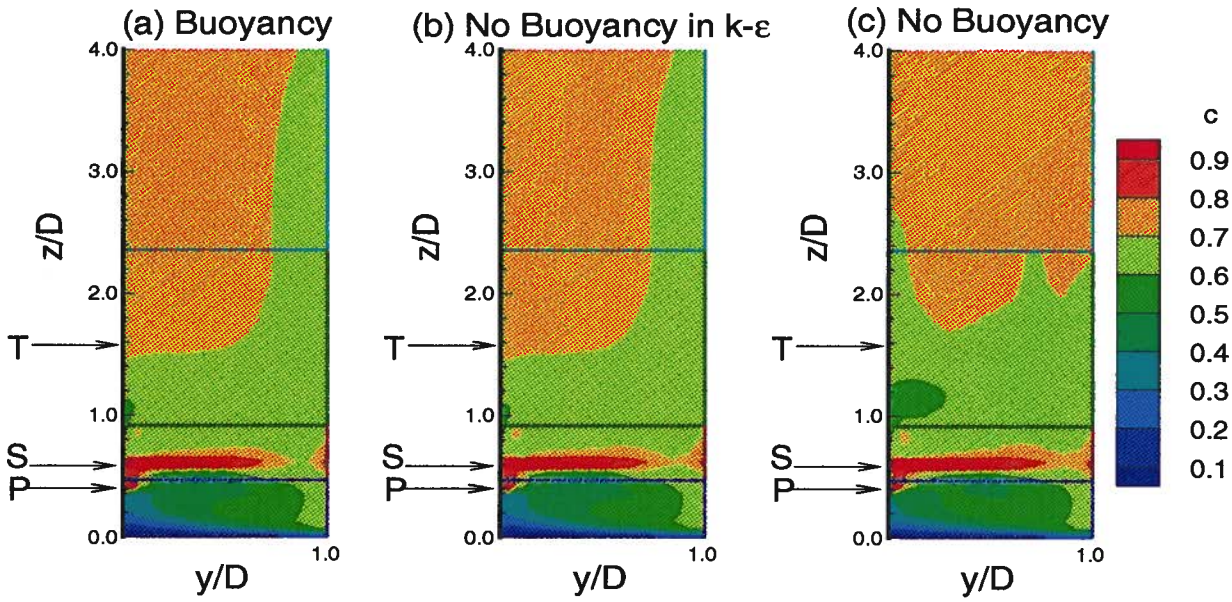

Figure 6.5: Concentration contours, $x = 4m$, computed heat source distribution.

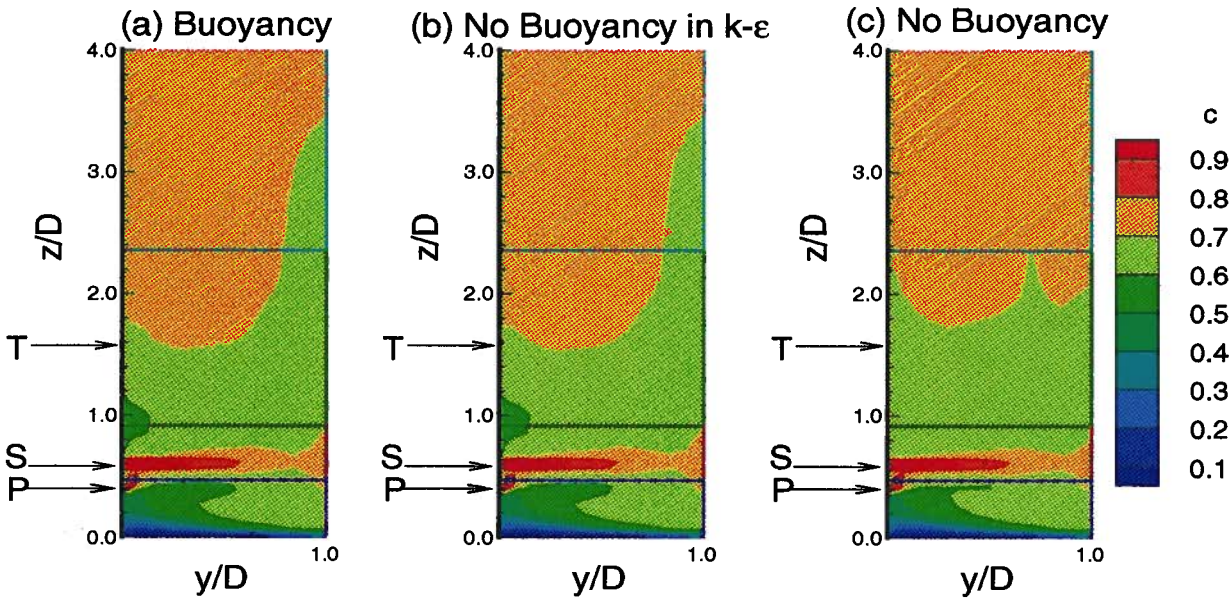

Figure 6.6: Concentration contours, $x = 4m$, assumed heat source distribution.

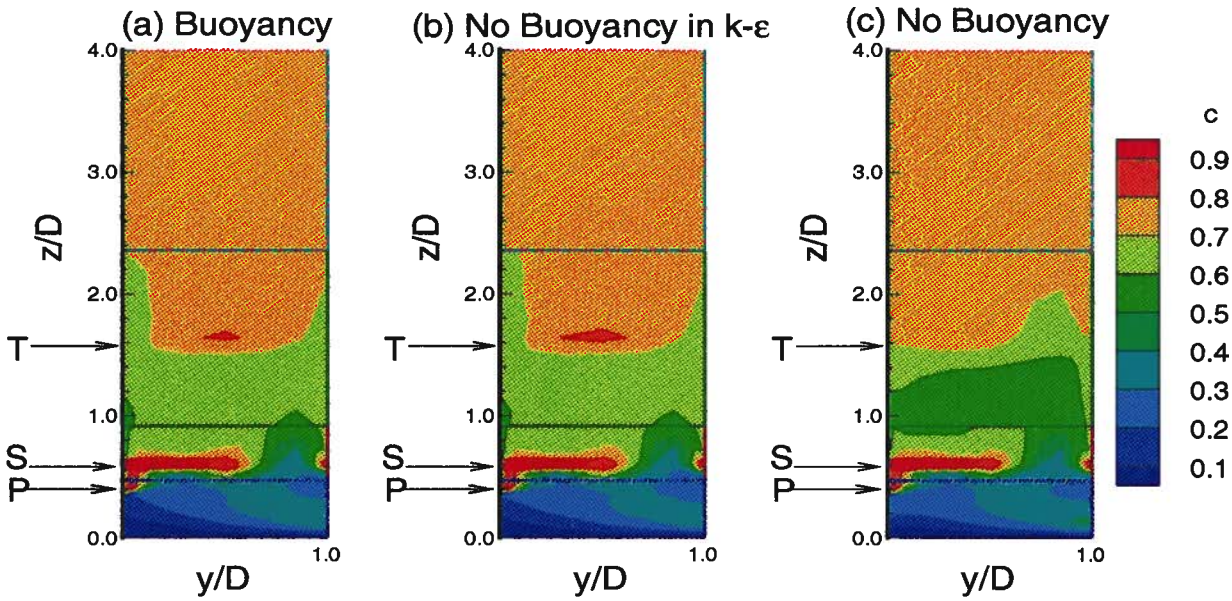

Figure 6.7: Concentration contours, $x = 2m$, computed heat source distribution.

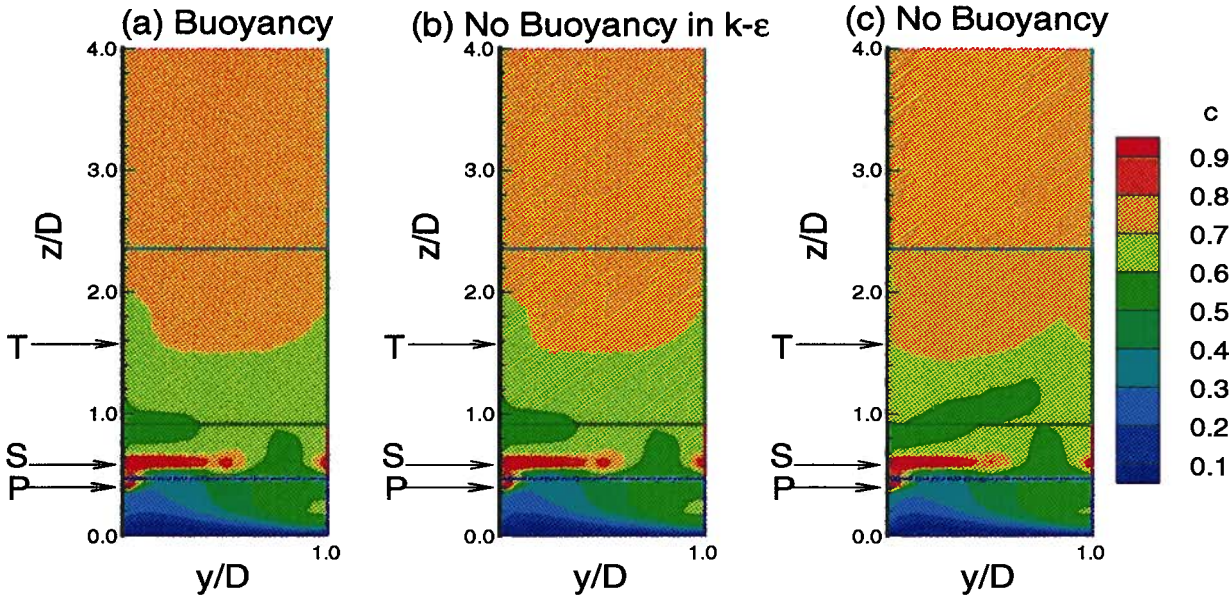

Figure 6.8: Concentration contours, $x = 2m$, assumed heat source distribution.

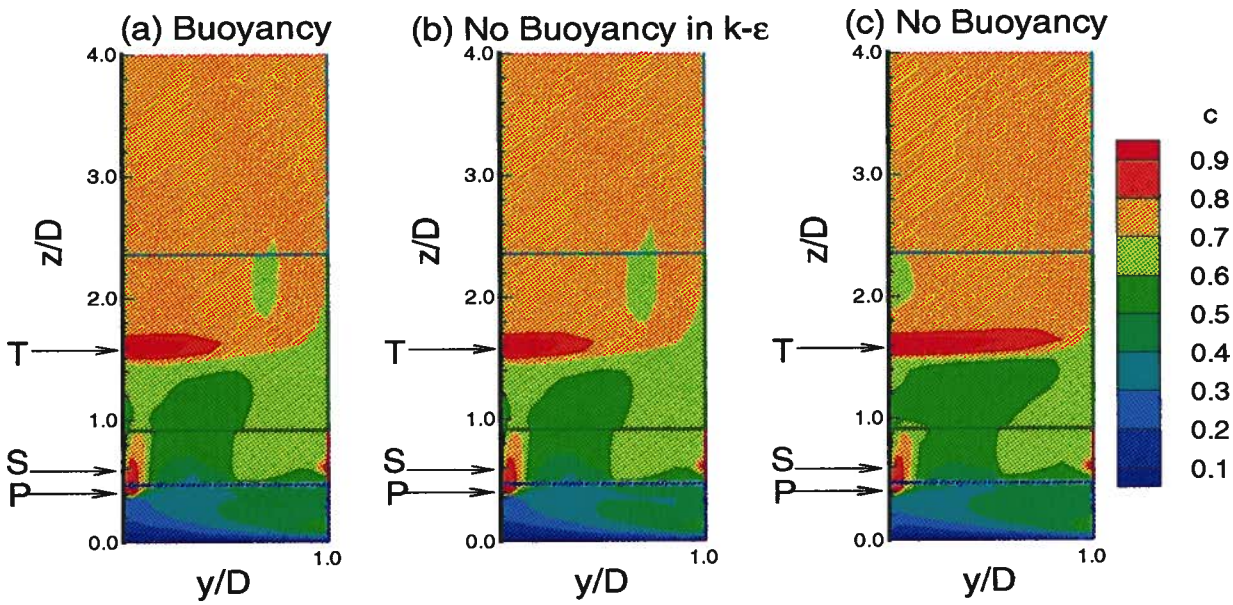

Figure 6.9: Concentration contours, $x = 3m$, computed heat source distribution.

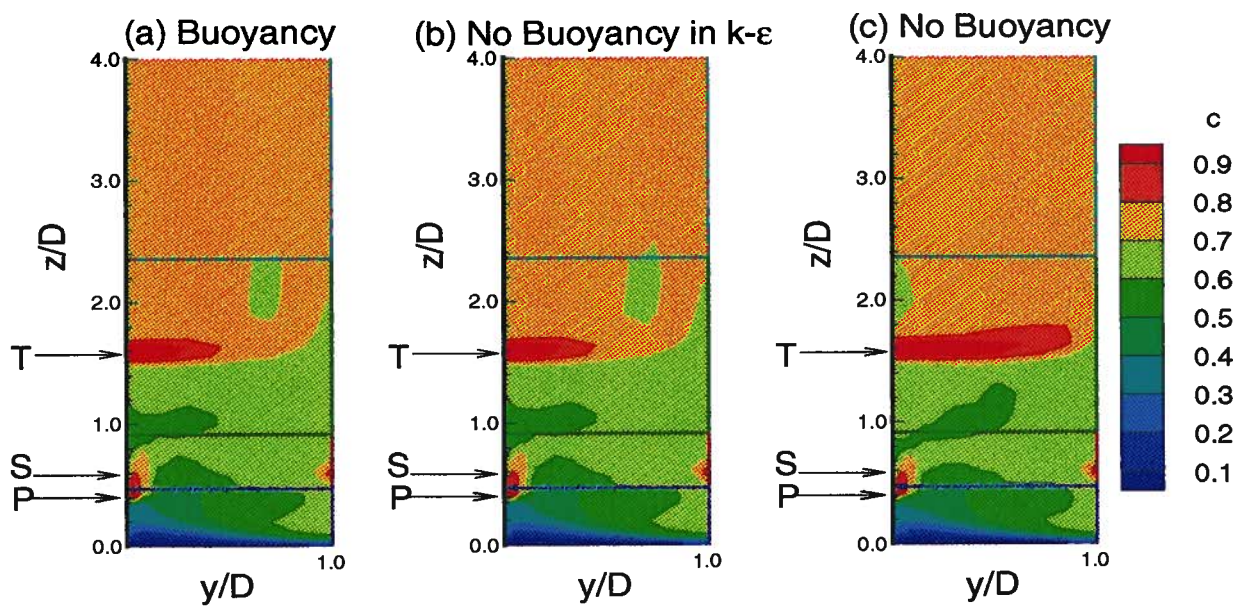

Figure 6.10: Concentration contours, $x = 3m$, assumed heat source distribution.

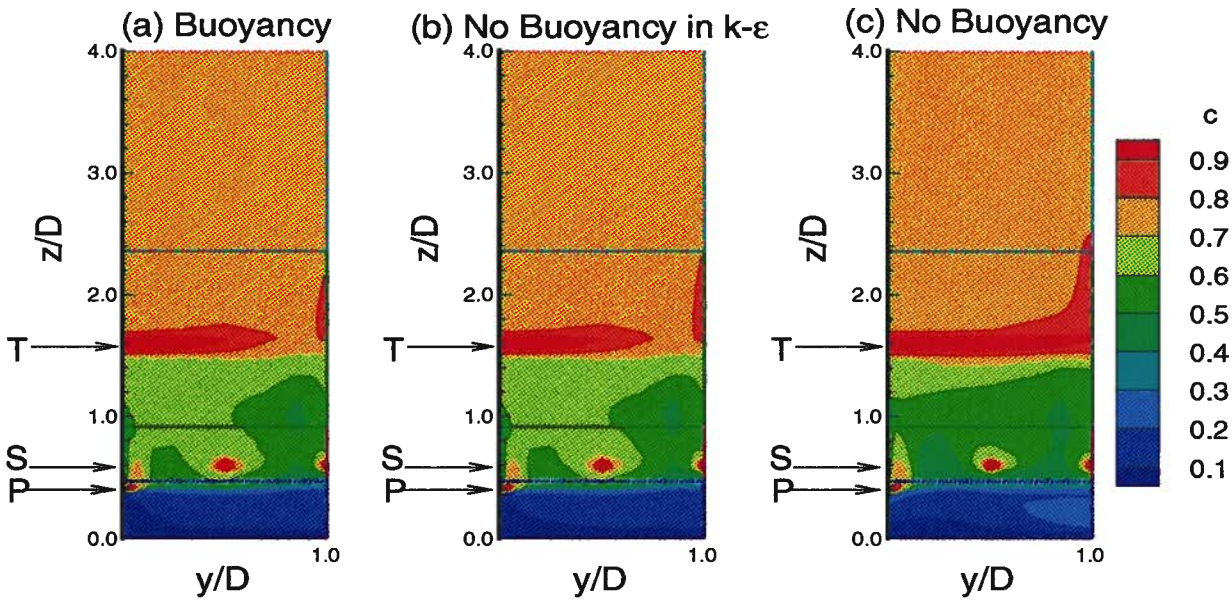

Figure 6.11: Concentration contours, $x = 1m$, computed heat source distribution.

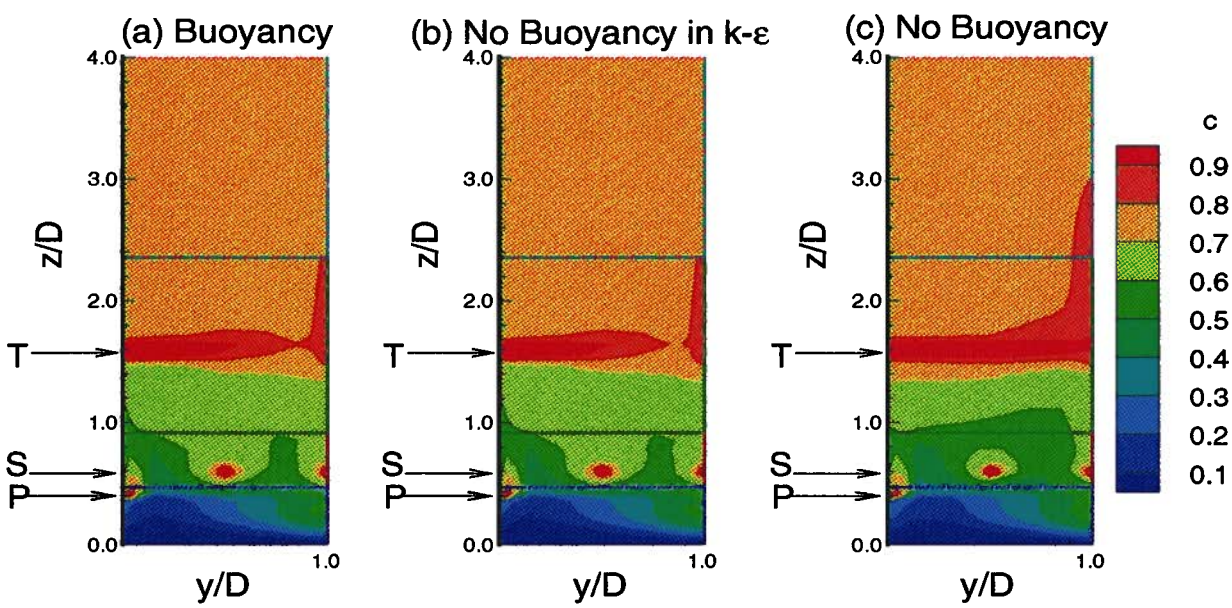

Figure 6.12: Concentration contours, $x = 1m$, assumed heat source distribution.

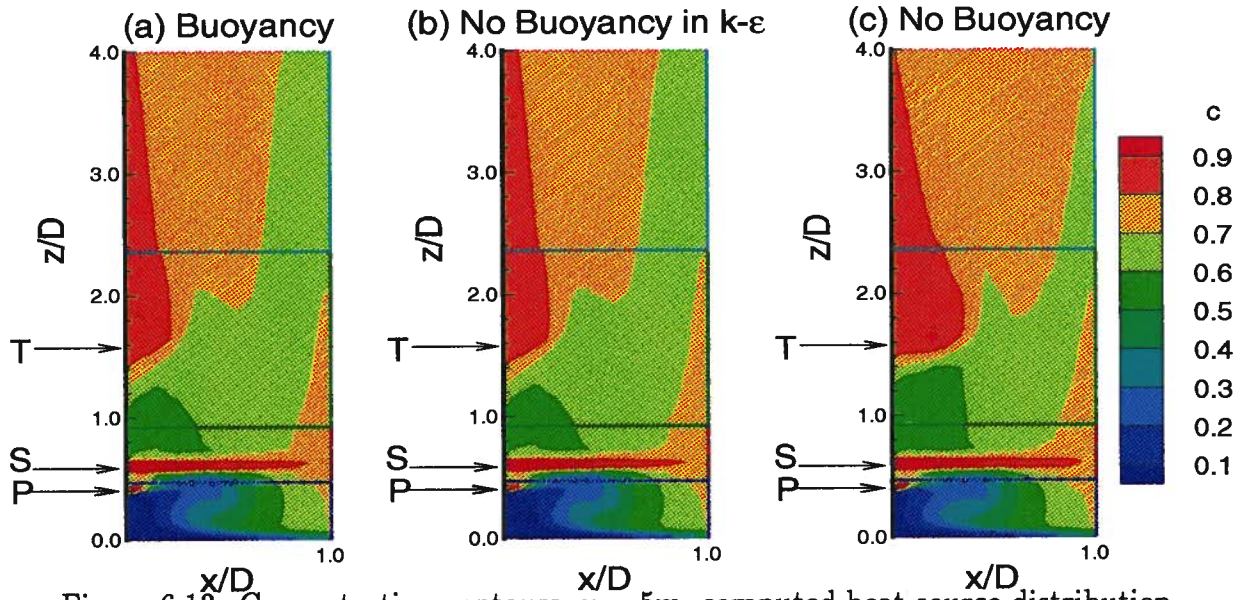

Figure 6.13: Concentration contours, $y = 5m$, computed heat source distribution.

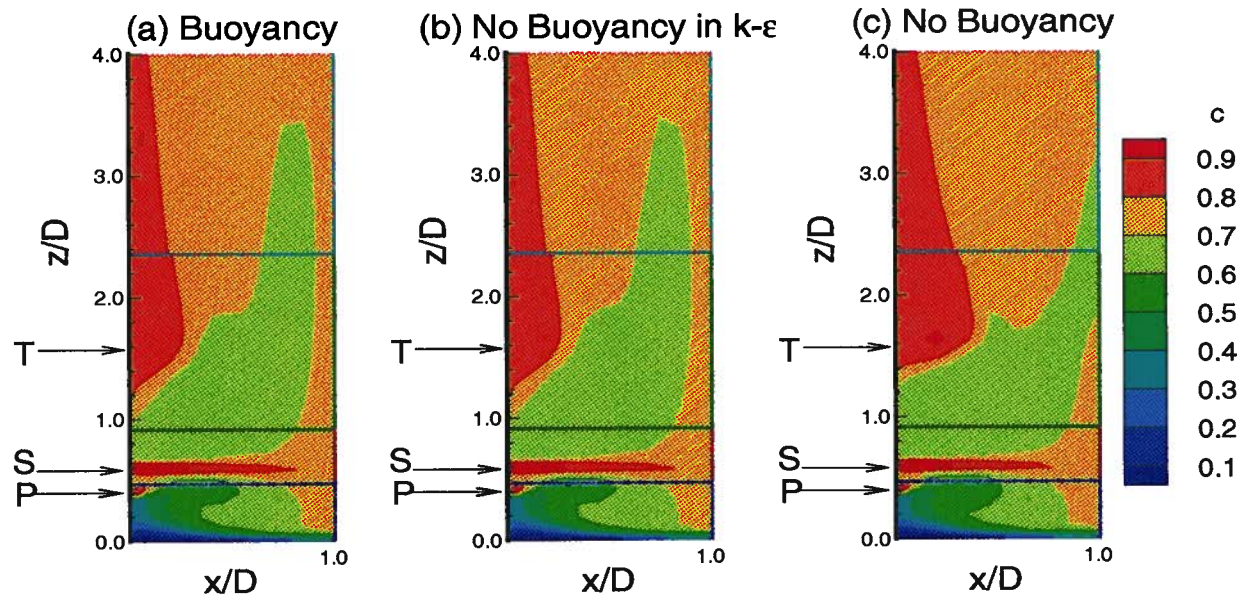

Figure 6.14: Concentration contours, $y = 5m$, assumed heat source distribution.

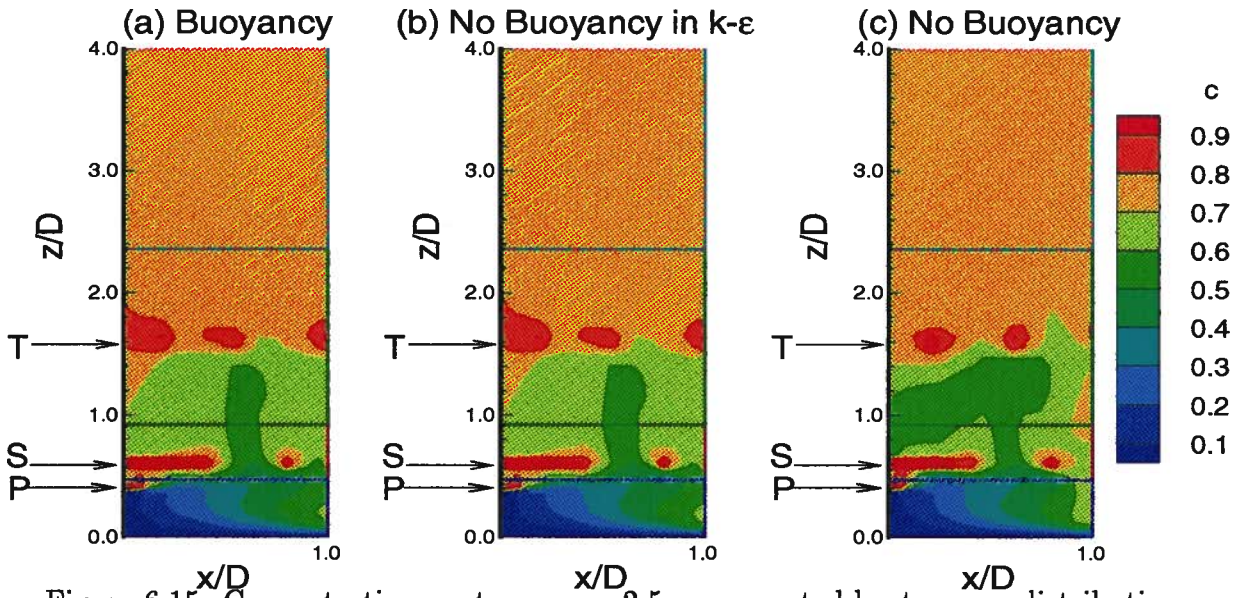

Figure 6.15: Concentration contours, $y = 2.5m$, computed heat source distribution.

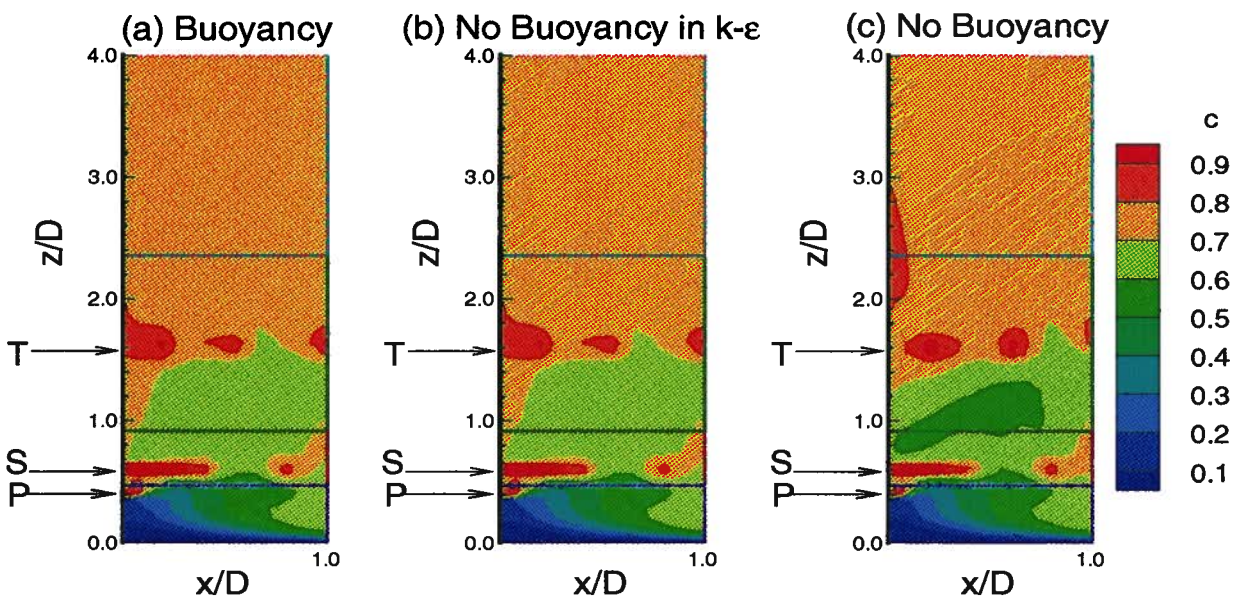

Figure 6.16: Concentration contours, $y = 2.5m$, assumed heat source distribution.

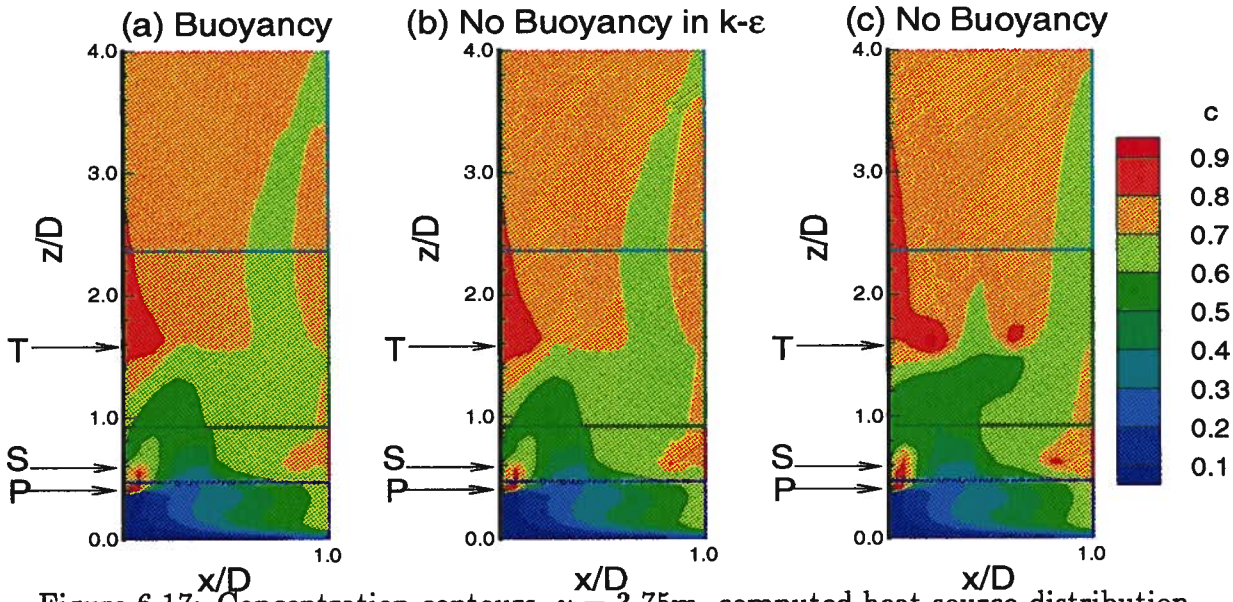

Figure 6.17: Concentration contours, $y = 3.75m$, computed heat source distribution.

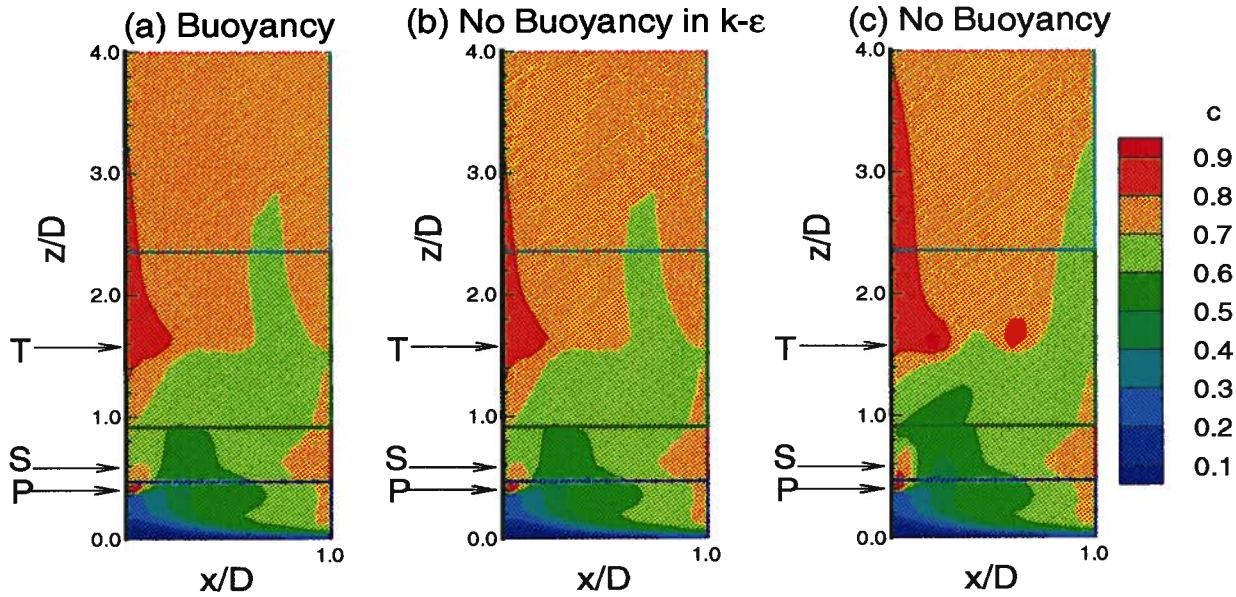

Figure 6.18: Concentration contours, $y = 3.75m$, assumed heat source distribution.

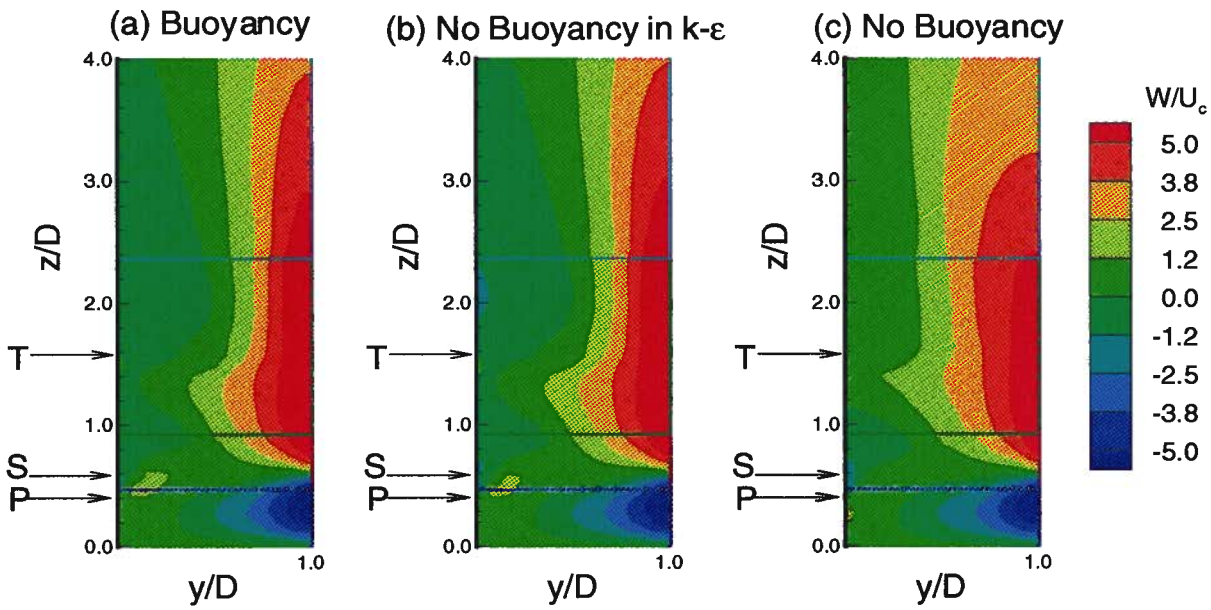

Figure 6.19: Vertical velocity contours, $x = 5m$, computed heat source distribution.

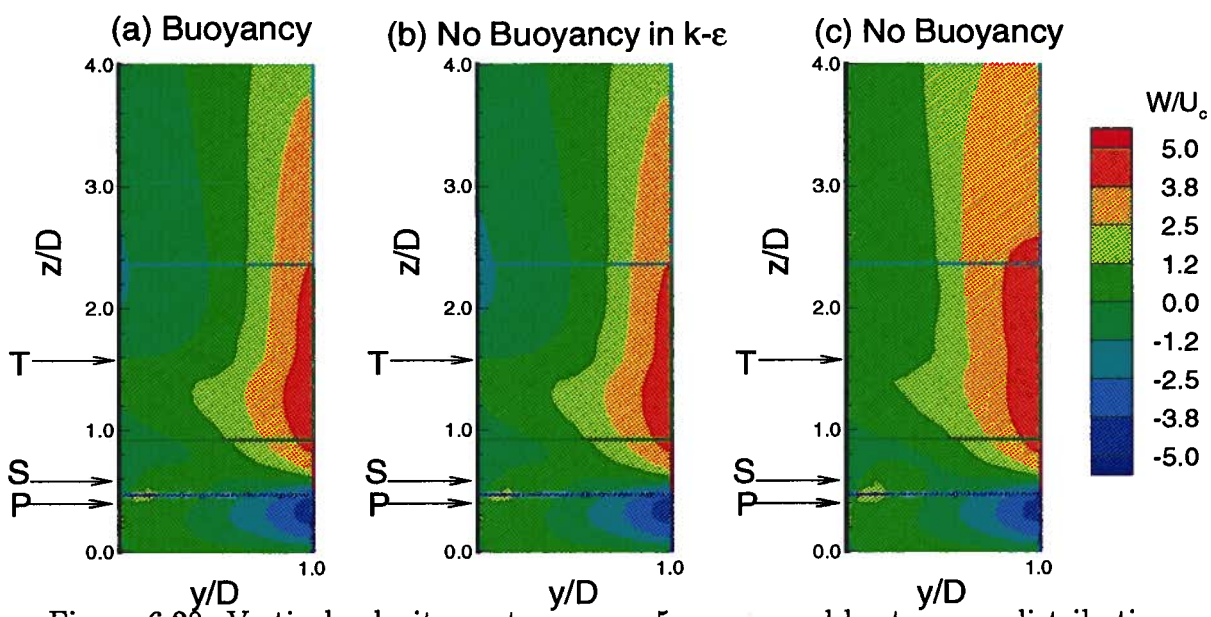

Figure 6.20: Vertical velocity contours, $x = 5m$, assumed heat source distribution.

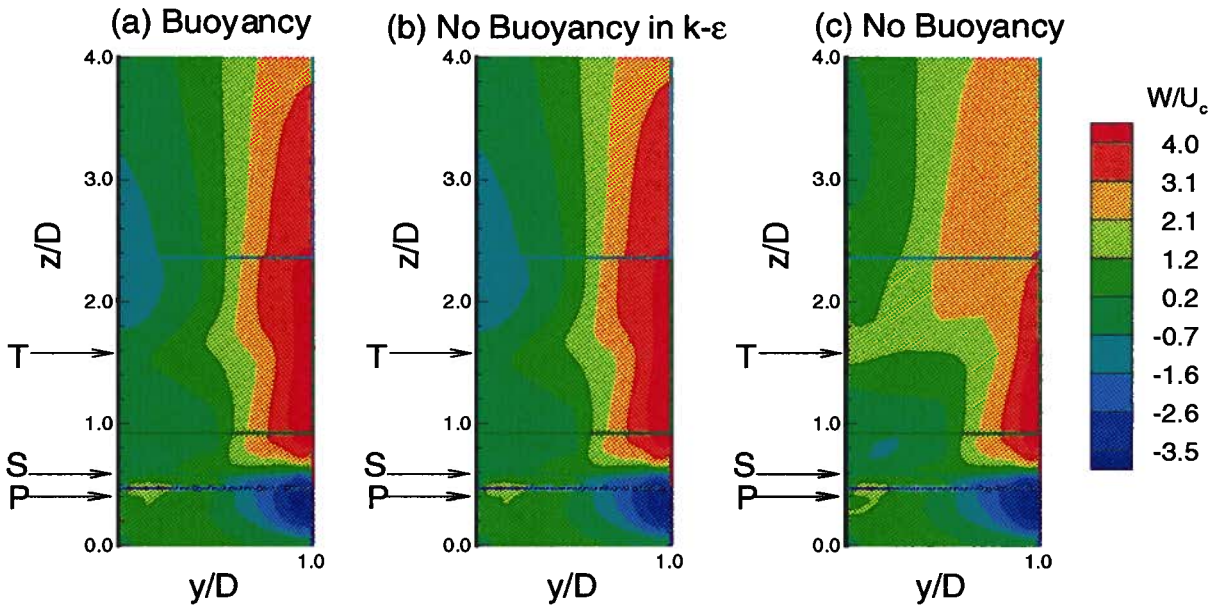

Figure 6.21: Vertical velocity contours, $x = 4m$, computed heat source distribution.

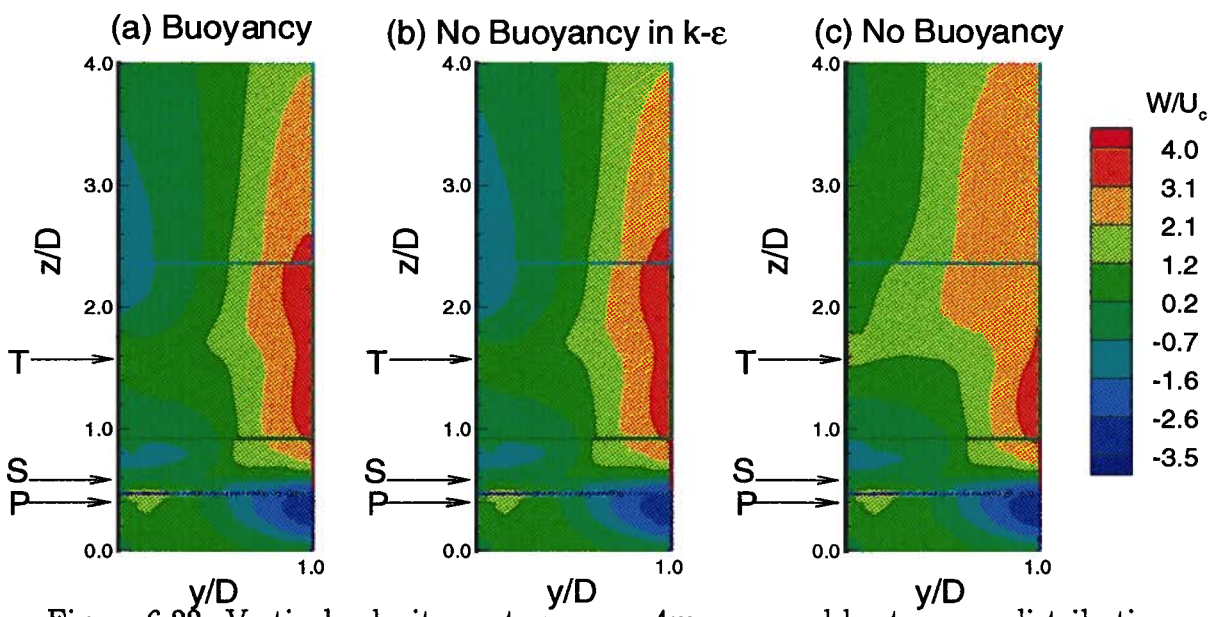

Figure 6.22: Vertical velocity contours, $x = 4m$, assumed heat source distribution.

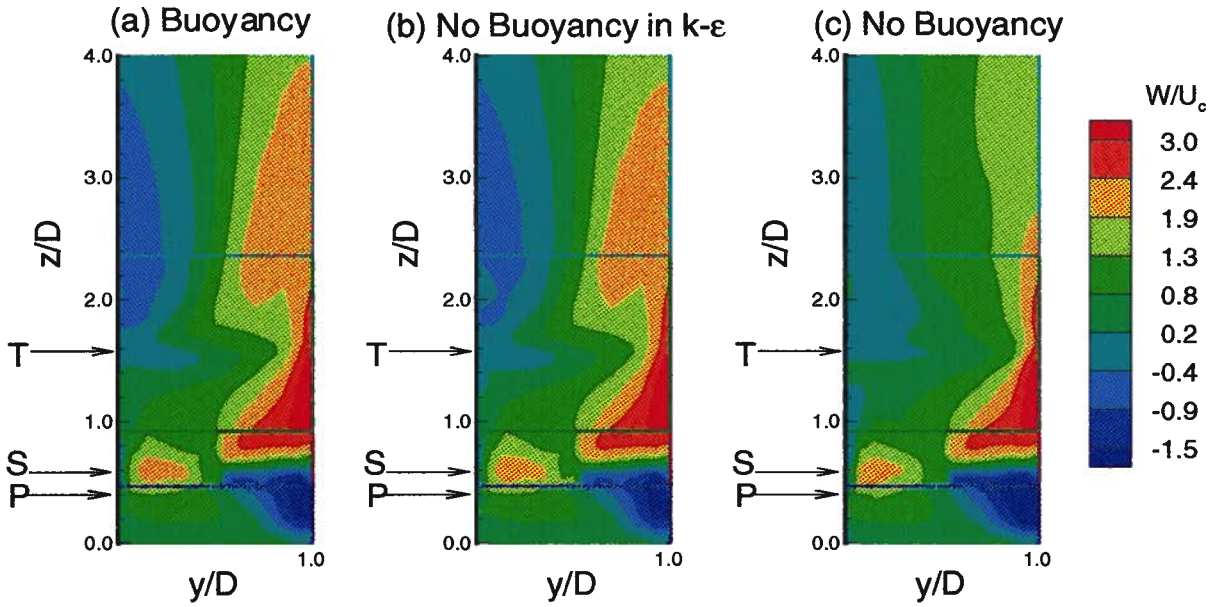

Figure 6.23: Vertical velocity contours, $x = 3m$, computed heat source distribution.

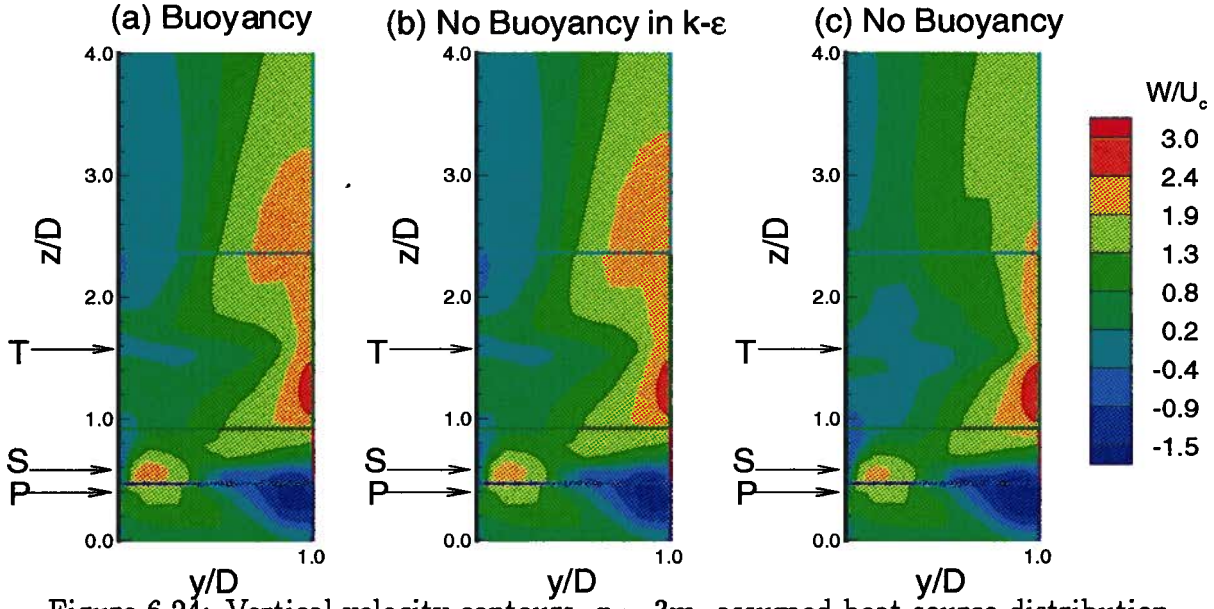

Figure 6.24: Vertical velocity contours, $x = 3m$, assumed heat source distribution.

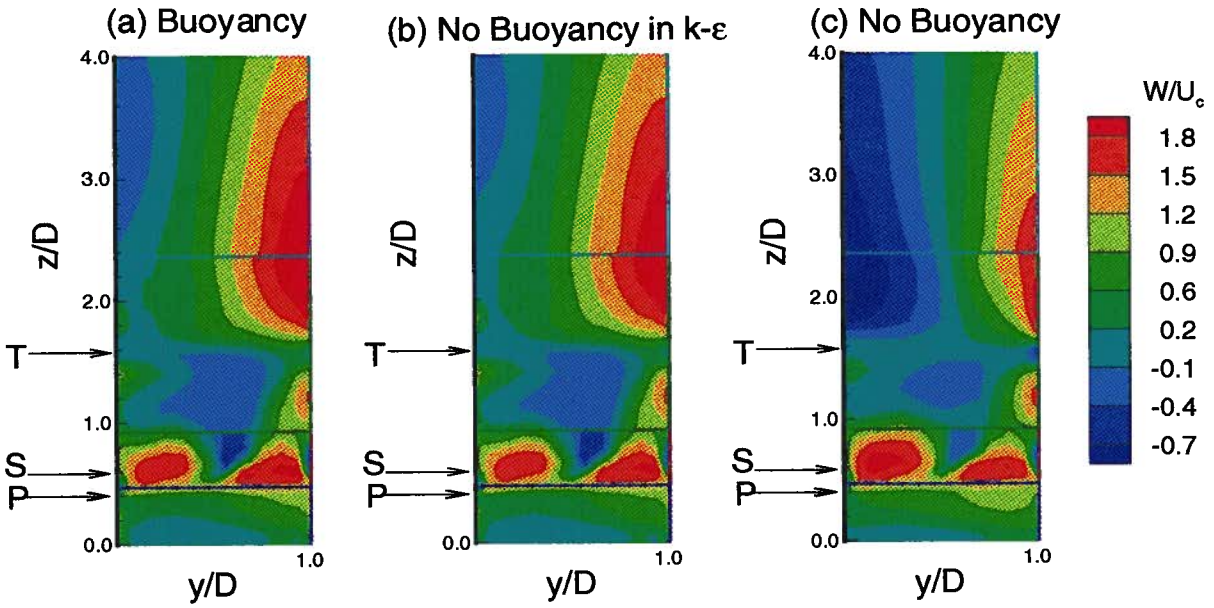

Figure 6.25: Vertical velocity contours, $x = 1m$, computed heat source distribution.

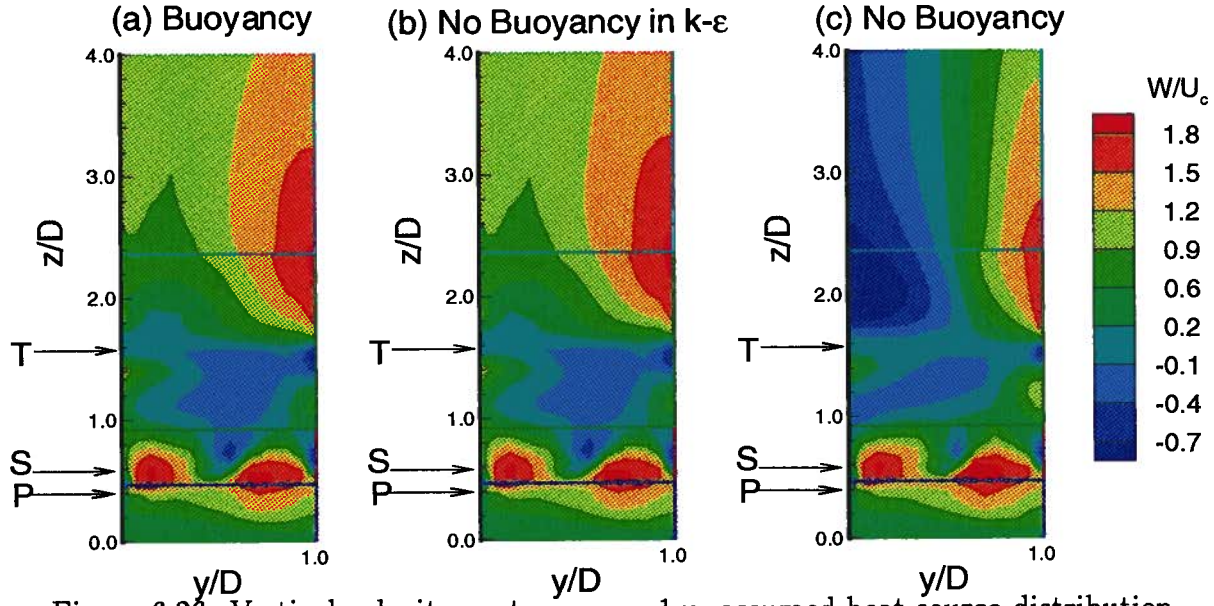

Figure 6.26: Vertical velocity contours, $x = 1m$, assumed heat source distribution.

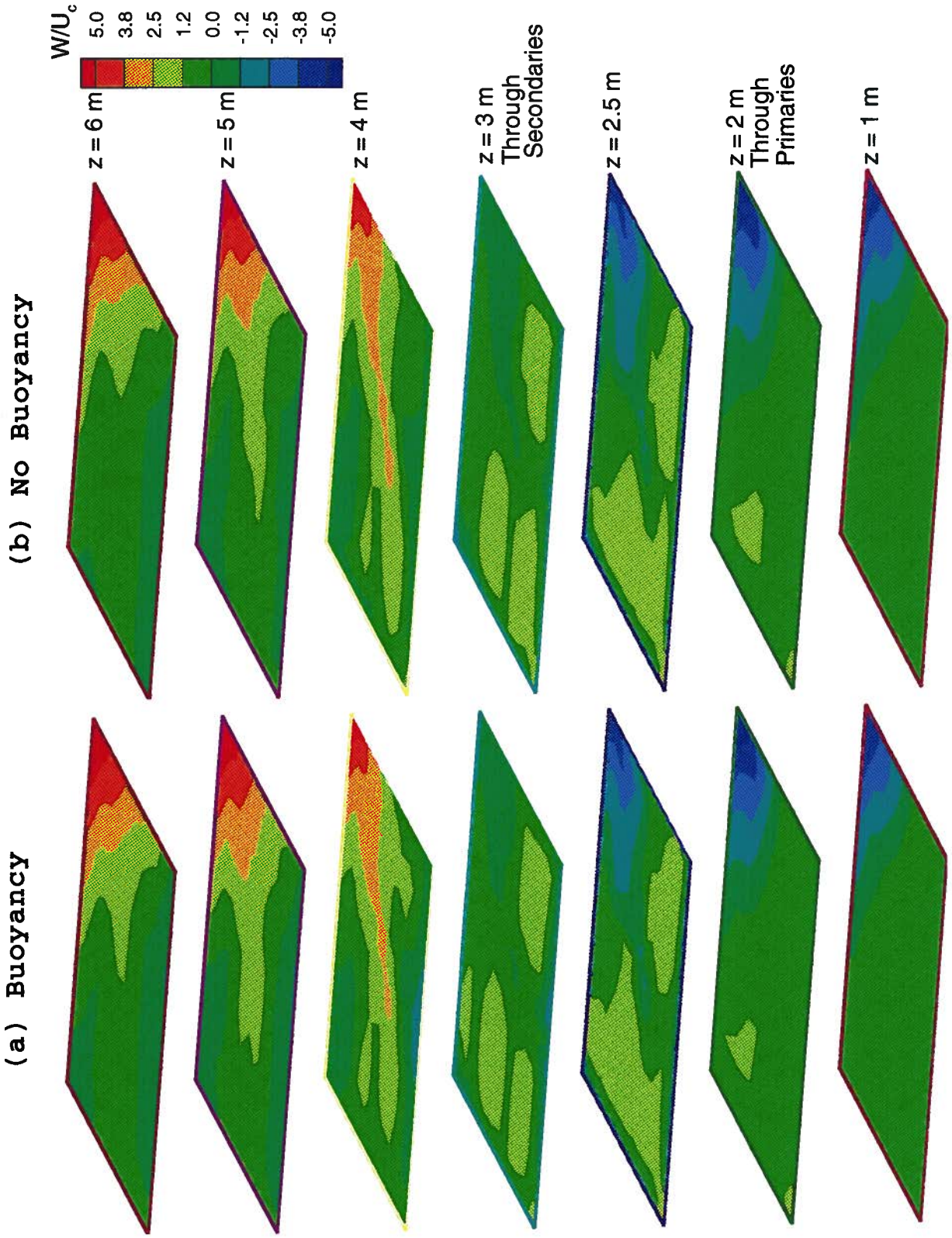

Figure 6.27: Vertical velocity contours in horizontal planes, computed heat source distribution.

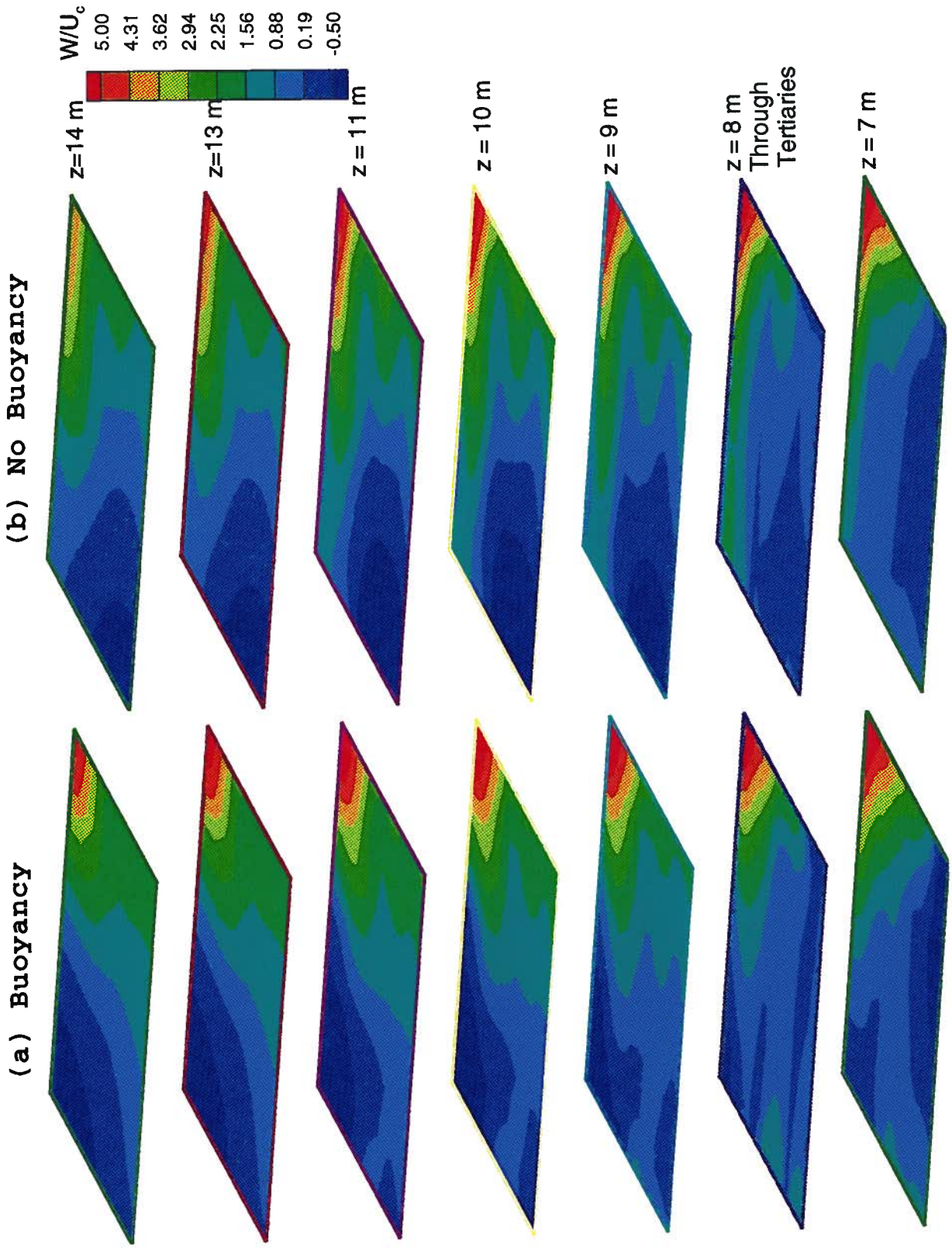

Figure 6.28: Vertical velocity contours in horizontal planes, computed heat source distribution.

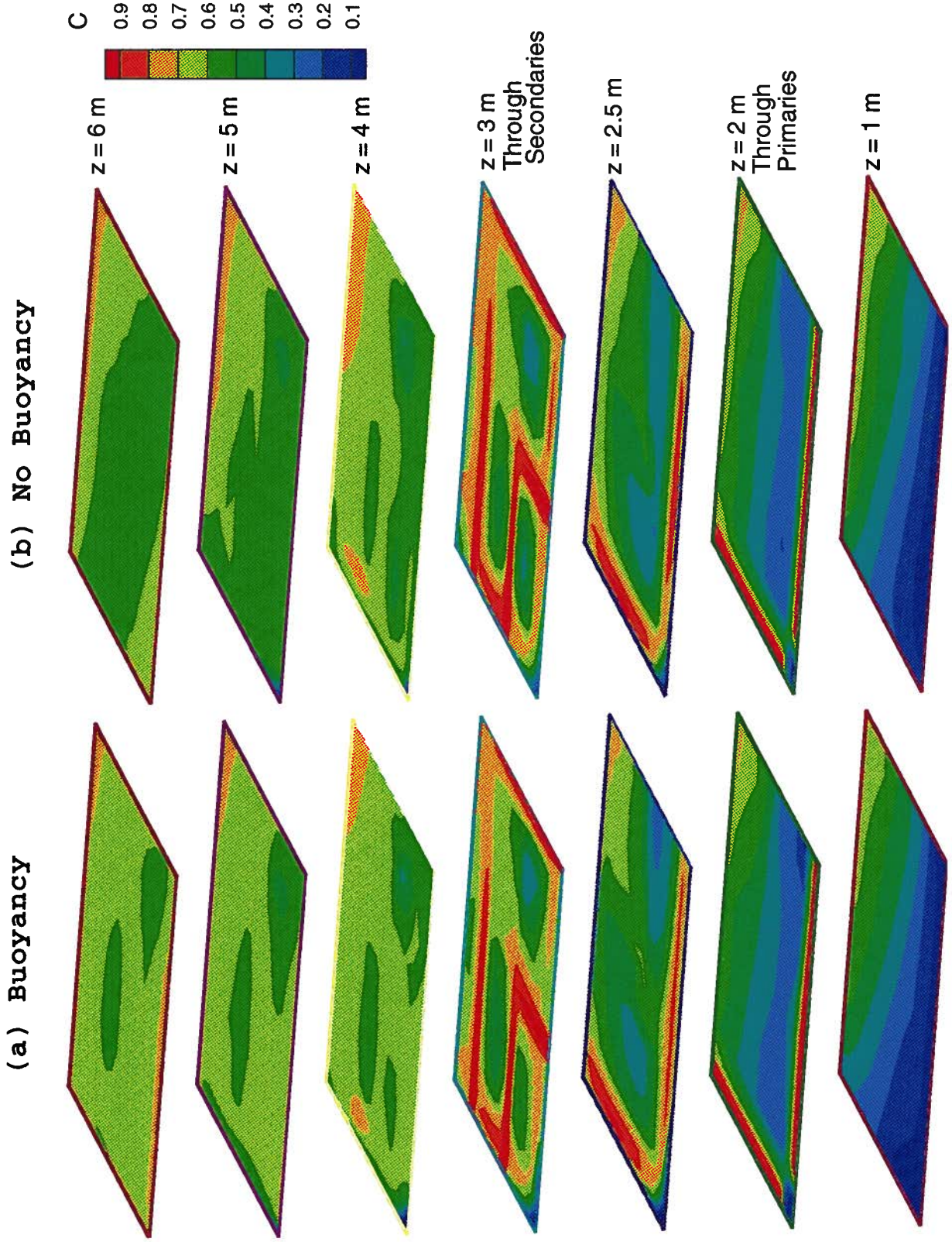

Figure 6.29: Concentration contours in horizontal planes, computed heat source distribution.

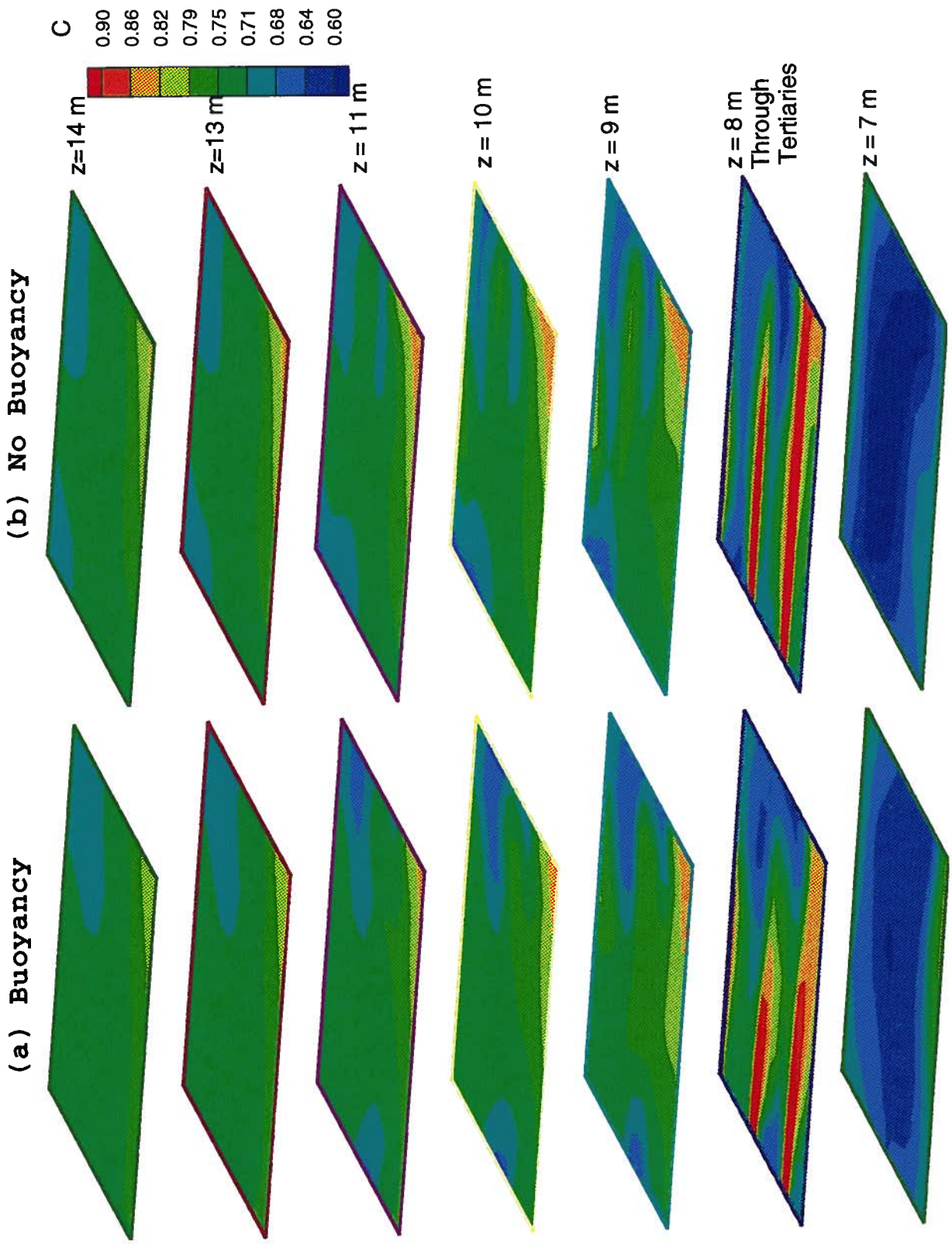

Figure 6.30: Concentration contours in horizontal planes, computed heat source distribution.

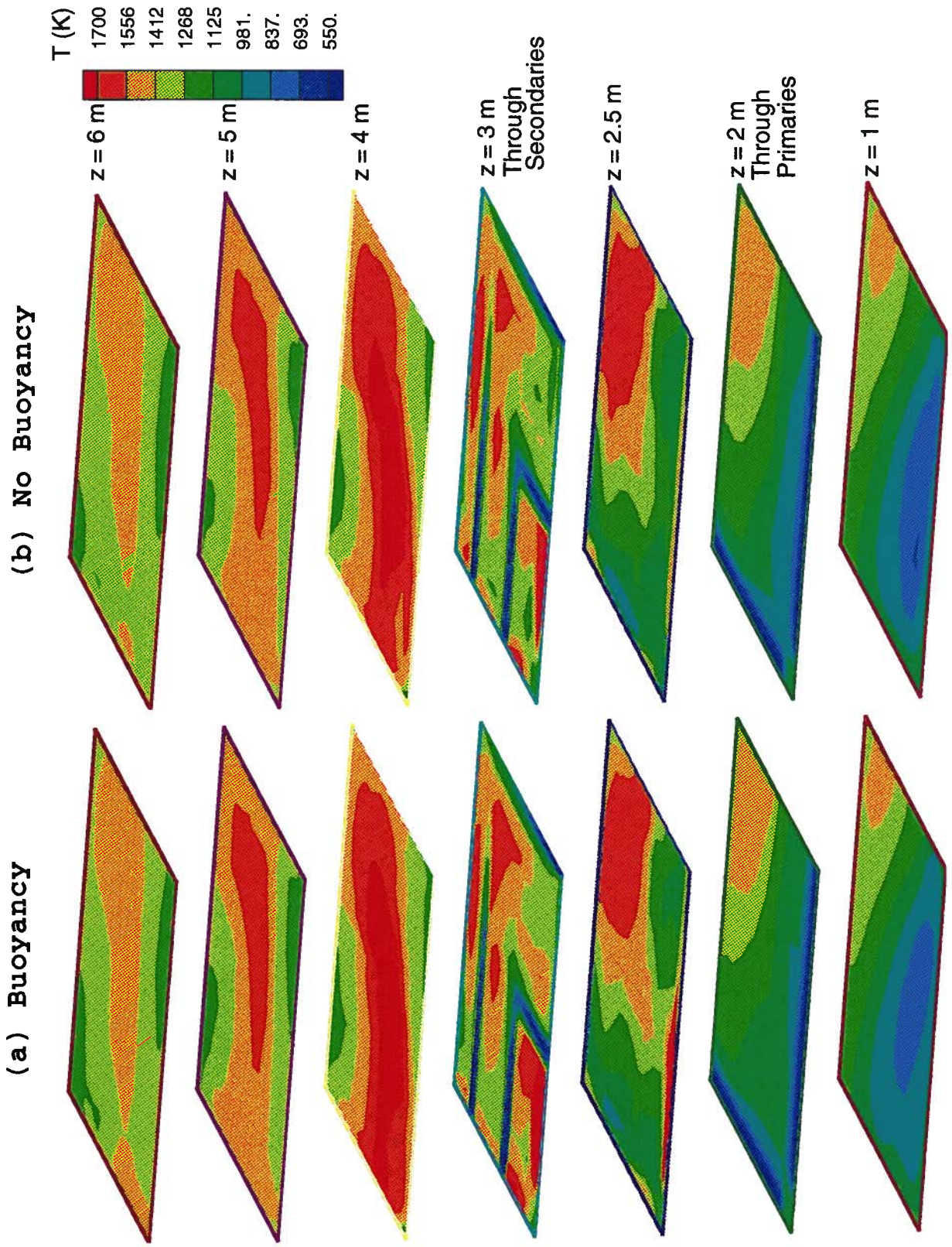

Figure 6.31: Temperature contours in horizontal planes, computed heat source distribution.

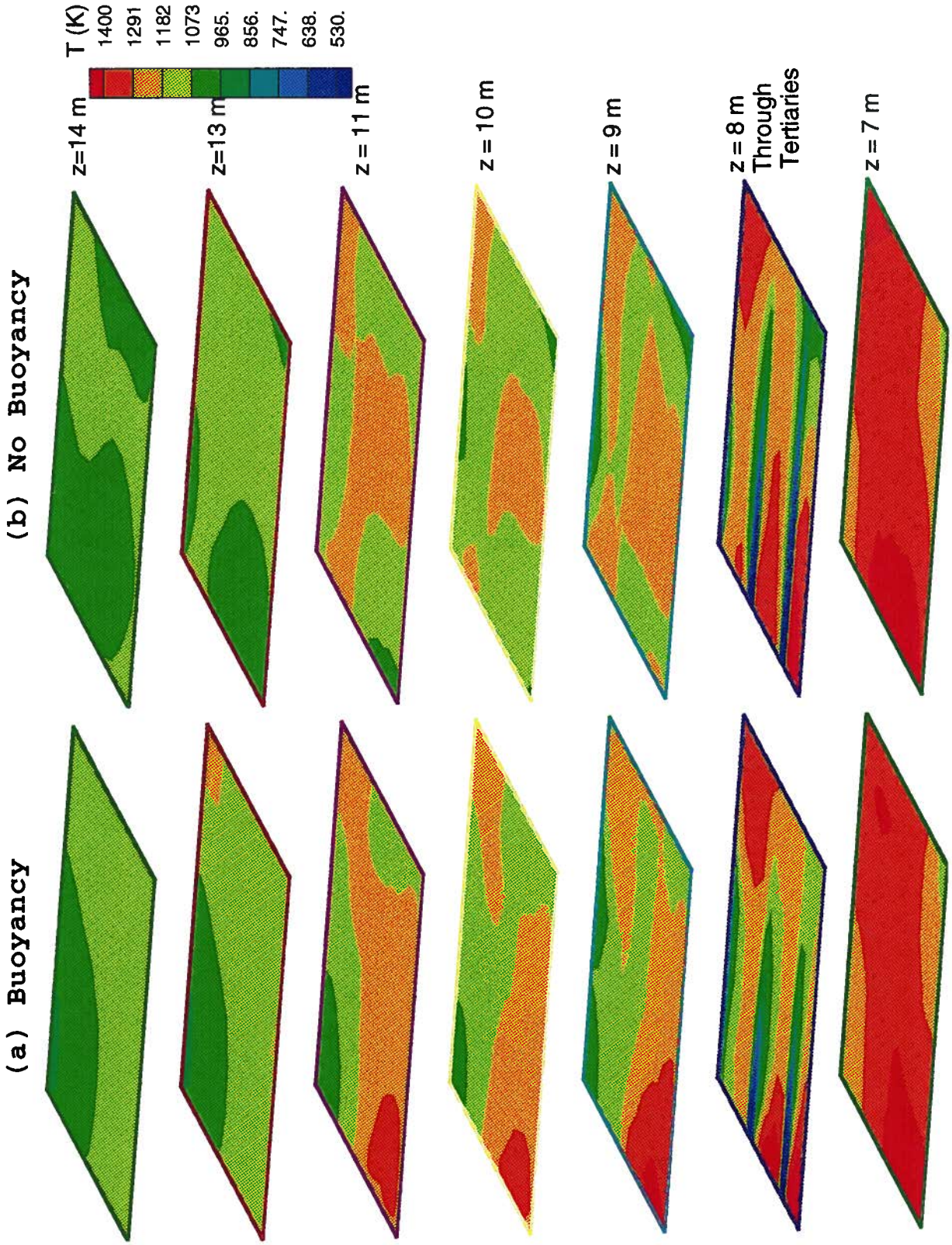

Figure 6.32: Temperature contours in horizontal planes, computed heat source distribution.

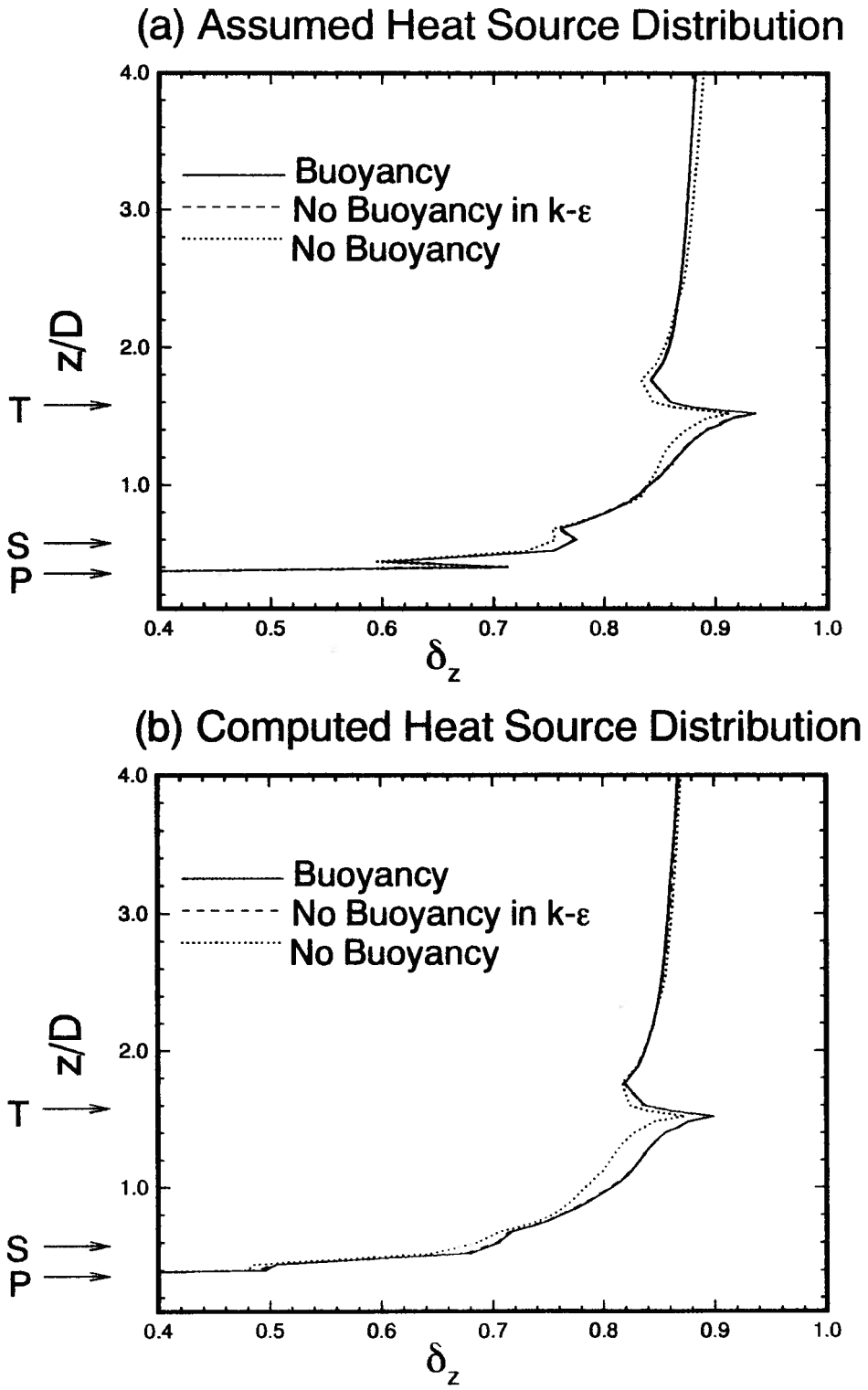

Figure 6.33: Extent of mixing of the jets and the crossflow in the furnace.

Chapter 7

Conclusions and Recommendations

The main conclusions of this investigation are divided into two parts:

1. Conclusions based on the experimental study:

   - In our experimental study, the ratio of jet to crossflow density was increased, under constant mass flow ratio conditions, and the jet penetration and consequently the size of the recirculation region formed downstream of the jet decreased. This indicates that jet penetration is not controlled by the jet to crossflow mass ratio and that the density and momentum flux ratios have a significant effect on the jet penetration.

   - When changing the density ratio of jet to crossflow, either the mass or the momentum flux ratio of jet to crossflow can be kept constant. The resultant variations in the flow behavior can not be attributed to the change in the buoyancy force only.

   - The good agreement between our experimental and numerical results for the carbon dioxide jet at mass ratios of 0.4, 0.6 and 0.8, indicates that our multigrid code can accurately predict such variable density flows. In the case of a helium/air jet, for the same mass ratios, the agreement in the near field was not good. The poor agreement was attributed to inaccuracies involved in turbulence modelling in the recirculation region. The larger size of the recirculation region formed downstream of the jet in this case results in larger

discrepancies than in the case of carbon dioxide.

- Our experimental study highlights the importance of using two suitable dimensionless numbers to compare the significance of buoyancy force for the problem of jet in crossflow under different flow conditions.

2. Conclusions based on the numerical study are summarized below.

In our simulations of the **two-dimensional jet issuing into a crossflow** , we have clarified certain basic characteristics of the effects of buoyancy force on the flow field. The blockage of the crossflow by the jet resulted in the formation of a recirculation region downstream of the jet.

For the high density jet issued horizontally into a vertically upwards low density crossflow:

- When the buoyancy force was ignored, the blockage of the crossflow by the jet was reduced and the size of the recirculation region was under-predicted.

- As the velocity ratio of jet to crossflow was increased from $R = 4$ to 6, jet penetration increased. For all cases simulated, omitting the buoyancy force resulted in underprediction of the jet penetration. However at $R = 4$ the differences were more significant.

- Decreasing the confinement width reduced the effect of the buoyancy force on the jet penetration. As the confinement width becomes smaller the jet penetration becomes more restricted by the opposite wall. The effect of this restriction is more significant on the jet with larger penetration. Due to this restriction the trajectories for the cases with and without buoyancy force come closer to each other.

- As the density ratio of jet to crossflow was decreased from 3 to 2, the jet penetration reduced. The difference between the jet penetration for the cases with and without

buoyancy force, however, increased. This result is due to the competing effects of the smaller density ratio, which weakens the buoyancy effects, and smaller momentum or mass flux ratios, which make the buoyancy effects of relatively greater importance.

- The buoyancy force enhances the spread of the jet. For all cases calculated, exclusion of the buoyancy force resulted in under-prediction of the spread of the jet. The extent of this under-prediction increases as the confinement width D/S increases and velocity ratio R decreases.

- The buoyancy force improves the mixing of the jet and the crossflow. This improvement is more significant in the far field, where the jet momentum has weakened.

- The effect of buoyancy on the decay of the maximum jet concentration is insignificant.

The **jet and crossflow orientation** was found to alter the effects of the buoyancy force on the flow field significantly. Four different flow orientations were tested. It was found that:

- In flows where the crossflow and buoyancy force are in the same direction, the jet penetration was found to be severely decreased by the buoyancy force.

- When the crossflow and the buoyancy force were in the opposite direction, the jet penetration was significantly enhanced, with a large recirculation region formed downstream of the jet. This was attributed to the effect of the buoyancy force in reducing the drag exerted by the crossflow on the jet.

- For a vertical jet injected downwards into a crossflow, where the jet momentum and the buoyancy force were in the same direction, ignoring the buoyancy force

results in small over-prediction of the jet penetration. The predicted jet trajectory remains closer to the injection wall resulting in a smaller recirculation region formed downstream of the jet than the case with no buoyancy force. The effect of the buoyancy force for this flow configuration is less significant than the case of the horizontal jet coming into a vertical crossflow. This was attributed to the orientation between the buoyancy force, the jet momentum, and the crossflow. As in the case of the vertical jets coming into a horizontal crossflow the line of action of the buoyancy force and the jet momentum is the same, the buoyancy adds or subtracts from a larger force and thus is less important.

- For a vertical jet injected upwards into a crossflow, where the jet momentum and the buoyancy force are in the opposite direction, ignoring the buoyancy force results in under-prediction of the jet penetration. The jet trajectory moves farther away from the injection wall and forms a larger recirculation region than the case of the jet with no buoyancy. The recirculation region formed downstream of the vertical jet injected downwards into the crossflow is smaller than the recirculation region formed by the same jet injected upwards. For all cases tested the effect of buoyancy force on the vertical jets was smaller than on the horizontal jets.

  These observations further indicate the complexity of the phenomena involved. These findings also suggest that in a study of the effects of buoyancy force on the flow field of jets in crossflow the orientation between the jet and the crossflow is an important factor. The results of a study on one flow configuration can not readily be extended to other flow configurations.

- In all cases calculated the effect of buoyancy force on the turbulence model did not alter the flow field significantly.

In our simulations of a **three-dimensional single jet and a row of jets** issuing horizontally into an upgoing confined crossflow, the effects of the buoyancy force on the flow field showed similar trends to those observed in the case of the two-dimensional jets. The effects of the flow variables such as jet to crossflow velocity ratio and the extent of the confinement, on the flow field were investigated. The results are summarized as follow.

- The omission of buoyancy force results in under-prediction of jet penetration.
- When buoyancy force is ignored the predicted jet trajectory remains closer to the injection wall than that of the jet with buoyancy force.
- The omission of the buoyancy force reduces the impingement of the jet on the opposite wall and the point of impingement moves further downstream.
- The exclusion of buoyancy force results in under-prediction of the lateral spread of the jet.
- As the ratio of jet to crossflow velocity increases the effect of buoyancy force on the flow field decreases.
- When the confinement width decreases the shape of the jet cross-section is significantly distorted by the opposite wall.
- The impingement of the jet on the opposite wall distorts the jet cross-section significantly.
- The exclusion of the buoyancy force results in under-prediction of mixing between the jet and the crossflow.
- Comparing the penetration and trajectory of the row of jets with the single jet, a smaller effect of buoyancy force in the case of single jet was apparent.

- The penetration of a row of jets with jet spacing of $5S$ into a crossflow is smaller than the penetration of a single jet.

Based on the results obtained from the simulations of the flow field inside a **kraft recovery furnace** it can be concluded that:

- The spread of the tertiary air jets can be restricted due to the presence of the side walls. As the jets with buoyancy spread more than the jets without buoyancy, the effect of the side walls on these jets is stronger. As a consequence of this, the calculations without the buoyancy force over-predicts the penetration of the tertiary jets which are next to the wall.

- The penetration of the secondary air jets is not significantly altered by the buoyancy force.

- The effect of the buoyancy force in the lower furnace (below the secondaries) is insignificant. The size of the core of the upwards gases in the center of the furnace, formed above the secondaries, is slightly under-predicted when the buoyancy force is omitted from the calculations. Ignoring the buoyancy force results in prediction of slightly lower values of temperature distribution in the upper furnace. However, the gross features of the flow are similar. Considering the uncertainties involved in radiation and combustion modelling, the inaccuracies introduced due to excluding the buoyancy force are insignificant.

- The effect of buoyancy force on the turbulence does not alter the flow field inside the boiler. Therefore these terms can be omitted from the calculations.

- The effect of buoyancy force on the flow field of the kraft recovery furnace was similar for both combustion models tested. This indicates that for the models

tested the trends observed are not significantly sensitive to variations in the heat source distributions.

The numerous calculations required in our study of jets in crossflow are performed efficiently and successfully with the use of the multigrid technique. In all cases the inclusion of the buoyancy terms in momentum and $k - \epsilon$ equations resulted in slower convergence.

A few suggested areas of **future research** and some **recommendations** follow.

- Our study has shown that the trajectory and penetration of the jet into crossflow and the effect of buoyancy force on these flows is significantly affected by the orientation of the jet and the crossflow. Further investigations are necessary to establish flow conditions under which results obtained from one flow configuration can be extended to the others. An extension of this study to a three-dimensional single jet is necessary.

- Though the $k - \epsilon$ model is adequate in simulating gross flow features such as the penetration and spreading rates of jets, the comparison of the experimental and predicted results indicated the inadequacy of the model in predicting the detailed features of the flow fields with larger recirculation regions. Further studies are needed in this area, possibly using higher order turbulence models described by Leschziner (1989).

- In simulations of the furnace geometry, the bullnose and the bed are not included. These obstructions will reduce the size of the available space for the penetration of the jets. This may have a similar effect as reducing the width of the confinement, that is, it will further reduce the effect of the buoyancy force on the flow field. However, this assumption needs to be further investigated.

- At the time of this study the radiation and combustion models used in the study of the flow field inside the furnace could be calculated only on one grid level. To reduce the number of required nodes, therefore, a symmetrical furnace geometry was simulated here. Because at high momentum flux ratios of jet to crossflow the interaction of the opposed jets may lead to flow instabilities (Quick et al. 1991), a full boiler geometry simulation is recommended for analysis of the combined effects of buoyancy and possible instabilities.

- It would be useful to study the effect of the buoyancy force in a furnace where the tertiaries were interlaced and not opposed. In such a case the spread of the jets would be more limited, and their penetration less constrained. This may alter the differences between the flow fields for the cases with and without buoyancy force.

Appendix A

Mixing of Variable Density Jets with Crossflow

In this appendix a quantitative measure is derived to describe the extent of jet mixing with the crossflow.

Consider a jet with volume flow rate Q_1 and density ρ_1 discharging into a main-stream of volume flow rate Q_2 and density ρ_2. We take the normalized concentration of the tracer in the jet to be one and that of the crossflow to be zero. Let C to be the normalized concentration of tracer per unit volume at any point in the mixture. The average concentration of the mixture can be defined as:

$$\bar{C} = \frac{\rho_1 Q_1}{\rho_1 Q_1 + \rho_2 Q_2} \tag{A.1}$$

At some cross-section downstream, perfect mixing is obtained and everywhere at this cross-section the value of concentration of jet in crossflow is $\bar{C}$. By continuity of fluid mass and tracer concentration, at a cross-section A downstream of the jet we have:

$$\int_A \rho v . dA = \rho_1 Q_1 + \rho_2 Q_2 \tag{A.2}$$

$$\int_A C \rho v . dA = \rho_1 Q_1 \tag{A.3}$$

Combining Equations A.1 through A.3:

$$\int_A C \rho v \cdot dA = \bar{C}(\rho_1 Q_1 + \rho_2 Q_2) \tag{A.4}$$

$$\int_A C\rho v \cdot dA = \bar{C}\int_A \rho v.dA \tag{A.5}$$

That is:

$$\int_A (C-\bar{C})\rho v \cdot dA = 0 \tag{A.6}$$

At each point on a given cross-section, $(\rho v dA)$ gives the mass flow rate and $(C-\bar{C})$ gives the deviation from average concentration. In this way we can determine the mass flow rate having a certain concentration range at each cross-section. This can be plotted in the form of a histogram or quantitatively as a probability density function $P(\zeta)$:

$$P_z(\zeta) \equiv \frac{1}{\Delta\zeta}\left[\frac{(v\rho dA)|_z \text{having concentration in range} \zeta \pm \frac{\Delta\zeta}{2}}{\rho_1 Q_1 + \rho_2 Q_2}\right] \tag{A.7}$$

where $\zeta = C - \bar{C}$.

We can verify that the area under the $P(\zeta)$ vs. ζ curve is unity and that $P(\zeta)$ has an expected mean of zero. From Equation A.2 and A.7:

$$\begin{aligned}\int_{-\infty}^{\infty} P(\zeta).d\zeta &= \frac{\int_A \rho v.dA}{\rho_1 Q_1 + \rho_2 Q_2} \\ &= 1\end{aligned} \tag{A.8}$$

From Equations A.1 to A.3 the first moment of $P(\zeta)$ is:

$$\begin{aligned}\int_{-\infty}^{\infty} \zeta P(\zeta)\cdot d\zeta &= \frac{\int (C-\bar{C})\rho v.dA}{\rho_1 Q_1 + \rho_2 Q_2} \\ &= \frac{\int C\rho v \cdot dA - \bar{C}\int \rho v \cdot dA}{\rho_1 Q_1 + \rho_2 Q_2} \\ &= \frac{\rho_1 Q_1 - \bar{C}(\rho_1 Q_1 + \rho_2 Q_2)}{\rho_1 Q_1 + \rho_2 Q_2} \\ &= \frac{\rho_1 Q_1 - \rho_1 Q_1}{\rho_1 Q_1 + \rho_2 Q_2} \\ &= 0\end{aligned} \tag{A.9}$$

In cross-sections where the jet and crossflow have not mixed well there will be a substantial mass flow rate having concentrations that are very different from $\bar{C}$. Further downstream where the fluids are well mixed values of C are very close to $\bar{C}$ and consequently a plot of $P(\zeta)$ vs. ζ will resemble a tall and narrow distribution. The variance of $P(\zeta)$ therefore is a quantitative measure of unmixedness. A perfectly mixed condition has variance equal to zero, while a perfectly unmixed condition leads to the maximum variance σ^2_{max}.

$$\sigma_z^2 = \int_{-\infty}^{\infty} \zeta^2 P(\zeta).d\zeta \tag{A.10}$$

where z is the distance downstream of the jet. σ^2_{max} can be evaluated by considering a surface which includes the jet exit and unmixed fluid upstream of the jet. At this cross-section $P(\zeta)$ is zero everywhere except for ζ corresponding to $C = 1$ (the unmixed jet) and $C = 0$ (the unmixed crossflow).

$$\begin{aligned}
\sigma_0^2 &= \int_{-\infty}^{\infty} \zeta^2 P(\zeta) \cdot d\zeta \\
&= (1-\bar{C})^2 \frac{\rho_1 Q_1}{\rho_1 Q_1 + \rho_2 Q_2} + (0-\bar{C})^2 \frac{\rho_2 Q_2}{\rho_1 Q_1 + \rho_2 Q_2} \\
&= \frac{(1-\bar{C})^2 \rho_1 Q_1 + \bar{C}^2 \rho_2 Q_2}{\rho_1 Q_1 + \rho_2 Q_2}
\end{aligned} \tag{A.11}$$

Finally the normalized measure of unmixedness can be defined as:

$$\delta_z' = \sqrt{\frac{\sigma_z^2}{\sigma^2_{max}}} \tag{A.12}$$

Alternatively the normalized measure of mixedness can be defined as:

$$\delta_z = 1 - \sqrt{\frac{\sigma_z^2}{\sigma^2_{max}}} \tag{A.13}$$

This analysis can be modified in a straightforward manner to account for multiple jets.

References

Abdullah, Z., Salcudean M., Nowak P., Xiao Z., Savage M., Markovic C., Uloth V., and Thorn P., "An Initial Validation of a Cold Flow Mathematical Model of a Recovery Boiler", TAPPI Proceedings, 1993 Engineering Conference, Orlando, August, 1993.

Abramovich, G. N., "The Theory of Turbulent Jets", M.I.T. Press, Cambridge, Mass., 1963.

Adams, T. N., "Air Jets and Mixing in Kraft Recovery Boilers", TAPPI Seminar Notes, pp.177-184, Kraft Recovery Operations, Orlando, Florida, 1987.

Adams, T. N., and Frederick W. J., "Kraft Recovery Boiler Physical and Chemical Processes", The American Paper Institute, Inc., New York, 1988.

Ammari, H. D., Hay, N., and Lampard, D., "The Effect of Density Ratio on the Heat Transfer Coefficient from a Film Cooled Flat Plate", ASME Paper No. 89-GT-176, 1989.

Anderson, D. A., Tannehill, J. C., Pletcher, R. H., "Computational Fluid Mechanics amd Heat Transfer", McGraw-Hill, New York, 1984.

Andreopoulos, J., "Heat Transfer Measurements in a Heated Jet-Pipe Flow Issuing Into a Cold Cross-Stream", Physics of Fluids, Vol.26, pp.3201-3210, 1983.

Barsin, J. A., "Recovery Boiler Design Considerations", TAPPI Seminar Notes, pp.223-238, Kraft Recovery Operations, Orlando, Florida,1989.

Bianca, J. D., Bauver, W. P., and McGowan, J. G., "An Aerodynamic Study of an Operating Tangential Fired Furnace", Fluid Mechanics of Combustion Systems, Boulder, Colo., pp.51-63, 1981.

Bolton, H. C., and McWilliam, I. G., "Ionization in Flames: Current-Voltage Relationships for the Flame Ionization Detector", Proc. Roy. Soc. Lond. A. Vol. 321, pp. 361-380, 1971.

Bird, R.B., Stewart W.E., and Lightfoot E.N. "Transport Phenomena", John Wiley, New York, 1960.

Blackwell, B., "Improved Gas Mixing in Kraft Recovery Boilers - Air Jet Theory", Report V7582, Sandwell, Vancouver, B.C., November, 1990.

Brandt, A., "Multilevel Adaptive Computations in Fluid Dynamics", AIAA Journal, vol.18, no.10, pp.1165-1172, 1980.

Briggs, G. A., "Plum Rise", AEC Critical Review Series, TID 25075, Atomic Energy Commission, Washington D. C., 1969.

Crabb, D., Durao, D. F. G., and Whitelaw, J. H., "A Round Jet Normal to a Cross-Flow", Trans. ASME J. Fluids Engrg., Vol. 103, pp.142-153, 1981.

Chao, Y. C. and Ho W. C., "Numerical Investigation of Heated and Unheated Lateral Jets Discharging into a Confined Crossflow", Numerical Heat Transfer, Part A, vol.22,pp.343-361, 1992.

Chapman, P. J., and Jones, A. K., "Recovery Boiler Secondary Air System Development using Experimental and Computational Fluid Dynamics", TAPPI Proceedings, Engineering Conference, pp.193-203, 1990.

Chu, V. H., and Goldberg, B., "Buoyant Forced-Plums in Cross Flow", Journal of the Hydraulics Division, ASCE, vol.99, No. HY9, pp.1203-1214, Sep. 1974.

Claus, R. W., and Vanka, S. P., "Multigrid Calculation of a Jet in Cross Flow", AIAA, Paper No. AIAA-90-0444, 1990.

David, D. J., "Gas Chromatagraphic Detectors", John Wiley and Sons, New York, 1974.

Davison, F. J.,"Nozzle Scaling in Isothermal Furnace Models", Journal of the Institute of Fuel, Vol.41, pp.470-475, 1968.

Demuren, A. O., "Numerical Calculations of Steady Three-Dimensional Turbulent Jets in Cross Flow", Computer Methods in Applied Mechanics and Engineering, Vol. 37, pp.309-328, North-Holland Publishing Company, 1983.

Demuren, A. O., "Multigrid Acceleration and Turbulence Models for Computations of 3D Turbulent Jets in Crossflow", Int. J. Heat Mass Transfer, Vol. 35, No. 11, pp.2783-2794, 1992.

Fackrell, J. E., "A System for Turbulent Concentration Measurements", The Institute of Physics, No. 0022-3735/78/0010-1015, pp. 1015-1023, 1978.

Fackrell, J. E., "A Flame Ionisation Detector for Measuring Fluctuating Concentration", J. Phys. E: Sci. Instrum., No. 0022-3735/80/08088, Vol. 13, pp. 888-893, 1980.

Ferrell, G. B., Abujelala, M. T., Busnaina, A. A., and Lilley, D. G., "Lateral Jet Injection into Typical Combustor Flowfields", AIAA Paper 84-0374, New York, 1984.

Ferrell, G. B., and Lilley, D. G., "Turbulence Measurements of Lateral Jet Injection into Confined Tubular Crossflow", AIAA Paper 87-1102, New York, 1985.

Franke, R., Leschziner, M. A., and Rodi, W., "Numerical Simulation of Wind- Driven Turbulent Flow in Stratified Water Bodies", Third International Symposium on Stratified Flows, California Institute of Technology, Passadena, 1987.

Goldstein, R. J., "Film Cooling", Advances in Heat Transfer, vol.7, pp.321-379 , 1971.

Gosman, A. D., Pun, W. M., Runchal, A. K., Spalding, D. B., and Wolfstein, M., "Heat and Mass Transfer in Recirculating Flows", Academic Press, 1969.

Grace, T. M., "Chemical Recovery in the Alkaline Pulping Processes", TAPPI Press, Atlanta, 1985.

Grace, T., Walsh, A., Jones, A., Sumnicht, D., and Farrington, T., "A Three- Dimensional Mathematical Model of the Kraft Recovery Furnaces", TAPPI short Course Notes, pp.173-180, Kraft Recovery Operations, 1990.

Gray, F. A. and Robertson, A. D., "The Deflection of Hot Jets due to Buoyancy", Journal of the Institute of Fuel, vol.29, No. 180, pp.424-427, 1956.

Haniu, H., "An Experimental Study of Two-Dimensional Buoyant Jets in Cross- Flow", M.A.Sc. Thesis, Department of Mechanical Engineering, The University of Iowa, Iowa City, U.S.A., 1979.

Hass, W., Rodi, W., and Shönung, B., "The Influence of Density Difference Between Hot and Coolant Gas on Film Cooling by a Row of Holes: Predictions and Experiments", ASME Paper No. 91-GT-255, 1991.

Hinze, J. O., "Turbulence", McGraw-Hill, New York, 1959.

Ideriah, F. J. K., "Turbulent Natural and Forced Convection in Plumes and Cavities", Ph.D. Thesis, Department of Mechanical Engineering, Imperial College, University of London, London, U.K., 1977.

Ince, N. Z., and Launder, B. E., "On the Computation of Buoyancy-Driven Turbulent Flows in Rectangular Enclosures", Int. J. Heat and Fluid Flow, Vol. 10, No. 2, June 1989.

Jones, A. K., "A Model of the Kraft Recovery Furnace", Ph.D. Thesis, The Institute of Paper Chemistry, Wisconsin, U.S.A., 1989.

Kamotani, Y. and Greber, I., "Experiments on a Turbulent Jet in a Cross Flow", AIAA Journal, vol.10, No. 11, pp.1425-1429, 1972.

Kamotani, Y. and Greber, I., "Experiments on Confined Turbulent Jets in Cross Flow", NASA CR-2392, 1974.

Ketler, S. P., "Physical Modelling of a Kraft Recovery Boiler", M.A.Sc. Thesis, Department of Mechanical Engineering, University of British Columbia, Vancouver, Canada, 1993.

Ketler, S. P., Savage, M. C., and Gartshore, I. S., "Physical Modelling of Flows in Black Liquor Recovery Boilers", TAPPI Proceedings, Engineering Conference, pp.581-599, 1992.

Ketler, S. P., Savage, M. C., and Gartshore, I. S., "Recovery Boiler Sensitivity to Secondary Level Flows", TAPPI Proceedings, Engineering Conference, pp.271- 285, 1993.

Khalil, E. E., "Modelling of Furnaces and Combustors", Abacus Press, Kent, Great Britain, 1982.

Kikkawa, S., and Ozaki, K., "The Effect of Density Ratio of Injectant and Main Stream Gases on Film Cooling Effectiveness on a Gas Turbine Blade", Heat Transfer-Japanese Research, Vol.21, No.6, pp.21-30, 1988.

Lai, K. Y. M., "TURCOM: A Computer Code for the Calculation of Transient, Multi-Dimensional, Turbulent, Multi-Component Chemically Reactive Fluid Flows. Part I: Turbulent, Isothermal and Incompressible Flow", NASA Technical Report, TR-GD-011, NRC No. 27632.

Launder, B. E. and Spalding, D. B., "Mathematical Models of Turbulence", Academic Press, London, 1972.

Launder, B. E. and Spalding, D. B., "The Numerical Computation of Turbulent Flows", Computer Methods in Applied Mechanics and Engineering, vol. 3, pp.269-289, 1974.

Lefebvre, B. E. and Burelle, R., "The Chemical Recovery Boilers Optimized Air System", TAPPI Seminar Notes, pp.239-246, Kraft Recovery Operations, 1989.

Leschziner, M. A., and Rodi, W., "Three-Dimensional Calculations of a Coaxial Heated Water Discharge", Internal Report No. SFB 80/T/218, University of Karlsruhe, 1982.

Markatos, N. C., and Malin, M. R., "Mathematical Modelling of Buoyancy Induced Smoke Flow in Enclosures", Int. J. Heat Mass Transfer, Vol. 25, No. 1, pp.63- 75, 1982.

McMurry, C. B., Ong, L. H., and Lilley, D. G., "Two Opposed Lateral Jets Injected into Swirling Crossflow", AIAA Paper 87-0307, New York, 1987.

McWilliam, I. G., "A Study of the Flame Ionisation Detector", Journal of Chromatography, Vol. 51, pp. 391-406, 1970.

Matys, P., "Black Liquor Combustion", Inter Departmental Report, Department of Mechanical Engineering, University of British Columbia, Vancouver, B.C., 1994.

Niessen, W. R., "Combustion and Incineration Processes : Applications in Environmental Engineering", Marcel Dekker Inc., New York, 1978.

Nowak, P. Z., "Multigrid Method", Internal Report, Department of Mechanical Engineering, University of British Columbia, 1992.

Ong, L. H., McMurry, B. C., and Lilley, D. G., "Hot-Wire Measurements of a Single Lateral Jet Injected into Swirling Crossflow", AIAA, Paper 86-0055, New York, 1986.

Patankar, S. V., "Numerical Heat Transfer and Fluid Flow", Hemisphere Publishing Corporation, McGraw-Hill, New York, 1980.

Patankar, S. V., Basu, D. K., and Alpay, S. A., "Prediction of the Three- Dimensional Velocity Field of a Deflected Turbulent Jet", J. Fluids Engrg. Vol. 99, pp.758-762, 1977.

Patterson, R. C., and Abrahamsen, R. F., "Flow Modelling of Furnaces and Ducts", Combustion, Vol.33-34, pp.47-55, 1962.

Perchanok, M. S., "Velocity Measurements in an Isothermal Scale Model of a Hog Fuel Boiler Furnace", M.A.Sc. Thesis, Department of Mechanical Engineering, University of British Columbia, Vancouver, 1988.

Perchanok, M. S., Bruce, D. M., and Gartshore, I. S., "Velocity Measurements in an Isothermal Scale Model of a Hog Fuel Boiler Furnace", Journal of Pulp and Paper Science, Vol.15, No.6, 1989.

Pietrzyk, J. R., Bogard, D. G., and Crawford, M. E., "Effects of Density Ratio on the Hydrodynamics of Film Cooling", ASME, Paper No. 89-GT-175, 1989.

Quick, J. W., Gartshore I.S., and Salcudean M., "The Bifurication of Steady States for Opposing Jets in Crossflow; Application to Recover Boilers", Proceedings of the Thirteenth Canadian Congress of Applied Mechanics, CANCAM 91, June 2-June 6, 1991.

Ramaprian, B. R., and Haniu, H., "Turbulence Measurements in Plane Jets and Plumes in Crossflow", IIHR Report No. 266, Institute of Hydraulic Research, The University of Iowa, Iowa City, IA, 1983.

Ramsey, J. W., and Goldstein, R. J., "Interaction of a Heated Jet with a Deflecting Stream", Journal of Heat Transfer, ASME, pp.365-372, 1971.

Reynolds, A. J., "Turbulent Flows in Engineering", John Wiely, New york, 1974.

Robins, A. G., "Experimental Model Techniques for the Investigation of the Dispersion of Chimney Plumes", Proc Instn Mech Engrs, No. 4, Vol. 189, pp. 44-54, 1975.

Rodi, W., "Turbulence Models and Their Application in Hydraulics-a state of the art review", International Association for Hydraulics, Delft, the Netherlands, 1984.

Rodi, W., and Srivasta, S. K., "A Locally Elliptic Calculation Procedure for Three-Dimensional Flows and its Application to a Jet in a Cross-Flow", Computer Methods in Applied Mechanics and Engineering, Vol. 23, pp.67-83, North-Holland Publishing Company, 1980.

Sabhapathy, P., "Radiative Heat Transfer in Kraft Recovery Boilers", Inter Departmental Report, Department of Mechanical Engineering, University of British Columbia, Vancouver, B.C., 1994.

Salcudean, M., Nowak P., and Abdullah Z., "Mathematical Modelling of Recovery Furnaces", TAPPI Proceedings, International Chemical Recovery Conference, Seatle, pp.197-208, June, 1992.

Schlichting, H., "Boundary Layer Theory", McGraw-Hill, 6th edition, 1978.

Sherif, S. A., and Pletcher, R. H., "Measurements of the Thermal Characteristics of Heated Turbulent Jets in Crossflow", Journal of Heat Transfer, Vol.111, pp.897-903, 1989.

Spalding, D. B., "The Art of Partial Modeling", 9th (Int.) Symposium on Combustion, Academic Press, New York, pp.833-843, 1962.

Thring, M. W., and Newby, M. P., "Partial Modelling", Fourth Symposium (International) on Combustion, pp.789-796, Williams and Wilkins, 1953.

Tse, D. C. M., "Multiple Jet Interaction with Special Relevance to Recovery Boilers", Ph.D. Thesis, Department of Mechanical Engineering, University of British Columbia, Vancouver, Canada, 1993.

Vanka, S. P., "A Calculation Procedure for Three-Dimensional Steady Recirculating Flows using Multigrid Methods", Computer Methods in Applied Mechanics and Engineering, vol.55, pp.321-338, 1986.

Watkins, A. P., "Flow and Heat Transfer in Piston/Cylinder Assemblies", P.h.D. Thesis, Imperial College, University of London, 1977.

Wright, S. J., "Effects of Ambient Crossflow and Density Stratification on the Characteristic Behavior of Round Turbulent Buoyant Jets", Ph.D. Thesis, California Institute of Technology, Pasadena, California, U.S.A., 1977.

Wylen, G. J. V., and Sonntag, R. E., "Fundamentals of Classical Thermodynamics", John Wiley & Sons, 1985.